Ph.D. Dissertation

Snow cover monitoring techniques with GB-SAR

Alberto Martínez Vázquez

Advisor:
Dr. Joaquim Fortuny Guasch
Joint Research Centre (JRC), Institute for
the Protection and Security of the Citizen (IPSC)
- Ispra, Italy -

Tutor:
Dr. Adriano Camps Carmona
Universitat Politècnica de Catalunya (UPC),
Dept. Teoria del Senyal i Comunicacions (TSC)
- Barcelona, Spain -

Barcelona, October 2008

A mi madre, padre y hermano,
por su esfuerzo y sacrificio constantes.

Contents

Preface

The work presented in this PhD thesis is the product of five years of research at the Joint Research Centre of the European Commision in Ispra (Italy). When I first arrived in 2003, the ground-based synthetic aperture radar LISA fully developed at JRC was a scientific success: a spin-off company had recently been created to start exploiting commercially this technology for monitoring large man-made structures, landslides and volcanoes. Scientific interest then gradually moved to a new field of application unknown at that time to the GB-SAR community: the snow cover. In this way I initiated, together with some colleagues, a route towards the unexplored...

Now, five years later, we feel much more confident of the possibilities of using GB-SAR to monitor snow cover. We have gained important experience and know-how, both in the sensor capabilities and in the snow field, which has dissipated the initial doubts about the whole project. A special emphasis has always been put on the operational use of the techniques presented in this PhD thesis. With eyes on the success of landslides real-time monitoring, the whole team's hope is to see one day also a community benefit from the results obtained with all the work carried out in the snow.

This PhD thesis owes much to the people I had the pleasure to work with during the past several years. Foremost I want to express my gratitude to my mentor in JRC and advisor of this thesis, Dr. Joaquim Fortuny Guasch, who offered me the opportunity to join his research group in 2003. Since then we enjoy a strong and productive complicity in the research field at work and a special friendship in the personal side for which I feel very fortunate.

Special thanks are due to Ing. Giuseppe Antonello for closely monitoring the proper functioning of the instruments and particularly for having the patience to implement all "suggested" software changes... The six field campaigns carried out would have been definitely not possible without his support.

I wish also to express my thanks to Dr. Dario Tarchi for his flexibility in allocating resources to make this project possible. Thanks also to Marco Basso and Jorge Figueiredo-Morgado for building all the mechanical structures and contributing to the deployment of the instruments in the test sites.

I am grateful to all my colleagues in the Sensors Radar technologies and Cybersecurity Unit of JRC for being always available to support me in all the different steps of this PhD thesis. In particular I want to mention Agnes Hegedus and Gian Luigi Ruzzante for their very special friendship and Adam Lewis for his constructive comments on this thesis and for taking the time to proofread it.

Sincere thanks also go to Dr. Adriano Camps Carmona from the Technical University of Catalonia in Spain (UPC) for his academic support at the beginning of my doctorate studies and for his continuous encouragement to complete this work.

Many people contributed to the deployment of the instruments and the collection and analysis of ground-truth data. I am particularly grateful to Urs Gruber and François Dufour from SLF Davos, to Michele Cucchi from the Corpo Guide Alpine d'Alagna, to Claudio Francione from Monterosa 2000 S.p.A. and to Andrea Pierrettori and Michele Freppaz from the Univerisy of Turin.

Finally, my father Cipriano, my mother Mª Ángeles, my brother Miguel-Ángel and my girlfriend Cristina, deserve a special mentioning for providing all the encouragement and support that led to this work.

Summary

Ground-based synthetic aperture radars (GB-SAR) are instruments that, although relatively young, are operationally used to monitor landslides with sub-millimetre accuracy. There are however other application fields that deserve some attention. Monitoring of the snow cover and, in particular, of those processes associated with the snow avalanches are a clear example of this. To date, monitoring of the snow cover has been traditionally carried out at local scale either with invasive sensors or with continuous wave (CW) radars, while at wider scales air- or satellite-borne sensors have been employed. The work presented in this PhD thesis is a first attempt to study the potential use of GB-SAR sensors to monitor the snow cover. Three techniques for monitoring snow cover with GB-SAR are presented through Chapters 5, 6 and 7: snow height retrieval, snow avalanche volume retrieval and avalanche events detection and classification.

Snow height is retrieved by using the differential interferometric phase of two consecutive SAR acquisitions under the assumption of single layer model and dry snow conditions. The volume displaced in a snow avalanche is computed by subtracting two digital terrain models (DTM) generated immediately before and after the avalanche event. DTMs are obtained with the topographic interferometric mode of the instrument: a spatial baseline separates two antennas that simultaneously receive the echoes of a third transmitting antenna. The third monitoring technique, avalanche detection and classification, is achieved identifying low-coherence anomalies in the coherence image between two successive SAR acquisitions. Snow avalanches present a low-coherence signature that can be identified by a morphological and statistical parameter model. A novel detection and classification scheme for snow avalanches is proposed.

The Joint Research Centre's GB-SAR sensor, upgraded to allow continuous operation 24 hours a day 7 days a week, also as part of the work of this thesis (Chapter 3), was used to develop and assess the before mentioned techniques. Measurements were carried out during six winters, providing more than 120000 SAR images at a rate of one image every 12 minutes approximately. Two test sites were studied, each with different characteristics in order to assess under real conditions the operational use of the monitoring techniques. Results show that snow height retrieval is achievable but remains, for the moment, an on-going research topic due to strong constraints limiting its use. A feasibility study is presented showing the accuracy limitations of GB-SAR to compute the snow volume involved in an avalanche. Finally, the most promising technique is snow avalanche detection and classification, which is demonstrated to be feasible and robust from an operational point of view and practical from an end user perspective.

Resumen

Los radares de apertura sintética basados en tierra (GB-SAR) son instrumentos que, aun siendo relativamente jóvenes, se utilizan con éxito para monitorizar operacionalmente deslizamientos de tierra. Por otra parte, el manto nivoso se ha estudiado tradicionalmente a nivel local con sensores invasivos o con radares de onda continua. El trabajo presentado en esta tesis contribuye a la conjunción de ambos campos: el uso de sensores GB-SAR para la monitorización del manto nivoso. En los Capítulos 5, 6 y 7 se muestran las tres técnicas desarrolladas: cálculo de la altura del manto nivoso, cálculo del volumen de nieve desplazado en una avalancha, y detección y clasificación de avalanchas.

La altura del manto nivoso se calcula a partir de la fase interferométrica diferencial de dos adquisiciones SAR consecutivas bajo la hipótesis de nieve seca y asumiendo un modelo de nieve de una capa. El volumen desplazado en una avalancha se obtiene mediante la resta de dos modelos del terreno digitales (DTM) generados justo antes y después del fenómeno avalancha. Los DTMs se obtienen con el modo topográfico del instrumento: dos antenas separadas una cierta distancia reciben simultáneamente los ecos de una tercera antena que transmite. La tercera técnica de monitorización, detección y clasificación de avalanchas, se realiza mediante la magnitud de la coherencia compleja entre dos imágenes SAR consecutivas. Las avalanchas de nieve presentan valores de coherencia muy bajos en el área afectada, que puede ser identificada mediante un modelo basado en características morfológicas y estadísticas. En la presente tesis se presenta un innovador algoritmo para la detección y clasificación de avalanchas.

El GB-SAR del Joint Research Centre, una vez mejorado para permitir su uso continuado 24h al día y 7 días a la semana (capítulo 3), ha sido utilizado para desarrollar y verificar las técnicas mencionadas anteriormente. Se han realizado medidas durante seis inviernos, que han proporcionado más de 120000 imágenes SAR a una frecuencia aproximada de 12 minutos por imagen. Se han estudiado dos emplazamientos, cada uno con características diferentes con el fin de verificar el uso operativo de las técnicas bajo condiciones reales. Los resultados muestran que la obtención de la altura del manto nivoso es posible pero su aplicación está limitada al campo experimental ya que su uso está condicionado por fuertes restricciones. Un estudio de viabilidad posteriormente confirmado con medidas muestra, en cambio, las limitaciones de precisión de los instrumentos GB-SAR para obtener una estima del volumen de nieve desplazado en una avalancha. Finalmente, la técnica más prometedora es la de detección y clasificación de avalanchas, la cuál se demuestra factible y robusta desde un punto de vista operativo y práctica desde una perspectiva de usuario final.

1. Introduction

1.1. Snow cover monitoring

Snow is a medium of high interest to hydrology, climatology, avalanche research, etc. and several methods are in use nowadays to monitor the snowpack in a more or less automatic way. From simple in-situ temperature measurements to complex satellite based radar sensors, a wide variety of instruments and techniques have been proposed. Experimental-based techniques contribute to increase our knowledge of the medium, while those operational-oriented are conceived for an optimal use of its resources or even to its control under certain circumstances.

Optical and near infrared sensors can discriminate snow-cover from bare ground and remote sensing data have been used as input to snow runoff models for near real-time and seasonal runoff forecast [1]. Passive microwave sensors have a long history in snow monitoring: several investigations have demonstrated the capability of multi-frequency microwave radiometer systems to locally map snow extent, snow depth, and snow water equivalent [2][3]. The availability of Seasat and ERS-1 SAR data has demonstrated the capability of spaceborne synthetic aperture radar to distinguish wet snow from bare ground [4][5], to estimate snow liquid water content [6] and to monitor the snow melting process [7]. On a more local scale, frequency modulated continuous wave (FM-CW) synthetic aperture radar has been employed to detect buried objects in the snowpack [8] and ultrawideband radar has demonstrated its capacity to measure the thickness of snow over sea ice [9]. Snow depth is usually measured with ultrasound ranging devices in standard snow-stations [10, pp.136], although multi-frequency FM-CW radars have also been employed for this purpose either buried in the ground [10, pp.145] or mounted in an aircraft [11]

Concerning remote sensing of snow avalanches, the objective has been principally devoted to the triggering of alarm systems that avoid or minimize entry into the affected area of persons and vehicles. In this sense, instruments based on the measurement of mechanical forces (pressure by direct contact) or vibrations are among those more effective [12]. Ultrasound, geophones or FM-CW profiling radars buried close to the release zone of the avalanches have also demonstrated their effectiveness, when the information provided by different sensors is combined in order to reduce false alarms [13]. Nevertheless, all these means cover a very limited field of action and imply complex installations in areas usually with difficult access.

Doppler radar and light beams with a range of several hundreds of meters have been used to measure avalanche occurrences and flow speeds [13][10, pp.129], although these sensors provide no information on the avalanche type or size and tend to record anything that moves across the beam: falling or drifting snow, birds, persons, etc. The imaging capacity of synthetic aperture radars, instead, seems to be an interesting solution to better discriminate artifacts, but the temporal and local characteristics of snow avalanches make it difficult to employ satellite- or air-borne sensors. And here it is where the use of ground-based synthetic aperture radars (GB-SAR) promises to play a role in monitoring such localized and relatively fast events.

1.2. The GB-SAR sensor

Ground-based synthetic aperture radars (GB-SAR) have attracted the attention of several research groups in the last 10 years: the Joint Research Centre (Italy) with its Vector Network Analyzer (VNA) based solution [14], the University of Florence (Italy) also with a sensor based on a VNA [15], the Technical University of Catalonia (Spain), using Direct Digital Synthesis (DDS) [16], and the University of Sheffield (UK) also using a VNA based sensor [17], just to mention some of them.

From an operational point of view, the use of GB-SAR sensors has been traditionally linked to the monitoring of large man-made structures and natural hazards like landslides or volcanoes. Its degree of maturity in this field, both on the hardware components as well as on the controlling and interferometric processing software, has reached a level high enough for the successful commercialization of the instrument and the related services of monitoring. LiSALab S.r.l. and IDS S.p.A., both in Italy, are examples of companies exploiting this technology.

On the research side, instead, interest has moved during the last 4 years to snow cover monitoring [18][19][20]. A new application of the sensor, interesting to the ski resorts' administrators and the Civil Protection services, is in fact emerging: the continuous monitoring of critical slopes where a snow avalanche can put at risk the skiers or the installations, buildings or roads in the surroundings. The all weather imaging capability and non invasive solution of SAR technology make it particularly suitable for such kinds of monitoring, overcoming some of the problems of the classical methods based on visual imagery, force measurements, geophones or continuous wave radars.

With similar pixel resolutions as satellite- and air-borne synthetic aperture radars, GB-SAR benefits from a much higher acquisition rate of the order of a few minutes per image, with current mechanical and stop-and-go sweeping techniques. This is though achieved only for areas much smaller (e.g., typically spanning a few square km) than those monitored with air-borne and space-borne SAR. Nevertheless, this kind of sensor is relatively young so it is expected that in the near future even higher acquisition rates of the order of several seconds per image will be possible with the use of continuous and/or electronic sweeps. This would definitely consolidate the operational use of current measurement techniques, but for the moment we will concentrate on the possibilities of the instrument in its current state and leave for the final chapter of this PhD thesis the guidelines for future research activities.

1.3. Objectives and organization of the PhD thesis

The general panorama is, thus, on the one hand mature techniques for long-term ice and snow cover monitoring on a large scale through SAR observations and on the other hand a relatively young instrument such as GB-SAR with mature interferometric techniques for the monitoring of large man-made structures and landslides. The work presented in this PhD thesis is a contribution to bringing together GB-SAR sensors with the snow cover monitoring application, so the general problem statement addressed in this study can be summarized as follows:

Is it possible to develop robust GB-SAR snow cover monitoring techniques to be used in an operational environment in benefit of end-users?

In order to be able to develop and assess these monitoring techniques the following specific objectives were posed:

a) To upgrade an experimental instrument to allow 24/7 unattended operation during an entire snow season in the Alps.

b) To perform continuous measurements with a variety of sensor parameters and environmental conditions in order to obtain a representative data archive.

c) To develop processing techniques to remotely sense the snow cover and validate them using the GB-SAR data archive.

d) To implement prototype versions of these techniques in a near real-time processing chain of the sensor in order to verify their operational use.

The rest of the PhD thesis addresses all these points as follows:

Chapter 2 reviews the SAR theory. First of all, a historical overview of the radar instrument and its main uses is presented. Then the technical details of a generic synthetic aperture radar relevant to the field campaign carried out in this PhD thesis are listed. A short section is devoted to the image focusing block employed in the linear GB-SAR processing chain. And finally the theoretical framework of SAR interferometry is presented, since it is instrumental in the three monitoring techniques presented in this PhD thesis: Chapter 5 makes use of zero-baseline differential interferometry, Chapter 6 employs topographic interferometry and Chapter 7 uses zero-baseline interferometry.

Chapter 3 presents the GB-SAR sensor used during the experimental part of this study. It is generically called LISA (linear SAR), although two different instruments were deployed for 3 winters each, one in a Swiss test site and the other in an Italian ski resort. The instrument used in Switzerland had a maximum aperture length of 5 m, and operated throughout the campaign at 5.83 GHz and VV polarization. On the other hand, the instrument deployed in Italy had a maximum aperture length of 2 m and was operated at 13.27 GHz and VV polarization. The second part of this chapter details the work performed on the initial instrument in order to make it robust and autonomous to operate unattended 24/7. This upgrade was instrumental for the successful achievement of the data

archive necessary to develop and assess the processing techniques presented in this PhD thesis.

Chapter 4 introduces the sites where the instruments were deployed. The first experiments were carried out in a Swiss test site managed by the Swiss Federal Institute for Snow and Avalanche Research, SLF Davos. The site is in the Sion Valley, Canton Valais of Switzerland, and the instrument was in place and active from December 2003 to May 2006. A second instrument was deployed on March 2006 in an Italian ski resort managed by Monterosa 2000 S.p.A., on Alagna Valsesia, Piedmont region of the North of Italy. This instrument was operative up until April 2008. The data archive obtained through all field campaigns is described also in this chapter.

Chapter 5 details the first monitoring technique developed. Snow height retrieval is performed through the differential interferometric mode of the instrument (DInSAR). With a single ground-truth control point, the differential interferometric phase is tracked along successive interferograms to create a snow height evolution plot of up to four days. The phase-to-height conversion is performed through the assumption of a layered model and under dry snow conditions. The absolute snow height retrieval requires two calibration parameters that are obtained from the ground-truth control point.

Chapter 6 shows a feasibility study on the retrieval of the snow volume displaced by an avalanche. The volume is computed by subtraction of two digital terrain models (DTM). DTMs are generated with the topographic mode of the instrument, that is, exploiting two reception channels, vertically separated, and simultaneously acquiring the echoes of a transmitting antenna. First of all a review of the formulation existing to generate DTMs with a GB-SAR sensor is presented. The typical accuracy obtained is in the order of 5 m. A novel processing technique, able to increase the accuracy under the same instrument parameters up to 3 m, is formulated. This new technique is first assessed under real data without snow conditions and then ported to a snow covered scenario. Results show that the accuracy of DTMs obtained with GB-SAR continues to be insufficient for the application of snow volume retrieval by DTM subtraction. The optimal sensor parameters for this application are described at the end of the chapter.

Chapter 7 contains the most important and innovative work presented in this PhD thesis. An algorithm for the automatic detection and classification of snow avalanches is developed using the coherence magnitude and systematically assessed through the whole archive of data acquired during six winter campaigns. The scheme, based on the classic steps of 1) pre-processing, 2) detection, 3) features extraction and 4) object classification is fully described in this chapter. Detection of avalanche events is performed by the combined application of thresholding and morphological filters to the differential coherence magnitude of consecutive images. Classification of events likely to be snow avalanches is based on statistics extracted from the whole image and features associated with the single regions. Results show a drastic reduction on the images that it is necessary to manually supervise (2.2%). With a 9% false negative rate and a 60% accuracy on the avalanches detected over the 2.2% of images to supervise, the processor represents an interesting operational support tool for the daily operations of avalanche risk assessment in a commercial ski resort.

Finally, in Chapter 8 the conclusions of this work are summarized. The original contributions of this PhD thesis are outlined and future research lines are commented.

2. Synthetic Aperture Radar

2.1. History and developments

2.1.1. Radar

Radio detection and ranging (radar) refers to a technique as well as an instrument. The radar instrument emits electromagnetic pulses in the radio and microwave regime and detects the reflections of these pulses from objects in its line of sight. The radar technique uses the two-way travel time of the pulse to determine the range to the detected object and its backscatter intensity to infer physical quantities such as size or surface roughness. A monostatic radar uses only one antenna, both for transmitting and receiving, whereas in a so-called bistatic radar, the transmitting and receiving antennas are physically separated. Two landmark discoveries in the development of radar were Maxwell's equations of electromagnetism in 1873, in "Treatise on Electricity and Magnetism," and Hertz's experiments in 1886. Hertz generated and detected the first known radio waves, and discovered that these waves were subject to reflection or scattering [22].

Although first radar systems were developed as early as 1903 for ship tracking and collision avoidance (the "telemobiloskop" of Hulsmeyer, 1904), pre-World War II military considerations boosted the development of radar in the 1930s and 40s.

The cavity magnetron was an important British invention which enabled the construction of small radars with short pulses, high transmitter power, and cm-scale wavelengths. Significant improvements of radar technology, triggered by the availability of the cavity magnetron, were achieved at MIT's Radiation Laboratory during the 40s, although similar developments occurred simultaneously at several locations around the world. Basically all current forms of radar can be traced back to those early developments.

Although the technology mainly gained momentum through military applications in those early years, civil and scientific applications arose quickly afterward. In particular radio astronomy profited from the advances in technology. Earth-based radars proved ideal for studying celestial bodies such as the Moon, Venus, Mars and the Sun.

The first tests to bring a radar into space started with JPL efforts in 1962, and lunar radar observations from Apollo 17 proved successful in 1972. Nadir-looking radar altimeter measurements from Earth orbiting satellites have been collected since Skylab (1973) and GEOS-3 (1975). Venus was first visited by a radar on Pioneer 1, launched in 1978. It carried a nadir-looking radar altimeter which enabled a global mapping with an

accuracy of about 300 m and a spatial resolution of about 50 km. The Soviet Venera 15 and 16 improved that resolution to about 2 km.

2.1.2. Synthetic Aperture Radar

A specific class of radar systems are the imaging radars, such as Side-Looking (Airborne) Radar (SLR or SLAR) and later Synthetic Aperture Radar (SAR). The side-looking geometry of a radar mounted on an aircraft or satellite provided range sensitivity, while avoiding ambiguous reflections. The first SLARs were incoherent radars: the phase information of the emitted and received waveforms was not retained. The resolution in the flight direction was obtained by using a physically long antenna, hence the name Real Aperture Radar (RAR). The practical restrictions on the antenna length resulted in a very coarse resolution in the flight direction, degrading with higher flight altitudes, even though high-frequency (K-band: 0.75-2.40 cm) radars were used.

The concept of using the frequency (phase) information in the radar signal's along-track spectrum to discriminate two scatterers within the antenna beam is generally contributed to Carl Wiley in 1951. Developments at the universities of Illinois and Michigan in the late 50s and early 60s culminated in the concept of the synthetic aperture radar. The key factor for these advances is coherent radar, in which phase as well as amplitude are received and preserved for later processing. Moreover, the phase behavior needs to be stable within the period of sending and receiving the signal. As a result, an artificially long antenna can be created synthetically using a moving antenna, combining the information of many received pulse returns within the synthetic antenna length. This methodology leads to a dramatic increase in azimuth resolution of about three orders of magnitude.

Satellite remote sensing started with optical-mechanical scanners such as the Landsat satellites, working in the visible and infrared parts of the electromagnetic spectrum. Although these first space-borne remote sensing images provided an unsurpassed new perspective of the planet, some strong limitations became evident soon. Almost continuous cloud cover, especially over tropical regions, lacking solar illumination of the polar regions for half the year, and the new physical properties to be derived from scattering in other parts of the spectrum triggered the development of satellite SAR missions.

The experience with mainly airborne SAR tests in the 60s and 70s culminated in an L-band Synthetic Aperture Radar system onboard Seasat, a satellite launched in June 1978 primarily for ocean studies. Although a short-circuit ended this mission prematurely after 100 days of operation, the SAR imagery was spectacular, and enabled SAR systems to be included in many satellites to come. Based on the success of Seasat, several Space Shuttle missions carried a synthetic aperture radar, starting from 1981. The first instrument was the Shuttle Imaging Radar (SIR) laboratory. SIR-A, an L-band instrument with a fixed incidence angle operated for 2.5 days in 1981 and provided valuable engineering experience. SIR-B, an improved version of SIR-A, orbited the Earth in 1984 and was able to steer its antenna mechanically to enable different look angles. Whereas all data from Seasat and SIR-A were recorded analogously on tapes, SIR-B was already equipped with full digital recording.

Cosmos-1870 was the first (S-band) SAR satellite of the former Soviet Union, launched in 1987 and orbiting at a height of 270 km. It operated for two years. ALMAZ-1,

the second satellite was launched in 1991, and operated for 1.5 years. The first satellite SAR mission to another planet, Venus, was launched on May 1989, and was named Magellan. Magellan mapped 98% of Venus with a resolution of about 150 m from September 1990 until September 1992.

The European Space Agency (ESA) launched its first satellite equipped with a SAR in July 1991: ERS-1 (European Remote Sensing Satellite). Although planned for a 5-years life time, the satellite operated until March 2000. Designed primarily for monitoring polar oceans and ice, it operated under a look angle of 23º, resulting in strong topographic distortion. Nevertheless, the systematic data acquisitions, the orbit control, and the data distribution policy resulted in impressive advances in science, and major improvements in radar interferometry. An almost exact copy of ERS-1, ERS-2, was launched in April 1995, which enabled a so-called "tandem-mode" operation of the two satellites, a period of nine months in which ERS-2 followed ERS-1 in the same orbit, with a temporal spacing of 30 minutes. This resulted in ground-tracks which repeated with an exact 24 hour interval. After 1996, ERS-1 acted as a backup satellite in hibernation mode, and was only activated for special occasions, mostly related to SAR interferometry. Such occasions were the eruption of volcanoes such as Vatnojokiill on Iceland, and severe earthquakes such as the Izmit earthquake in 1999. Both ERS satellites operated from the same near-polar orbits at an altitude of 785 km. The satellite data are used for many environmental purposes (oil slick monitoring, wind and wave field observations, transport of sediments, ice cover and movement) over the oceans. Over land, the data reveal useful information on land use, agriculture, deforestation, earthquake and volcanic deformation, and general geophysics.

Japan started its space-borne SAR program launching the Japanese Earth-Resources satellite (JERS) in 1992. JERS was designed for solid Earth remote sensing, and carried an L-band (23.5 cm) radar with a look angle of 35º, more favorable regarding topographic distortion. JERS operated until October 1998. The L-band acquisitions proved to be well-suited for repeat-pass interferometric applications, due to their reduced sensitivity for temporal changes in the scattering mechanisms at the Earth's surface. Unfortunately, orbit control and maintenance was not as advanced as for the two ERS satellites.

Started in 1995, the Canadian Space Agency (CSA) operates Radarsat, a SAR satellite designed to perform especially Arctic observations of ice coverage, e.g., for shipping route planning, apart from many other applications.

The experience with the repeat pass missions for topographic mapping, especially the problem of temporal decorrelation and atmospheric disturbances, culminated in the Shuttle Radar Topography Mission (SRTM). This Space Shuttle mission was performed between 11 and 23 February 2000 and used a single-pass configuration with a fixed 60 m arm to carry the two radar antennas. It mapped all land masses between 60ºN and 58ºS using C-band, and tiles of this area with a higher accuracy using X-band.

While Earth observation from space was strongly focused on scientific purposes, satellite data and the derived information products have been increasingly used for a variety of commercial applications. To this aim, TerraSAR-X was launched on June 2007, being the first satellite built in a public-private partnership between the German Aerospace Centre (DLR) and Europe's satellite system specialist Astrium. TerraSAR-X is a fully polarimetric sensor with three different imaging modes: spotlight (up to 1 m resolution), stripmap (up to 3 m resolution) and scan (up to 16 m resolution). The synthetic aperture is implemented through an active phased array operating at X-band, while the revisit rate is of 11 days.

2.2. Sensor characteristics

2.2.1. SAR sensor

The term SAR sensor encompasses all electronics required to generate, transmit, and receive SAR signals. It includes the radar antenna and a data link to store the acquired raw data. Different platforms may carry the SAR sensor: ground-based stations, unmanned aerial vehicles (UAV), airborne vehicles or space vehicles.

A SAR generates and transmits a series of coded pulses at regular time intervals or a continuous frequency wave as the radar platform moves along its path. The ideal path is a straight line traversed at constant velocity, which is more complex to obtain in satellite- or air-borne sensors and instead very easily achievable in a ground-based sensor.

A practical SAR system incorporates frequency conversion and both low-pass and band-pass filtering stages to generate and maintain the desired signals. A stable reference clock provides the timing and coherent phase reference for all signals in the radar. The transmitter in a modern SAR system generates a wide-bandwidth signal via digital-to-analog (D/A) conversion of a sampled waveform stored in memory. The transmitter band-pass filter filters this digitally synthesized signal, mixes the resulting analog signal up to radio frequency (RF), amplifies it, and sends it to the transmit antenna.

A receiver accepts the backscattered signal (optionally within a selected range gate) from the receiving antenna, provides low noise RF amplification, and mixes the amplified RF signal with a digitally generated and filtered reference signal. This reference signal removes the RF carrier and, if desired, the transmit signal modulation. Next, an analogue-to-digital (A/D) converter produces the digitized signal for data storage.

2.2.2. SAR modes

Figure 2.1 illustrates the three common SAR imaging modes [23, p.4]: spotlight, stripmap, and scan. During a spotlight mode data collection, the sensor steers its antenna beam to continuously illuminate the terrain patch being imaged (azimuth steering). In the stripmap mode, antenna pointing is fixed relative to the sensor movement line. The result is a moving antenna footprint that sweeps along a strip of terrain parallel to the path of motion. The stripmap mode involves either a broadside imaging geometry (example of Figure 2.1-c), or a squinted imaging geometry. The antenna pointing in this last mode has no azimuth movement but an elevation steering.

Because scan mode involves additional operational and processing complexity, spotlight and stripmap modes are the most common SAR modes. The spotlight mode is a practical choice when the objective is to collect fine-resolution data from one or more localized areas. The stripmap mode is most efficient when used for coarse-resolution mapping of large regions.

A fourth operating mode called inverse SAR (ISAR) produces radar signal data similar to that of spotlight mode SAR. However, the ISAR mode is different in that data collection is accomplished with the radar stationary and the target moving. The signals are similar because it is the relative position and motion between the sensor and the scene

being imaged that is important. Since the signals are similar, the processing required to produce an image is similar also.

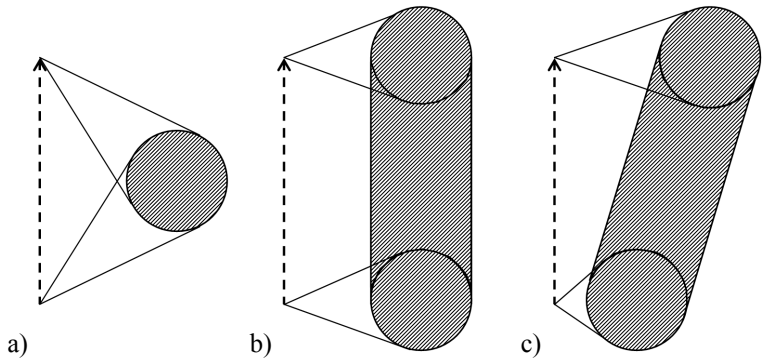

Fig. 2.1. SAR modes: a) spotlight, b) stripmap, c) scan.

Three attributes distinguish spotlight and stripmap modes [23, p.5]. First, spotlight mode offers finer azimuth resolution than that achievable in stripmap mode using the same physical antenna. Second, spotlight imagery provides the possibility of imaging a scene at multiple viewing angles during a single pass. Third, spotlight mode allows efficient imaging of smaller scenes whereas stripmap mode naturally images a long strip of terrain. SAR azimuth resolution improves with the length of the synthetic aperture. In stripmap mode, antenna pointing is fixed relative to the platform movement line; azimuth antenna beamwidth limits the available synthetic aperture length because it determines the transit distance over which the sensor illuminates each scatterer. Spotlight mode avoids this limitation on synthetic aperture length by steering the antenna illumination pattern to illuminate the scene for a long period. Consequently, antenna beamwidth does not limit azimuth resolution in spotlight mode.

2.2.3. GB-SAR sensor

A ground-based SAR is a particular implementation of a SAR sensor in which the instrument is anchored to the terrain. Different apertures or movements of the platform carrying the antenna set can be generated, resulting in different image geometries. Linear and circular apertures are those more frequently used because of the simplicity in their mechanical implementation [14][15][16][17]. A single horizontal aperture provides bi-dimensional (2-D) images, while the combination of two apertures (horizontal and vertical) allows the creation of three-dimensional (3-D) radar images [14][15].

Contrary to space- or air-borne sensors, GB-SAR sensors scan only a limited aperture length of a few meters due to the limited space available for the synthetic aperture to be physically implemented. As will be shown in Section 2.2.5, a limited aperture length reduces the resolution in the cross-range direction compared to that ideally obtainable from space- or air-borne sensors. Nevertheless, considering the typical distances to the scene centre and the reduced areas monitored with ground-based sensors (of the order of a few square kilometres), the apertures typically used (2 – 5 m) produce azimuth resolutions comparable to that obtained with space- or air-borne sensors (5 – 10 m).

2.2.4. Resolution in range direction

For pulsed radar systems, the determination of range is done by measuring the time delay between the transmission and the reception of the signal. Having a target at distance r the round-trip propagation delay is $T=2r/c$, thus a pulse of length τ corresponds to a range increment of:

$$\Delta R = c\frac{\tau}{2}. \tag{2.1}$$

This means that two targets separated at greater distances than ΔR are distinguishable. Hence, narrowing the pulse width length will enhance the resolution, but also increase the bandwidth BW of the radar, since $BW\,\tau \approx 1$.

In contrast to the direct method of a pulsed radar in which all the spectral components of the signal are present simultaneously, it is also possible with synthetic methods to collect sequentially the spectral components. A typical example of such a radar type is a stepped frequency continuous wave (SF-CW) radar, in which several narrow band measurements are executed at discrete frequencies. Although the single narrow band responses have insignificant resolution potential, the coherent combination of all the responses provides a resolution equal to that of a pulsed radar system with the same total bandwidth. In this case, the resolution in range is:

$$\Delta R = \frac{c}{2BW}. \tag{2.2}$$

2.2.5. Resolution in cross-range direction

For real aperture radars (RAR) the resolution in cross-range (or azimuth) directions depends on the radiation pattern of the antennas. Two characteristics of the radiation pattern are crucial for the resolution: the 3 dB beamwidth both in azimuth (Φ_{3dB}) and elevation (Θ_{3dB}) and the main lobe to sidelobes level ratio. If λ is the central wavelength of the transmitted signal and D the dimension of the antenna in the cross-range direction, the radar beam angular spread can be expressed as: $\Phi_{3dB}=\lambda/D$. Hence, the resolution in cross-range for a real aperture radar is approximately given by [24]:

$$\Delta X_{RAR} = \Phi_{3dB} r = \frac{\lambda r}{D}. \tag{2.3}$$

In order to improve the azimuth resolution, a synthetic aperture technique is used. This technique is based on the fact that the target stays in the beam for a significant amount of time and is observed by the radar from numerous locations along the aperture path. In that case, two adjacent scatterers can be resolved if their phase histories, observed across the synthetic linear aperture of total length L, differ by 2π rad or more. A differential path length of $\lambda/4$ at the aperture extremes causes the required phase variation, leading to the SAR cross-range resolution [23, p.33]:

$$\Delta X_{SAR} = \frac{\lambda r}{2L}. \tag{2.4}$$

To illustrate the equivalence in the resolution of real and synthetic apertures, the responses of a linear real array and a linear synthetic array are compared [25, pp.17-21]. A real aperture array with uniform illumination can be treated as an array of N identical elements separated a distance d, excited simultaneously for transmission, and summed coherently upon reception. The response of the array to a unit-amplitude point object is the superposition of field values received by the individual elements. If r_n is the distance from each real antenna to the object, the output of the entire array can be expressed as:

$$v_o^{RAR} = \sum_{n=1}^{N} \exp(-j2\pi r_n / \lambda) \sum_{m=1}^{N} \exp(-j2\pi r_m / \lambda) = \left[\sum_{n=1}^{N} \exp(-j2\pi r_n / \lambda) \right]^2. \tag{2.5}$$

The term inside the square brackets of (2.5) is the one-way array response, while the response of the array when it is used for both transmitting and receiving (two-way) is the square of the one-way response. Note that a $e^{+j\omega t}$ time dependence is assumed.

The synthetic array is formed by sequentially transmitting and receiving with each individual element and subsequently coherently summing the received signals. With an array geometry identical to that of the preceding case, the response of the synthetic array will be:

$$v_o^{SAR} = \sum_{n=1}^{N} \exp(-j2\pi (r_n + r_n) / \lambda) = \sum_{n=1}^{N} \left[\exp(-j2\pi r_n / \lambda) \right]^2. \tag{2.6}$$

The difference between (2.5) and (2.6) can be better appreciated when determining the far-field responses of both arrays. The real aperture array has a response of the form $[\mathrm{sinc}(x)]^2$, while the synthetic aperture array has a response of the form $\mathrm{sinc}(2x)$. The one way responses of both real and synthetic aperture arrays are identical; however, the two-way responses differ considerably: the two-way response of a synthetic array is equivalent to the one-way response of a real array of twice the length. This relationship can also be appreciated when comparing (2.4) to (2.3).

Because a scatterer is only visible when it is traversed by the beam of the single real antenna, the maximum length a synthetic aperture can be in stripmap mode is the length of the main footprint on the surface in the cross-range direction: $L = r \cdot \Phi_{3\mathrm{dB}}$. An interesting observation can be made by substituting the beamwidth of the real antenna $\Phi_{3\mathrm{dB}} = \lambda / D$ in (2.4):

$$\Delta X_{SAR}^{\min} = \frac{\lambda r}{2L} = \frac{\lambda r}{2r\Phi_{3dB}} = \frac{\lambda r}{2r\lambda / D} = \frac{D}{2}. \tag{2.7}$$

Equation (2.7) indicates that the best achievable resolution of a linear SAR in stripmap mode equals one-half the size of the real aperture D. The apparent paradox that finer resolution is achieved by using a smaller antenna is explained by noting the following two points [24, pp.73-74]:

a) The farther the sensor is, the larger the footprint is on the ground, thus the longer the synthetic array. This leads to a finer synthetic beam which exactly counterbalances the increase in distance.

b) The smaller the antenna is, the larger the footprint and the synthetic array. This leads to a finer synthetic beam, therefore a finer resolution.

2.2.6. Ambiguities

When responses of complex objects are sampled at discrete frequency steps, the step size must be sufficiently small to limit variations in the phase of the received signal between steps. This constitutes the well known Nyquist sampling criterion, which arises in the sampling of continuous functions. If the criterion is violated, the sampled frequency responses of objects at different ranges produce ambiguous responses, also called aliases.

For a SF-CW radar system as that used in the experimental part of this PhD thesis and presented in Chapter 3, the unambiguous range when sampling the total transmitted bandwidth BW into n_f frequency points is [25, p.52]:

$$R_U \leq \frac{n_f c}{2BW}, \tag{2.8}$$

where c is the propagation velocity of the electromagnetic field.

In order to avoid aliasing caused by the limited number of looks over a linear aperture in stripmap SAR mode, the spacing between acquisitions along the antenna trajectory, Δx_a, needs to satisfy the condition that the return phase difference between consecutive acquisitions is less than π rad:

$$\Delta\varphi \leq \pi \quad \Rightarrow \quad 2r_{one-way}\frac{2\pi}{\lambda} \leq \pi \quad \Rightarrow \quad r_{one-way} \leq \frac{\lambda}{4}. \tag{2.9}$$

Considering a geometry as that of Figure 2.2 in which the azimuth angle is called θ and the maximum alias-free image area is delimited by $\pm\theta_{\max}$, the spacing between samples Δx_a along the antenna trajectory of a linear SAR needs to satisfy the following relationship:

$$r_{one-way} = r_2 - r_1 = \Delta x_a \sin\theta \leq \frac{\lambda}{4} \quad \Rightarrow \quad \Delta x_a \leq \frac{\lambda}{4\sin\theta_{\max}}. \tag{2.10}$$

As a summary, it can be stated that image extent is controlled by the step size both in the frequency transmitted bandwidth and in the linear aperture acquisition points. On the other hand, resolution is controlled by the total bandwidth and aperture length.

2.3. Image formation

There is a wide variety of imaging algorithms that have been used to reconstruct reflectivity images of a scene by using SAR techniques. A 2-D reflectivity image can be

formed by synthesizing a 1-D aperture with a wide-band radar. Accordingly, a 3-D reflectivity image is formed by synthesizing a 2-D aperture.

An imaging algorithm with an arbitrary spatial and frequency diversity can be formulated as in (2.11). The radar instrumentation provides frequency diversity by varying the irradiating frequency and spatial diversity by varying the relative orientation between object and radar. If *g(x,y)* is the image to be determined from the complex object response measured as a function of frequency and a spatial or angular coordinate θ, the image can be formed by the expression [25]:

$$g(x,y) = \sum_{f}\sum_{\theta} G(f,\theta)\cdot \exp(j4\pi rf/c). \tag{2.11}$$

The exponential function in (2.11) is unique to each *x, y*, where the dependence on θ, *x* and *y* is implicit in the range *r*. In addition, the exponential function represents the set of basis functions which are the complex conjugate of the response to a unit-strength scatterer (i.e. the impulse response) located at a particular *(x,y)*. When the object consists of a single scatterer located at *(x,y)*, the measured data and the basis function for that coordinate have a conjugate phase relation, and therefore sum to a maximum in (2.11). All other basis functions produce a lesser value, ideally zero.

Computational considerations aside, the imaging algorithm for any form of frequency and spatial diversity is simple: the image is formed by the integrated product of the measured data multiplied by the conjugate phase history postulated for a point located at each pixel in the image space. This process can accommodate all forms of frequency and spatial diversities, including the various types of synthetic apertures and near-field geometries. The quality of the image is thus determined by the accuracy to which the diversities are known.

Practical aspects of SAR imaging involve the application of efficient algorithms to numerically evaluate (2.11). Nearly every imaging scheme in current use formulates the basis functions in terms of two-dimensional Fourier transforms that can be implemented using the FFT algorithm and thus be computationally efficient.

As regards the working principles of the existing radar imaging algorithms for satellite and air-borne sensors, a general classification is the following [23]: Polar Format Algorithm, Range Migration Algorithm and Chirp Scaling Algorithm. In all three types of SAR imaging algorithms, when the radar is within the far-field zone of the target, the illuminating wavefront can be considered to be planar and, hence, the processing reduces to an interpolation plus an inverse Fourier transform. Nevertheless, a common requirement for these algorithms is that of producing imagery with the higher possible resolution, particularly in the cross-range direction. In practice, a criterion to assess the optimality of a SAR system is to compare the achieved cross-range resolution in the imagery with the physical dimension of the radar's antenna, where (2.7) dictates the best achievable resolution of a linear SAR in stripmap mode.

Unfortunately the optimal resolution in cross-range cannot be typically achieved with GB-SAR systems, and in particular in the scenarios monitored during the two field campaigns carried out as part of this PhD thesis' work. In these cases the radar system has an aperture length of a few metres and is illuminating a scene spanning a few square kilometres located within the far-field of the radar aperture. This is quite a different

scenario than for satellite- and air-borne SAR, which usually have aperture lengths of several kilometres.

In the following sections three focusing algorithms suitable for the image formation in the typical GB-SAR scenarios are described.

2.3.1. Time-domain back-propagation

The first algorithm presented is the time-domain back-propagation algorithm (TDBA), which consists of a direct implementation of (2.11) in the time domain without any kind of optimization in terms of the basis functions before mentioned.

Let us assume a scene consisting of a single point scatterer located at a point p, with cylindrical coordinates (ρ,θ) with respect to the radar position. Let us assume also that a linear radar array acquires the backscatter signal $G(f,x_a)$ as a function of two parameters: the frequency of the signal, f, and the position of the antenna set in the linear array, x_a. Finally, let us assume that the backscatter data is sampled uniformly both in the frequency and the space domain. A measurement with this radar array will give as a result the following two-dimensional matrix of complex values:

$$G(f_m, x_{a,n}) = G(f = f_c - BW/2 + \Delta f \cdot m,\ x_a = -L/2 + \Delta x_a \cdot n), \tag{2.12}$$

where $m = 0, 1, ..., M-1$; $n = 0, 1, ..., N-1$; f_c is the radar central frequency; BW is the frequency bandwidth in the measurement; Δf is the frequency step; M is the number of frequencies measured; Δx_a is the spacing of the physical radar array elements or the movement step used in the linear scan and N is the number of array elements or points measured within the linear scan.

The synthesis of a radar image can be achieved by coherently summing the signal contributions relative to different radar positions and different continuous wave frequencies as in (2.11). This technique is known as wavefront back-propagation. Thus, with the assumed imaging geometry the radar reflectivity at the point $p(\rho,\theta)$ can be calculated as follows:

$$g(\rho,\theta) = \sum_{m=0}^{M-1} \sum_{n=0}^{N-1} G(f_m, x_{a,n}) \cdot \exp(j4\pi\rho_n f_m / c), \tag{2.13}$$

where c is the propagation velocity and

$$\rho_n = \sqrt{(\rho\sin\theta - x_{a,n})^2 + (\rho\cos\theta)^2}\,. \tag{2.14}$$

The synthesis of an entire reflectivity image using (2.13) has associated a high computational cost, which is O(*MNM'N'*), where *M'* and *N'* denote the number of pixels in the y and x directions respectively. The algorithm described in (2.13) is a frequency-domain back-propagation algorithm. The formulation of the same algorithm in the time domain, TDBA, is usually preferred as it is computationally more efficient than that in the frequency domain. The algorithm in the time domain estimates the radar reflectivity at $p(\rho,\theta)$ as follows:

$$g(\rho,\theta)=\sum_{n=0}^{N-1} G_t(t=2\rho_n/c, x_{a,n}), \tag{2.15}$$

where $G_t(t,x_{a,n})$ denotes the time domain backscatter data. The computational cost of this algorithm is approximately O(*NM'N'*). Furthermore, when the reflectivity is calculated at a limited number of points (and not the whole image area with *M'N'* points), the computational cost is significantly reduced and becomes O(*NJ*), where *J* is the number of points where the reflectivity is calculated.

2.3.2. Polar format focusing

The polar format algorithm, also known as Range-Doppler algorithm, originates from optical signal processing. It is based on the polar nature of the frequency domain backscatter data, works with motion compensation to a point and as such needs to be used under the far field condition. It formulates the basis functions in terms of two-dimensional Fourier transforms that can be implemented using the FFT algorithm, but requires interpolation prior to the Fourier transform and only partially compensates the range curvature [23, pp.81-111].

Although this algorithm was initially developed to be used with satellite- and air-borne SAR, it can be also be used with GB-SAR scenes under certain constraints. Since the motion compensation is applied to a single point in the image, usually the central one, the image extents need to be smaller than the range to the centre of the scene in order to minimize the geometrical distortions originated in the rest of points in the focused image. Anyhow, a certain amount of geometrical distortion will be present in the focused image and the larger are the image extents, the larger also will be the distortion.

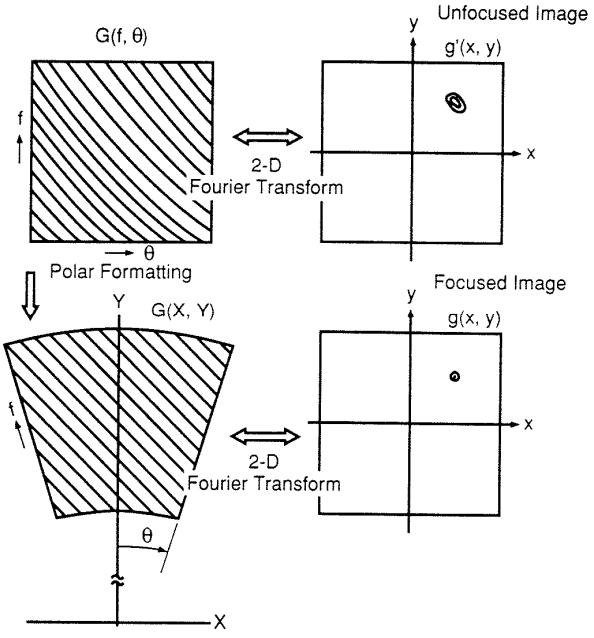

Fig. 2.2. Polar formatting data re-ordering and iso-phase lines rectification. Figure extracted from [25, p.160]

The basic polar formation itself is simply a modification in the data storage format. In effect, the polar formatting operation means recording successive pulses not side-by-side, but in an annular geometry as depicted in Figure 2.2.

The procedure for the image formation starts with a motion compensation block that completely removes the range curvature for the scene central point, while leaving residual range curvatures for points at other distances. Then, range and azimuth interpolation (polar formatting) is applied to reduce those residual range curvatures. A weighting function is afterwards applied to the data in the range dimension and the FFT into that dimension computed. At this point, an autofocus algorithm can be applied in order to reduce the phase errors present after conventional motion compensation and data formatting procedures. Next, a weighting function is applied to the data in the azimuth dimension and the FFT into that dimension computed. The result is a complex focused image in rectangular coordinates.

2.3.3. Pseudo-polar format focusing

Besides the constraint of the image extent with respect to the centre's scene range, the weakest point of the polar format algorithm is the interpolation prior to the Fourier transform, which is particularly time-consuming.

This interpolation can be avoided by defining a pseudo-polar coordinate system ρ',θ' such that [26]:

$$\begin{aligned} \rho' &= 2\rho / c, \\ \theta' &= 2\sin\theta / \lambda_c, \end{aligned} \tag{2.16}$$

where λ_c is the central wavelength transmitted by the radar system. The radar reflectivity according to the far-field pseudo-polar format algorithm (FPFA) can be then calculated as a series expansion of 2-D Fourier transforms. Under the condition of having a range resolution comparable to the aperture length ($L/\Delta R \approx 1$, as is the case of the two field campaigns described in Chapter 4), the series expansion can be approximated by the zeroth order term, since higher orders present reflectivity values typically 30 to 40 dB below the zeroth-order term:

$$g(\rho',\theta') = \sum_{p=0}^{\infty} g_p(\rho',\theta') \approx g_0(\rho',\theta'). \tag{2.17}$$

Considering the two-dimensional data matrix defined in (2.12), the reflectivity image obtained with the FPFA at the point $p(\rho',\theta')$ can be expressed as [26]:

$$g_0(\rho',\theta') = \mathrm{FFT2}[G(f_m, x_{a,n})], \tag{2.18}$$

where FFT2[.] is the two-dimensional Fast Fourier Transform operator and the transformation from the pseudo-polar to the polar grid or to the rectangular grid can be easily done by inverting (2.16). The computational cost of this algorithm is $O(NM \log_2 M)$.

The pseudo-polar format algorithm requires the image scene to be located in the far-field or the radar's aperture. However, provided this condition is satisfied, the extent of the

scene is only limited by the field of view of a single antenna array element (which implies a highly sub-optimal cross-range resolution, typical of GB-SAR scenes). This condition overcomes the limitation of the polar format algorithm of considering the image extents smaller than the range to the centre of the scene. In addition, the FPFA does not introduce any geometrical distortion at any point of the image, which is only true in the central point of the scene in the case of the polar format algorithm.

2.4. SAR interferometry

Whereas conventional SAR uses a single receiving antenna, interferometric SAR (InSAR) requires two receiving antennas separated by a baseline (B). Signals from both antennas are recorded and processed to yield two complex SAR images of the same scene. Phases measured in each of the scenes are differenced on a pixel-by-pixel basis to obtain additional geometrical information about the scene.

When the receiving antennas have a certain vertical separation (B_v), this phase difference can be interpreted as pixel height as illustrated in Figure 2.3. In repeat-pass interferometric SAR pixel height, h, and phase difference, $\Delta\varphi$, are related by [27]:

$$\Delta\varphi = \frac{4\pi}{\lambda}\Delta r = \frac{4\pi}{\lambda}\left[B_v \cos\theta_n - B_h \sin\theta_n\right], \tag{2.19}$$

$$h = H - r_1 \cos\theta_n. \tag{2.20}$$

where the parameters are those shown in Figure 2.3 and λ is the radar wavelength.

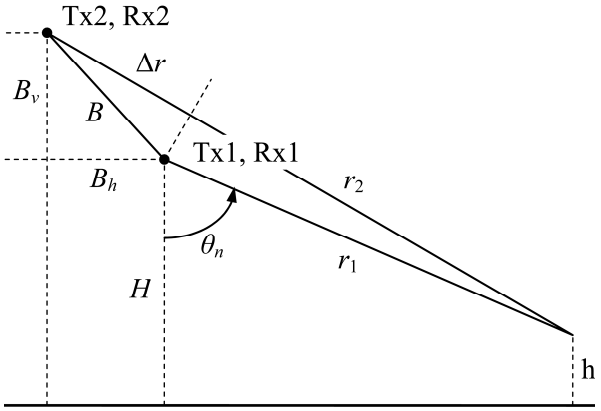

Fig. 2.3. Typical geometry of a repeat-pass interferometric SAR.

Equation (2.19) and Figure 2.3 assume a repeat-pass system; i.e., different Tx and Rx pairs at each end on the baseline: $\Delta r^{r\text{-}p} = 2r_2 - 2r_1 = 2(r_2 - r_1)$. When single-pass interferometry is used as it is the case of the sensor used in this PhD thesis (single transmit antenna and dual receive antennas), the 4π term in (2.19) should be replaced by 2π: $\Delta r^{s\text{-}p} = (r_2 + r_1) - 2r_1 = r_2 - r_1 = 0.5\Delta r^{r\text{-}p}$.

Interferometry can also be applied when a temporal baseline, instead of a spatial one, separates the two image acquisitions. Interferograms obtained that way are called

"zero-baseline interferograms" in reference to the fact that acquisitions are done illuminating the scene from the same position (zero-base spatial line) with a single transmit and a single receive antenna. Although there are several workarounds, zero-baseline interferograms are very difficult to achieve with satellite-borne sensors, either because it is often not possible to position the satellite in a zero-baseline orbit or because the baseline varies with the look angle, yielding only one zero-baseline range-bin in the interferogram. The intrinsic operation mode of GB-SAR sensors (continuous acquisition always over the same aperture), instead, provides such kind of images necessary for zero-baseline interferometry. Actually, zero-baseline differential interferometry is the key processing step in landslides monitoring and, as it will be shown in Chapter 7, also in snow avalanche identification with GB-SAR.

2.4.1. Decorrelation

SAR interferometry can only be properly exploited when the two SAR images are highly correlated. Evidently, this is the most important condition for interferometry. Loss of coherence, known as decorrelation, can be due to a number of driving mechanisms. The effect of some sources of decorrelation, e.g., as introduced by the alignment and interpolation of the images, can be reduced by using well-designed filtering procedures. Other sources of decorrelation like atmospheric effects are more difficult to address.

The major contributors to phase measurement uncertainty are signal-to-noise ratio, speckle and pixel misregistration, all leading to decorrelation. Noise will corrupt the phase measurement and, hence, the signal-to-noise ratio will determine the measurement uncertainty. When a resolution cell contains multiple scatterers, the random coherent interference gives rise to a modulation of the backscattered amplitude. This results in speckle and, like noise, this also will degrade the phase measurement. Similarly, pixel misregistration between the two complex SAR images to be differenced will result in a lack of coherency at the pixel level resulting in degraded phase measurement.

Decorrelation refers to three additional sources of phase measurement uncertainty: baseline decorrelation, decorrelation due to target rotation, and decorrelation from surface motion of individual scattering centres within a resolution cell. The same effect that gives rise to the fading phenomenon will also result in differing phase measurements when a distributed scatterer is viewed from antennas separated by the baseline. This is referred to as baseline decorrelation. Likewise, when a complex collection of scatterers is viewed from two different aspect angles, a decorrelation of the phase measurement will result, attributed to target rotation. Finally, should the arrangement of scatterers physically change between observations, this will result in temporal decorrelation. Temporal decorrelation may be significant in repeat-pass InSAR.

The degree of correlation or decorrelation (due to the causes listed above) between two complex SAR images can be measured and is called the coherence. Given a pair of complex pixel values, v_1 and v_2, the coherence is defined as [28]:

$$\gamma = \frac{\left\langle v_1 v_2^* \right\rangle}{\sqrt{\left\langle v_1 v_1^* \right\rangle \left\langle v_2 v_2^* \right\rangle}}, \tag{2.21}$$

where $\langle . \rangle$ is the spatial averaging operator. The coherence magnitude ranges from 0 to 1, where the higher the magnitude the higher the similarities between the complex pixels v_1 and v_2.

2.4.2. Double difference

Gabriel, Goldstein, and Zebker introduced in 1989 the concept of differential interferometric SAR (DInSAR) [29], a technique capable of detecting sub-centimetre elevation changes over large areas. Two interferograms made from three (or more) complex SAR images collected at different times are differenced producing a third interferogram, termed "double difference interferogram" or "differential interferogram." Phase changes due to static topography are removed, leaving a new phase image with nonzero phases in areas where the local topography has been disturbed between observation times.

There are several ways to construct a differential interferograms [30, pp.38-39]. The two-pass method uses an external digital elevation model (DEM) that is converted into radar coordinates, scaled using the baseline, and subtracted from the interferograms. Of course, errors in the DEM will propagate into the deformation results, depending on the baseline characteristics.

A second method is the so-called three-pass method. Here, an extra SAR acquisition is used and combined with a suitable partner acquisition to create the so-called topographic pair. This pair is assumed to have no deformation, a suitable baseline providing sensitivity to topography, and sufficient coherence. This pair is unwrapped, scaled to the baseline characteristics of the deformation pair, and subtracted from it, yielding the differential interferogram, the so-called differential pair. The three-pass method can only be applied when both the topographic pair and the deformation pair have a common image, as it is the case of GB-SAR images because of their intrinsic acquisition geometry: all images are acquired through the same synthetic aperture.

2.4.3. Phase unwrapping

The two-dimensional relative phase signal, which is the 2π modulus of the (unknown) absolute phase signal, is one of the two products available from a coherence image: angle of (2.21), key parameter in interferometric SAR. Although the forward problem, that is, wrapping the absolute phase to the $[-\pi, \pi)$ interval is straightforward, the inverse problem is one of the main difficulties in radar interferometry, essentially due to its inherent non-uniqueness and non-linearity.

Variable phase noise as well as geometric problems such as foreshortening and shadowed areas are the main causes why many proposed techniques do not perform as desired. Without additional information, the assessment whether the results of phase-unwrapping are trustworthy will always be based on strong assumptions on the data behaviour.

Many phase unwrapping algorithms have been proposed since SAR interferometry became an active field of research (see [33] for general reference). Some of the more popular ones are briefly discussed:

a) Residue-cut method: In the residue-cut method, also known as the branch-cut or (minimum spanning) tree algorithm, all residues are connected (unloaded) with branch cuts, under the condition that the total length of all cuts is minimal. The algorithm starts at one residue and searches within a window of 3×3 around it for another residue. If a residue of different sign is found, the branch cut is applied and the algorithm continues to the next residue. If the found residue is of equal sign, the search continues from this new position, and repeats until all plus and minus residues are unloaded, hereby spanning a "tree". If there are no new residues within the search region, but the found ones are not unloaded yet, the search radius is doubled to prevent the algorithm from breaking off. While integrating the phase gradients, the cuts constitute an obstacle through which the integration cannot continue.

b) Least-Squares Method: These methods appear in a weighted and unweighted fashion, and are based on minimizing the sum of the quadratic errors between the unwrapped phase gradients and the estimated phase gradients in a global way. FFT techniques can be applied to solve the least-squares technique in an efficient way. The method can also be applied in a Green's-function formulation.

c) Minimal cost flow methods: Minimal cost flow or network flow methods consider the phase unwrapping problem as a global minimization problem with integer variables. Comparing the difference between the estimated and the unknown phase gradient of the unwrapped phase should yield 2π multiple integer differences. These methods follow the residue-cut methods, adding integer cycles to cross the cuts. Positive and negative residues are the surplus and demand nodes, and the "flow" that equalizes the nodes can travel along paths determined by the cost function. An optimal solution is reached if the predefined objective function is minimized.

Interferometry leading to phase wrapping is only used in Chapters 5 and 6. A weighted least-squares algorithm, solved by the preconditioned conjugate gradient method [33, pp.223-227] has been implemented in order to unwrap the 2-D interferograms, where the coherence magnitude is used as the weight function for the algorithm.

2.4.4. Spectral shift

The origin of the spectral shift problem is the difference between the object spectrum and the data spectrum [31]. The object spectrum is a function of the object properties, in this case the radar reflectivity of the terrain, and is independent of the imaging system and its viewing geometry. In contrast, the data spectrum reveals the characteristics of the imaging system: its bandwidth contains the measurable width of the spectrum, and its Nyquist frequency is determined by the system's sampling frequency.

Ideally the object spectrum should be mapped identically to the data spectrum in order to apply interferometry between images. In practice, a spectral shift is caused by the difference in the local incidence angles towards the sensors acquiring the images from different positions. If both sensors would be at exactly the same position and look in the same direction, no phase-differences would occur in the image as is the case of the zero-baseline interferometry.

Considering instead a different geometry, with sensor 2 at a slightly different position from sensor 1 as depicted in Figure 2.4, phase differences (fringes) will appear in the image. Although the location of the data spectrum is not different (f_0), its contents have shifted to other frequencies (f_1 and f_2). In other words, the ground to slant range mapping causes a wavenumber shift: the wavenumbers of the object spectrum have shifted to other frequencies in the data spectrum.

The problem of the wavenumber shift is that both images have an overlapping spectral part which contains information, and two non-overlapping parts, which can be considered as a source of noise for interferometric purposes. Therefore, a bandpass filter needs to be applied to eliminate the two parts containing noise (also known as common-band pre-filtering). To tune the bandpass filter it is necessary to determine the extent of the wavenumber shift as accurate as possible. The fringe frequency reflects the amount of spectral shift and hence the amount of decorrelation due to the non-overlapping parts of both spectra.

While space-borne interferograms may suffer from spectral shift, as demonstrated in [32] the GB-SAR typical interferograms present a common frequency content higher than 99% (i.e., a spectral shift of 200 kHz in the worst case over 60 MHz bandwidth). This, and the fact that a frequency windowing function (e.g., a four-terms Blackman Harris window) is needed to suppress side-lobes in the imagery eliminate the need for the bandpass filtering in the GB-SAR case of interest here.

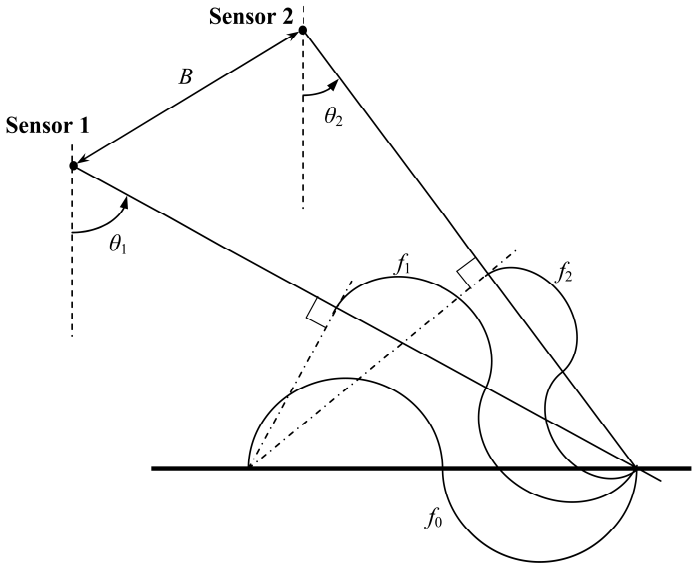

Fig. 2.4. Spectral shift in range caused by the different local incidence angles θ_1 and θ_2.

3. LISA instrument

3.1. General description

The system used to monitor the snow cover, LISA (acronym for LInear SAr), is a ground-based linear synthetic aperture radar fully developed and built at the Joint Research Centre of the European Commission (Ispra, Italy) [14].

It was designed and built in 1999 applying the knowledge gained in the European Microwave Signature Laboratory (EMSL) [34], also in the Joint Research Centre of the European Commission. Actually the system concept and data structure was the same, such that for system operation and signal processing the existing programs for the EMSL needed only slight modifications.

The LISA instrument was designed to be as versatile as possible in order to provide a prototype instrument for many different applications. Initially it covered the upper L-band, the S-band, the lower C-band and the K_u-band with two different apertures: a linear aperture of up to 5 m and a circular synthetic aperture implemented with a parallelogram shaped arm. Two separated receivers made possible real-time measurements in polarimetric-on-receive mode or single-polarization single-pass interferometric mode.

Since its conception in 1999 it has undergone a few modifications. Basically all the initial versatility has been simplified in order to smooth the way to a more operational-based instrument. In fact, the circular aperture has been removed and the radio-frequency section reduced to a single Vector Network Analyzer (VNA) that directly synthesizes the desired frequency band without intermediate front-ends.

The following is a description of the different instrument sections and components. It should be noted that two field campaigns have been carried out within the scope of this PhD thesis, with a different instrument each. Although both GB-SAR sensors are conceptually equal, the LISA instrument used for the field campaign in Switzerland is the initial instrument developed in 1999 and referenced in [14]. For the second field campaign, that of Italy, a completely new LISA sensor was built which was very similar to the initial one but with reduced dimensions to fit into the new emplacement at the ski resort. Both systems' components are detailed in the next sections.

3.1.1. Block diagram

The LISA instrument is mounted in a temperature-controlled container for ease of transportation and deployment and to control the humidity and temperature conditions of the electronics. The main components are depicted in Figure 3.1.

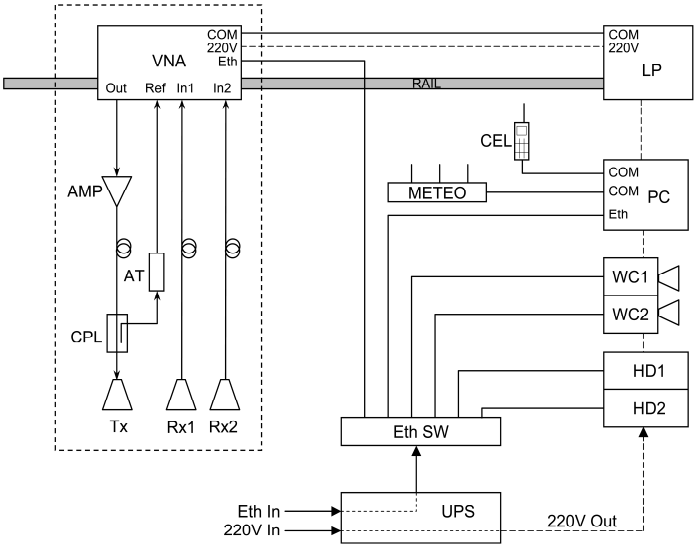

Fig. 3.1. Components view of the LISA instrument.

The core of the instrument is a vector network analyzer (VNA), which is used to generate the SF-CW radar signals and receive the coherent responses. A sled carrying the network analyzer, the power amplifier (AMP) and the antennas (Tx, Rx1 and Rx2) slides along a rail directed by a linear positioner (LP). Two external hard disks (HD1 and HD2) implement the data archiving and backup, while the visualization of the instrument inside the container and outside (radar field-of-view, FOV) is performed by means of two video cameras (WC1 and WC2). A meteorological station (METEO) monitors the temperature, pressure and humidity of the instrument inside the container. A personal computer (PC) operates all the systems and is used for the data processing. An uninterruptible power supply (UPS) guaranties continuous operation of the instrument even under short energy cuts and isolation against current discharges coming from the external Ethernet connection. Finally, an air conditioning unit with heating/cooling modalities keeps the humidity and temperature inside the container under stable values.

Note that the integration of all the radio frequency components in the moving sled avoids folding the RF cables, a possible source of phase distortions in ground based SARs because of the continuous bending of the cables caused by the movement of the linear positioner.

Since the instrument operates uninterruptedly 24/7, connectivity to the outside is necessary to monitor the proper functioning of all elements. Basic communication is performed through a mobile phone (CEL), while, when available, a high speed Internet connection can be fed to the network switch of the instrument (Eth SW) permitting also some data transfer for manual analysis and interpretation at the headquarters.

It is worth noting that two simultaneous reception channels are available on the VNA used. These channels can be used either for acquiring a co-polarized and a cross-

polarized response (polarimetric-on-receive mode) or for acquiring two co-polarized responses with a vertical baseline separation. This last configuration has been chosen for this PhD thesis, also called topographic mode, in order to be able to create a digital terrain model (DTM) of the field-of-view in which to project the radar images for easier interpretation [35]. In fact, cross-polarized signals appear to have a lower backscattering on the dry snow cover than co-polarized ones [36], so they were initially discarded, concentrating only on the *vv* channel that shows, at 5.3 GHz, a slight higher backscatter than in *hh* [36].

3.1.2. Radio frequency section

The stepped-frequency continuous wave (SF-CW) method of obtaining object responses over a wide range of frequencies is a relatively simple extension of CW measurements, in which the procedure is repeated for a number of discrete frequencies. The process is accomplished by using tunable, narrow band receivers operated in synchronism with programmable signal synthesizers controlled to step in uniform frequency increments. The principal advantages of SF-CW systems compared to frequency modulated FM-CW are two [25, pp.52-55]:

a) They are relatively simple, requiring only the addition of frequency tuning to a conventional CW system.

b) They have a high degree of amplitude sensitivity, which is normally obtained from narrow band CW receivers.

If the dwell time for each frequency step approximately equals the inverse of the receiver bandwidth, the receiver operates essentially as a matched filter, and optimum signal to noise ratio (SNR) performance can be achieved. In a conceptual sense, this system provides optimum performance in terms of both range resolution and SNR.

Two practical considerations limit the utility of stepped-frequency CW systems: their high level of transmitter signal leakage and their susceptibility to aliased responses. Because the transmitter and receiver are simultaneously active, the performance of CW systems is limited by signals directly coupled from the transmitter into the receiver channel, even in the absence of object echoes. The degree of coupling in systems using separate antennas as is the case of the LISA instrument is determined by the channel isolation. Since the amplitude of the coupled signal usually exceeds that of the object signal by several orders of magnitude and is frequency dependent, the receiver must provide sufficient dynamic range to accommodate the large transmitter coupling signal without distorting the relatively weak object signal.

The effects of the transmitter coupling signal can be separated from the object signal subsequent to the range processing. This is possible because the transmitter coupling signal appears at shorter ranges than the object signal, and can therefore be virtually eliminated by range gating. This feature, termed software range gating, allows the range-selective suppression of contributions of unwanted echoes from the total measured signal. Because the effects of the transmitter coupling signal can only be removed after processing, software range gating has no effect on the dynamic range requirements of the receiver, which must be capable of accepting the total received signal without saturation.

The unambiguous range of the SF-CW system, given by (2.8), is established by the frequency step size. Because the frequency sampling process occurs at the transmitter, no antialiasing filtering is available prior to sampling. Consequently, spurious responses from ranges beyond the unambiguous range can be aliased into the range of interest and be indistinguishable from desired object responses.

In summary, SF-CW systems require a wide dynamic range to accommodate strong spurious echoes due to transmitter leakage. In addition, these systems are vulnerable to spurious responses that can be aliased into the range of interest and be indistinguishable from object responses. These systems are used, therefore, when it is possible to establish a priori that no aliased responses can occur.

SF-CW systems can be readily implemented using commercially available laboratory equipment consisting of computer-controlled microwave synthesizers and narrow band receivers. High-quality narrow band receivers, tunable over wide frequency ranges and with 100 to 120 dB of dynamic range, are embodied in modern vector network analyzers designed for component testing. These instruments, properly adapted provide a very practical alternative to a complete specific system design, perfectly overcoming the problems of transmitting signal leakage and susceptibility to aliases inherent to SF-CW systems. Actually this has been the choice for the LISA instrument since its conception in 1999 and has proven during all this years to be perfectly suited for the application of landslides monitoring and recently for the application of the snow cover monitoring.

3.1.3. LISA deployed in Switzerland

As stated in the Section 3.1, the LISA instrument deployed in Switzerland corresponds to the first GB-SAR sensor developed in JRC in 1999. The main difference with the original design is the upgrade of the VNA and the removal of the circular synthetic aperture. Figure 3.2 shows two external pictures of the LISA instrument.

a) 

b) 

Fig. 3.2. External view of LISA instrument in Switzerland: a) back side with the access door open; b) front side with the aperture.

Note on the front side view (Figure 3.2-b) three details:

a) The external unit of the air conditioning system is protected by an aluminum enclosure to protect it from the weather conditions.

b) A pitched wooden roof was specially constructed to allow the evacuation of snow since the application of snow cover monitoring of course implies the deployment of the instrument in areas prone to heavy snow fall.

c) The antennas are not directly exposed to the exterior, but protected all along the linear aperture by Rohacell material. Rohacell is a polymethacrylimide hard foam that shows outstanding mechanical and thermal properties with an impedance close to that of free space. It offers an optimum ratio of weight and mechanical properties as well as excellent heat resistance.

At the end of the last winter campaign the roof felt down because of strong wind conditions, even though it was anchored with cables to the ground. Since this roof was an adaptation of the original instrument for snow cover monitoring, the lesson was learnt and this aspect of the instrument was improved in the sensor installed on the second test site.

Figure 3.3 shows a couple of pictures of the instrument, this time from the interior. On the first picture, Figure 3.3-a, the PC for controlling the whole system is shown. Also the mobile phone used to control externally the instrument can be seen. On the right side of Figure 3.3-a a portion of the 5 m long linear rail used to synthesize the aperture is also visible. Figure 3.3-b shows, instead, the radio frequency section of the instrument. From bottom to top, the VNA can be seen, a solid state power amplifier is placed right over the VNA and a directional coupler is inserted in the cable before feeding the transmitting antenna (CPL in Figure 3.1) to get a good reference phase. Finally, three antennas are installed: one is used for transmitting (that in first plane) and two vertically separated 40 cm approximately are used for receiving. Note on the right side of Figure 3.3-b the Rohacell foam covering the aperture of the trailer that serves to isolate the components from external weather conditions.

a)  b) 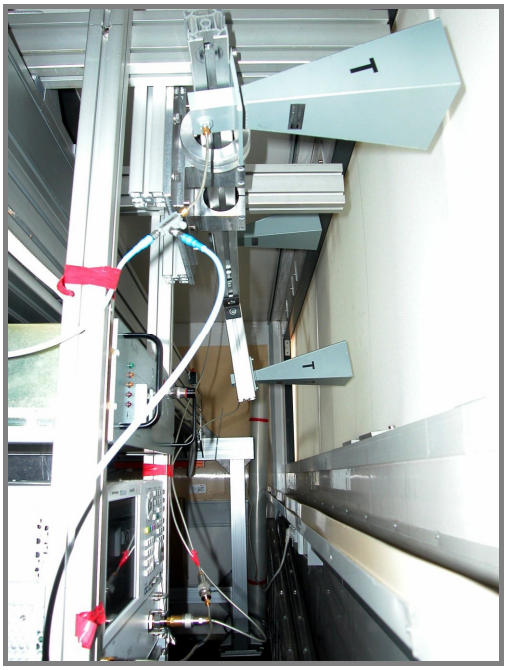

Fig. 3.3. Internal view of LISA instrument in Switzerland: a) controlling PC; b) radio frequency section.

Two different VNAs were used in this field campaign. The network analyzer the first winter was an 8753D from HP, covering the band 30 kHz to 6 GHz and featuring a dynamic range of 105 dB and an acquisition time of 500 μsec/point. The network analyzer used the second and third winters, instead, was an E8362B from Agilent Technologies, covering the band 10 MHz to 20 GHz and featuring a dynamic range of 122 dB and an acquisition time less than 26 μsec/point. The solid state power amplifier used was, in all three winters, an ARSA-CS50 from Advantech, featuring 40 W of output power with a gain up to 65 dB at C-band.

It should be noted that the higher dynamic range and acquisition rate possible with this later VNA were the principal responsibles for a higher image quality (higher SNR and higher coherence between images) during the second and third winters. Nevertheless, for the application of snow cover monitoring both VNAs performed perfectly.

3.1.4. LISA deployed in Italy

In parallel to the last winter campaign in Switzerland a new LISA instrument was deployed in the Italian ski resort of Alagna Valsesia (winter 2005-2006). This instrument was built from scratch following the same system concept as that used for the original LISA but adapting the dimensions of the container to the constraints in space of the place where it was later on deployed (see Section 4.3 for details).

a) b)

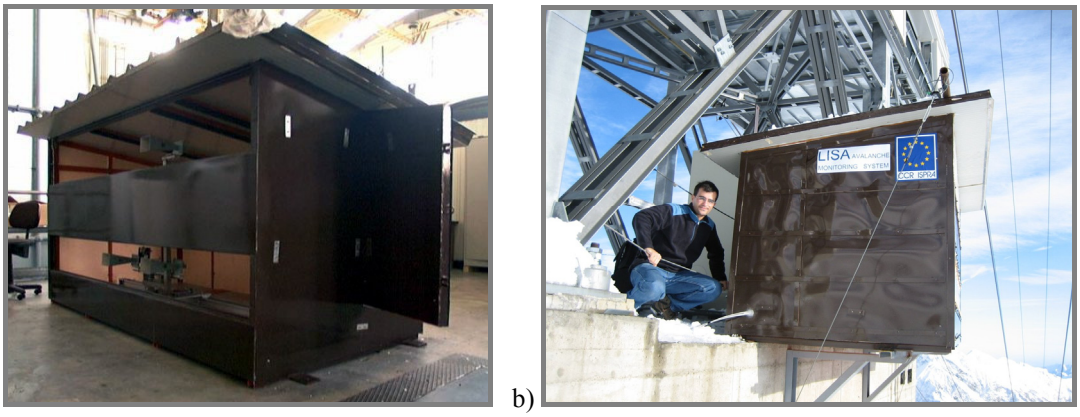

Fig. 3.4. External view of LISA instrument in Italy: a) front view with the three antennas and linear rail visible during the building phase; b) lateral side of the instrument once deployed.

Figure 3.4 shows a couple of pictures of the external container enclosing the instrument. In Figure 3.4-a the antennas set can be observed during the building phase of the instrument. Note that the two apertures that permit the pass of the radio frequency signals will be later on covered with Rohacell in order to minimize the effects of weather conditions on the instrumentation. In Figure 3.4-b the instrument can be seen once deployed on the concrete base of the intermediate station of a cable-car.

Due to space constraints no air conditioning unit was installed on that instrument. During the three winter campaigns temperature excursions of up to 20 °C were observed in the interior of the container, but the electronics worked properly. Again, the solution of implementing the radar system with a commercial VNA proved to be right since such laboratory instruments provide an excellent performance under different temperature

conditions. In that occasion the roof was designed from the very beginning in view of the installation of the instrument on a ski resort and the previous experience with the instrument in Switzerland. A pitched metallic structure, laminated and filled with thermo-isolating foam, was firmly screwed to the metallic chassis of the container. In addition, as can be appreciated from Figure 3.4-b the whole container was secured with steel cables to the concrete base in order to keep it in position during strong winds.

Figure 3.5 shows a couple of views of the interior of the instrument on the building and operative phases respectively. Figure 3.5-a shows the linear rail carrying the three antennas set. The rail for that instrument was 2 m long, while the two receiving antennas were vertically separated 80 cm approximately. Note that the antenna apertures to the exterior have been already protected with Rohacell.

a)  b) 

Fig. 3.5. Internal view of LISA instrument in Italy: a) linear rail and antennas set during the building phase; b) full components view.

Figure 3.5-b shows the instrument once completed and in full operation in the ski resort. From bottom to top the first device that appears in the picture is the VNA. On its back, a power supply feeds the RF power amplifier and next to it, although not visible in the picture, a directional coupler sends the reference signal to the VNA. On the very left a couple of antennas can be seen, of which one is used for transmitting and the other one for receiving. On the back of the container, from left to right can be seen the external video camera, the electrical cabinet of the instrument, the internal video camera, the controlling PC, external disks for data archiving and the UPS. On the very right side the big cabinet houses the linear positioner control unit.

Apart from the linear rail that changes from 5 to 2 m, compared to the instrument deployed in Switzerland, it can be appreciated that the internal space has been substantially reduced. This demonstrates how an experimental instrument such as the original LISA of 1999 can be easily transformed to fit a particular application where ease of deployment is mandatory. In a similar way, the path towards an instrument able to operate uninterrupted with a very specific objective (such as snow cover monitoring) can be done by industrializing this prototype and obtaining and even smaller instrument.

Similar to the LISA instrument in Switzerland, the VNA in Italy was also replaced after the first winter of field campaign. The network analyzer the first winter was an Agilent PNA E8358A, covering the band 300 kHz to 9 GHz and featuring a dynamic range of 113 dB. The network analyzer used the second and third winters was an Agilent PNA

N5230A, covering the band 300 kHz to 13.5 GHz and featuring a dynamic range of 120 dB.

3.2. Upgrades for 24/7 operation

Apart of upgrading the VNA and removing the circular synthetic aperture, prior to this PhD thesis' work little modifications were done to the LISA instrument since its development in 1999. In order to develop processing techniques to remote sense the snow cover and assess them through the data archive (see the objectives of this PhD thesis in Section 1.3), it was necessary to perform continuous measurements during several winter field campaigns. This was definitely not possible with the instrument in its initial state, so a couple of objectives related to the instrument itself - a) and b) in Section 1.3 - precede those related to the monitoring techniques - c) and d) in Section 1.3. -

The main objective of the instrument upgrade described in this PhD thesis was to increase the uptime of the sensor to the higher possible values: objective a) of Section 1.3. Although no systematic statistics are available to quantify the past uptime performances of the instrument, a qualitative improvement can be clearly observed in the data concerning the two field campaigns carried out in the scope of this PhD thesis. The uptime performance of the LISA instrument can be roughly quantified as follows:

a) Prior to the field campaigns carried out in this PhD thesis (before 2003): a few days of continuous measurements were possible.

b) After the second field campaign (2005 approximately): a few weeks of continuous measurements were typical.

c) During the last field campaign (winter 2007-2008): a few months of continuous measurements were possible. Actually during four months of operation the instrument needed manual intervention to recover from a block status only in a single occasion.

The data catalogue in Annex D shows in the last column a mark (<-) when measurements where interrupted. Periodical maintenance is also marked with the same symbol since only data continuity has been considered when setting this mark. Nevertheless, periodical maintenance situations show typical instrument downtimes of a few hours, while unexpected system blocks or power shutdowns are characterized by downtime intervals of several days. Auto-recovered small interruptions occurring within the day are not marked either. Two things can be noted when observing the interruptions evolution at each test site all along the field campaigns:

a) The number of interruptions not caused by periodical maintenance decrease in both test sites. Sion: 5 » 2 » 2; Alagna: 0 » 4 » 0 (the first winter campaign in Alagna was exceptionally short).

b) The recovery time after interruptions qualitatively decreases all along the campaigns from several days of downtime to several hours.

In order to increase the uptime operation, the first step was to identify the main causes of actual system blocks and those potentially problematic or that could help in resolving in an easier way an unexpected problem. These are listed as follows:

a) The VNAs used didn't allow auto power on after power failure and subsequent power recovery.

b) No system of data storage was foreseen to save the several gigabytes of data corresponding to the continuous acquisitions over a few months time neither to quickly move them to the headquarters during the periodic visits to the instrument.

c) No remote control of the instrument was available to check the system status or remotely recover from software problems.

d) No visual images of the container inside were available to better diagnose the causes and propose solutions to problems with the linear positioner.

In the following sections solutions are proposed and implemented for the above mentioned problems. As stated before, the aim of this chapter is double. On one side to provide the means for the proper data acquisition necessary for the further development and assessment of snow cover monitoring techniques, and on the other side to evidence some relevant problems and particularities in the transition from an experimental to a semi-operational instrument.

3.2.1. Ethernet-based infrastructure

The interconnection of instruments in the original LISA instrument was based on GPIB (General Purpose Interface Bus), also known as HP-IB or IEEE-488 bus to which the controlling workstation, the network analyzer, an RF switch matrix and the positioner for the synthetic linear and circular apertures were connected [14]. Some simplifications to the instrument led at the beginning of 2003 to the removal of the circular aperture, the removal of the RF switch matrix and to the upgrade of the old network analyzer by a modern VNA. The GPIB bus was then completely eliminated, since the VNA was able to run the control software in an integrated processor unit. The linear positioner, initially connected by means of a serial interface (RS-232) to the controlling workstation, was then connected to a serial interface of the VNA. The VNA became, thus, the unique instrument implementing and controlling all core functions of the GB-SAR.

Optionally and mainly because of the limited storage and processing capabilities of the VNA, a direct Ethernet connection between the personal computer (PC) and the VNA allowed the data transfer to the internal disks in the PC and a preliminary near-real time analysis of the data.

Following the industry trend towards the use of Ethernet based solutions because of their easy deployment, easy interconnection, high reliability and low economic cost, a Gigabit 8 port Ethernet switch was installed on the LISA instrument as the first step on the instrument upgrades described in this chapter.

This component, labelled Eth SW in the blocks diagram of Figure 3.1 interconnects all subsystems in an economic and flexible way, allowing the easy repositioning of any

element inside the instrument's container. The use of an Ethernet switch allowed, besides the interconnection between the VNA and the PC, the easy addition and control of two new devices to the LISA instrument:

a) Two Ethernet video cameras for external and internal monitoring of the instrument, labelled WC1 and WC2 in Figure 3.1.

b) Two network attached storage servers (NAS) to archive the measurements data, shared both by the VNA and the PC and labelled HD1 and HD2 in Figure 3.1.

The network attached storage servers are covered in more detail in the next section. The Ethernet video cameras, instead, are controlled from the PC, which allows the continuous visualization of both video cameras signal in real-time. In addition, the PC saves a snapshot of every video camera into the data storage server every 10 minutes through a scheduled task. The models installed are listed in Table 3.1.

Table 3.1. Ethernet video cameras installed in the LISA instrumet

	Inside	**Outisde**
LISA deployed in Switzerland	Axis 206	Intellinet 550710
LISA deployed in Italy	Axis 206	Axis 210

Another big advantage in the use of an Ethernet network is the fact that, once a remote connection is established with the LISA controlling PC, access to the rest of subsystems is easily done through standard Internet protocols (IP) from the remote PC without the need to use a remote desktop like application. In summary, direct access to the LISA network devices can be done from the remote PC, increasing the flexibility to control them and to solve possible problems.

3.2.2. Data storage

Data storage in the LISA instrument presents three particularities when continuous monitoring a test site in an operational mode:

a) The data archive needs to be available both for the VNA (producer of the data) and for the PC (consumer of the data). In case of malfunctioning of the PC no real-time processing will be possible, but the data needs to be saved for later analysis as far as the VNA continues to work.

b) Depending on the sensor parameters (see Chapter 4 for more details), 750 to 1500 MB of raw data is generated per day of monitoring. Processed data occupies approximately the same space as the raw data. This implies a consumption of 45 to 90 GB of disk space per month.

c) When visiting the instrument for general maintenance, the data stored in the instrument archive needs to be moved to the headquarters central data archive. This means moving some 100 to 150 GB of data between disks and that innocent operation can take several hours.

Actually, the before mentioned constraints are not exclusive of the LISA instrument. Any operational instrument with the imaging capabilities of LISA needs to face such problems if data archiving for later analysis is desired. A direct processing chain without storage of the raw and pre-processed data would be an alternative, but technical solutions exist nowadays to overcome the before mentioned particularities without renouncing having the data available for *off-line* study.

The solution implemented for the LISA instrument consists of two external hard disks, of which at least one is a network attached storage server (NAS). The second disk can be either a NAS or a simple external disk directly connected to the PC through any of its interfaces (USB, FireWire, eSATA, etc.)

The data storage subsystem works as follows: the NAS disk is directly connected to the Ethernet switch, and thus available from the VNA and the PC even if the PC fails to operate properly. The VNA local processor runs the acquisition software and saves the raw data directly into the NAS independently of the status of the rest of subsystems. The PC, on the other side, runs two less critical tasks: the data processing for subsequent visualization of results and alert sending and the data backup into the second external disk.

The data backup into the second external disk has a double purpose: to keep a backup in case the primary disk fails and to facilitate the data transfer to the central data archive by physically bringing the disk (and its contents) to the headquarters to copy the data directly there. When visiting the instrument, thus, a second external and empty hard disk is necessary to replace that installed into the instrument.

Considering the space requirements, disks of 150 to 500 GB have been employed all along the 5 years of field campaigns carried out. State of the art storage technology has also accompanied the improvements on the uptime of the LISA instrument: while in 2003 typical off-the-shelf disk capacities ranged from 100 to 200 GB, the instrument was able to operate uninterrupted only during a few weeks, so data fitted without problems in the storage servers available. In 2008, off-the-shelf disk capacities of 500 to 750 GB are available at reasonable prices, so for the current unattended operation of the LISA instrument, there is no problem archiving data for a few months.

3.2.3. Remote communication and operation

Inherent to the application of snow cover monitoring there is the fact that the instrument is typically deployed in mountainous areas, which implies many periods of difficult access, even by 4×4 vehicles. This means that an engineer may take several hours or days to reach the instrument and solve any problem arising. The most desirable scenario is an instrument that autonomously recovers from any errors which may happen, but it is virtually impossible to predict all possible causes of problems and foresee automatic solutions for all of them.

The remote communication with the instrument becomes, then, of high utility to avoid costly displacements and to quickly solve minor problems that do not require physical presence of an engineer. In addition, the remote visualization of the external and internal video cameras signal helps in better evaluating the scale of the problem and, hence, in better organising the resources to send to the instrument.

A direct connection to a broadband Internet provider would be the ideal solution. Nevertheless, considering the difficulties in providing a stable 220V power line to

electrically feed the instrument in mountainous areas, a broadband data connection remains unlikely.

Several solutions are technically available to interconnect a remote station, and those satellite-based appear to be the best in terms of coverage. A point-to-point radio link can also be an alternative when a cabled broadband connection is available a few kilometres away from the instrument. Nevertheless, because of the good mobile phone coverage in the area where the instrument was deployed, a GSM modem solution was selected. The implementation of this solution is its main advantage, since it can be done with economic of-the-shelf components very quickly. The main drawback is the data rate available: 9.6 kbps in the most basic implementation (pure GSM). Unfortunately some telecommunications operators do not offer more advanced data services as GPRS, EDGE or UMTS in mountainous areas, and this was actually the case in the location of the first field campaign in Switzerland.

The GSM modem is labelled CEL in the blocks diagram of Figure 3.1. It is actually connected by means of a serial interface (either USB or RS-232) to the controlling PC, which is configured to accept incoming connections through the modem. This way it is the operator at the headquarters that initiates the communication.

In the case of the sensor deployed on the second test site, the Italian ski resort, a cabled network port from the ski resort's intranet was available some 50 m away from the radar location. This fact was providential, since it allowed to interconnect the instrument network switch with a simple Ethernet cable to the ski resort's intranet, and from there direct access from the headquarters through a virtual private network (VPN) connection was possible.

Once the remote connection is established all components in the local network of the instrument are easily accessible thanks to the Ethernet based infrastructure. The real-time signal of the video cameras or the snapshots regularly saved can be examined; the integrity and available free space of the data storage servers can be checked; some preliminary results of the processed data can be visualized; and what is more important: subsystems (VNA, linear positioner, video cameras, hard disks and PC) can be manually overridden or reset to try recover them from any block situations.

It may also happen that the controlling PC experiences a problem that even prevents a remote connection. To minimize the effects of those cases, rare although not exceptional, a weekly reboot of the PC is scheduled. This was the lesson learnt after two winters of field campaign, and in fact during the rest of field campaigns the PC allowed without problems all remote connections.

The use of the VNA for the radar core activities and the separated use of the PC for the auxiliary functions as data storage control, video control, data processing and remote connection results in a reliable redundant system. A hypothetical problem of the VNA can be remotely solved from the PC, whereas a problem of the PC doesn't necessarily stop the radar acquisitions.

A final aspect also very much important regarding the remote connection of the instrument is the possibility to send alerts originated from the instrument itself. Two kinds of alerts can be generated by the instrument:

a) Those regarding the malfunctioning of a subsystem in the instrument.

b) Those regarding the purpose of the radar itself, this is the identification of a dangerous situation on the snow cover.

The first group of alerts has not been implemented since they would be required only on a real operational scenario. The second group of alerts, instead, have been implemented during the last winter campaign in the Italian ski resort. More details of these alerts are available in the Section 7.6.1.

3.2.4. Auto-start after power failure

Power failures are not common nowadays in industrialized cities, but the panorama changes when moving to mountainous areas. Storms happen frequently and tend to cause instabilities on the power supply or even short cuts of current. The presence of spuria on the 220V power line or even micro cuts of energy are enough to switch off the VNA and the PC of the instrument.

The first solution an electrical engineer would apply to minimize the effects of such power cuts is the installation of an uninterrupted power supply (UPS) before any other electrical equipment in the instrument. This solution was in fact already present on the LISA instrument from its early development in 1999.

A step forward was done with the new LISA instrument specifically developed and built for the second field campaign on the Italian ski resort. Considering the possibility of connecting the instrument informatics network to an external Ethernet network or to a telephone line for remote access to the instrument subsystems, a UPS with isolation capabilities for the Ethernet and modem ports was selected. In particular the model used was the APC Back-UPS RS 1500VA, with autonomy for approximately 5-10 minutes of full radar operation when fully charged.

Nevertheless, longer power shutdowns may empty the UPS batteries or current peaks may activate the circuit breaker protections of the instrument. Hence, automatic procedures to re-start all subsystems are necessary.

On one side, miniature circuit breakers (MCB) and residual current circuit breakers (RCCB) that automatically try to re-arm themselves after several minutes of power interruption are available on the market. These devices should be used on the electrical cabinet of an operational instrument. In the case of the field campaigns carried out with the LISA instrument, instead, no auto re-arm MCBs were used. Although several power interruptions affected the measurements, no current peaks caused the activation of the electrical protections of the instrument.

On the other hand, all electrical and electronic devices inside the LISA instrument need to be programmed to automatically re-start after power failure. This presents no difficulties for almost all electronic devices used… except the VNAs: all four VNAs used during the field campaigns did not allow this possibility (see Sections 3.1.3 and 3.1.4 for details on the VNA models used).

In order to overcome this difficulty without breaking the warranty of the instrument by disassembling it, an external actuator in the form of a mechanical finger controlled by the PC was implemented. It is fixed in front of the power-on button of the VNA, and pushes it in a similar way to the way a human operator would do with his own finger. With

a simple software that communicates with the actuator through the Universal Serial Bus (USB) port of the PC, it is possible to remotely turn on and off the VNA at the user's will. This device was called *Fingertron*. Figure 3.6 shows a picture of the device once installed, shown by two white arrows.

The *Fingertron* is composed of two elements: a solenoid (the electromechanical actuator) that is installed in the device to be switched on and off, and a box containing the power supply and the electronics to control the solenoid. In the Figure 3.6, the box with the power supply, the electronic circuit and the USB interface to the PC are pointed by an oblique white arrow (a). The solenoid and its support to the VNA by means of an aluminium plate, instead, are more evident and are marked with a vertical white arrow (b).

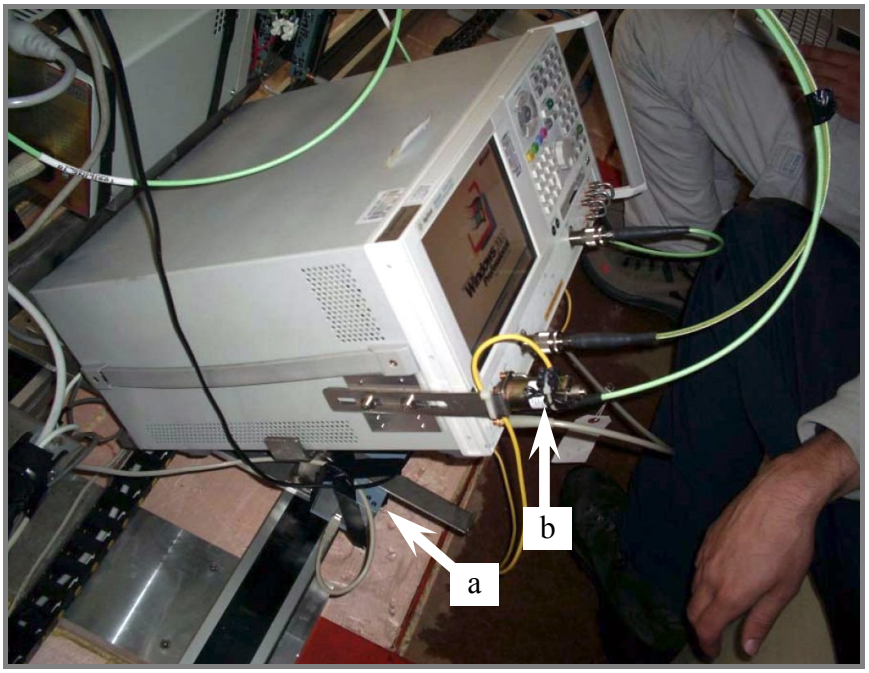

Fig. 3.6. Picture of the *Fingertron* once installed. a) Box containing the control circuit with the power supply and USB interface; and b) Solenoid and its support to the lateral of the VNA.

The *Fingertron* can operate either in automatic or manual mode. In manual mode it is controlled from a PC through an USB connection and the appropriate specifically developed software. The software reads a configuration file and tries to switch on or off the VNA by sending to the solenoid a pulse of the length specified in the configuration file. In automatic mode the *Fingertron* responds when 220VAC power is back after a power shut-down situation. Actually when power is back, after an intentioned pause of 5 min for proper line stabilization, the *Fingertron* tries to switch on the device by sending a pulse of approximately 1 second to the solenoid that pushes the power-on button of the VNA.

The automation of the manual mode through a scheduled task on the controlling PC allows one to periodically check the status of the VNA and to send a pulse through the *Fingertron* to switch it on in case the VNA is off. The scheduled task executes a batch file that interrogates the VNA through a network ping command taking advantage of the Ethernet based infrastructure that interconnects all subsystems of the LISA instrument. If no response is received from the VNA, the appropriate command is sent to the *Fingertron* to switch the VNA on.

The manual mode operation through a USB interface and the periodical check of the VNA status with the possibility to power it on with the *Fingertron* are two original solutions applied to the LISA instrument. These solutions have never been used, to date, in a GB-SAR to the knowledge of the author. A schematic diagram of the electronic circuit controlling the *Fingertron* and more information on its implementation can be found in Annex C.

Fortunately, newer VNA models incorporate from the factory an option in their BIOS to automatically switch the instrument on after power failure, so a device like *Fingertron* would not be necessary in such models.

3.2.5. Detailed view of components

Figure 3.7 presents a picture of the internal side of the LISA instrument deployed in the Italian ski resort. It is actually the same picture as that of Figure 3.5-b, but enlarged and with all subsystems described in the preceding sections signalled with text boxes. Some of the nomenclature used corresponds to that already used in Figure 3.1.

The only devices not directly visible are the second receiving antenna (Rx2), the Ethernet switch (Eth SW) and the rail that synthesizes the linear aperture (RAIL).

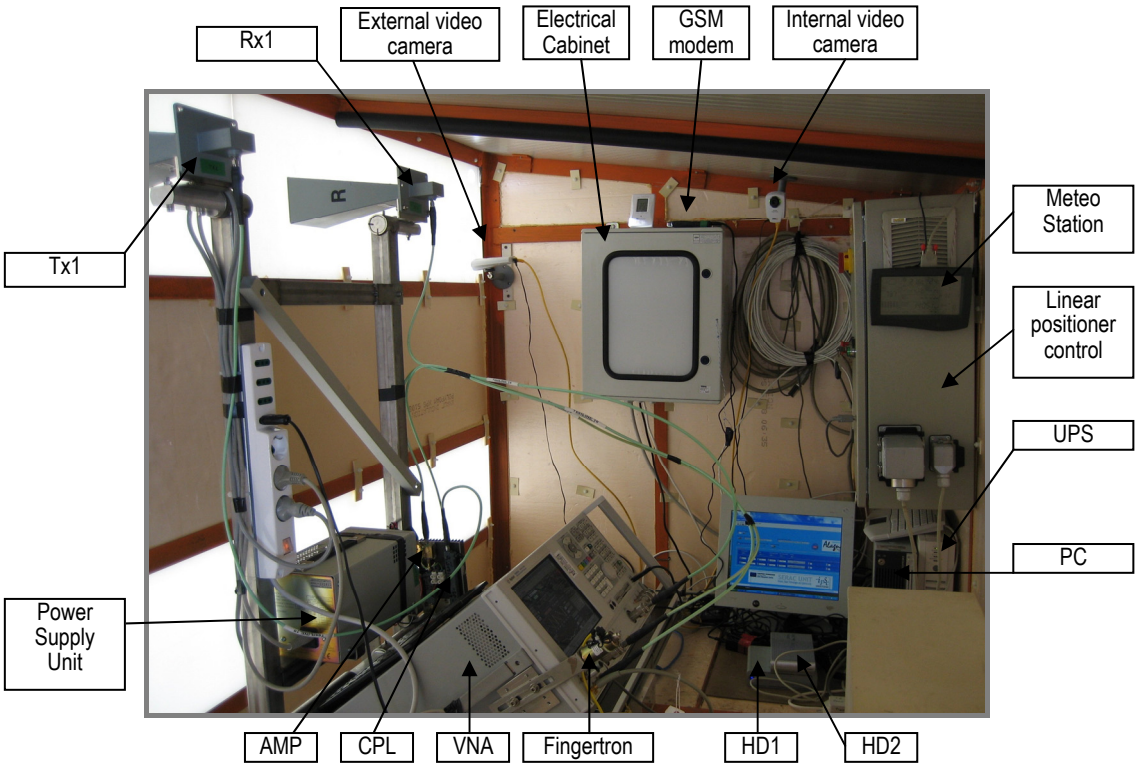

Fig. 3.7. Detailed internal view with components identification of the LISA instrument in Italy.

4. Field campaigns

4.1. Introduction

As previously stated one of the objectives of this PhD thesis was to obtain a representative data archive in order to properly develop and validate snow cover monitoring techniques. No similar data archive was available to the author's knowledge prior to this work. At local scale, snow cover has been mainly studied with scatterometers and radiometers in order to retrieve basic snow properties such as permittivity or snow water equivalent or ice crystal size. On more experimental set ups, snow height has been retrieved and buried objects in the snow cover successfully identified with FM-CW radars. At global scale, instead, satellite- and air-borne SARs are operationally employed to create maps of snow covered areas (SCA) and snow water equivalent (SWE). Section 1.1 gives a wider overview on the remote sensing techniques applied so far to the snow cover.

Our aim, instead, was to create an extensive archive of SAR images of the snow cover with the major number of different signatures available, with particular interest to observe the effects on the SAR imagery of natural avalanches, snow drift, snow melting and skiers passing by the FOV of the radar.

Two different test sites were monitored during three years each, particularly in winter time. The characteristics of each site and the data collected are described in the following sections. In addition, the Annex D shows the complete list of days and time intervals of monitoring activities that result in the data archive mentioned in the objective b) of Section 1.3.

4.2. Sion Valley (Switzerland)

4.2.1. The test site

The Swiss Federal Institute for Snow and Avalanche Research (SLF, Davos) manages this test site for avalanche experiments in the Sion Valley, in the Canton Valais of Switzerland [37]. The site consists of a concave shaped channel of 1200 m vertical drop and an average slope of 27 degrees. The avalanche path length is 2.5 km, starting from the highest elevation level at 2650 m at Creta Besse and finishing at the level of 1450 m.

Several instruments are available in the test site providing ground truth data. Three pairs of FM-CW radars are located in the avalanche corridor to determine the height of the

avalanche, its speed, turbulences and density. A network of geophones automatically triggers the measuring equipment when spontaneous avalanches occur. For impact studies a narrow wedge steel construction 20 m high is in the middle of the avalanche track. It is equipped with force transducers and pressure and strain gauges to determine the avalanche flow height through contact with the moving snow mass. Two meteorological stations provide data concerning temperatures, wind speed and direction as well as snow height:

a) Donin Du Jour: at 2 km of the slope (CH1903 coordinates 594450E-129930N, h=2390 m).

b) Montana: at 9 km of the slope (CH1903 coordinates 602960E-129160N, h=1590 m).

In order to observe the avalanches under the best possible conditions, a bunker is located in the mountain opposite to the corridor 50 meters above the lower level of the valley. It holds a 5 Mpixel digital photo camera that continuously takes a picture every 30 minutes. When a geophone detects an avalanche, the camera switches to burst mode with a rate of 1 picture every 4 seconds. The bunker is also used for recording the measurements made by SLF in the corridor and to provide the power energy to the LISA instrument.

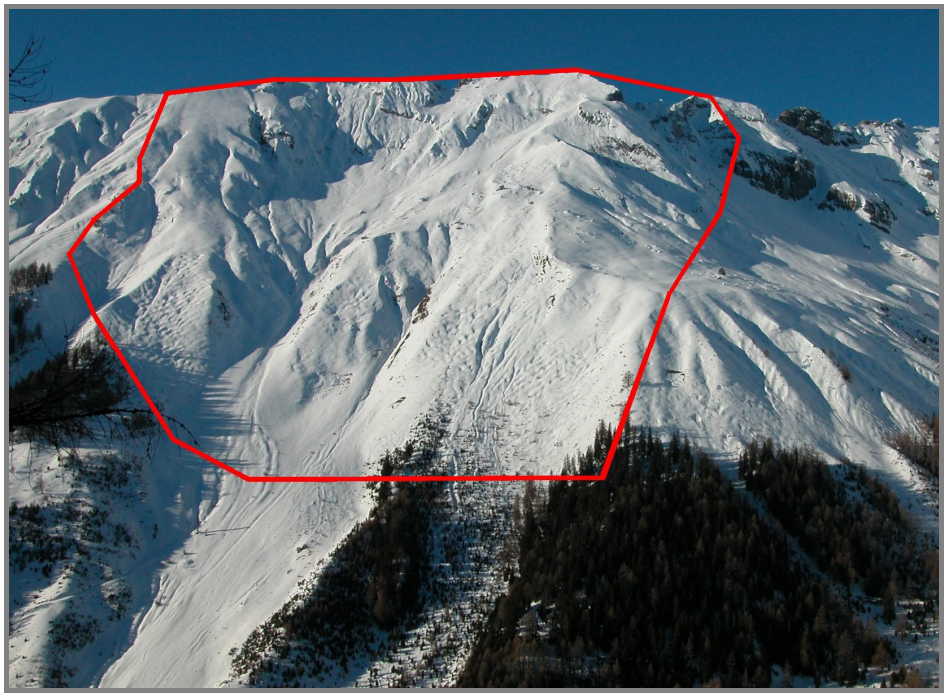

Fig. 4.1. Picture of the Sion Valley test site with the instrument FOV delimited in red.

The LISA system is located in the mountain opposite the avalanche corridor at an approximate level of 1780 m (330 meters above the lower level of the valley). In that way the instrument has direct visibility of the scenario, covering a cross range section of more than 2000 m. The distance of the instrument to the slope ranges approximately from 1000 m to 2900 m, hence, the area covered by the radar is nearly 2 km by 2 km as can be seen in the figure 2. Figure 4.1 shows a picture taken from the location of the LISA instrument,

where the FOV has been delimited by a red poly-line. The exact position of the instrument in UTM coordinates was 595634E - 126830N (CH1903 datum).

The transportation of the instrument to the test site was done by trailer up to the closest possible point to the final location. Because of the mountainous area and the dimensions of the instrument the trailer had to stop some 5 km far away from the selected monitoring position. The rest of the distance was covered by helicopter: Figure 4.2 shows a picture of the deployment of the LISA instrument by a Super Puma helicopter from Helog-Heliswiss.

The LISA container itself, together with the linear rail 5 m long, the UPS and its batteries and the air conditioning system were the main components contributing to the total weigh of the instrument. For the deployment, all the electronic instrumentation was removed from the container: it was brought later on by car to the container and installed only after the LISA was positioned in its final location.

The external dimensions of the LISA container deployed in this test site were 9.50×2.70×2.20 m, while the weight the helicopter had to lift was close to 2.5 tons.

Fig. 4.2. Instrument deployment in the Sion Valley.

Figure 4.3 shows a picture with the LISA instrument in its privileged position for monitoring the Swiss test site. The wooden platform where the LISA sits was used in the past for holding an observatory cabin employed by SLF personnel to do mainly visual observations of the slope when artificial avalanches were triggered. Figure 4.3 also shows on the left-most side a portion of the instrument's field of view. Note that the access to the instrument is done by a back door that can be seen at the right of the tree trunk. A frontal-lateral picture of the instrument can be seen in Figure 3.2-b.

Fig. 4.3. Instrument final location in the Sion Valley.

4.2.2. Coordinates system

Similar to any other SAR, the radar images generated by the LISA instrument are referenced to a local coordinate system with origin in the central point of the rail synthesizing the linear aperture. Considering the extension of the images produced by LISA (2×2 km in this test site), the geo-referencing of such images to a local map becomes necessary in order to better appreciate and interpret the results.

It is out of the scope of this chapter to formulate the coordinate transformations necessary to go from the LISA coordinates system to a map projection based on Easting-Northing coordinates. This transformation is covered in detail in Annex E. Nevertheless, the Figure 4.4 shows the FOV of the instrument once geo-referenced in a local map of the area. The location of the LISA instrument and a dashed line pointing in the zero-cross-range direction have been also included.

Note that the FOV geo-referenced in Figure 4.4 is only an approximation. Actually, the FOV is a perfect rectangle only in the LISA coordinates system, since rectangular coordinates have been used during the focusing of the raw data. As it is shown in Annex E, the geo-referencing process involves a first step of coordinates rotation, a subsequent step of projection of the radar images over a DTM of the area and a later step of projection of the DTM 3-D points to a 2-D map. The second step before mentioned involves a non-linear process that causes straight lines to appear modulated by the terrain topography. The FOV presented in Figure 4.4 considers only the first step of the geo-referencing, that is, the rotation part. Hence, the four points defining the rectangular FOV in the LISA coordinates system, once rotated to the Easting-Northing (E-N) system and united by straight lines result in the FOV presented in Figure 4.4.

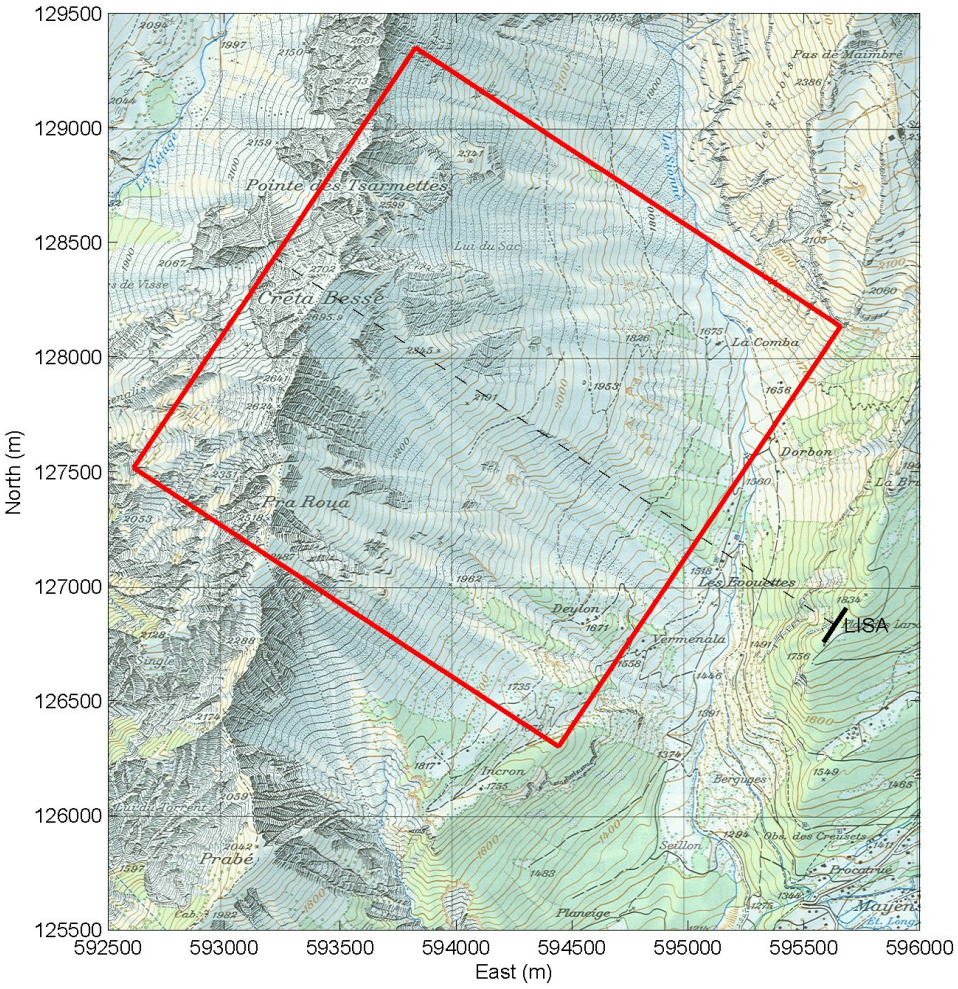

Fig. 4.4. Field-of-view over the map in CH1903 coordinates, Sion Valley.

The Universal Transverse Mercator (UTM) coordinate system is a grid-based method of specifying locations on the surface of the Earth. The UTM system uses a series of sixty zones each of which is based on a specifically defined secant Transverse Mercator projection for mapping a region of large North-South extent with a low amount of distortion. The ellipsoid used as the underlying model of the Earth is the WGS84. Each zone is referred to by the longitude zone number and the latitude zone character. In the case of the Sion Valley test site the zone is denominated 32T.

A position on the Earth is referenced in the UTM system by the UTM longitude zone, and the Easting and Northing coordinate pair. The Easting is the projected distance of the position from the central meridian, while the Northing is the projected distance of the point from the equator. The point of origin of each UTM zone is the intersection of the equator and the zone's central meridian. In order to avoid dealing with negative numbers, the central meridian of each zone is given a "false Easting" value of 500000 meters. Thus, anything west of the central meridian will have an Easting less than 500000 meters.

Similar to the UTM system, the Swiss coordinate system (or Swiss grid) is a geographic coordinate system used in Switzerland for maps and surveying by the Swiss Federal Office of Topography (Swisstopo) [38]. The map projection used is Oblique Mercator on an 1841 Bessel ellipsoid. The geodetic datum is called CH1903 and uses as fundamental point the old observatory of Berne.

Although similar, the UTM and the Swiss grid differ by several meters, so coordinates conversions need to be applied when acquiring GPS points (usually referred to the WGS84 datum) and porting them over Swiss maps (CH1903 datum). The map on the Figure 4.4, actually, being produced by Swisstopo, is based on the Swiss grid and the CH1903 datum.

4.2.3. Sensor parameters

The sensor parameters used to monitor this test site, except for the measurement time, were unchanged during the three winters that lasted the field campaign in this site, from 2003 to 2006. Table 4.1 shows the main parameters used:

Table 4.1. Measurement parameters in Sion Valley

	2003-2004	**2004-2006**
Polarization	VV	VV
Central frequency (GHz)	5.83	5.83
Bandwidth (MHz)	60	60
Bandwidth steps	1601	1601
Aperture length (m)	3.5	3.5
Aperture steps	251	251
Measurement time (min)	27.0	11.7
Vertical baseline (cm)	40.0	40.0
Horizontal baseline (cm)	-6.3	-6.3
Azimuth coverage (m)	-1100…1100	-1100…1100
Distance to slope (m)	700...2900	700...2900
Image size (pixels)	601×601	601×601

According to the radar band designations listed in Annex B.3, the frequency used during this field campaign corresponds to the C-band. Regarding the polarization used, see the last paragraph of Section 3.1.1 for more details on the selection of this parameter.

The theoretical resolutions in range and cross-range according to (2.2) and (2.4) are $\Delta R = 2.5$ m and $\Delta X_{SAR} = 5.1 \ldots 21.3$ m respectively. According to (2.8), the unambiguous range is $R_U < 4000$ m and, finally, the alias-free angular extension is 134.6 deg according to (2.10), where $\theta_{\max} = 1.17$ rad = 67.3 deg. Considering the area monitored and the before mentioned parameters, no aliased responses are expected on the radar imagery. Even the use of a SF-CW radar system that lacks, by implication, a range-gating mechanism in reception (see Section 3.1.2 for more details) will not be problematic for the imagery obtained from this test site.

4.2.4. Data availability

The complete list with the days and time intervals where data was acquired on this test site can be consulted in Annex D.2. Following are some numbers referring to this data archive, while more information can also be found in [39].

The campaign started on 2003/12/17 and finished on 2006/05/14, with 501 days of data acquisition divided in three winter seasons. The instrument was mainly switched-on

during winter time, although some data of the site without snow was acquired during the summer of 2005.

Regarding the SAR images, during the first two winters the instrument operated with a single antenna in reception (Rx1). Since the winter 2005-2006 a second antenna in reception, Rx2, vertically separated 40 cm from the first one was installed to allow the generation of single-pass interferograms for topographic purposes. This doubled the amount of data acquired (two Rx channels instead of one). Table 4.2 shows the approximate amount of radar images acquired in this test site divided by winter seasons.

Table 4.2. Data acquired in the Sion Valley with the LISA instrument

	2003-2004	**2004-2005**	**2005-2006**
Radar images, Rx1	7240	26323	17165
Radar images, Rx2	-	-	12909
Visual images, outside	-	-	14345
Visual images, inside	-	-	-

The radar raw data acquired in this test site occupies 190 GB of disk space. During the winter 2003-2004 raw data was acquired at a rate of 1 image every 30 minutes approximately. During the winter 2004-2005 an improvement of the network analyzer made it possible to acquire raw data at a rate of 1 image every 11 minutes. Finally, during the winter 2005-2006, using the same instrument than the preceding year, but 2 reception channels, raw data was acquired at a rate of 2 images (1 image per reception channel) every 11 minutes.

Before any other processing technique is applied, focused images need to be created for every data raw available at the end of every sweep of the linear aperture. This represents another set of data with the same number of images than the data raw archive but occupying 171 GB.

Concerning the visual imagery, because of time constraints and other project priorities the internal camera was not implemented. For the outside, a total of 14345 pictures are available from 2005/12/12 to 2006/05/15 (see Table 4.2) in JPEG format acquired at a rate of one picture every 15 minutes. This archive occupies 263 MB.

As explained in Section 4.2.1, the test site of the Sion Valley had a number of automatic sensors acquiring information of the slope and of the weather conditions. Three types of *ground-truth* data was available and are listed below. Note that data interruptions are present and frequent in these data because of problems with the respective instruments unfortunately outside of our control.

a) Meteorological data from the automatic station of Donin Du Jour. The data comprises the following parameters: snow depth, temperature of the air, temperature of the snow, relative humidity, wind speed, wind direction and solar radiation. The available data spans from 2003/11/01 to 2006/09/13, with a constant acquisition rate of one datum every 30 minutes.

b) Visual imagery acquired from the bunker location. This data archive spans from 2005/01/07 to 2006/05/23 with a variable acquisition rate that ranges from 1 picture per day to 1 picture every 30 minutes.

c) Visual imagery acquired from the bunker location triggered by the geophones network if an avalanche happens. This data archive spans from 2005/01/10 to 2006/05/22, with a total of 114 alarms triggered by the geophones.

Finally, three topographic products from the Swiss Federal Office of Topography were available for the monitored slope:

a) A high resolution DTM produced from aeroplane with a state-of-the-art laser scanner [38]. The ground-truth DTM pixel size was 0.84m×0.84m, while the height information had ±0.5m accuracy.

b) A high resolution orthophoto in black and white with pixel size of 1.01m×1.01m.

c) A digitized map: Carte nationale de la Suisse 1:25000. St-Leonard, Feuille 1286.

4.3. Alagna Valsesia (Italy)

4.3.1. The test site

The second field campaign was carried out in a more representative test site: the LISA instrument was deployed in the middle of a ski resort. The Monterosa ski complex (Monterosa 2000 S.p.A.) comprises currently three valleys, from West to East: Champoluc, Gressoney and Alagna, all of them in Italy, Piedmont region. The LISA was placed at Alagna Valsesia (http://www.freerideparadise.it).

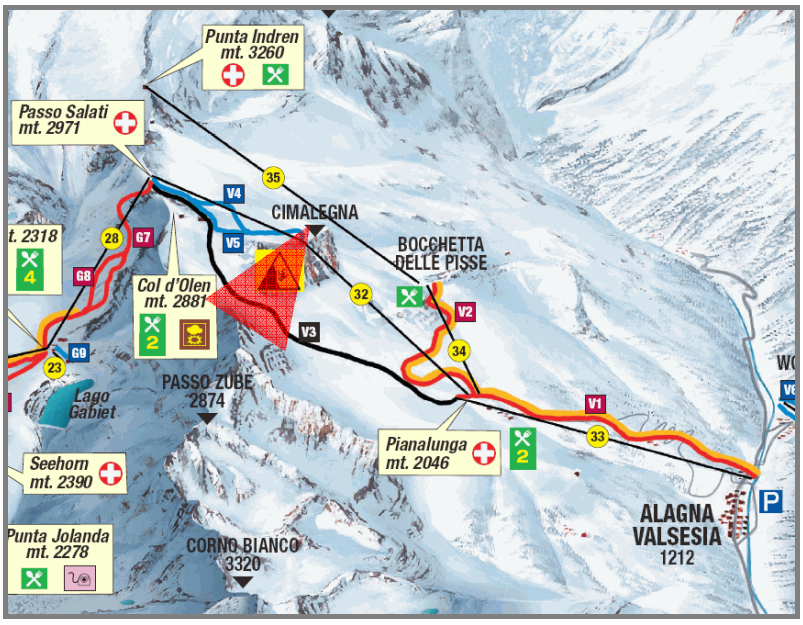

Fig. 4.5. Ski map of the Alagna Valsesia ski resort; the LISA was located at Cimalegna, covering the area delimited by the red triangle.

The system was located on the concrete base of the intermediate's stop of the cable car Funifor Pianalunga - Cimalegna - Passo Salati. This place is locally known as Cimalegna and is situated at 2656 m of altitude. The exact position of the instrument in

UTM coordinates was 413655E - 5080376N (WGS84 datum). The location and FOV of the instrument is marked in Figure 4.5 with a semi-transparent red triangle. Figure 4.6, instead, shows a picture taken from the location of the LISA instrument, where the FOV has been delimited by a red poly-line.

The area monitored consists of a slope with 30 to 50 degrees of inclination, ranging from 2300 m to 2700 m a.s.l. The bottom part corresponds to the Olen Valley (Val d'Olen), where a ski track passes through (V3 black track in Figure 4.5) putting at risk skiers when snow avalanches fall down.

The instrument covered an area of nearly 800 m by 800 m, ranging approximately 750 m to 1550 m to the radar. The picture on Figure 4.6 has been taken from the radar position so it represents approximately the field-of-view of the instrument. Note that the ski track itself cannot be seen from the radar position.

Fig. 4.6. Picture of the Alagna test site with the instrument FOV delimited in red.

Similarly to that for the field campaign in Switzerland, the transportation of the instrument to this test site was done by trailer up to the closest possible point to the final location. The rest of the distance was covered by helicopter: Figure 4.7 shows a picture of the deployment of the LISA instrument in the intermediate station of the cable car by a Lama helicopter.

The LISA instrument installed in this test site was smaller and lighter than that installed in the Sion Valley of Switzerland. Actually, the linear rail was only 2 m long, no air conditioning unit was present, and the UPS batteries were substantially smaller. The external dimensions of the LISA container deployed in this test site were 2.85×1.50×1.50 m, while the weight the helicopter had to lift was close to 800 kg.

Following the usual criteria of careful management of the electronic components of the radar, all the electronic instrumentation was removed from the container for the deployment of LISA. The electronics (VNA, PC, disks, video cameras, etc.) were brought

later on in the cabin of the cable car Funifor Cimalegna to the container and installed only after the LISA was firmly anchored in its final location.

Fig. 4.7. Instrument deployment in Alagna Valsesia (Cimalegna).

a) 

b) 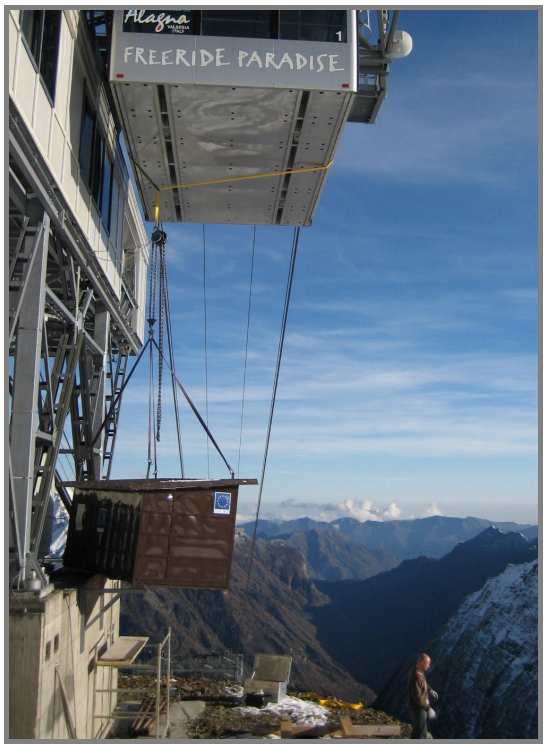

Fig. 4.8. Instrument location in Alagna during a) first winter; and b) second and third winters.

The location of the LISA instrument slightly changed from the first to the second and third winter campaigns. Figure 4.8 shows both locations, always next to the concrete basement of the intermediate stop of the cable car.

During the first winter campaign, 2005-2006, the instrument was deployed, partially elevated by wooden joists, on the ground next to the concrete basement. Figure 4.8-a shows the final location of the instrument during this winter.

Unfortunately, the snow accumulation in front of the instrument degraded the radar imagery because of the multiple reflections produced a few meters away from the radar antennas. So for the following winters it was decided to elevate the instrument in order to minimize the effect of such reflections. The picture in Figure 4.8-b corresponds to a moment of the installation of the instrument on top of the concrete basement. The cabin of the cable car was used to help elevate the instrument from its initial position.

For the winters 2006-2007 and 2007-2008, hence, the container of the LISA instrument was partially supported by the concrete base and by two steel squares specifically installed to hold the system. The final location of the instrument can be better appreciated from the picture of Figure 3.4-b.

4.3.2. Coordinates system

As stated in Section 4.2.2, the radar images generated by the LISA instrument are referenced to a local coordinate system with origin in the central point of the rail synthesizing the linear aperture. The geo-referencing of such images to a local map, thus, facilitates the interpretation of the results.

Figure 4.9 shows the FOV of the instrument once geo-referenced in a local map of the area. The location of the LISA instrument (in top of the map) and a dashed line pointing in the zero-cross-range direction have also been included.

Following the same reasoning as in Section 4.2.2, the FOV geo-referenced in Figure 4.9 is an approximation based on the rotation of the four points defining the rectangular FOV in the LISA coordinates system. Once these points are rotated to the Easting-Northing coordinates system and united by straight lines, the result is that of Figure 4.9.

Italian maps produced by the Italian Military Geographic Institute (Istituto Geografico Militare, IGM) are based on a coordinate system similar to the UTM presented in Section 4.2.2. Nevertheless, as happens with the Swiss datum, the Italian datum also differs by several meters to the worldwide standard WGS84. The Gauss-Boaga projection was proposed in 1940 by Giovanni Boaga when he was chief officer of the IGM. In addition, the Gauss-Boaga system also defines the reference datum Roma40. Some old maps issued by the IGM, thus, are referenced to that datum, while others are referenced to the European standard ED50. In fact, the map shown in Figure 4.9 is called Carta Tecnica Regionale (CTR), it is produced by the Piedmont region and originally referenced with the ED50 datum. ED50 (European Datum 1950) is a geodetic datum which was defined after World War II for the international connection of geodetic networks. It was based on the International Ellipsoid of 1924 and was widely used all over the world up to the 1980s, when GRS80 and WGS84 were established.

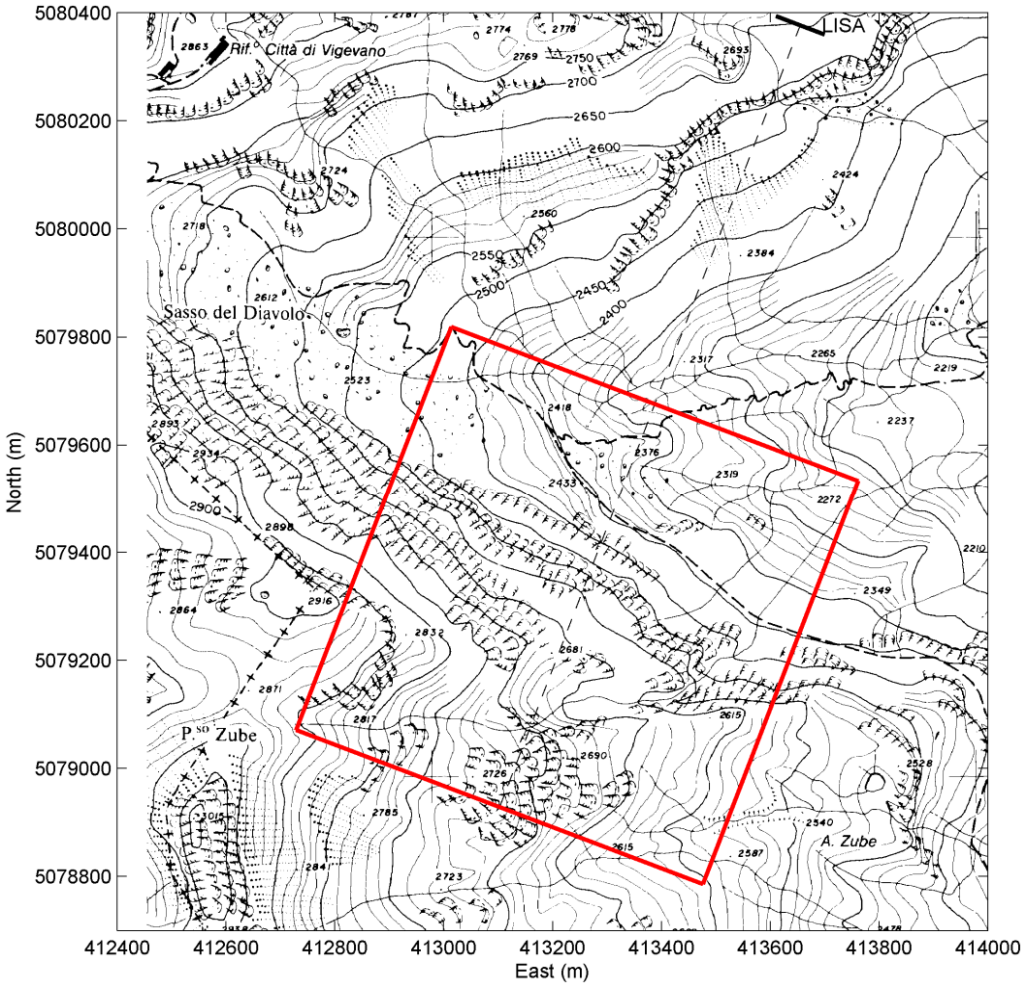

Fig. 4.9. Field-of-view over the map in UTM coordinates, Alagna Valsesia.

Nevertheless, to simplify the overlapping of *ground-truth* GPS points and tracks to the CTR map, the coordinates in Figure 4.9 have already been converted to UTM WGS84.

4.3.3. Sensor parameters

The sensor parameters used to monitor this test site suffered some modifications after the first winter campaign. Table 4.1 shows the main parameters used during the first winter (2005-2006) and the next two winters (2006-2007 and 2007-2008).

According to the radar band designations listed in Annex B.3, the frequency used during the first winter was X-band, while during the rest of campaign the Ku-band was employed. Regarding the polarization used, VV, see the last paragraph of Section 3.1.1 for more details on the selection of this parameter.

In the rest of this section we will focus only on the parameters of the second and third winters (column 2006-2008 of Table 4.3) because the imagery obtained in that case was of higher quality as already explained in Section 4.3.1.

Table 4.3. Measurement parameters in Alagna Valsesia

	2005-2006	**2006-2008**
Polarization	VV	VV
Central frequency (GHz)	8.86	13.27
Bandwidth (MHz)	120	250
Bandwidth steps	1601	3201
Aperture length (m)	1.9	1.9
Aperture steps	231	301
Measurement time (min)	9.9	12.6
Vertical baseline (cm)	80.5	80.5
Horizontal baseline (cm)	0.0	0.0
Azimuth coverage (m)	-400…400	-400…400
Distance to slope (m)	750...1550	750...1550
Image size (pixels)	641×641	641×641

The theoretical resolutions in range and cross-range according to (2.2) and (2.4) are $\Delta R = 0.6$ m and $\Delta X_{SAR} = 4.4 \ldots 9.2$ m respectively. According to (2.8), the unambiguous range is $R_U < 1920$ m and, finally, the alias-free angular extension is 127.2 deg according to (2.10), where $\theta_{\max} = 1.11$ rad = 63.6 deg. Considering the geometry of the area monitored and the before mentioned parameters, no aliased responses are expected on the radar imagery in this test site either.

4.3.4. Data availability

The complete list with the days and time intervals where data was acquired on this test site can be consulted in Annex D.3. The following are some numbers referring to this data archive, while more information can also be found in [40].

The campaign started on 2006/03/26 and finished on 2008/03/31, with 303 days of data acquisition divided in three winter seasons. Table 4.4 shows the approximated amount of radar images acquired in this test site divided by winter seasons.

Table 4.4. Data acquired in Alagna Valsesia with the LISA instrument

	2005-2006	**2006-2007**	**2007-2008**
Radar images, Rx1	10498	16651	12021
Radar images, Rx2	10498	16648	12245
Visual images, outside	4475	16430	11303
Visual images, inside	4752	23911	16940

Regarding the SAR images, the instrument operated all the time with two antennas in reception (Rx1 and Rx2) vertically separated 80 cm to allow the generation of single-pass interferograms for topographic purposes. The radar data raw acquired in this test site occupies 441 GB of disk space.

The image acquisition rate suffered of little modifications in this test site. During the first winter (2005-2006) raw data was acquired at a rate of 2 images (1 image per reception channel) every 9.9 minutes approximately. During the following winters (2005-2006 and 2006-2007) the raw data acquisition rate was of 2 images (1 image per reception channel) every 12.6 minutes.

Before any other processing technique is applied, focused images need to be created for every data raw available at the end of every sweep of the linear aperture. This represents another set of data with the same number of images than the data raw archive, but occupying 240 GB.

Concerning the visual imagery, pictures are available both of the interior and the exterior of the LISA instrument for the three winters of field campaign (see Table 4.4). Pictures of the inside of the container were acquired at a rate of 1 image every 10 minutes, and the complete archive, in JPEG format, occupies 1.3 GB. On the other hand, pictures of the outside of the container (radar field-of-view) were acquired at a rate of 1 image every 15 minutes, and the complete archive, always in JPEG format, occupies 1.2 GB.

The only instrument available in this site for automatic ground-truth data collection was a meteorological station approximately 1 km away from the monitored slope, at the Istituto Mosso, situated at 2900 m a.s.l. This meteorological station is situated at Passo dei Salati and is managed by the Comando Truppe Alpine – Servizio Meteomont. The available data spans from 2006/03/01 to 2007/04/30, with an acquisition rate of one datum every 3 hours. Note that data interruptions are present in the before mentioned archive of *ground-truth* data because of problems with the instruments.

Two topographic products were also available for the monitored area:

a) A digitized map issued by the Istituto Geografico Militare: Carta d'Italia alla scala di 1:25000, foglio n. 29, Alagna Valsesia. Roma40 datum.

b) A digitized map issued by the Piedmont region: Carta Tecnica Regionale (CTR), 1:10000, tavola 071110, Alagna Valsesia. ED50 datum.

Finally, the GPS tracks of two avalanches (one artificial and one natural) falling in the FOV of the LISA instrument are available for the last winter of field campaign. These tracks, together with the GPS points necessary for the geo-referencing of the radar images (see Annex E), where kindly collected by Andrea Pierrettori of the Univerisy of Turin.

5. Snow height retrieval

5.1. Introduction

This chapter studies the feasibility of retrieving changes in the depth of snow cover by means of SAR differential interferometry (DInSAR) of consecutive images, that is, using a temporal baseline instead of spatial baseline. This is the first of the three monitoring techniques of the snow cover presented in this PhD thesis.

Retrieval of snow cover depth at local scale in areas where traditional meteorological stations cannot be placed is useful to determine the volume of snow present on a slope and thus to better evaluate the risk of avalanche. In addition, snow cover models for avalanche forecasting as the Swiss SNOWPACK [41] use as an input parameter the snow cover depth retrieved from an automatic meteorological station. By feeding these models with more localized data of the slope concerned, more accurate forecasts could be produced.

One of the main advantages of GB-SAR is its capability of providing images at a much higher acquisition rate than satellite- or air-borne sensors. This characteristic results in very large time-series of repeat-pass radar images and so allows assessing the feasibility of retrieving the local snow cover height evolution over time. Unfortunately, the technique is not mature enough to provide absolute snow heights at the moment, but the results obtained so far evidence the high potential to continuously map snow cover fluctuations [18].

The availability of a meteorological station close to the monitored slope with automatic snow height logging gives the possibility of validating the snow height retrieval scheme and is fundamental for the calibration of the absolute height, as will be shown in Section 5.3.6. Since the meteorological stations measure the snow height over a plane surface, in order to validate the results it is necessary to concentrate on an area of the monitored FOV with an extension and inclination which allow the deposition of snow in a similar way to that which would be on a plane surface.

The selection of the area to monitor for the snow height retrieval plays, thus, a fundamental role on the success of this technique. Unfortunately the test site of Alagna is not adequate for applying this technique mainly because the areas with a suitable slope for the proper accumulation of snow are frequently transited by skiers. The rest of areas are rock formations with more than 50 deg of inclination with respect to the normal where snow drifts naturally down. In addition, the North-oriented slope in Alagna suffers of strong wind conditions that frequently cause snow drift and hence temporal decorrelation

on the repeat-pass interferograms necessary for retrieving the snow height. This technique is, thus, applied only to the data acquired on the Sion test site of Switzerland.

5.2. Single layer, dry snow model

5.2.1. Review of the state of the art

Remote sensing has been used successfully for snow monitoring. Passive microwave sensors have a long history in snow monitoring. Several investigations have demonstrated the capability of multi-frequency microwave radiometer systems to locally map snow extent, snow depth, and snow water equivalent [2][3]. Experiments with satellite-borne synthetic aperture radars have demonstrated the capability of SAR to distinguish wet snow from bare ground and estimate snow liquid water content [7].

For water resources planning and management the snow water equivalent (SWE) is the most important variable. It is defined as the amount of water contained within the snowpack and can be thought of as the depth of water that would theoretically result after melting the entire snowpack. Snow water equivalent can be presented in units of [kg/m^2] or metres of depth of liquid water that would result from melting the snow. SWE is the product of depth and density, so both values are directly related as follows:

- SWE (units [kg/m^2]) = depth [m] × snow density [kg/m^3]
- SWE (units [m]) = depth [m] × snow density [kg/m^3] / density of water [kg/m^3]

The problem of retrieving the snow cover depth, thus, is directly related to the SWE mapping. Because of the high spatial variability of SWE, in-situ point measurements are not a suitable basis for SWE mapping. Presently no remote sensing method exists which enables reliable observation and mapping of SWE in complex terrain: retrieving SWE from SAR backscattering data, for example, suffers from the insensitivity of long wavelengths (L- and C-band) to dry winter snow, whereas at short wavelength the snow metamorphic state becomes important. On the other hand, the interferometric phase shift in snow due to differences in the propagation constant relative to the atmosphere offers a direct method for retrieving SWE and consequently for snow height retrieval, as first proposed in [42]. A more recent study [43] has demonstrated the feasibility of combining backscattering and InSAR correlation observations for retrieving snow accumulation parameters by means of a model that considers both volume scatter and surface scatter from hoar layers at depth. Nevertheless, the before mentioned model works under very restrictive conditions and a-priori knowledge of some ground-truth parameters, so the use of the interferometric phase remains the more promising technique to infer snow cover depths with SAR imagery.

Concerning the modelling of the snow cover, two main trends have been explored. A multi-layer model, including volume scatter and the incoherent addition of echoes from hoar layer interfaces in which the scattering from a single layer is found by small-perturbation methods was used in [43]. This approach entails precise knowledge of the different snow pack stratums and is particularly suited to estimating the backscattering properties of a given snow pack. On the other hand, the reduction of the snow cover into a single layer has proved to be effective both under dry and wet snow conditions for the retrieval of snow covered areas [44] and the creation of SWE maps [42]. A single layer

model is again used in [45] to infer the SWE, snow depth and particle size with a complex scattering model that takes into account the scattering of the dry snow layer at particle level and its interactions with the air and ground boundaries.

Backscattering measurements have been the only input to most of the before mentioned studies mainly because of lack of sufficient and adequate images to produce interferograms. GB-SAR overcomes this limitation because of its high image acquisition rate, where repeat-pass interferometry can be applied several tens of times a day to accurately generate snow cover height evolution plots.

5.2.2. Phase-to-height conversion

The propagation of radar waves in snow is governed by the complex permittivity of snow which is strongly dependent on its liquid water content. The penetration depth d_p of microwaves at the wavelength in free space λ_0 can be estimated from the real ε' and imaginary ε'' parts of the complex permittivity of snow according to [46]:

$$d_p = \frac{\lambda_0 \sqrt{\varepsilon'}}{2\pi\varepsilon''}. \tag{5.1}$$

The imaginary part of the permittivity, ε'', of dry snow at C- and L-band is of the order of 0.001 to 0.0001, whereas the real part, ε', depends only on the snow density ρ_s [46], where ρ_s is specified in g/cm^3:

$$\varepsilon' = 1 + 1.60\rho_s + 1.86\rho_s^3. \tag{5.2}$$

The result is a typical penetration depth of dry winter snow of $d_p \approx 20$ m at C-band [47]. The dielectric losses of wet snow, on the other hand, are large and the typical penetration depth of wet snow with liquid water of several per cent by volume is of the order of few centimetres only.

The DInSAR snow depth retrieval algorithm presented in this chapter exploits the large penetration depth in dry snow, taking into account that the main contribution of backscattering from ground covered by dry winter snow stems from the ground surface. It is assumed that the dielectric properties are constant all over the snow cover (single layer model). In the case in which this is not true, an equivalent single dielectric constant should be computed considering the geometry and properties of the different layers. This is outside the scope of this work since the calibration procedure for the interferometric phase-to-snow depth conversion presented below directly assumes a single snow layer (see Figure 5.1) with a single dielectric constant for all the period in which the calibration parameters are valid (typically one day).

Repeat-pass differential interferometry is based on the phase comparison of a pair of complex coherent radar images of the same scene taken in different instants of time. Let d_s be the depth of the whole snow cover at some instant as shown in Figure 5.1-a. After some minutes, during which the snow depth may have changed, the radar sends another pulse. Let the new snow cover depth be d_s' as shown in Figure 5.1-b. The two-way propagation path difference, $2\Delta r = 2\Delta r_s - 2(\Delta r_s' + \Delta r_a)$, in the form of a phase shift, $\Delta\varphi_s$, is actually the information measured by the radar with resolution of millimetres in C-band ($\lambda_0 \approx 5$ cm).

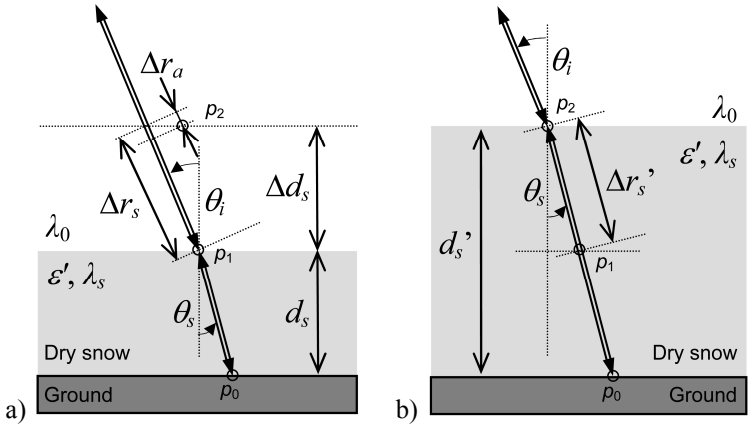

Fig. 5.1. Propagation path of microwaves with a snow layer of depth a) d_s; and b) d_s'.

The propagation path difference Δr can be expressed from the geometry in Figure 5.1 as a function of the change in the snow cover depth $\Delta d_s = d_s' - d_s$ and the incidence and refraction angles θ_i and θ_s:

$$\Delta r = \Delta r_s - (\Delta r_s' + \Delta r_a) = \Delta d_s \frac{\cos(\theta_i - \theta_s) - 1}{\cos\theta_s}. \tag{5.3}$$

Taking into consideration the different propagation constants ($\lambda_s = \lambda_0 / \sqrt{\varepsilon'}$) and the relationship between θ_i and θ_s according to the Snell's law, the interferometric phase shift in dry snow related to Δd_s can be written as [42]:

$$\Delta\varphi_s = -\frac{4\pi}{\lambda_0}\Delta d_s \frac{\cos(\theta_i - \theta_s) - \sqrt{\varepsilon'}}{\cos\theta_s} = -\frac{4\pi}{\lambda_0}\Delta d_s \left(\cos\theta_i - \sqrt{\varepsilon' - (\sin\theta_i)^2}\right). \tag{5.4}$$

Thus, the phase shift $\Delta\varphi_s$ and the differential snow depth Δd_s can be related by a very simple linear relationship depending only on three variables: λ_0, θ_i and ε'. When the area under study is small enough, the incidence angle and the snow permittivity can be considered constant, allowing the reduction of the above-mentioned three variables to a single constant α [m/rad]:

$$\alpha = -\frac{\lambda_0}{4\pi}\left(\frac{1}{\cos\theta_i - \sqrt{\varepsilon' - (\sin\theta_i)^2}}\right). \tag{5.5}$$

The differential snow depth, thus, can be simply expressed as:

$$\Delta d_s = \alpha \cdot \Delta\varphi_s. \tag{5.6}$$

Because the phase shift values come from differential measurements, an offset constant β [m] needs to be added to the previous equation in order to calibrate the results to absolute snow heights. The resulting snow depth is:

$$d_s = \alpha \cdot \Delta\varphi_s + \beta. \tag{5.7}$$

The constant and offset parameters α and β, also named calibration parameters, are directly retrieved from a single ground-truth control point and are treated in more detail in Section 5.3.6.

Provided that continuous image acquisitions are available for a given test site, a single offset constant β would be required to calibrate the absolute snow height, d_s, during the first interferometric pair formation. For the rest of interferograms, the differential snow depth Δd_s as expressed in (5.6) would be simply added to the preceding values of snow depth. The parameter α, instead, depends of the central radar wavelength and the incidence angle, that can be assumed constant over the field campaign. But it also depends of the snow permittivity, which may change over time depending on the snow density as shown in (5.2). A ground-truth control point is, hence, necessary every time the snow density varies to accurately obtain the parameter α and consequently the snow cover depth.

5.2.3. Permittivity and density retrieval

Another interesting application is that of the permittivity and snow density retrieval from the snow depth measurements, always based on the single layer, dry snow model presented in the preceding sections.

As stated in (5.7), the absolute snow depth retrieval can be done through the interferometric phase and a single ground-truth calibration point. This calibration technique, and in particular the parameter α as defined in (5.5), comprises all the geometric algebra involved in the scene analyzed and depicted in Figures 5.1 and 5.2.

If the parameter α, instead, is retrieved by fitting a time-series of interferograms as described in (5.7) to the snow depth evolution available from the data logger of an automatic meteorological station, the snow permittivity and density can be retrieved through (5.5) and (5.2) respectively.

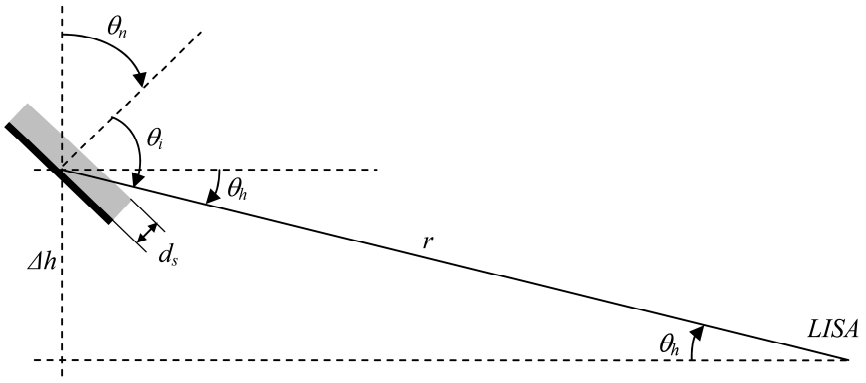

Fig. 5.2. Geometry of the acquisition scenario for the permittivity and density retrieval.

From the field campaign carried out in the Sion Valley in Switzerland, the differential height between the LISA instrument and the monitored test point, Δh, the slant-range to the test point, r, and the normal to the surface where the snow depth is retrieved,

θ_n, as described in Figure 5.2 are know. From these parameters, the incidence angle θ_i can be directly expressed as:

$$\theta_i = \theta_h + \pi/2 - \theta_n, \tag{5.8}$$

$$\theta_h = \text{asin}\left(\Delta h / r\right). \tag{5.9}$$

The snow permittivity is finally obtained by inverting (5.5):

$$\varepsilon' = (\sin\theta_i)^2 + \left(\cos\theta_i + \frac{\lambda_0}{4\pi\alpha}\right)^2. \tag{5.10}$$

The snow density inversion ρ_s, instead, requires solving the third order equation (5.2). However, the typical dry snow densities (~0.1 g/cm^3, [52]) allow (5.2) to be approximated by the linear term only.

5.3. Processing methodology

This section covers the issues related to the practical implementation of the snow depth retrieval algorithm presented in the previous section. The full processing chain is analyzed in detail, starting from the raw data acquired by the LISA instrument up until the generation of snow height evolution plots.

The DInSAR technique proposed for the snow depth retrieval is based on the repeat-pass mode of the LISA instrument, in which a single reception channel is necessary. Being a ground-based system, the re-visiting time of the instrument is identical to the image acquisition rate. According to Table 4.1 the acquisition rate for the instrument deployed in the Sion Valley was of 11.7 minutes approximately per image.

The input data for the proposed technique is, thus, a time-sequence of single-channel SAR images acquired from the same identical location with the same instrument parameters pointing to the same field-of-view at a rate of 1 image every 12 minutes approximately. Table 4.1 summarizes the rest of sensor parameters used.

5.3.1. Atmospheric effects

Interferometric techniques are based on phase instead of intensity measurements as stated in Section 2.4. The single-channel repeat-pass mode of the instrument implies a temporal baseline (in contrast with the spatial baseline required for topographic measurements) that introduces a decorrelation between images because of changes in the snow cover, but also because of different atmospheric conditions between acquisitions.

The first source of decorrelation, the changes in the snow cover, is actually the phenomenon to measure for retrieving the snow depth. The second source instead, different atmospheric conditions between acquisitions, overlaps to the first one masking it out with the so-called atmospheric phase screen (APS).

The problem of atmospheric changes between image acquisitions and even during the aperture synthesis is manifested as a change on the refractive index of the propagation

medium (the air) that causes a tiny (~10 ppm) change on the propagation velocity of microwaves.

Several techniques derived from satellite- and air-borne interferometry have been proposed for the correction of the atmospheric effects in ground-based SARs: [48] and [49]. Most of them are based on a model of the atmosphere in which the refractive index needs to be estimated as a function of air pressure, temperature and relative air humidity. Alternatively, the refractive index can be inferred with the use of fully static permanent scatterers if available on the area monitored [50]. Once the refractive index is estimated, the atmospheric effects can be compensated. Nevertheless, the results of the compensation depend on how well the refractive index is estimated (particularly in terms of its temporal variability) and how accurate is the atmosphere model used. This is a very complex task as the atmosphere is generally highly variant in space and time.

Under the hypothesis of a time-dependent homogeneous atmosphere (the refractive index displays slow variations over time and can be considered constant during the aperture synthesis itself), two echoes from the same motionless point scatterer at nominal distance r_n acquired with different refractive indexes n_1 and n_2 of the atmosphere result in the following interferometric phase [51]:

$$\Delta\varphi = \frac{4\pi}{\lambda_0} r_n (n_2 - n_1). \tag{5.11}$$

It can be observed that the interferometric phase associated with the same point scatterer is not null but follows a linear relationship with range. Assuming that the atmospheric medium is homogeneous and isotropic, targets at the same range distance are equally affected by the atmospheric changes so a single range cut is sufficient for the estimation of the phase ramp in (5.11) and, thus, for its compensation.

The estimation of the above mentioned phase ramp requires the knowledge of stable points on the radar FOV in order to use them as a reference to quantify the change on the refractive indexes. Stable points can be found on time-series of SAR images either by use of the permanent scatterers techniques [50], identification of highly-coherent scatterers [51] or detection of pixels with low standard deviation on their backscattered intensity over time.

Both the atmospheric model that requires precise knowledge over time of temperature, pressure and relative air humidity conditions on the monitored area, and the phase flattening technique, that assumes slow changes on the atmospheric conditions and requires stable points on the FOV to be effectively applied are not suitable for the slope monitored in the Sion test site of Switzerland. The radar FOV is fully covered by snow in winter time as can be appreciated in Figure 4.1, so no stable points can be found on the SAR time-series of images required for the retrieval of the snow cover depth. Naturally, in late-spring, summer and early autumn time the slope is almost completely free of snow. In these periods the phase flattening technique for atmospheric correction could be applied, taking as reference different rock formations that remain visible. This correction, however, cannot be extended to the whole winter season.

On the other hand, atmospheric data is only available for a point 2 km far away from the slope and accessed off-line only a few days after it has been retrieved, so its information cannot be included on the near real time processing chain of the LISA instrument.

5.3.2. Co-registration

The technique proposed in this PhD thesis for the reduction of the decorrelation caused by atmospheric effects, instead, is based on the direct correction of the effects caused by different propagation velocities in the raw data acquired. Thus, no atmospheric model, no external atmospheric information and no stable points in the slope are required.

Let us assume a scenario like that of Figure 5.3-a in which a point p is scanned by a linear aperture that moves the antenna set from left to right. If no changes in the atmosphere occur during the time interval necessary to complete the whole aperture sweep, at the end of the acquisition the refractive index will be the same as that at the beginning, this is n_1. The propagation paths Δr_1 and Δr_2 will be properly estimated, and the resulting image will not suffer any distortion because of atmospheric effects.

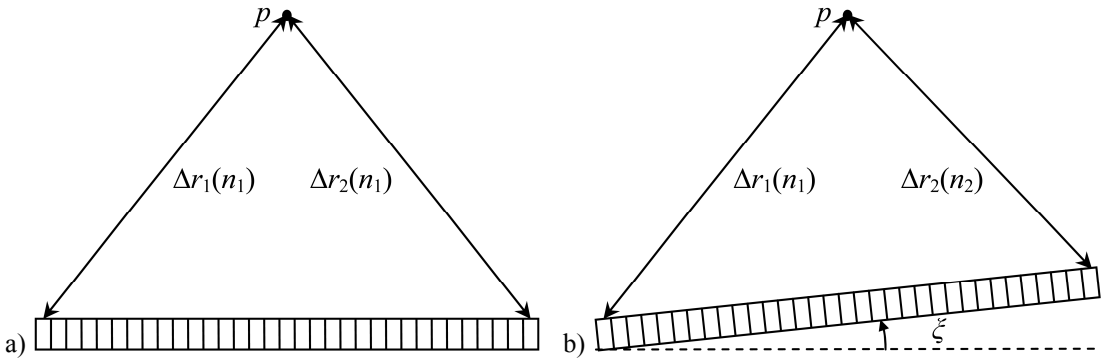

Fig. 5.3. Propagation path of microwaves with a) refractive index n_1 at the beginning and end of the aperture; b) refractive index n_1 at the beginning and n_2 at the end of the aperture.

With the same scenario let us assume now that a change in the atmospheric conditions results on a change of the refractive index at the end of the measurement. In this case, at the beginning of the measurement, the refractive index will be n_1 while at the end of the measurement the refractive index will be n_2. Since the image formation assumes a constant refractive index all over the scanned positions of the linear aperture (let us suppose this index is n_1), the distance Δr_1 will be properly estimated while the distance Δr_2 will be underestimated if $n_2 < n_1$ or overestimated if $n_2 > n_1$. The resulting SAR image will provide a missed position for the point p: this point will appear closer to the sensor than it actually is. Equivalently, the SAR image will appear to have been formed by a linear aperture rotated by an angle ξ (Figure 5.3-b) with respect to the previous acquisitions in which the refractive index was n_1 (Figure 5.3-a).

In addition, the phase associated with the point p will be different between the first and the second images (Figures 5.3-a and 5.3-b respectively). This will imply a temporal decorrelation in the pixel corresponding to the point p when forming the interferogram between both images, even if no changes occurred to the physical properties of p.

The line of reasoning above can be extended to subsequent acquisitions when the atmospheric conditions change progressively with time. As a consequence, the SAR images will present a rotation ξ with respect to the aperture direction modulated by the changes in the refractive index as shown in Figure 5.4.

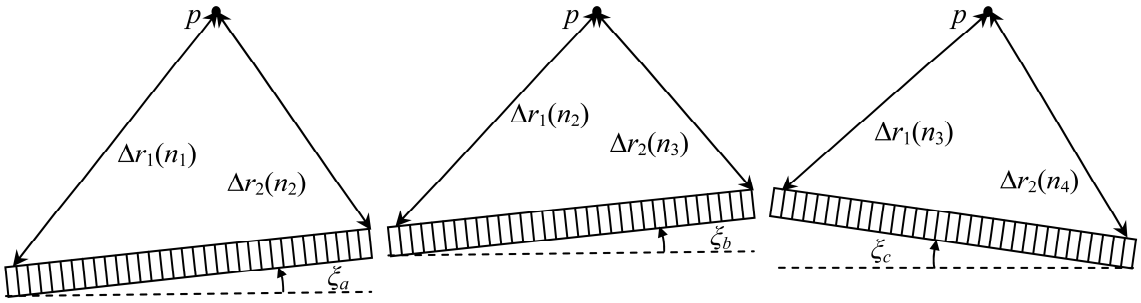

Fig. 5.4. Propagation path of microwaves with different refractive indexes during a series of 3 synthetic aperture radar acquisitions.

The compensation process is done by comparing all the raw data SAR images in a set (G_1, G_2, G_3, … $G_{\#}$,) with a reference one (G_0) and adjusting these images to maximize their cross-correlation in azimuth with the reference one. Since snow depth plots are typically computed on a daily basis, the image selected as a reference will be that first acquired each day. Nevertheless, the only relevant criterion is having a reference image with good signal to noise ratio, so any other image could be selected for this purpose.

Since the rotation angles ξ are expected to be very small, the raw data in the radar aperture dimension is zero padded in order to increase the sampling rate in the transformed domain and, thus, achieve sub-pixel co-register displacement resolution. Considering that the raw data is ordered in a matrix of N_f rows by N_x columns where N_x stands for number of acquisitions in the linear aperture and N_f number of frequency points on the frequency band swept, two matrices ZP of N_f×1024 (rows×columns) of zeros are padded right before and after the raw data matrices:

$$G_{\#zp}(f, x_a) = [ZP \quad G_{\#}(f, x_a) \quad ZP]. \tag{5.12}$$

Then, the image is transformed from the frequency-radar aperture domain (f, x_a) to the time-azimuth domain (t, x_φ) by means of a two-dimensional inverse Fast Fourier Transform (iFFT2[.]):

$$G_{\#zp}(t, x_\varphi) = \text{iFFT2}\left[G_{\#zp}(f, x_a) \cdot W_{4BH}(f) \cdot W_{Ham}(x_a) \right]. \tag{5.13}$$

Note that prior to the Fourier transform a Hamming window $W_{Ham}(x_a)$ is applied to the radar aperture dimension of the raw data matrix. A 4-term Blackman-Harris window $W_{4BH}(f)$ (92 dB sidelobes rejection ratio), instead, is used in the frequency dimension to lower the sidelobes associated with the Tx/Rx coupling and increase the dynamic of the image. In the Fourier transformed domain the shift displacement between images is computed as a weighted sum among the time dimension of the correlation indexes. To this aim, the cross-correlation between the reference and the target image is computed:

$$xcr_{\#}(t) = G_{0zp}(t, x_\varphi) \otimes G_{\#zp}(t, x_\varphi), \tag{5.14}$$

where ⊗ stands for the cross-correlation operator. Noting that the function $\max_v(.)$ stands for the maximum value of the elements operated and $\max_i(.)$ stands for the index where the

maximum value is located, the weighted shift displacement between images in terms of the azimuth indexes (bins) in the zero-padded intensity image $G_{\#zp}(f,x_a)$ can be expressed as:

$$d_{\#shift} = \frac{\sum_t \left[\max_i \left(xcr_{\#}(t) \right) \cdot \max_v \left(xcr_{\#}(t) \right) \right]}{\sum_t \max_v \left(xcr_{\#}(t) \right)} - N_{xzp}. \tag{5.15}$$

where N_{xzp} is the number of columns (azimuth dimension) of the resulting zero-padded image as expressed in (5.12). Higher weight is given to pixels with higher backscattered power by means of the value of the cross-correlation. Note that the shift displacement as defined in (5.15) can take either negative or positive integer values depending on whether the image analyzed $G_{\#}$ is delayed or anticipated with respect to the reference image G_0.

The atmospheric effects in the Fourier transformed domain $G_{\#}(t,x_{\varphi})$ are manifested as the convolution of the image in polar coordinates with a delta function ($d_{\#shift}$) in the azimuth dimension. In the original domain (data raw, $G_{\#}(f,x_a)$) the shift displacement is translated into a phase rotation so, applying the inverse rotation to the raw images with a complex exponential factor, the temporal decorrelation is finally compensated:

$$G_{\#}(f,x_a) = G_{\#}(f,x_a) \cdot \exp\left(-j2\pi x_a \frac{d_{\#shift}}{N_{xzp} \cdot \Delta x_a} \right), \tag{5.16}$$

where Δx_a is the native spacing between samples along the antenna trajectory (radar aperture dimension without zero padding).

5.3.3. Differential interferometry

Once the raw data is co-registered according to the procedure explained in the preceding section, the images can be formed by means of a focusing algorithm, such as that presented in Section 2.3.3. The next step is the computation of the phase difference between consecutive focused images.

The interferogram between two images is defined as the angle of the complex coherence as presented in (2.21), where the averaging operator has been implemented as a two-dimensional convolution with a 3×3 square matrix with all coefficients to one.

The snow depth retrieval technique requires the use of differential interferograms, that is, the angle difference of consecutive interferograms. Hence, interferograms and differential interferograms are continuously computed over all the time-series of SAR images acquired by the instrument.

When computing the interferograms the issue of the proper selection of the master image arises. The time-series of differential interferograms for the snow depth retrieval can be generated with several strategies for the selection of the master image, all of them providing the same snow depth differential values as defined in (5.6). The master image for the interferogram can be refreshed at each interferogram, or it can be re-used for an arbitrary number of interferograms provided that the coherence magnitude is kept high. At the acquisition rate of the LISA instrument in Switzerland, one image every 12 minutes, it

has been observed that the coherence is kept above 0.7 when computing interferograms with images separated by up to 2 hours even under light snow fall conditions.

Nevertheless, the continuous generation of interferograms at the image generation rate of the instrument, that is, refreshing the master image at each interferogram, significantly minimizes the temporal decorrelation caused by atmospheric effects. Hence, temporal decorrelation is limited to a time window of 24 minutes, equivalent to the time required for the acquisition of the two images necessary to form the interferogram.

In addition, since the central wavelength used in the Swiss monitoring campaign is 5 cm approximately, phase wrapping may easily occur if computing interferograms and differential interferograms separated by a long time window in which heavy snow fall accumulates more than 5 cm. Thus, the shorter the time window in the interferograms computation, the better.

5.3.4. Phase averaging

The interferometric phase under typical weather conditions in Alpine areas (turbulence, high temperature gradients, raining, snow falling, etc.) is highly variant in space and time.

Although the snow depth could be retrieved for the whole radar FOV, it was decided to concentrate on point locations where the snow accumulation would be more similar to that measured by the automatic meteorological station. The concentration on point locations is based on the selection of a square area of 20×20 pixels of the focused radar images. According to Table 4.1 the before mentioned area is of 73×73 m approximately, while in terms of radar resolution cells it is 30×5 cells in range and cross-range as defined in (2.2) and (2.4) respectively.

The concentration on those relatively small areas where the snow depth is supposed to be approximately the same all over the area allows the interferometric phase averaging over all the pixels in the image appertaining to the before mentioned areas. Hence, a single interferometric phase is obtained for each of the test locations studied of 20×20 pixels. Nevertheless, the procedure described in this chapter can be extended to the whole image just by sliding the 20×20 pixels window all over the FOV of the instrument and obtaining an averaged interferometric phase for every pixel of the complete image.

A second criterion used for SNR optimization of the interferometric phase necessary to retrieve the snow cover depth is also related with the use of an area of 20×20 pixels. Only those pixels presenting a coherence magnitude over a given threshold are used in the interferometric phase averaging described in the preceding paragraph. For the results presented in the Section 5.4 of this chapter, a value of 0.7 was used as a coherence threshold although it has been observed that typical coherence values are 0.9 and even higher due to the high acquisition rate of the instrument and the phase stability of the VNA used for implementing the microwave section of the sensor.

The motivation for the selection of small areas where to apply the snow cover depth retrieval technique is, thus, to increase the SNR of the interferometric phase related to the snow height by (5.7). A representative number of pixels are necessary in order to properly apply the averaging and coherence selection techniques described below. The selection of the window size is determined by the image resolution both in terms of range and cross-range cells and the physical size. On the one hand, independently of the focused image

resolution, a representative number of resolution cells are necessary in the selected window in order to effectively reduce the artifacts and increase the SNR by averaging. On the other hand, the physical dimensions of the window need to be small enough to guarantee that the snow cover depth is approximately homogeneous all over the selected area.

A Digital Elevation Model of the monitored area is instrumental for successfully applying this technique, since the selected spatial windows for phase averaging also need to have a homogeneous slope in order to avoid phase modulations because of the terrain underlying the snow cover.

Since the snow height retrieval technique uses repeat-pass interferograms consecutively acquired over the same position (zero spatial baseline), no phase wrapping is expected on the interferograms. Thus, no two-dimensional phase unwrapping is required on the processing chain. This fact speeds up the snow height retrieval part of the processor, since the 2-D phase unwrapping is one of the most time consuming steps on the interferogram computation.

5.3.5. Phase unwrapping

Once the differential interferometric phase is obtained for the selected test point in the different instants of time $\Delta\varphi_s(t)$ as described in the preceding sections, the time series of interferometric phases $\Delta\varphi_s^{cum}(t)$ is composed by accumulating the preceding values of differential interferometric phase at each given instant of time t_n:

$$\Delta\varphi_s^{cum}(t_n) = \sum_{t=1}^{t_n} \Delta\varphi_s(t). \tag{5.17}$$

Figure 5.5 shows a graphical example in which both the time and the processing sequence are represented up to the instant t_4. The first column represents the instants of time corresponding to each SAR image acquisition (second column). The third column states each individual interferogram, which is formed with the current and preceding images. And finally the fourth column contains the time sequence of cumulative differential interferograms for each instant of time t_n that is used in (5.7) for the snow depth retrieval algorithm.

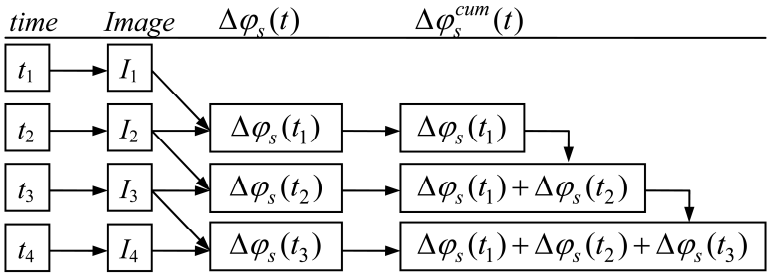

Fig. 5.5. Time sequence of SAR image acquisitions, differential interferograms and final time-series of cumulative differential interferograms.

As stated in Section 5.3.4, wrapping of the differential interferograms may occur because of the short wavelength used in this study, 5 cm, compared to the snow height

variations that may occur in short instants of time. This is particularly true when refreshing the master image for the interferogram computation at any rate different than the maximum the instrument can provide. In this case, a 1-D phase unwrapping step of the time series of differential interferograms $\Delta\varphi_s^{cum}(t)$ is necessary prior to the retrieval of the snow cover depth evolution over time.

If exploiting the maximum acquisition rate of the instrument for reducing the time window of the interferograms (as in the example of Figure 5.5), the before mentioned 1-D phase unwrapping step is unnecessary since any phase wrapping may only be embedded in the phase variations caused during the acquisition of both consecutive images. In this later case no unwrapping technique will be able of deliver the proper phase information and only the use of larger wavelengths will help.

Finally, the time series of differential interferograms $\Delta\varphi_s^{cum}(t)$ is smoothed by means of a 3-elements averaging filter. The filter is simply applied by cross-correlating the time series of differential interferograms with the array [1 1 1] and correcting the scale and dimension of the final vector to match those of the original one.

5.3.6. Calibration parameters

According to the dry snow model presented in Section 5.2 it would be possible to obtain both calibration parameters α and β with a single control point of ground-truth snow depth provided that the equivalent permittivity of the simplified single layer snow cover is known. This permittivity, though, is very difficult to infer because the snow cover is typically formed by different layers with different levels of wetness in each of them caused by the different cycles of snow melting, water percolation and re-freezing [10].

Considering the above mentioned limitation, the strategy adopted for the snow depth retrieval has been to obtain the calibration parameters α and β by fitting the time series of cumulative differential interferograms to the snow cover depth provided by the automatic meteorological station, usually in periods of one to a few days. This approach has a double purpose: to assess the potential of retrieving snow cover depth changes by means of DInSAR; and to infer from the parameter α the dry snow equivalent permittivity assuming a single layer snow cover model.

From the typical dry snow dielectric constants and densities reported in [52] at C-band, the expected range of the real part of the dielectric constant for the dry snow in the Sion test site is between 1.001 and 2.000. According with the geometry in Figure 5.2 and the sensor parameters reported in Table 4.1, the incidence angle θ_i is expected to fall in the range from 70 to 80 deg for almost all points in the radar FOV. With the before mentioned parameters and using (5.5) the parameter α is found to be in the range 0.1 to 300 cm/rad.

The parameter α is, hence, iteratively found by looking for the best fit of the model described by (5.7) to the ground-truth snow cover depth all along a number of radar images that span from one to several days. Consequently, the parameter α is unique for every time-series of radar images and can be extended to longer periods provided that the dry snow model is still valid under the new weather conditions in the extended periods. The parameter β, instead, is directly forced to the absolute value of snow height at the beginning of the time series analyzed.

Once the parameter α is properly determined, results of the real part of the dry snow permittivity can be obtained by using (5.10). The validity of the methodology employed for the snow depth retrieval can be assessed by comparing the permittivity values obtained with those reported in [52]. Similarly, the snow density can be inferred and qualitatively assessed from the permittivity by using (5.2).

5.4. Results

5.4.1. Location of test points

As introduced in Section 5.3.4, the technique of snow height retrieval has been tested under single point locations without regard to the possibility of extending this technique to the whole number of pixels of the radar image. Two different locations have been chosen in order to have a representative number of results, one of them at moderate altitude level and with moderated inclination, and a second one at high altitude and with a significant tilt angle. Table 5.1 summarises the characteristics of the test points and the meteorological station from which the ground-truth data is used.

Table 5.1. Tests points for snow height retrieval and meteo station geographical characteristics

	Test point 1	**Test point 2**	**Meteo stn.**
Altitude h (m)	1942.38	2621.15	2390.00
Distance to sensor r (m)	1393.53	2666.76	3318.40
Vertical elevation θ_n (deg)	18.81	36.14	0.00

Note that the distance of the meteorological station to the sensor is not exactly the distance of the station to the test points. In fact this meteorological station is some 2000 m away from the monitored slope and hence from the test points. This is a fundamental point when interpreting the results since snow heights retrieved 2 km away from the monitored area and under different atmospheric conditions (particularly regarding the wind and hypothetical turbulences) may not be always directly comparable to those retrieved with the DInSAR technique presented in this chapter.

The following four figures show the geo-location of both test points under different maps of the monitored test site. For a geo-physical map localization of the test points the E-N coordinates in the Figures 5.6 and 5.8 can be directly re-used in the local map in Figure 4.4. The exact position of the points in UTM CH1903 coordinates is 594600E, 127750N, h=1942 m for the first test point and 593564E, 128286N, h=2621 m for the second one.

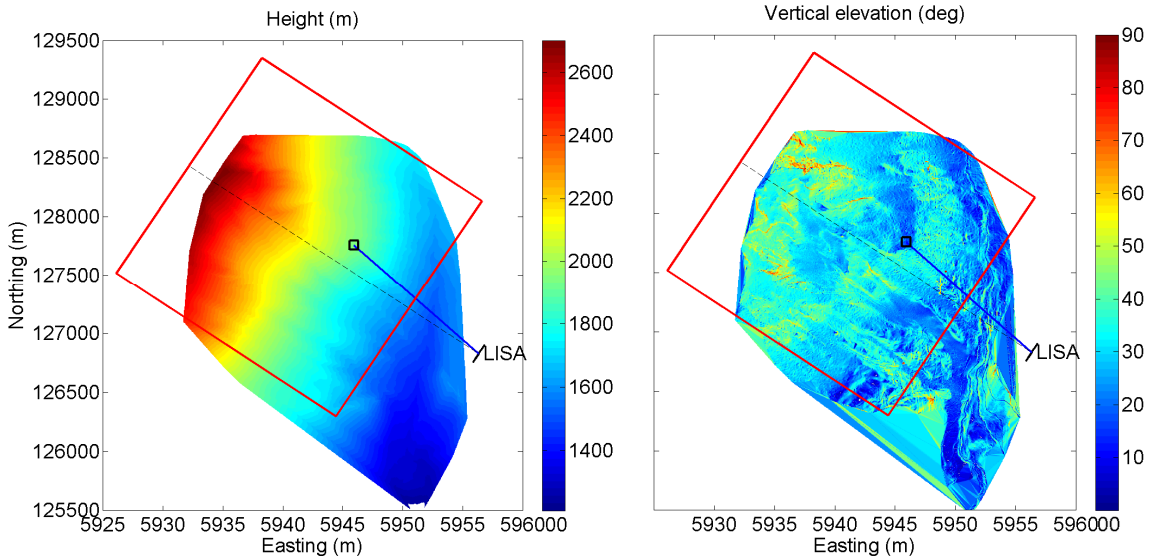

Fig. 5.6. Geo-location of the first test point over a heights and vertical elevation map.

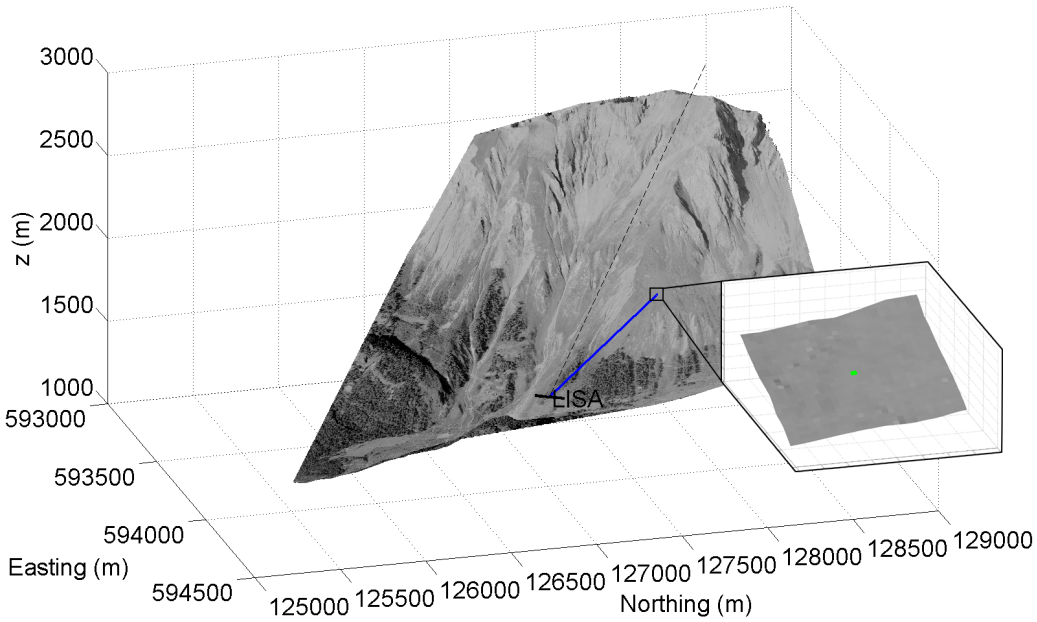

Fig. 5.7. Geo-location of the first test point over a DTM with an orthophoto overlapped. Detail of the 20×20 pixels area used for phase averaging.

Similarly, the second test point is geo-located in Figures 5.8 and 5.9. Note that the dashed line in all maps indicates the zero-cross-range direction of the LISA instrument. The test point slant-range, instead, is indicated by a thicker continuous blue line that starts from the LISA location and ends up into the test point. Note also that the location of the LISA instrument is off the DTM of Figures 5.7 and 5.9 even if it may not seem so from the perspective view. The test points, instead, are over the DTM as it is confirmed by the magnified detail of the 20×20 pixels area used for phase averaging.

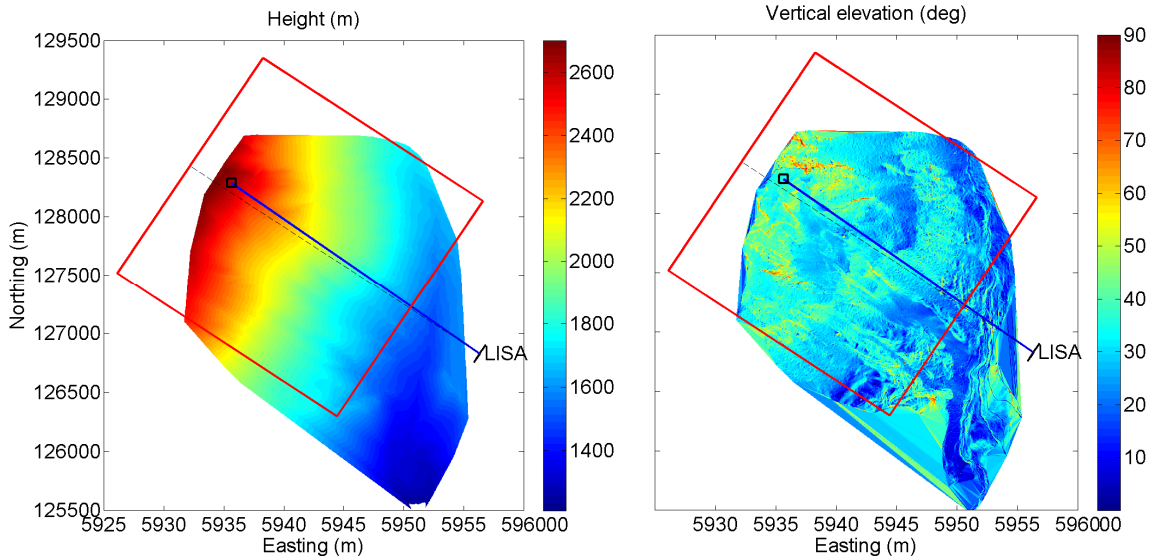

Fig. 5.8. Geo-location of the second test point over a heights and vertical elevation map.

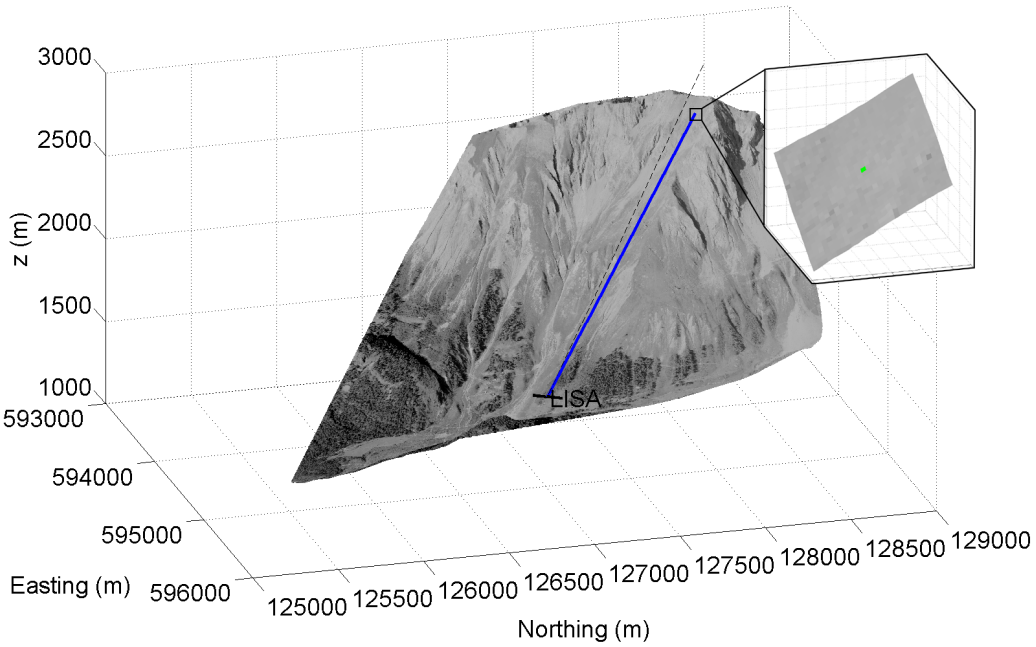

Fig. 5.9. Geo-location of the second test point over a DTM with an orthophoto overlapped. Detail of the 20×20 pixels area used for phase averaging.

5.4.2. Permittivity versus α

According to the data in Table 5.1 and the definition of θ_i in (5.8), the incidence angles of both test points are found to be $\theta_i = 77.88$ deg and $\theta_i = 72.24$ deg for the first and second points, respectively. The real part of the permittivity, thus, can be retrieved with (5.10) as a function only of the calibration parameter α since the central wavelength was kept constant during the whole test campaign (Table 4.1).

Figure 5.10 shows a plot of the real part of the dry snow permittivity as a function of the calibration parameter α in both test points. Note that the parameter α is expressed in the plot in [cm/rad] units and in logarithmic scale since this way the curves can be read more easily. It can be observed that little difference exists between both test points.

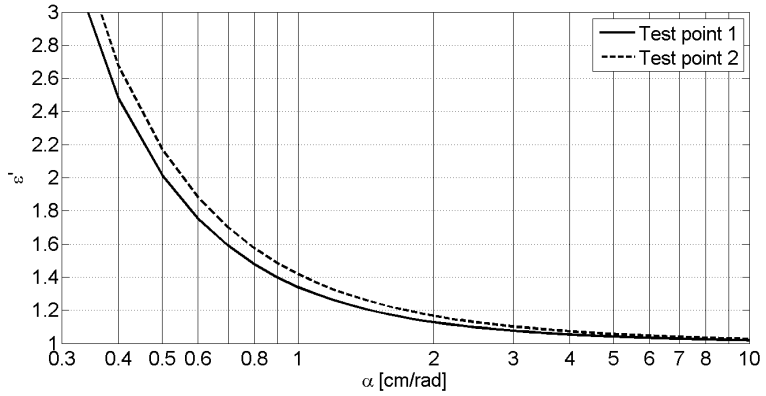

Fig. 5.10. Real part of the dry snow permittivity ε' as a function of the calibration parameter α.

When the real part of the permittivity tends to 1 (very light snow density, as can be expected during and right after snow fall) the parameter α takes values larger than 10 cm/rad independently of the location of the test point. For $\alpha = 300$ cm/rad the permittivity of the first test point is 1.0006 and the permittivity of the second test point 1.0008, practically indistinguishable from free space propagation.

5.4.3. Co-registration process

After co-registering the 501 days of SAR data available for the test site of the Sion Valley it has been observed that the typical values of shift displacement according to (5.15) are $d_{shift}^{typ} = 2$ bins, whereas maximum values are $d_{shift}^{max} = 10$ bins. Figure 5.11 shows an example of the shift displacement values for January 15th, 2004.

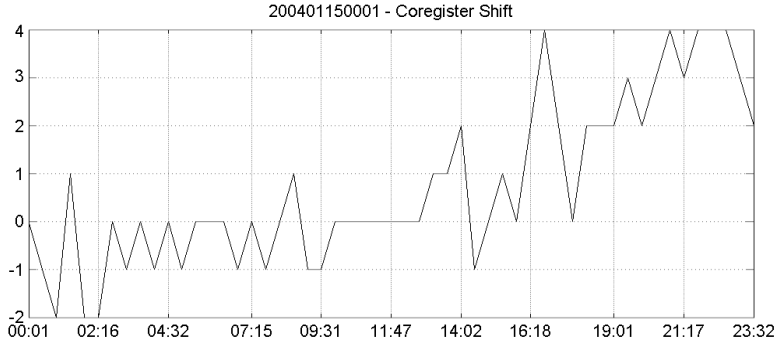

Fig. 5.11. Shift displacement values in zero-padded azimuth bins for January 15th, 2004, function of time.

The typical and maximum shift displacement values entail an azimuth rotation of 1.6 m and 8.3 m respectively, which are under the cross-range resolution cell of the system (see Section 4.2.3). At 2000 m range, the equivalent typical and maximum azimuth rotation are of 0.045 deg and 0.238 deg approximately.

Even if the co-registration technique proposed in 5.3.2 accounts for the rotation of the scatterer but not for its associated phase, according to the results obtained the effects of this step on the interferometric phase for the snow height retrieval have been found to be minimal. In addition, the spatial averaging applied in the computation of the coherence -3×3 pixels, see Section 5.3.3 and (2.21)- and in the computation of the interferometric phase -20×20 pixels, see Section 5.3.4- minimizes even more the effects of the co-registration step.

Figure 5.12 shows two examples of the coherence magnitude improvement obtained after the co-registration process. The plots correspond to the same day, January the 15th, 2004. Figure 5.12-a shows the results in the test point 1, where the coherence of each of the 20×20 pixels of the area under study is plotted for all the interferograms computed that day. Similarly, Figure 5.12-b shows the same results for the test point 2.

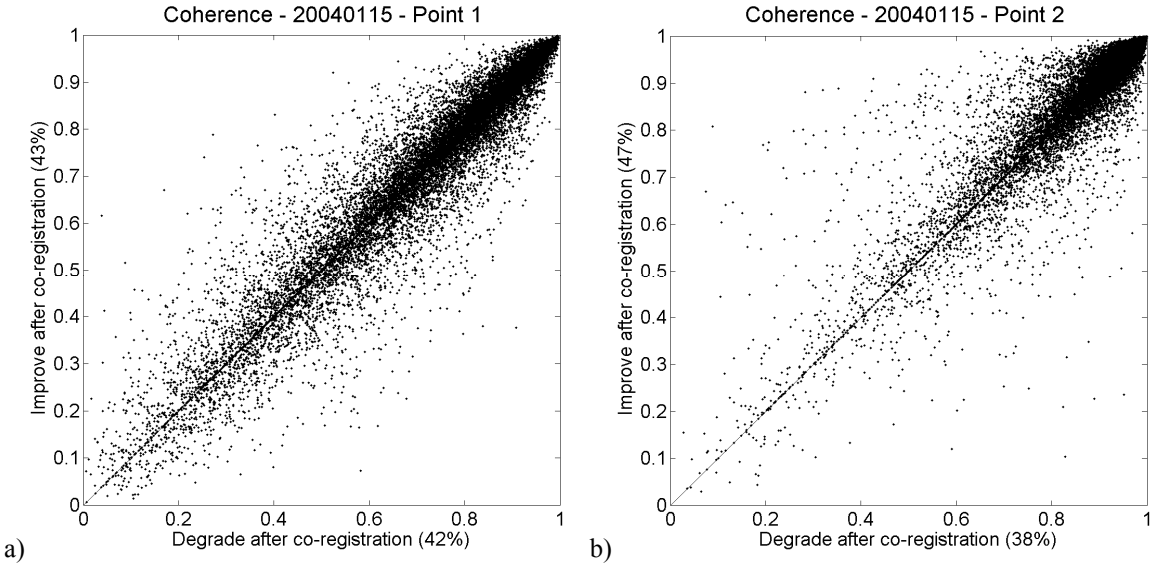

Fig. 5.12. Coherence improvement after the co-registration process for a) test point 1; and b) test point 2.

The results in Figure 5.12 have different interpretations. First of all, as shown on the axes labels, after the co-registration process 43% of the pixels improve their coherence while 42% degrade it in the test point 1. In the test point 2 the effects of the co-registration process are a bit more notable, with a 47% of pixels that improve their coherence and a 38% that degrade it. The rest of pixels up to the 100% maintain their coherence magnitude unmodified. These results confirm the low impact on the co-registration process as already derived from the maximum shift displacements obtained. It is also observed that the co-registration process introduces a degradation of the coherence in an important number of the pixels in the image. This is due to the fact that the proposed co-registration method statistically finds the best shift displacement over the whole radar image by compressing the whole azimuth and range dimensions to a single displacement value according to (5.15) and this does not guarantee an improvement on the coherence on every single pixel. The trade-off between the pixels' coherence degradation and improvement, hence, needs to be considered and the co-registration process should not be applied indiscriminately, but only when decorrelation degrades substantially the interferometric information and there is no better alternative to improve the imagery. As mentioned, this is not the case of the data

acquired by the LISA instrument in the Sion Valley, particularly because of the high image acquisition rate that naturally minimizes temporal decorrelation.

Notably, the coherence magnitude level observed over the whole day for both test points is above 0.7. In the first case the coherence for the selected pixels is mainly distributed above 0.6 while on the second test point it is more concentrated above 0.8. These results confirm, in line with those obtained for most of the days analyzed, the high phase stability of the LISA instrument and the feasibility of using the interferometric phase for retrieving the snow cover depth. The coherence magnitude is stably high, permitting the use of interferometric techniques even under snow fall conditions, as shown in the ground-truth information of Figure 5.13.

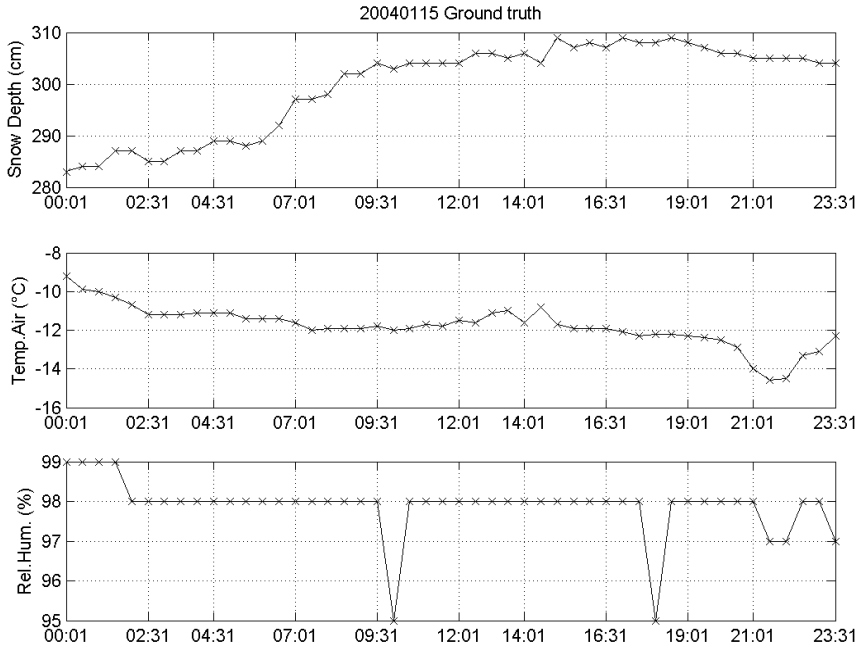

Fig. 5.13. Meteorological conditions for January 15th, 2004, provided by the automatic meteorological station of Donin Du Jour function of time: snow depth, temperature of air and relative humidity.

Nevertheless, even if both test points are on the same slope and separated only some 1300 m, the spatial and temporal variability on the coherences obtained evidence the different atmospheric conditions to which each test area is subject to. Unfortunately this phenomenon entails a very difficult solution. Therefore, temporal and spatial averaging, when available, are shown to be the most effective tools in order to improve the coherence. GB-SAR systems, contrary to satellite- and air-borne sensors, are optimal instruments in terms of image acquisition rate, instrumental for effectively applying temporal averaging techniques.

5.4.4. Snow height retrieval

The snow height retrieval technique presented in the preceding sections has been applied to the data available on the months of December, January, February and March of the three years of field campaign in the Sion Valley. The full table of results can be consulted in Annex F, where the calibration parameters and the mean and standard

deviation of the differences between the ground-truth snow depth and that retrieved with DInSAR are tabulated for each of the two test points analyzed on a daily basis.

Note that colder months were selected for the assessment of the snow height retrieval technique so that the dry snow model is valid. In fact the plots presented together with the snow height estimates include, as do those in Figure 5.14, an upper graphic entitled "Quality indicators" that quantifies the quality of the snow height retrieval technique by means of 3 indicators:

a) *#(pixThr)/#(pixTot)* is the ratio between the number of pixels with coherence magnitude above the defined threshold (0.7) and the total number o pixels in the test area (20×20 pixels as stated in Section 5.3.4).

b) *avg(coh)* is the averaged coherence magnitude in the 20×20 pixels test area of all pixels above the threshold defined (Thr = 0.7).

c) *Dry snow* is a binary indicator that equals to 1 when the air temperature is under 0 °C and, thus, the snow cover can be considered mostly dry.

All three indicators range from 0 to 1, 0 being a low confidence in the retrieved snow depth because one or more constraints are not fulfilled and 1 high probability of success.

The main constraints on the application of this technique are, hence, summarized on the three points above: sufficient number of pixels with a high coherence magnitude in order to have an adequate SNR in the interferometric phase; sufficient number of pixels in order to effectively increase the SNR of the interferometric phase by spatial averaging; and dry snow conditions on the area monitored.

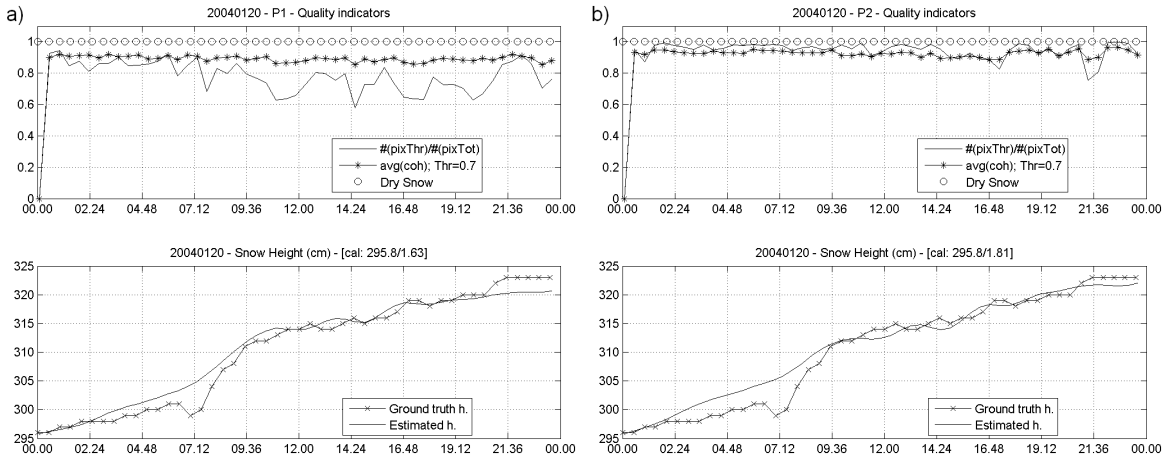

Fig. 5.14. Snow depth retrieval for January 20th, 2004, function of time. a) Test point 1; and b) Test point 2.

Figure 5.14 presents the results of the snow height retrieval by DInSAR for January 20th, 2004, in both test points. As stated in 5.3.6, the calibration parameters α and β have been found by fitting the ground-truth snow height evolution over the whole day to the cumulative interferometric phase $\Delta\varphi_s^{cum}(t)$. The bottom plots show how the estimated snow cover depth matches the ground-truth heights in both test points. According to the tables in Annex F, the mean and standard deviation of the differences between ground-

truth and estimated values of snow height are 1.3 cm and 1.2 cm respectively for the test point 1 and 1.5 cm and 1.4 cm, respectively, for the test point 2.

Note on the quality indicators that the dry snow condition is satisfied for the whole day. Regarding the coherence of the pixels selected for spatial averaging of the interferometric phase on both test points the values are well over 0.8, which guarantees a high SNR in the interferometric phase. Regarding the ratio of pixels with coherence above the threshold, instead, significant differences can be appreciated depending on the test point. In the first test point, Figure 5.14-a, the ratio indicates that the number of high coherent pixels in the test rectangle is of 60% on several instants of time, with a mean value of 70-80% for the whole day. In the second test point instead, Figure 5.14-b, during the whole day the coherence is over the threshold in 90% of the pixels of the test area.

The ratio of pixels with coherence above the threshold has a double interpretation. First of all, 60% of pixels with coherence magnitude above 0.7 in a 20×20 pixels rectangle means that the spatial averaging will be carried out over some 240 pixels, which is a representative number of pixels to expect a substantial improvement on the interferometric phase SNR. Hence, the snow depth retrieval technique is expected to work properly under these circumstances. Secondly, the fact that coherence values are so different in both test points confirms that different atmospheric phenomena in the form of temperature gradients, precipitation, wind conditions, etc. in each test point. This fact was already noticed on Figure 5.12 but here it is repeated again since this is an extremely important issue that needs to be considered when comparing the retrieved snow cover depth with ground-truth data: ground-truth data for the complete assessment of this technique should be available in the exact location of the test points and not 2 km away from them. Differences on the estimates of the snow height are, thus, expected not only between the test points and the ground-truth data coming from the meteorological station, but also between the test points themselves. The causes for these differences, as stated, are the different atmospheric conditions that affect each point at local scale and to which the interferometric phase is highly sensitive.

Unfortunately no ground-truth information on the snow cover depth on any point of the slope covered by the radar FOV is available. Actually, the traditional mean of remotely measuring the snow height on areas where no meteorological station is present is by visual observation of the horizontal marks painted on a stick driven in the ground. This methodology is conditional on the accessibility to the areas of interest and by the stability of the stick, which may fall down because of the wind or avalanches.

Regarding the calibration parameters they can be read on the titles of the snow height plots under the [cal] label. In Figure 5.14-a $\alpha = 1.63$ cm/rad and $\beta = 295.8$ cm while in Figure 5.14-b it can be read that $\alpha = 1.81$ cm/rad and again $\beta = 295.8$ cm. As already analyzed in Section 5.4.2 the α parameter fits in the expected range for both test points, and very similar values are obtained at each of the test points, so these are additional qualitative proofs that show that the technique is correctly yielding the snow cover depth. According to the plot in Figure 5.10, the real part of the permittivity is approximately $\varepsilon' = 1.20$ in the first test point and $\varepsilon' = 1.20$ also on the second one. These permittivities are translated to the snow density $\rho_s = 0.12$ g/cm^3 according to (5.2) and in agreement with the data reported in [52].

Figure 5.15 shows similar results for both test points but in this occasion for a period of three consecutive days, from January the 18th to the 20th, 2005. Note on the upper plots that the #(pixThr)/#(pixTot) ratio is equal to zero at the first image of every day since the

differential interferometric phase and the quality indicators are computed on a daily basis and the first instantaneous value of every day is initialized to zero. The cumulative interferometric phase, derived as shown in Figure 5.5, does not present these discontinuities among different periods of time. Note also that the horizontal axis is labelled in these sequences DDTHH, where DD stands for the day in the month and HH for the hour in 24h format of the corresponding datum.

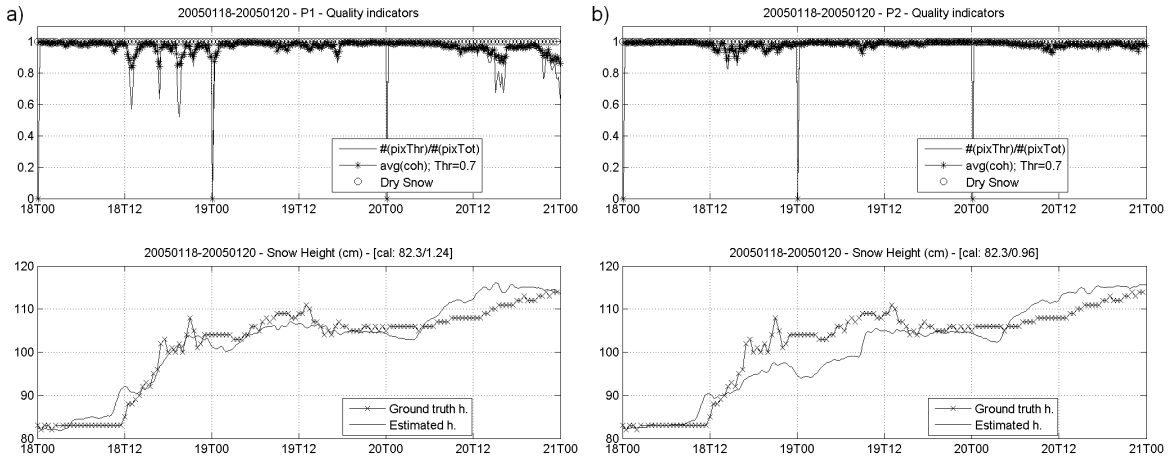

Fig. 5.15. Snow depth retrieval for January 18th-20th, 2005 in a) test point 1; and b) test point 2.

The quality indicators for the three days time series of snow cover depth show excellent values on both test points. The second test point (Figure 5.15-b), though, shows again a slight higher coherence magnitude and a higher proportion of high coherent pixels on the test rectangle than the first test point (Figure 5.15-a). This could seem contradictory since the second test point according to Table 5.1 is at a higher elevation (2621 m versus 1942 m) and has a more pronounced inclination (36 deg versus 18 deg). In addition the second test point is very close to the mountain crest, so more exposed in theory to winds coming from the other side of the mountain that can also carry loose snow particles.

Even if both curves of the estimated snow height may appear very similar, the best fitted calibration parameter α is equal to 1.24 cm/rad on the first test point and 0.96 cm/rad on the second one. This difference is not surprising since the parameter α, as defined in (5.5), depends on the incidence angle θ_i and on the dry snow density which are different in every test point. According to the Figure 5.10 the real part of the permittivity is approximately $\varepsilon' = 1.30$ in the first test point and $\varepsilon' = 1.45$ on the second one. These permittivities are translated to the snow densities $\rho_s = 0.18$ g/cm^3 and $\rho_s = 0.26$ g/cm^3 respectively according to (5.2), which represents 44% difference. Contrary to what was observed in Figure 5.14 where the snow densities of both test points were practically identical at the same instant of time, in this example the densities retrieved are different by 44%. These results confirm the fact that the snow pack changes at local scale because of the topography and also because of the local atmospheric conditions.

Similar results are presented in Figure 5.16 for the winter 2005-2006 this time with a series of four consecutive days: from February 18th to 21st, 2006. The quality indicators present high values for all the days in both test sites. Nevertheless, the curves of the snow height estimated with DInSAR slightly diverge from one test point to the other one. The highest difference is found during the first day of the second test point. Even if the cumulative interferometric phase increases as does the ground-truth snow height, the α

factor estimated for the whole period is smaller than that required to accurately estimate the snow height absolute values during the first day.

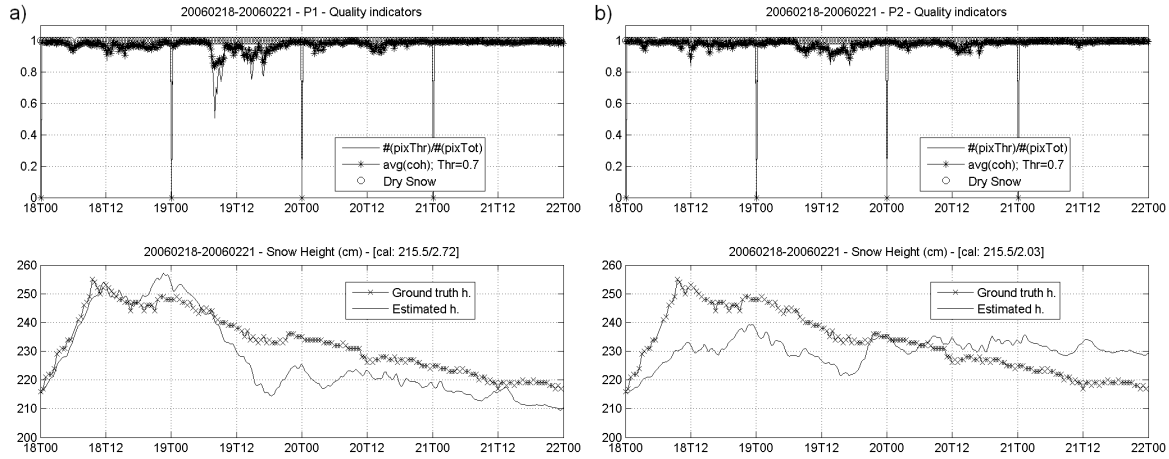

Fig. 5.16. Snow depth retrieval for February 18th-21st, 2006 in a) test point 1; and b) test point 2.

Figure 5.17 confirms this point when estimating the α parameter on a daily basis instead on the longer period of 4 days in the example above. In fact the estimated snow heights on both test points fit perfectly the ground-truth data, but the calibration parameters are significantly different: $\alpha = 2.65$ cm/rad in the first test point while $\alpha = 4.20$ cm/rad on the second one. These calibration parameters translate into almost identical permittivities, that is $\varepsilon' = 1.10$ in the first test point and $\varepsilon' = 1.08$ in the second one, which indicates similar snow conditions on both test points for that day. When trying to use a single calibration parameter α for a longer period, results show that the snow conditions are kept approximately constant in the first test point (Figure 5.16-a) and the same single calibration parameter can be used during all four days. On the second test point (Figure 5.16-b), instead, the snow density varies during the period analyzed and the use of a single calibration parameter during the whole time series provides a slightly poorer accuracy even if the quality indicators are higher than in the first test point.

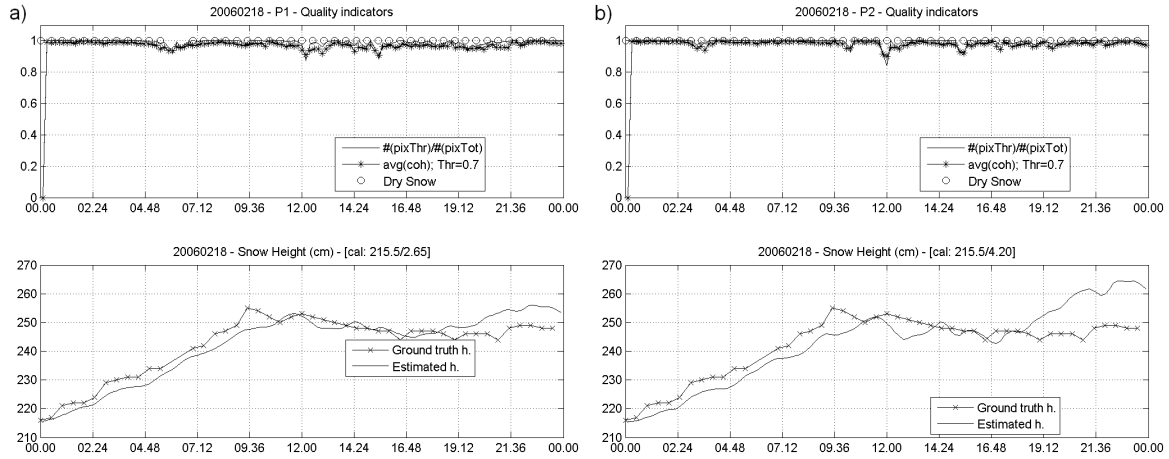

Fig. 5.17. Snow depth retrieval for February 18th, 2006 in a) test point 1; and b) test point 2.

Since no ground-truth data is available for the snow height at the precise location of the test points, it is impossible to determine whether the calibration parameter α cannot be extended to longer periods. The discrepancies may be because of changes in the snow cover properties or because the calibration parameters may have been properly estimated but the ground-truth snow depth curve that should be used in the assessment has not been measured in the right place.

5.4.5. Statistical validation

As stated at the beginning of this section, the Annex F lists the calibration parameters obtained after the analysis of all the radar images available against the ground-truth data also available. Figure 5.18 presents a summary of the calibration parameter α in graphical format for all the days available separated by test point and winter season.

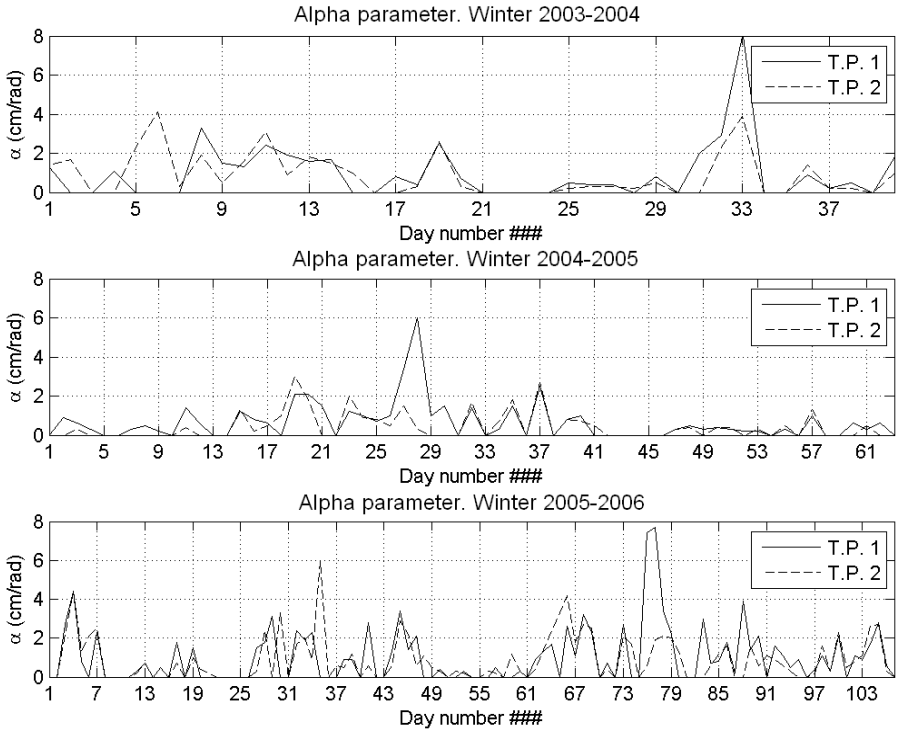

Fig. 5.18. Calibration parameter α by winter season for both test points (T.P.).

Similarly, the histogram of the calibration parameter α is presented in Figure 5.19 separated by test point and winter season. From the observation of the plots in Figures 5.18 and 5.19 it is difficult to extract conclusions regarding the two different test points. Even if they are situated at different altitude levels and present different inclination with respect to the normal, results show similar values of the parameter α in both points for most of the days even if calibrating it with the same ground-truth data. When entering into the details day by day, however, substantial differences can be found as a function of the snow density, depending on the test point, as demonstrated in the preceding section.

The values observed of the calibration parameter, on the other hand, fit perfectly on the expected dry snow permittivity depicted in Figure 5.10 and also reported in [52]. The

values of permittivity are, thus, consistent, so it can be concluded that the DInSAR technique presented properly retrieves the snow cover depth.

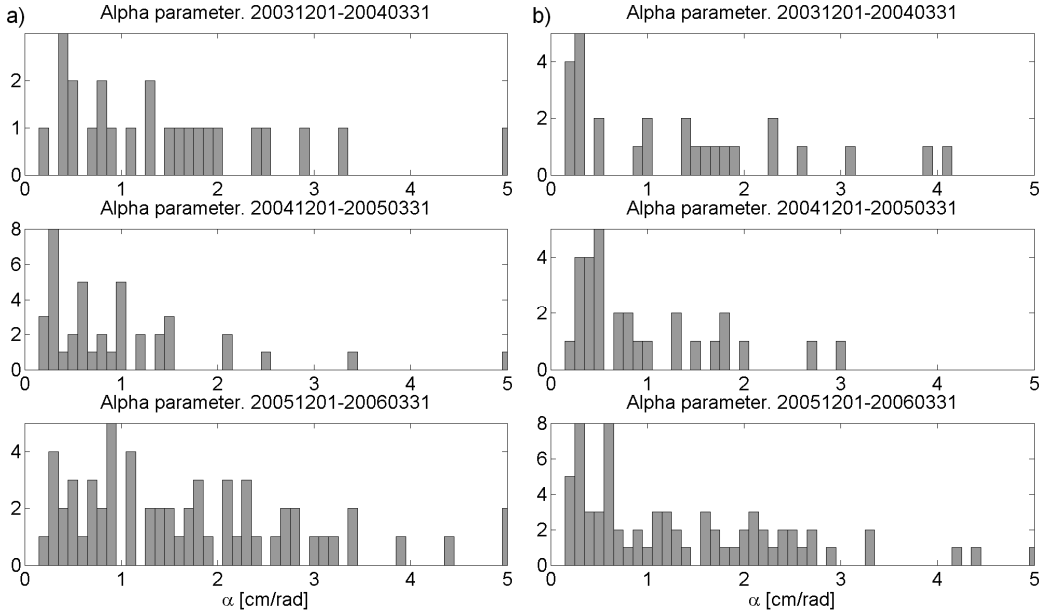

Fig. 5.19. Histograms of the calibration parameter α by winter season for a) test point 1; and b) test point 2.

Finally, Table 5.2 reports the statistics on the accuracy of the DInSAR show height retrieval technique based on the tables in Annex F, that is, with a daily calibration. The matching between the ground-truth data and the estimated snow height is defined to be achieved when the calibration parameter α fits in the range defined in Section 5.3.6, that is, between 0.1 and 300 cm/rad.

Table 5.2. Matching of the snow depth between ground-truth and DInSAR estimates for each test point

	Test point 1	**Test point 2**	**Test points 1 & 2**
Winter 2003-2004	60.0%	67.5%	52.5%
Winter 2004-2005	63.4%	46.0%	42.9%
Winter 2005-2006	56.0%	65.4%	50.4%

Results show a typical accuracy of the order of 60% for each test point separately, that is reduced to 50% approximately when the matching is produced on both test points simultaneously. Results are, thus, consistent and confirm the potential of the DInSAR technique for the retrieval of the snow depth even during snow fall conditions. Unfortunately, an important uncertainty remains. The lack of ground-truth snow height data in the exact positions of the test points makes it impossible to determine whether the accuracy obtained could be even better if comparing the DInSAR snow height estimates with the real snow height evolution on the test points. Nevertheless, with the data available, the accuracy obtained can be considered consistent and reasonably good.

5.5. Conclusions

A dry snow height retrieval algorithm has been presented and validated through data gathered with a ground-based synthetic aperture radar in the test site of the Sion Valley. The main advantage of ground-based systems compared to those air- or space-borne is the high coherence of the interferograms formed, which translates into accurate snow depth profiles with a single calibration at the beginning of the period under study. Regarding the length of the periods analyzed, it appears from the results that the snow conditions on the whole single layer model can be considered approximately constant over a whole day. Snow height evolution plots have been successfully produced for periods up to four days, although periods longer than a few days may entail significant changes on the snow pack properties and hence on the calibration constant.

Since no snow height ground-truth data is available at the precise location of the test points analyzed, it is not possible to fully determine whether the calibration parameter α cannot be extended to longer periods because of changes in the snow cover properties or because of the ground-truth data available does not properly represent the snow height at the test points. Nevertheless, the dynamics of the snow pack make us think that the calibration parameter α can be reasonably extended over few days.

Further, fast atmospheric perturbations not properly modelled with the co-registration method presented in the processing methodology introduce an additional source of uncertainty when comparing the interferometric results with ground-truth data.

Nevertheless, considering the statistical validation carried out it can be concluded that the use of a GB-SAR positively allows the monitoring of the snow cover depth. This technique, in addition, is of particular interest in steep slopes where in-situ sensors are difficult to be installed or can be easily destroyed in case of strong winds or avalanches.

6. Digital terrain mapping

6.1. Introduction and state of the art

The scope of this chapter is double. In the first place a novel processor is presented for improved Digital Terrain Model (DTM) generation with GB-SAR interferometric data. In the second part, a study on the feasibility of retrieving the volume of snow displaced in an avalanche from a differential DTM is presented. This is the second monitoring technique of snow cover presented in this PhD thesis.

Topographic mapping using interferometric SAR techniques with a radar sensor on-board an aircraft or satellite has been extensively studied over the last 15 years [35][60]. Recent advances in GB-SAR sensors, such as those of the Joint Research Centre [35] and the University of Florence [49], have brought this technology to a point where it can achieve a similar performance to those of air- and space-borne SAR, but with a much smaller field of view and a much higher acquisition rate. Problems specific to the Digital Terrain Model (DTM) generation with GB-SAR sensors in the C-Band have already been addressed by G. Nico [35] and L. Noferini [49]. Among the issues studied in the earlier works, specific formulation has been presented for the DTM computation with a GB-SAR antenna system, a sensitivity analysis has been conducted on all variables involved in the DTM generation and local atmospheric effects have been characterized and compensated.

Typical differential heights standard deviations of 5 m have been obtained in [32], [35] and [49] when computing the differences between ground-truth DTMs and those generated with GB-SAR interferometry in the C-Band. The processor presented in the first part of this chapter achieves standard deviations of approximately 3 m (i.e., a height estimate error reduction of 40%) by exploiting the availability of a high number of interferograms -as typically happens with ground-based systems- by using a new formulation for the DTM generation avoiding the approximations incurred when truncating to the first order a Taylor series and by introducing a new calibration method for the differential signal path [53].

The novel processor is assessed with interferometric data of the Sion Valley test site because only for this site a high resolution laser scanner DTM [38] is available to assess the results derived with the GB-SAR sensor.

Regarding the second part of this chapter, the estimation of snow volume with SAR techniques has only been addressed so far in large areas by measuring two principal variables: snow areal coverage and snow depth [54]. In addition, it is necessary to estimate the SWE to establish the volume of water in the form of snow. This approach leads to a

gross estimation of the snow volume that is not suitable to feed dynamic models of local snow avalanches. In fact, most avalanche dynamics models assume that avalanche mass is constant along the track, hypothesizing that no entrainment takes place. In reality, post-event observations of avalanche paths show that much of the snow cover has been entrained into the avalanche and deposits are left along the avalanche path [55][56]. Photogrammetry has been the most successful technique used so far to map local snow avalanches by measuring the surface of the snow cover before (when possible) and after the avalanche. This allows an estimation of the released mass of snow in the starting and deposition zones [57][58]. The DTM accuracy obtained by protogrammetry on the snow cover is of the order of 15-30 cm, but the following constraints need to be fulfilled:

a) An undisturbed cover of fresh snow has very low contrast. Hence, a precise measurement of the snow cover in the release zone before the triggering is difficult. Moreover, a favourable daylight illumination condition is necessary.

b) An artificial avalanche release cannot be planned shorter than 3 days in advance. Therefore, the implementation of the mapping procedure must be quick and flexible. Natural avalanches typically cannot be mapped since no permanent instrumentation is available for such kind of measurements.

c) The surveying of the ground control points in the release and deposition areas is very difficult, since these points must be placed on exposed rocks that remain clearly visible even after a heavy snowfall and out of reach of the avalanche runoff. Temporary signalization is not conceivable since it is extremely dangerous to go on-site during experiments.

The use of laser scanner altimeters onboard helicopters overcomes the previous constraints, at the price of a high system cost and complexity [57]. On the other hand, the use of GB-SAR could represent an interesting alternative between classical photogrammetry and laser scan technologies, helping to overcome the two first constraints before mentioned with a reasonable flexibility and price. But as it will be shown later on, the DTM accuracy obtained with GB-SAR is on the order of 3-5 m [53], which poses serious problems to snow volume retrieval involved in natural or artificial avalanches with SAR technologies [59].

A possible work around could be the use of the differential interferometric phase of two consecutive SAR acquisitions right before and after the avalanche event. By employing the technique described in the preceding chapter, an estimation of the differential snow height could be provided at several locations of the radar FOV without the need of any ground control point. These differential snow depth estimations multiplied by the area involved in the avalanche path would provide a realistic estimation of the snow volume displaced. Unfortunately, the radar wavelengths employed in the two field campaigns (5.1 and 2.2 cm) allow for very little snow depth variations between acquisitions to be properly unwrapped when computing consecutive interferograms.

The only alternative for snow volume mapping in avalanches with GB-SAR, although with limitations, is then the subtraction of a DTM created right before the avalanche from a DTM created after the avalanche event. In the second part of this chapter some results on the application of this technique are presented for the test site of the Sion Valley.

6.2. Formulation review

Several approximations have been proposed for the problem of converting the interferometric phase to vertical heights. In this section three of them are reviewed, the first two being specifically tailored for GB-SAR sensors.

Figure 6.1 shows the geometry of the GB-SAR antenna system of the LISA instrument. A single transmit antenna is used, located at the sensor's local coordinates' origin (y,z)=(0,H). Two receiving antennas are located respectively at (y,z)=(0,H) and at b=(y,z)=(B_h,H+B_v). Note that the parameters h, H and B_v are defined always positive, while the horizontal component of the baseline, B_h, can be either positive or negative depending on the inclination of the baseline B. In the example depicted in Figure 6.1 B_h has a negative value. Finally, the differential signal path Δr is approximated as $\Delta r \approx r_2 - r_1$.

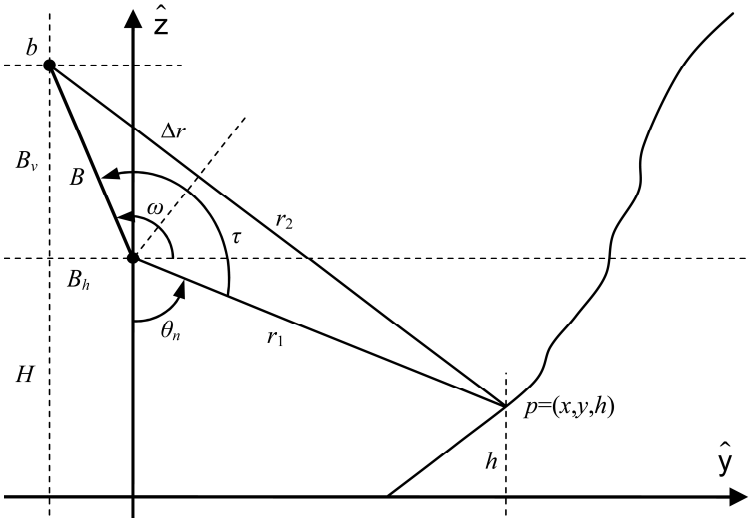

Fig. 6.1. GB-SAR geometry in the topographic mode of LISA (single-pass). Plane x=0, with the Tx and one Rx antenna at (y,z)=(0,H) and a second Rx antenna at b=(B_h,H+B_v).

Generalizing the geometry to three-dimensional space, an arbitrary point p will be defined in a cylindrical coordinate frame by its distance r_1 to the antenna system origin and its horizontal azimuth θ = atan(x/y). In this case, the horizontal component of the baseline, as already pointed out in [35], will depend on the azimuth angle as follows:

$$B_h = B_h(\theta) = B_h(0) \cdot \cos\theta. \tag{6.1}$$

The interferometric technique for topographic mapping is based on the property that the measured phase of the interferogram, $\Delta\varphi$, is directly proportional to the path difference Δr according to (6.2), where λ is the central wavelength. Note that 2π is used instead of 4π because the LISA sensor uses a single antenna for transmitting and two different antennas for receiving (single-pass interferometric mode), as already discussed in Section 2.4.

$$\Delta r = \frac{\lambda}{2\pi}\Delta\varphi. \tag{6.2}$$

A little algebra and geometry yield the equation for the DTM heights h as a function of Δr, and thus, of $\Delta\varphi$. However, different approximations result in different equations as will be shown in the following sections.

6.2.1. Taylor and r_2 approximation

L. Noferini presents in [49] a formulation for the particular case in which B_h=0. Nevertheless, the series expansion proposed can be extended to the general case of a tilted baseline if r_2 is approximated in the following manner:

$$r_2 \approx \sqrt{r_1^2 + B_v^2 + 2(H-h)B_v} - B_h. \tag{6.3}$$

The exact formulation of r_2 can be found in (6.7). Note that the approximation proposed in (6.3) assumes $|B_h| << \sqrt{r_1^2 - (H-h)^2}$, which is reasonable in the typical scenarios monitored by GB-SAR sensors. As an example, in the field campaign carried out in the Sion test site H = 1780 m, h ranged from 1800 m to 2600 m and r_1 ranged from 700 m to 2900 m, yielding $17\,\text{m} < \sqrt{r_1^2 - (H-h)^2} < 50\,\text{m}$. The horizontal component of the baseline was instead only B_h = −6.3 cm.

Assuming the approximation of r_2 defined in (6.3), the slant-range signal path difference Δr can be expressed as:

$$\Delta r = r_2 - r_1 = r_1\left(\frac{r_2}{r_1} - 1\right) = r_1\left(\sqrt{1 + \frac{2(H-h)}{r_1}\frac{B_v}{r_1} + \left(\frac{B_v}{r_1}\right)^2} - \frac{B_h}{r_1} - 1\right). \tag{6.4}$$

Since (B_v/r_1) is small enough (e.g., a typical value is 10^{-3}), the square root in (6.4) can be approximated to its Taylor expansion in terms of (B_v/r_1) to the first order:

$$\Delta r \approx r_1\left(\left(1 + \frac{H-h}{r_1}\frac{B_v}{r_1}\right) - \frac{B_h}{r_1} - 1\right) = \frac{(H-h)B_v}{r_1} - B_h. \tag{6.5}$$

The final expression for the heights is then:

$$h = H - \frac{r_1\left(\Delta r + B_h\right)}{B_v}. \tag{6.6}$$

6.2.2. Taylor approximation, exact r_2

G. Nico in [35] starts with the exact expression of r_2 as a function of r_1 and the baseline components B_h and B_v:

$$r_2 = \sqrt{\left(\sqrt{r_1^2 - (H-h)^2} - B_h\right)^2 + \left((H-h) + B_v\right)^2}. \tag{6.7}$$

The slant-range signal path difference Δr is then expressed as:

$$\Delta r = r_2 - r_1 = r_1\left(\frac{r_2}{r_1} - 1\right) = r_1\left(\sqrt{1+\psi} - 1\right), \tag{6.8}$$

$$\psi = \frac{B_v^2}{r_1^2} + \frac{2B_v}{r_1}\frac{H-h}{r_1} + \frac{B_h^2}{r_1^2} - \frac{2B_h}{r_1}\sqrt{1 - \left(\frac{H-h}{r_1}\right)^2}. \tag{6.9}$$

Considering the typical values of the baseline components and the slant-range r_1 mentioned in the preceding section, it can be assumed $\psi << 1$. The expression $\sqrt{1+\psi}$ can then be approximated by its first order Taylor expansion in terms of ψ, yelding a new expression for Δr equivalent to Equation (11) in [35]:

$$\Delta r \approx B_v\left(\frac{B_v}{2r_1} + \frac{H-h}{r_1}\right) + B_h\left(\frac{B_h}{2r_1} - \sqrt{1 - \left(\frac{H-h}{r_1}\right)^2}\right). \tag{6.10}$$

The DTM heights h are finally found by solving (6.10). Note that (6.11) is formulated according to the scheme depicted in Figure 6.1, so the result is very similar but not identical to Equation (12) in [35]. In addition, the complete solution (±) has been provided in (6.11) and a missed B_h^2 term in [35] has been corrected by B_v^2.

$$h = H - \frac{r_1 B_v}{B_v^2 + B_h^2}\cdot\left(\Delta r - \frac{B_v^2 + B_h^2}{2r_1}\right) \pm \frac{r_1 B_h}{B_v^2 + B_h^2}\cdot\sqrt{B_v^2 + B_h^2 - \left(\Delta r - \frac{B_v^2 + B_h^2}{2r_1}\right)^2}. \tag{6.11}$$

6.2.3. No Taylor approximation, exact r_2

The final formulation analyzed is that of H.A. Zebker presented in [60]. This formulation is more exact since it avoids any approximation with a series expansion, and although it is referred to an airborne sensor it is easily adaptable to the ground-based case depicted in Figure 6.1.

In a first step, the quantity $\cos(\tau)$ is computed since it only depends on the slant-range distance (r_1) and the baseline ($B = \sqrt{B_v^2 + B_h^2}$), where both parameters are known:

$$r_2^2 = (\Delta r + r_1)^2 = r_1^2 + B^2 - 2r_1 B\cos\tau, \tag{6.12}$$

$$\cos\tau = \frac{r_1^2 + B^2 - (\Delta r + r_1)^2}{2 r_1 B}. \tag{6.13}$$

From the geometry in Figure 6.1 it can be easily established that $\theta_n = \omega + \pi/2 - \tau$. Similarly to B_h in (6.1), the before mentioned angles have a dependence on the horizontal azimuth angle θ: $\theta_n = \theta_n(\theta)$, $\omega = \omega(\theta)$ and $\tau = \tau(\theta)$. This dependence in the case of ω can be expressed from the scalar product of the normalized vectors defining the baseline and the ground-range according to:

$$\begin{bmatrix} \hat{b} \\ \hat{r}_g \end{bmatrix} = \begin{bmatrix} 0 & \cos\omega(0) & \sin\omega(0) \\ \sin\theta & \cos\theta & 0 \end{bmatrix}, \tag{6.14}$$

$$\hat{b} \cdot \hat{r}_g = \cos\omega(0) \cdot \cos\theta = \cos\omega(\theta), \tag{6.15}$$

$$\omega(\theta) = \operatorname{acos}\left(\cos\omega(0) \cdot \cos\theta\right). \tag{6.16}$$

Since a direct relationship exists between θ_n and the angles ω and τ as depicted in Figure 6.1, ω can be directly retrieved from (6.16) and τ can be obtained from (6.13), the heights of the DTM can be expressed as follows:

$$\begin{aligned} h &= H - r_1 \cos\theta_n, \\ \cos\theta_n &= \cos\left(\omega + \pi/2 - \operatorname{acos}(\cos\tau)\right). \end{aligned} \tag{6.17}$$

6.3. Topographic mapping processor

6.3.1. Processor description

The complete implementation of the topographic mapping processor in absence of snow is outlined in this section. The major elements of the processor can be seen in the block diagram in Figure 6.2, where dashed boxes indicate the novel steps. First of all, the frequency domain backscatter is acquired simultaneously at each of the two receiving antennas of the sensor Rx1 and Rx2, where n indicates the number of successive acquisitions over time. The raw data is then focused in a rectangular grid with any of the algorithms presented in Section 2.3. In order to minimize the impact on the final averaged interferogram of different atmospheric conditions in each of the N images acquired at different instants of time, a calibration of the radar images' phase is applied. This calibration simply shifts pixel by pixel the phase $\varphi_{\#,n}$ of the whole image to match the phase value $\varphi_{\#,0}$ at a reference point: $I_{\#,n} = I_{\#,n} e^{j(\varphi_{\#,0} - \varphi_{\#,n})}$. # = {1,2} depending on the Rx channel being processed. A reference point is selected such that it presents the highest absolute value of zero-baseline temporal coherence accumulated over all the time series analyzed. It is important to note that for the calibration step of the image phase a reference point not covered by snow is necessary to be visible in the radar FOV.

Once the phase calibration has been applied, the interferometric coherence between the two images $I_{1,n}$ and $I_{2,n}$ is obtained according to (2.21) with a spatial averaging of 3×3 pixels (4×1 resolution cells approximately). Taking advantage of the high acquisition rate of the GB-SAR sensors (typically on the order of several images per hour) a time series of N coherence images can be averaged to reduce the impact of the phase instability due to the atmospheric effects and the radar phase noise introduced during the aperture synthesis.

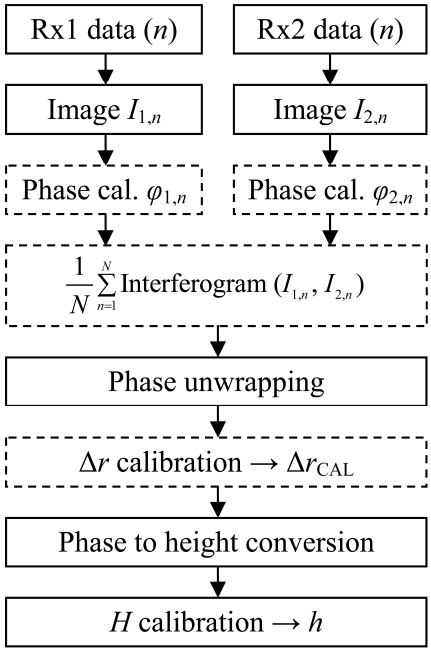

Fig. 6.2. Block diagram of the interferometric processor for DTM generation, where the dashed boxes indicate the novel steps of the processor.

It is interesting to note that the simultaneous acquisition in the LISA instrument of both reception channels separated by a vertical baseline cancels out possible atmospheric effects introduced by a temporal delay in the acquisitions (as is the case of repeat-pass interferometers). Nevertheless, the temporal interferogram averaging proposed in this technique re-introduces the problem of temporal decorrelation of the scene. This problem is addressed through the phase calibration step before mentioned, in which the whole image phase is shifted to match the phase value at a reference point.

While space-borne interferograms may suffer from spectral shift, as demonstrated in Section 2.4.4 GB-SAR interferograms typically present very high common frequency content. Actually, the interferograms used in this study have a spectral shift of 200 kHz in the worst case over 60 MHz bandwidth (i.e., a common frequency content higher than 99%). This and the fact that a frequency windowing function (e.g., a four terms Blackman Harris window) is needed to suppress side-lobes in the imagery eliminate the need for the common band pre-filtering.

Phase unwrapping, instead, is necessary since fringes are present in the interferometric phase as shown in Figure 6.3-a. A weighted least-squares algorithm solved by the preconditioned conjugate gradient (PCG) method is used [33], with the weight function given by the averaged absolute value of the coherence. The unwrapped phase of the example in Figure 6.3-a can be observed in Figure 6.3-b.

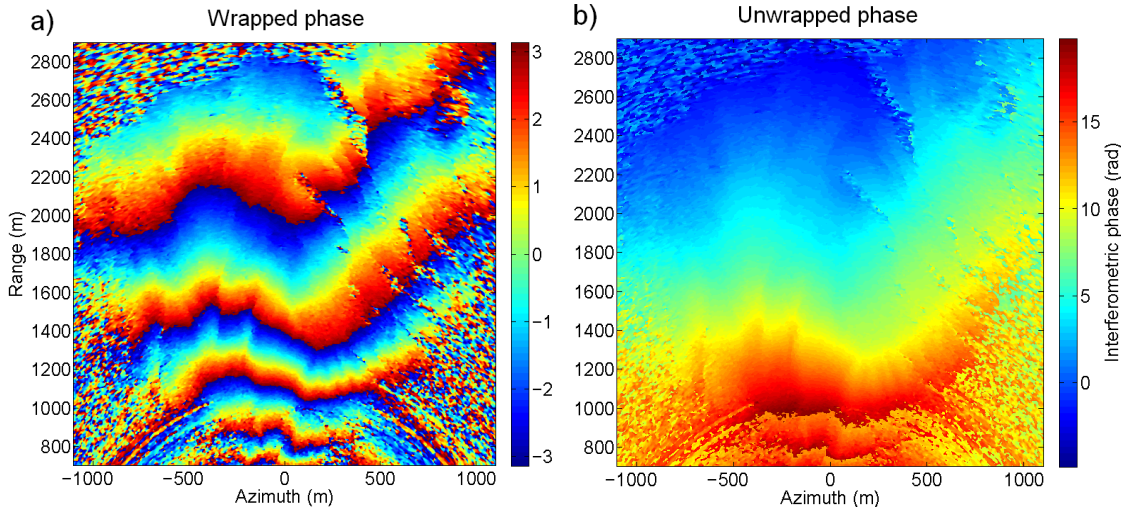

Fig. 6.3. Wrapped and unwrapped interferometric phase, scale in radians.

Next after the phase unwrapping, a calibration of the differential signal path Δr is performed in order to minimize the effects of an inaccurate measurement of the baseline components B_h and B_v in the sensor. Considering that the unwrapping procedure reconstructs the absolute phase up to a constant, knowledge of the precise terrain height at least in one ground control point (p_{REF}) is necessary. The calibration consists first in calculating the theoretical differential path Δr_{REF} corresponding to the reference point $p_{REF} = (x_r, y_r, h_r)$:

$$\begin{aligned} \Delta r_{\mathrm{REF}} &= r_2 - r_1 = \sqrt{r_1^2 + B^2 - 2 r_1 B \cos\tau} - r_1, \\ r_1 &= \sqrt{x_r^2 + y_r^2 + (H - h_r)^2}. \end{aligned} \tag{6.18}$$

Then, the differential path at each pixel of the whole image is shifted in order to match Δr_{REF} in the reference point (p_{REF}):

$$\Delta r_{\mathrm{CAL}} = \Delta r - \Delta r(p_{\mathrm{REF}}) + \Delta r_{\mathrm{REF}}. \tag{6.19}$$

At this stage the phase to height conversion can be done by any of the three methods reported in (6.6), (6.11) and (6.17) of the preceding section. To complete the process a final calibration of the height with the ground control point p_{REF} is necessary in order to determine the value of the constant H. As mentioned, the unwrapping procedure reconstructs the phase up to an unknown constant, so with the knowledge of p_{REF} it is possible to provide the absolute DTM heights h.

6.3.2. Results without snow

The processor has been assessed with some 20 days of GB-SAR C-Band interferometric imagery acquired in August 2005 in the Sion Valley test site. A high resolution DTM of the study area was available from the Swiss Federal Office of Topography, produced from an aerial survey with a state-of-the-art laser scanner [38]. The

ground-truth DTM pixel size was 0.84 m×0.84 m, while the height information had ±0.5 m accuracy.

Since the objective is to obtain a DTM with the best possible accuracy, results are measured against the standard deviation of the differences between the ground-truth DTM and those obtained with the GB-SAR in its topographic mode (one transmitting and two receiving antennas).

First of all, the standard deviation in meters of the DTM differences without the Δr calibration step is presented in Table 6.1. Results are presented for n = {1, 4, 8, 16, 32, 64 and 128} averaged interferograms using the formulation presented in Sections 6.2.1, 6.2.2 and 6.2.3. It is worth noting that at an acquisition rate of 12 minutes per image, n=128 corresponds approximately to the data acquired in a complete day, from 0h to 24h for example.

Table 6.1. Standard deviation of the DTM differences without Δr calibration

n	1	4	8	16	32	64	128
A	11.7	11.1	11.2	11.3	11.1	11.0	11.0
B	6.62	5.89	5.74	5.68	5.37	5.28	5.21
C	6.58	5.86	5.71	5.64	5.33	5.24	5.17

Note also that in Tables 6.1 and 6.2 the rows A, B and C stand respectively for the formulations presented in Sections 6.2.1, 6.2.2 and 6.2.3. Hereinafter these formulations will be referred directly as A (Taylor and r_2 approximation), B (Taylor approximation, exact r_2) and C (No Taylor approximation, exact r_2).

Examining Table 6.1, the following conclusions can be drawn:

a) The standard deviation is clearly reduced by increasing n. A 20% decrease is achieved when comparing n=1 to n=128 in B and C formulations.

b) The DTM accuracy obtained with the formulation C is higher than that with formulation B. Likewise, formulation B gives more accurate results than those obtained with formulation A.

c) The standard deviation values are on the order of 5-6 m, as reported in [32], [35] and [49] with similar sensor parameters, but different instruments and test areas.

Table 6.2, instead, shows the same results, but incorporating to the processor the Δr calibration step. The accuracy improvement is clearly observed in the column n=128. The standard deviation is reduced by 37% when compared to the results without Δr calibration (from 5.17 m to 3.28 m). In addition, it is observed that the formulation used has a minor impact on the DTM accuracy in this case.

Table 6.2. Standard deviation of the DTM differences after Δr calibration

n	1	4	8	16	32	64	128
A	5.68	5.03	4.53	4.33	4.06	3.98	3.84
B	5.33	4.64	4.09	3.86	3.55	3.41	3.28
C	5.34	4.65	4.10	3.86	3.55	3.41	3.28

Concerning the number of coherence images averaged, it has been observed that after n=128 the standard deviation tends to saturate or even slightly increase in the order of centimetres. For example, with Δr calibration using formulation B or C the following standard deviations are obtained: n=192 → 3.31 m; n=256 → 3.39 m; n=384 → 3.41 m. The saturation may indicate that the remaining height uncertainty comes from the radar instrument itself and does not depend on the measurement conditions. n=128 corresponds to a time window of about 1 day considering the acquisition rate of the LISA instrument reported in Table 4.1 (12 minutes per image approximately). Nevertheless, with the available data it is difficult to extract conclusions on whether the accuracy saturation is achieved after a given number of averaged samples or after a given temporal window regardless of the number of interferograms used for averaging. Different atmospheric conditions during the aperture synthesis itself could also be the cause of the slight increase in the DTM differences' standard deviation after n=128.

Similar experiments have been conducted to observe the behavior of the DTM differences as a function of the phase calibration step, but no relevant impact on this processor step has been observed. The reason for this result is the homogenous atmospheric conditions observed during the field experiments, with temperature gradients equal or less than 8 °C over a 24h period. Nevertheless, the phase calibration step has been kept in the processor summarized in the block diagram of Figure 6.2 for the sake of completeness.

Figure 6.4 shows the DTM differences in a map and histogram for the best case achieved with the presented processor: Δr calibration, n=128 and C formulation.

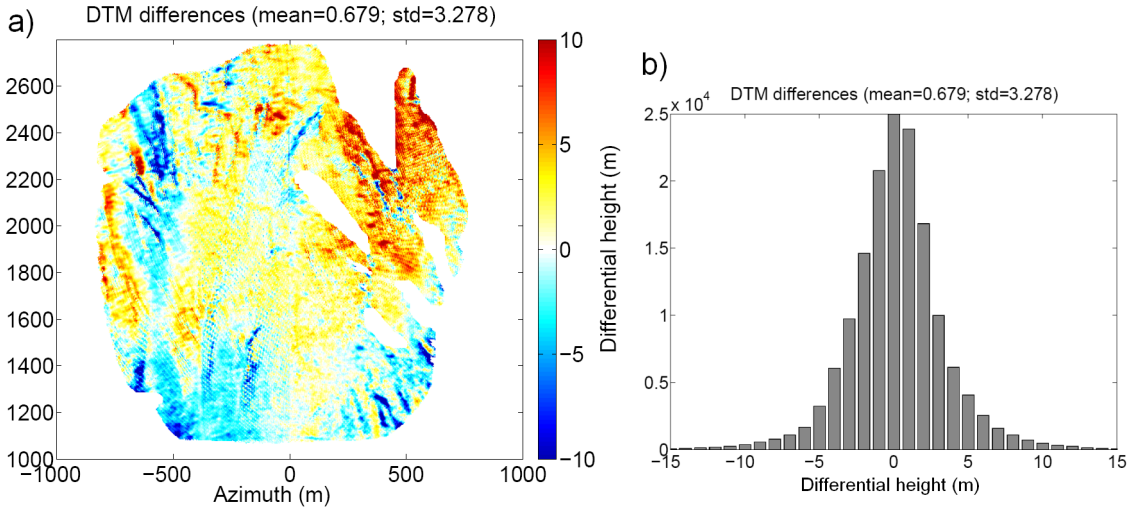

Fig. 6.4. DTM differences after Δr calibration for n=128 and using the C formulation. a) Masked map of the whole radar FOV; b) Corresponding histogram.

Figure 6.5 instead shows the DTM absolute heights map and the normals map of the Sion Valley test site obtained with the LISA instrument. Normals are defined as the angle subtended by the vector (x,y,z) = (0,0,1) and the vector normal to each facet of the DTM. Normals can be seen as a qualitative indicator of the interferometric DTM, since they show evident random values in the areas where interferograms are noisy.

Note that the results presented in Figures 6.4-a and 6.5 are masked out to discard noisy pixels (white background in the figures). The mask is computed with a double

criterion: backscattered intensity level and zero-baseline temporal coherence. Only pixels within 50 dB dynamic range of backscattered signal over a whole day and with zero-baseline (only one reception channel used) coherence values greater than 0.85 are selected.

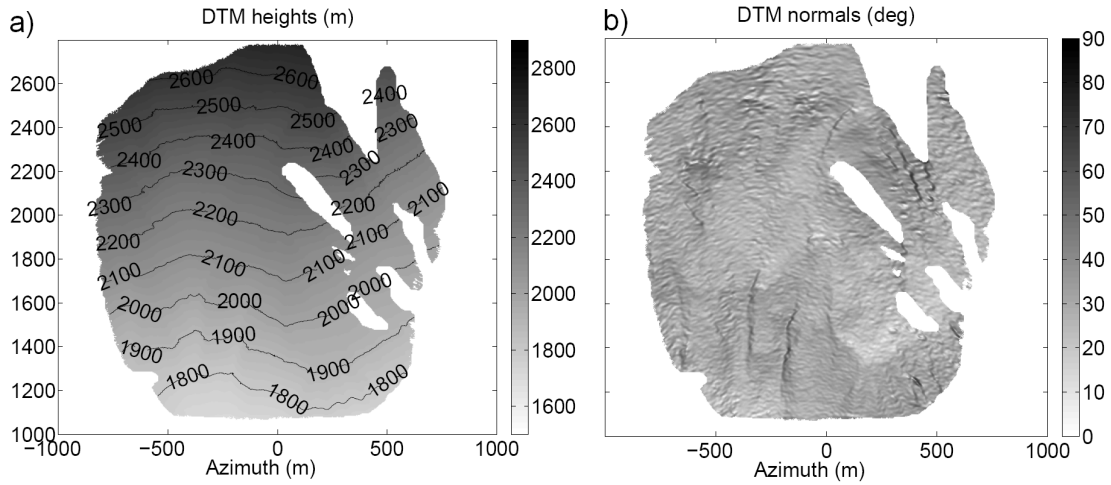

Fig. 6.5. a) DTM heights and b) DTM normals of the test site retrieved with the novel processor: n=128, Δr calibration and C formulation.

6.4. Snow avalanche volume retrieval

The feasibility of retrieving the volume of snow displaced in an avalanche by subtracting a DTM generated right before the avalanche from a DTM generated just after the avalanche event is studied in this section. As stated in the introductory section of this chapter, the only technique available at the moment with SAR to estimate the snow volume displaced by an avalanche is the subtraction of two consecutive DTMs.

First of all, some results of the application of this technique are presented for the test site of the Sion Valley. Unfortunately, the interferometric data available for the DTM generation in the test site of Alagna Valsesia have a single-pass coherence magnitude which is so low and noisy that it significantly reduces the accuracy of the generated DTMs and discards any practical use. The reason for this low coherence could be coupling effects of the second antenna in reception with the metallic structure of the instrument and/or higher sensitivity to atmospheric effects due to the higher frequency used in this site. Nevertheless, the reasons are not fully clear at the moment, so no results for the test site of Alagna Valsesia are presented. In view of the results obtained, in the second part of this section a sensitivity analysis is conducted on the DTM generation capabilities of GB-SAR sensors, particularizing the analysis to the sensor used in the Swiss test site of the Sion Valley.

6.4.1. Results with snow

To assess the feasibility of snow volume retrieval with the DTM subtraction technique before mentioned, a big natural avalanche is taken as an example. Figure 6.6

shows the repeat-pass coherence magnitude of an avalanche happening on December 30th, 2005, at 22.57h. The avalanche path can be appreciated as the low coherence vertically-oriented area in the mid-left side of the image, occupying an area of more than 300000 m^2 with a path length of 1800 m. Note that the low-coherence area on the bottom part of the image (range below 1000 m) corresponds to a forested area that presents an almost permanent temporal decorrelation, so it is not related to the avalanche event.

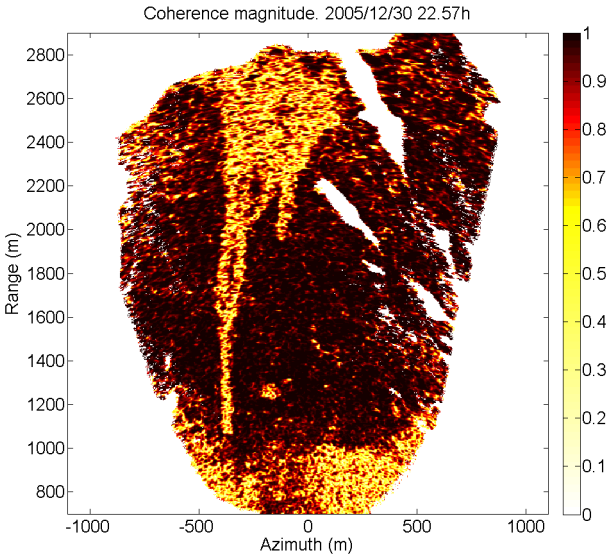

Fig. 6.6. Coherence image of a natural avalanche in the Sion Valley on December 30th, 2005, at 22.57h.

The topographic mapping processor presented in the preceding section is then used to compute a DTM right before and after the avalanche event. Figures 6.7 and 6.8 show the DTM differences corresponding to the instant of time at which the avalanche in Figure 6.6 is happening for different number of averaged coherence images n={1, 8, 32, 128}.

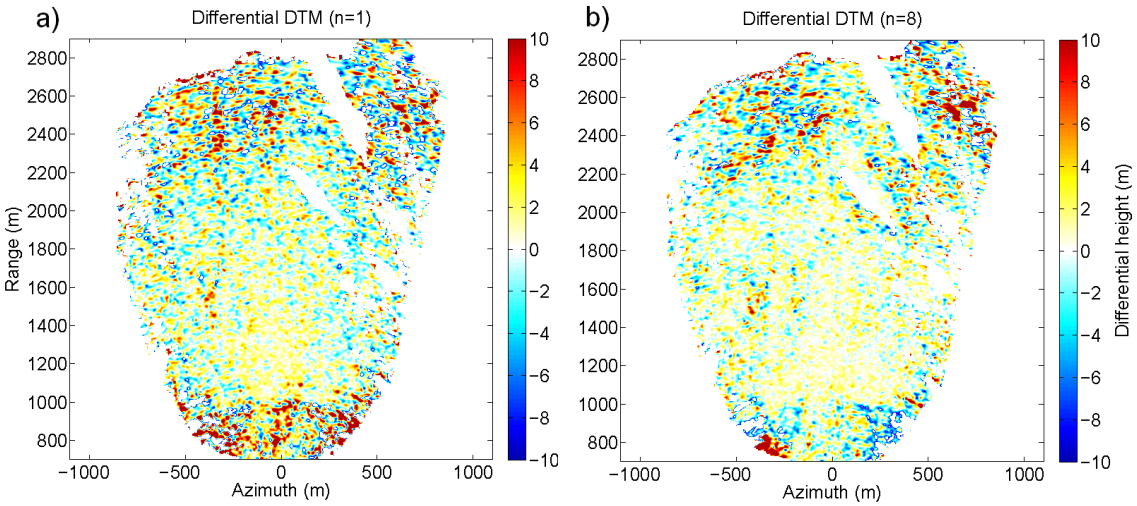

Fig. 6.7. Differential DTMs corresponding to the avalanche in Figure 6.6, scale in metres. a) n=1 image averaged; and b) n=8 images averaged.

The formulation in Section 6.2.3 and the Δr calibration have been used since it has been shown in the preceding section that this combination provides the most accurate results. Note also that, pivoting on the image of December 30th, 2005, at 22.57h, n backwards coherence images have been averaged to create the DTM before the avalanche event and n forwards coherence images have been averaged to create the DTM after the avalanche. The spatial averaging in the coherence computation (2.21) has been of 3×3 pixels for the results of Figures 6.6, 6.7, 6.8, 6.9 and 6.10.

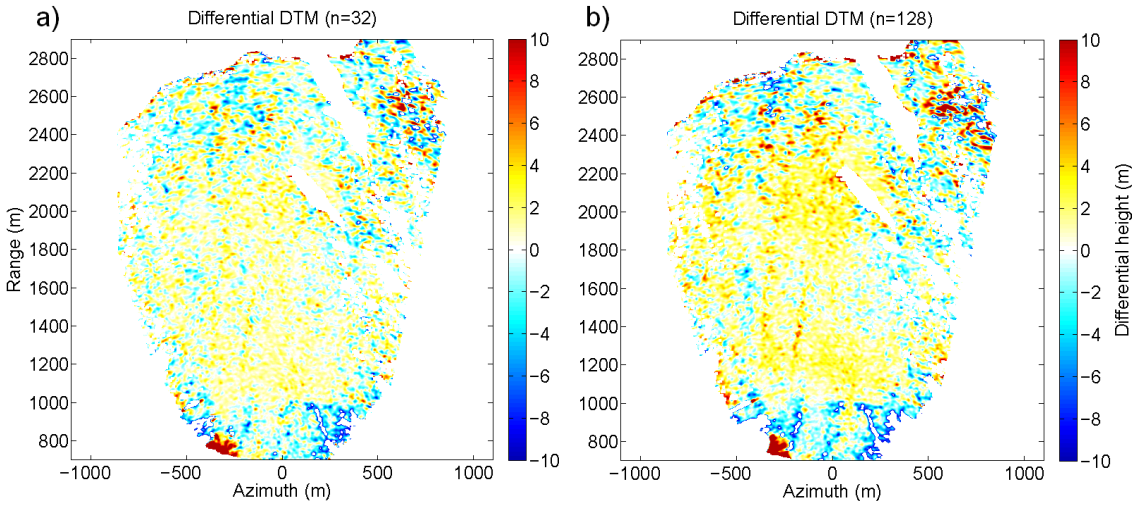

Fig. 6.8. Differential DTMs corresponding to the avalanche in Figure 6.6, scale in metres. a) n=32 images averaged; and b) n=128 images averaged.

Two fundamental facts are observed on the differential DTMs:

a) A very low or even inexistent contrast on the avalanche path, and

b) A decrease in the contrast as the number of averaged interferograms n increases.

The reason of the low contrast on the avalanche path is the accuracy of the order of 5 m of the GB-SAR used for the DTMs generation. Even with the accuracy improvement technique presented in the preceding section, the best achieved accuracy with the LISA instrument used in the Sion Valley test site is of the order of 3 m, while the snow displaced by an avalanche is expected to be in the range of several centimetres.

Figures 6.9 and 6.10 show the single-pass coherence magnitude corresponding to the instant of time at which the avalanche in Figure 6.6 is happening for different number of averaged coherence images n={1, 8, 32, 128}. Note that the colour scale ranges from 0.8 to 1. It is observed first of all that there is a high spatially averaged coherence, of the order of 0.95 or even higher. These values guarantee a highly accurate interferometric DTM (although always within the limits of the sensor). As an example, the typical single-pass coherence magnitude values observed in the test site of Alagna Valsesia were of the order of 0.6 and with a very noisy distribution. This evidences serious problems in the interferometric data and has motivated the exclusion of these results from the analysis performed in this section.

Regarding the decrease of contrast with an increasing number of averaged interferograms n, it needs to be considered that the novel processor presented in the

preceding section was initially tailored for a scene with a very low temporal decorrelation (free of snow and vegetation). High coherence over time allowed the averaging of different coherence images separated by a temporal baseline. It is important to note that for the calibration step of the image phase a reference point not covered by snow is required to be visible in the radar FOV. The lack of stable reference points on the radar FOV over time thus limits the use of the averaging technique proposed to increase the DTM accuracy. Other temporal decorrelation causes such as snow falling, snow drifting because of wind, snow melting and changes in the snow cover water content over the averaged period limit the extension of the temporal window in which the interferogram averaging technique is effective.

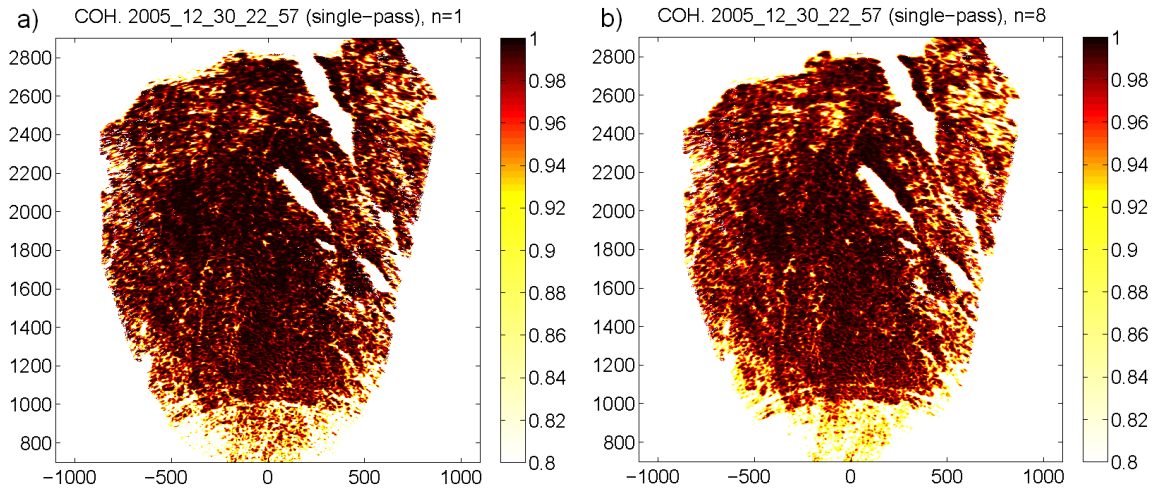

Fig. 6.9. Single-pass coherence corresponding to the avalanche in Figure 6.6. a) n=1 image averaged; and b) n=8 images averaged.

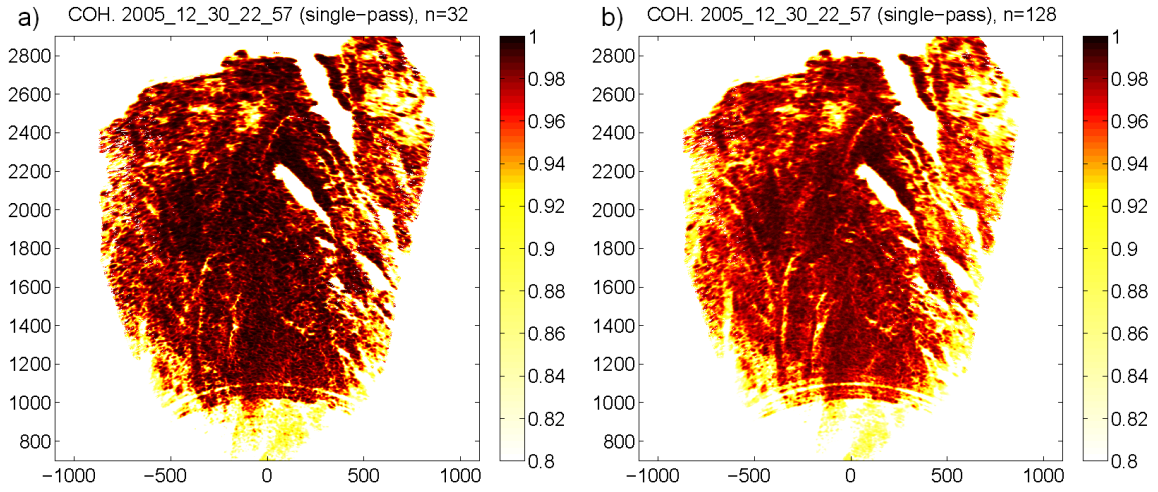

Fig. 6.10. Differential DTMs corresponding to the avalanche in Figure 6.6. a) n=32 images averaged; and b) n=128 images averaged.

Therefore, for the application of snow avalanche volume retrieval the number of averaged coherence images n not only does not improve the DTM accuracy, but slightly

degrades it because of temporal decorrelation inherent to the meteorological conditions of the test sites in winter time.

Keeping the temporal averaging to its minimum value, that is n=1, a spatial averaging can also be applied to improve the DTM accuracy by reducing the interferometric phase noise. This spatial averaging is implemented through the $\langle . \rangle$ operator in (2.21). Figure 6.7-a shows the differential DTM for n=1 and a spatial averaging of 3×3 pixels, while Figure 6.11 shows the same differential DTM for n=1 and a spatial averaging of 8×8 and 16×16 pixels.

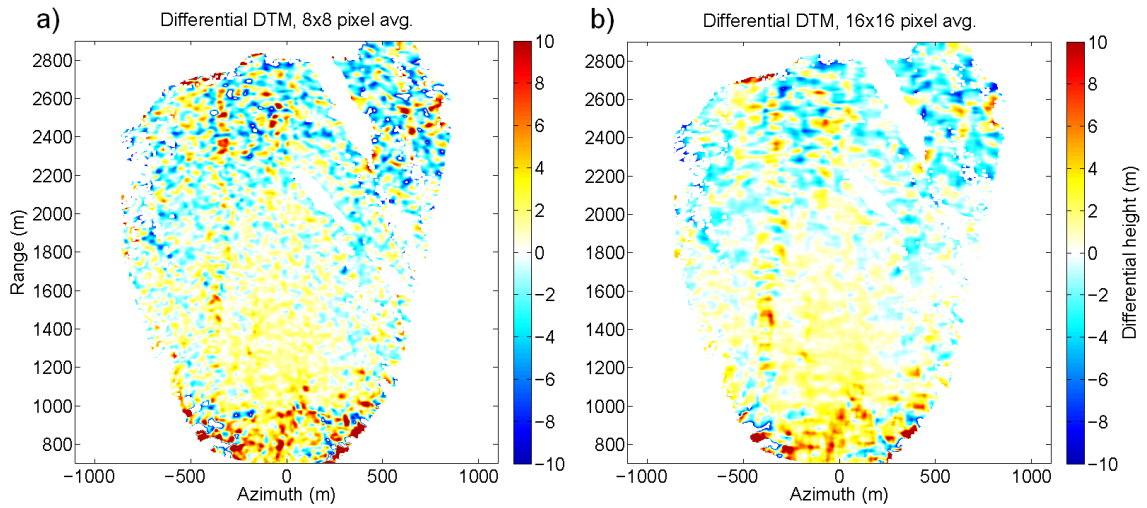

Fig. 6.11. Differential DTMs corresponding to the avalanche in Figure 6.6, n=1, scale in metres. a) Spatial averaging of 8×8 pixels; and b) Spatial averaging of 16×16 pixels.

The differential DTMs as a function of the spatial averaging show that the accuracy is not substantially changed; this is because the DTM accuracy with the LISA instrument used in the Sion Valley test site is in the order of metres while the expected snow variations are of the order of centimetres. The spatial averaging thus is neither a determinant solution for the improvement of the DTM resolution in view of the snow volume retrieval application.

Unfortunately, in the topographic mode the maximum accuracy has been found to be about 3 to 5 m and, therefore, differential DTMs cannot be used to retrieve the snow volume associated to an avalanche event. In addition, the snow cover as already explained in Section 5.2.2 of the preceding chapter introduces a propagation delay that mainly depends on the snow cover depth, the real part of the snow permittivity and the incidence angle. The high penetration depth into the snow cover of microwaves in the C-band, makes the instantaneous interferograms very insensitive to snow cover changes under dry snow conditions. As a consequence, the differentiation of instantaneous interferograms is also very insensitive to snow depth variations, as can be appreciated in Figure 6.12-b.

Figure 6.12 illustrates the before mentioned low sensitivity. The interferometric phase and differential interferometric phase are presented directly in radians instead of converting them into vertical heights. Note that the differential heights presented in Figures 6.7, 6.8 and 6.11 are computed with the formulation developed in the preceding section for snow-free areas, so the heights derived this way are artificial and do not correspond to real snow depth variations but to qualitative indicators of changes in the snow cover.

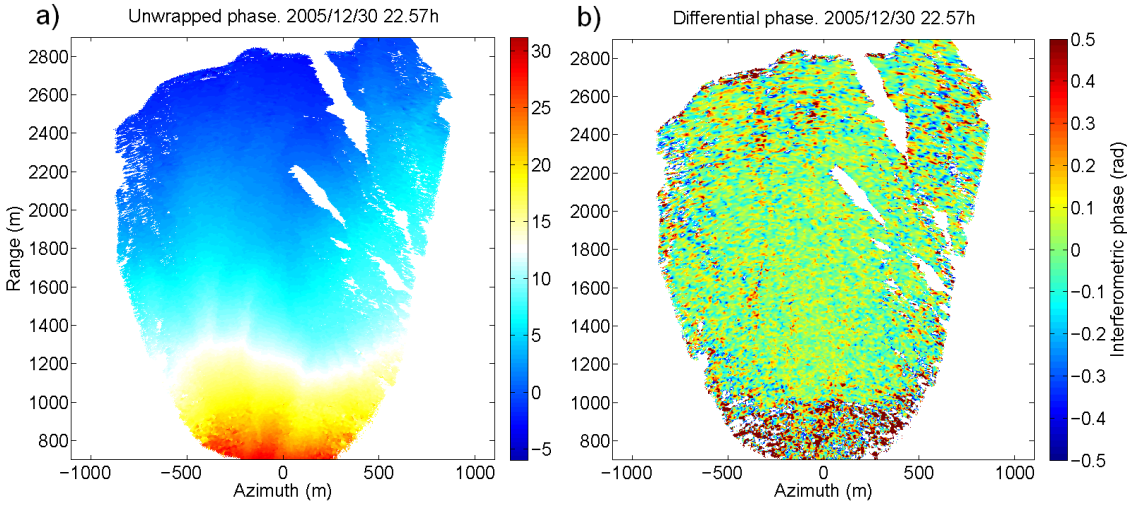

Fig. 6.12. Interferometric phase corresponding to the avalanche in Figure 6.6, n=1, 3×3 pixels spatial averaging, scale in radians. a) Single-pass topographic mode; and b) Differential phase.

The instantaneous interferogram right after the avalanche event, once unwrapped, can be observed in Figure 6.12-a. A very similar interferogram is obtained for the instant of time right before the avalanche event. On the other side, Figure 6.12-b presents the differential phase obtained by subtracting the interferometric phase right before and after the avalanche event. Similarly to that which was observed in the differential (artificial) heights maps, the avalanche event has a very tiny contrast in the differential phase map, and it is even masked by the phase noise present over the whole image. Under these conditions, hence, the application of snow avalanche volume retrieval by DTM subtraction with GB-SAR is not possible.

6.4.2. Sensitivity analysis

The precision of the interferometric DTM depends on the phase noise, the radar wavelength and the precision with which the baseline components and the antennas' height are measured. Even if the topographic height in (6.17) is a function of the kind $h = h(B_h, B_v, H, \Delta\varphi, \lambda, r_1, \theta)$, the last two variables, that is range r_1 and azimuthal angular position θ, are not actually measured by the operator. In fact, when focusing a SAR image a rectangular grid is created as a function of r_1 and θ and it is used to enter the raw data matrix. Similarly, the stability of the wavelength λ depends on the instrument's clock and its measurement can have a small error that can also be neglected in this analysis. Regarding the baseline components B_h and B_v, the Δr calibration with one ground control point introduced in Section 6.3.1 minimizes the error propagation because of inaccuracies in the measurement of these parameters.

Modelling the errors as independent random variables and summing the variances of the relevant contributions, the standard deviation σ_h of the topographic height remains:

$$\sigma_h = \sqrt{\left(\frac{\partial h}{\partial H}\sigma_H\right)^2 + \left(\frac{\partial h}{\partial \Delta\varphi}\sigma_\varphi\right)^2}. \tag{6.20}$$

where σ_H and σ_φ are the standard deviations of the absolute height and phase, respectively.

Concentrating on the formulation given in Section 6.2.3 (No Taylor approximation, exact r_2) which is the one providing the most accurate results, differentiation of (6.2), (6.13) and (6.17) yields the partial derivatives in (6.20) [60]:

$$\frac{\partial h}{\partial H} = 1, \tag{6.21}$$

$$\frac{\partial h}{\partial \Delta\varphi} = \frac{\lambda r_1}{2\pi B}\left[\sin\omega - \cos\omega \tan(\omega - \theta_n)\right]. \tag{6.22}$$

According to (6.21), a measurement error in the quantity H is directly translated into the same error magnitude in the topographic height h. Considering current GPS processing techniques, using geodetic receivers, a good network for adjustment and long-period (4 to 8 hours) data acquisition, accuracies of the order of a few centimetres can be achieved for absolute height measurements with such technology [61]. Nevertheless, for differential height measurements such as those required in the volume retrieval of snow avalanches, centimetre scale accuracies can be easily achieved with simple in-situ measurements with a metric tape or even with a domestic GPS receiver. Therefore, the error on the absolute height H determination has a minor impact on the standard deviation σ_h of the topographic height regarding the application of snow volume retrieval.

More relevant in the sensitivity analysis is, instead, the error on the interferometric phase $\Delta\varphi$, that is, the phase noise. Equations (6.20) and (6.22) suggest that optimization of system performance is achieved through minimization of phase error, wavelength and slant range and maximization of baseline.

Regarding the minimization of phase error, either temporal or spatial averaging techniques have already been attempted in Section 6.4.1, but in both cases the accuracies obtained (of the order of metres) are well below those required for snow avalanche volume retrieval (in the order of centimetres). Considering the above mentioned discussion regarding the relevance of a measurement error on H, the standard deviation σ_h of the topographic height can be approximated as follows:

$$\sigma_h = \frac{\lambda r_1}{2\pi B}\left[\sin\omega - \cos\omega \tan(\omega - \theta_n)\right]\sigma_\varphi. \tag{6.23}$$

Since the spatial averaging in (2.21) is implemented as a two-dimensional convolution with an $ns \times ns$ square matrix with all coefficients to one, the coherence images obtained can be considered multi-look, and in particular $ns \times ns$-look. For an averaged coherence magnitude of 0.95 (as it can be appreciated in Figure 6.9-a), the phase difference standard deviation is 0.100 rad in a 9-look interferogram and 0.075 rad in a 16-look interferogram [62]. Note also that these phase difference standard deviations (0.100 and 0.075 rad) are in line with the phase noise observed in Figure 6.12-b.

Considering the sensor parameters used in the test campaign of the Sion Valley and reported in Table 4.1, the DTM heights' sensitivity (σ_h in meters) to phase noise can be seen in Figure 6.13 for a 9-look and 16-look interferogram according to (6.23). The values obtained, in the range of 3 to 5 m, are in line to those reported in [53] and in Section 6.3.2. In addition, these results evidence that the limiting factor on the accuracy of the LISA

instrument in the Sion Valley test site under the current sensor parameters is the phase noise inherent in the single-pass interferograms.

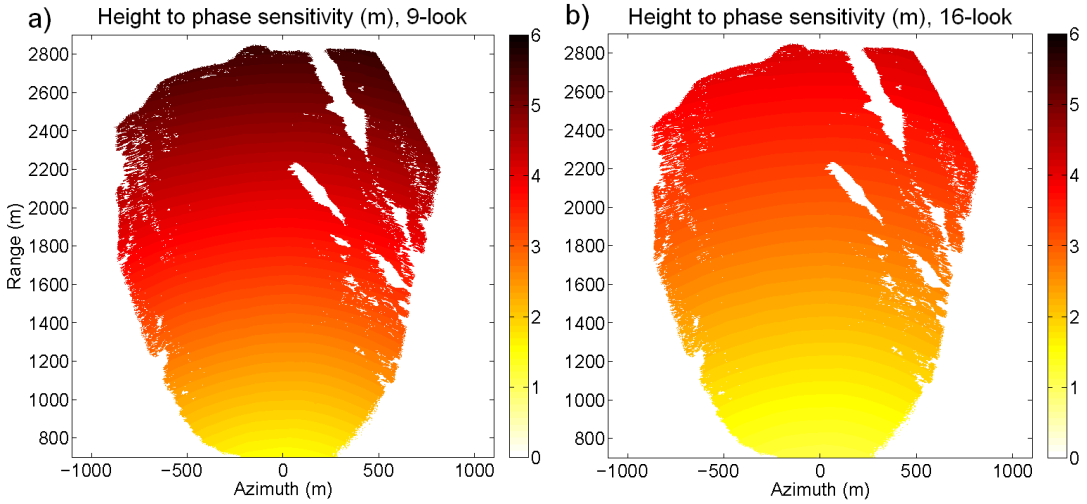

Fig. 6.13. Height sensitivity to phase noise considering a) coherence magnitude of 0.95 with 3×3-look interferogram; and b) coherence magnitude of 0.95 with 4×4-look interferogram.

Regarding the maximization of the baseline in order to optimize the system performance, it needs to be considered that the spatial baseline decorrelaion due to the Van Cittert-Zernike theorem increases also with increasing the baseline distance [63]. A critical baseline exists where the radar echoes are no longer correlated and the effective signal to noise ratio is zero. Thus, there exists an optimum baseline distance that minimizes the total height error, that is in the range of 0.2 - 0.8 of the critical value. The critical baseline perpendicular to the line of sight, B_{crit}, may be expressed as [64]:

$$B_{crit} = \frac{\lambda r_1}{\Delta R} \tan(\theta_n - \zeta), \tag{6.24}$$

where ζ is the averaged topographic slope and ΔR the resolution in range direction.

According to the sensor parameters in Table 4.1 for the LISA instrument in Sion and considering that the averaged topographic slope is $\zeta = 27$ deg, the critical baseline B_{crit} ranges from 25 m to 425 m for the Sion Valley test site. This distance is far from any baseline feasible with GB-SAR sensors. Considering the more favourable case, that is, a critical baseline of 25 m and a baseline distance 0.2 times that critical, the resulting optimum baseline for the test site of the Sion Valley would be of 5 m, also of difficult implementation in an operational instrument.

Considering the sensor parameters of the Sion Valley test site and assuming a central point on the radar FOV ($r = 1800$ m, $\theta = 0$ deg), the height to phase sensitivity σ_h is plotted in Figure 6.14 as a function of the vertical baseline component B_v according to (6.23). 9-look and 16-look interferograms are assumed, so a phase noise of $\sigma_\varphi = 0.100$ rad and $\sigma_\varphi = 0.075$ rad respectively is considered under the assumption of a coherence magnitude of 0.95 [62]. Note that in order to better appreciate the heights' standard deviation, two plots have been produced, the first one (Figure 6.14-a) for short baselines

ranging from 0.1 to 10 m, and the second one (Figure 6.14-b) for longer baselines ranging from 10 to 100 m.

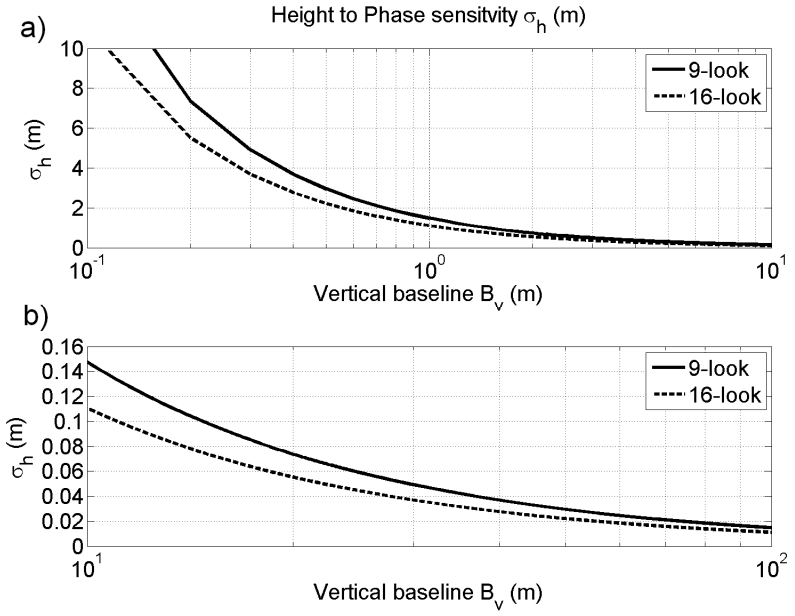

Fig. 6.14. Height sensitivity to phase noise as a function of the vertical baseline B_v, considering a central point on the radar FOV.

Regarding the Figure 6.14-a, it can be observed that for the vertical baseline of the LISA instrument in its configuration when monitoring the Sion Valley (40 cm), the standard deviation of the heights error is of the order of 3-4 m. This result is in line with the accuracy obtained for the novel topographic processor presented in Section 6.3. It has been shown that the accuracy on the height determination reaches a saturation point from 128 averages onwards that is approximately 3.28 m in 9-look interferograms. The accuracy of the novel processor due to the interferogram averaging process is, actually, very similar to the theoretical accuracy obtained considering the phase noise related to the coherence magnitude of a given interferogram. As already pointed out in Section 6.3.2 the remaining accuracy after the averaging process could come from the radar instrument itself and does not depend on the measurement conditions, so the only way to improve this accuracy would be by increasing the vertical baseline.

Regarding the results in Figure 6.14-b, first of all it can be seen that little practical differences exist between 9- and 16-look interferograms. In second place, for the application of snow avalanche volume retrieval where accuracies of the order of centimetres (e.g., 10 cm) are required, the necessary vertical baseline length is 10.5 m for 9-look interferograms and of 10.0 m for 16-look interferograms. As already stated above, these baselines would be difficult to implement in operational instruments, so the application of snow avalanche volume retrieval by DTM subtraction with GB-SAR is not feasible at the moment.

6.5. Conclusions

In the first part of this chapter a novel processor has been presented for the improved generation of a DTM using C-Band GB-SAR imagery and fully exploiting its high image acquisition rate to increase the DTM accuracy. The novel steps of the processor are evidenced in Figure 6.2 by dashed boxes. They are: the phase calibration of the whole image with a reference point; the temporal averaging of interferograms; and the differential path calibration with a reference point. Results on a snow-free area show how averaging over a whole day reduces the standard deviation of the DTM differences by 20%, while an additional reduction of 37% is achieved when calibrating Δr to a single ground reference point. In this last situation, the formulation used has a minor impact on the DTM accuracy.

In the second part of this chapter, the topographic processor previously developed is used to infer the snow volume displaced by an avalanche. Preliminary results show that the vertical accuracy obtained with the GB-SAR sensor in its current configuration is not high enough for the application of snow avalanche volume retrieval, where accuracies of the order of a few centimetres are required. Neither temporal nor spatial averaging help increase the DTM accuracy to the centimetre range. In addition, the low sensitivity of the single-pass interferometric phase to snow cover changes at C-band causes avalanches to be masked by phase noise.

A sensitivity analysis has been carried out, showing that the limiting factor on the accuracy of the LISA instrument in the Sion Valley test site under the current sensor parameters is the phase noise inherent in the single-pass interferograms. Finally, the optimal vertical baseline for the application of snow volume retrieval after avalanche events is computed. Results show that the required baseline is difficult to implement in operational GB-SAR instruments, so the technique of snow volume retrieval by GB-SAR remains an experimental activity where more research is necessary. Since the implementation of a vertical baseline of the order of some metres is complex, the combination of two radar units vertically separated some tens of meters appears to be the most promising solution for this application using GB-SAR technology.

7. Snow avalanche detection and classification

7.1. Introduction and state of the art

This chapter studies the feasibility of monitoring the avalanche activity of a local area of a few square kilometres by means of GB-SAR coherence images. This is the third monitoring technique of the snow cover presented in this PhD thesis.

The continuous monitoring of critical slopes where a snow avalanche can put at risk the skiers or the installations, buildings or roads in the surroundings is of interest to the ski resorts' administrators and the Civil Protection services [12]. The all weather conditions, non-invasive solution and imaging capability of SAR technology make it particularly suitable for such kind of monitoring, overcoming some of the problems of the classical methods based on force measurements [13], visual imagery, Doppler radar [13] or geophones [21].

Even if avalanche forecasting is not possible at the moment, it has been demonstrated that avalanches can be detected with GB-SAR interferometry immediately after they occur [65]. An automatic alert of the avalanche is useful even if the alarm arrives within the first 5-10 minutes after the event: entry of the public into the affected area can be prevented, for example by turning red a traffic light or closing an automatic barrier. Concerning ski resorts, a daily report of the avalanche events monitored during the night is of high utility to artificially trigger potentially dangerous accumulations of snow. This would minimize the necessity of sending an expert to visually assess the state of the snow in-situ.

Compared to classical sensors, the proposed technique presents several potential advantages. The principal one is related to the imaging capability of GB-SAR, which allows covering areas of a few square kilometres with a single instrument remotely deployed in a safe and relatively easy accessible location. Compared to optical sensors, GB-SAR has the advantage of being very robust against adverse weather and poor visibility conditions. Compared to Doppler radar, the imaging radar allows the reduction of false alarms due to the availability of 2-D information that facilitates the interpretation of the results.

To date very little attention has been paid to local monitoring of the snow cover with imaging radars due to the long re-visit times (typically of several days). The main introductory chapter of this PhD thesis (Section 1.1) reviews some of the works more relevant in the field of microwave snow monitoring, where it can be seen that satellite-borne sensors are mainly used to produce seasonal maps of snow covered areas and

sometimes of snow water equivalent (SWE) estimates. No literature has been found on the use of space-borne SAR to monitor the avalanche activity. Only in [66] a preliminary study is presented to validate the potential of snow avalanche identification by SAR backscatter images in a similar way as it is done with oil spills over the sea [67][68]. Nevertheless, other than validating with an example the simplified forward model in which a higher backscatter in the avalanche area is generally expected, this study cannot conclude with any specific technique since the lack of proper images difficulties a comprehensive study.

The data archive of GB-SAR images obtained with the two field campaigns described in Chapter 4, instead, allows for the first time to tackle the problem of snow avalanche identification [69][70]. The processor presented in this chapter represents the first reported attempt to systematically assess thousands of GB-SAR images in order to produce a robust detection and classification scheme for snow avalanches. Although there is no literature on the specific subject, substantial similarities have been found with the problem of oil slick detection in SAR imagery, so a similar approach has been taken regarding the architecture of the processor [67][68]. Nevertheless, specific problems arise with the use of a ground-based sensor and the monitoring of areas with high variability of weather conditions. The need for a fast algorithm able to continuously produce results at the acquisition rate of the sensor (in the order of 12 minutes per image) and the need to discriminate between avalanches and look-alikes caused by snow falling, snow melting, strong wind or dense fog are some of the issues studied in this chapter.

7.2. Identification principles

Avalanche signatures in SAR images can be identified from the backscattered signal according to a simplified forward model in which a higher backscatter in the avalanche area is generally expected [66]. Nevertheless, as for oil slicks on the sea [67][68], this approach depends very much on the snow conditions surrounding the avalanche cone area so the backscatter image does not appear to be a robust indicator of avalanche. Instead, since avalanches represent a significant physical change of the affected area, they result in a temporal decorrelation. The degree of correlation between two complex SAR images can be measured and is called coherence. Considering the subscript n a index for time, given a pair of complex images im_{n-1} and im_n acquired right before ($t_{n\text{-}1}$) and after (t_n) the avalanche, the complex coherence γ_n is defined as [28]:

$$\gamma_n = \frac{\left\langle im_{n-1} \cdot im_n^* \right\rangle}{\sqrt{\left\langle |im_{n-1}|^2 \right\rangle \left\langle |im_n|^2 \right\rangle}}, \tag{7.1}$$

where $\langle . \rangle$ is the spatial averaging operator. Note that a similar definition of the complex coherence at pixel scale was already used in (2.21).

From the complex coherence, avalanches can be detected either using the interferometric phase or the coherence magnitude (hereinafter called simply coherence, $coh_n = |\gamma_n|$). A study on snow height retrieval from the interferometric phase was already presented in Chapter 5 and can also be found in [18], and this principle could be used for avalanche detection. Nevertheless, taking advantage of the imaging capabilities of a SAR sensor, avalanches can be also recognized by a random interferometric phase as shown in

Figure 7.1-a. For our processor, instead, it was preferred to use the coherence magnitude (Figure 7.1-b), since it is much less sensitive to external decorrelation sources (e.g. vegetation) than the interferometric phase.

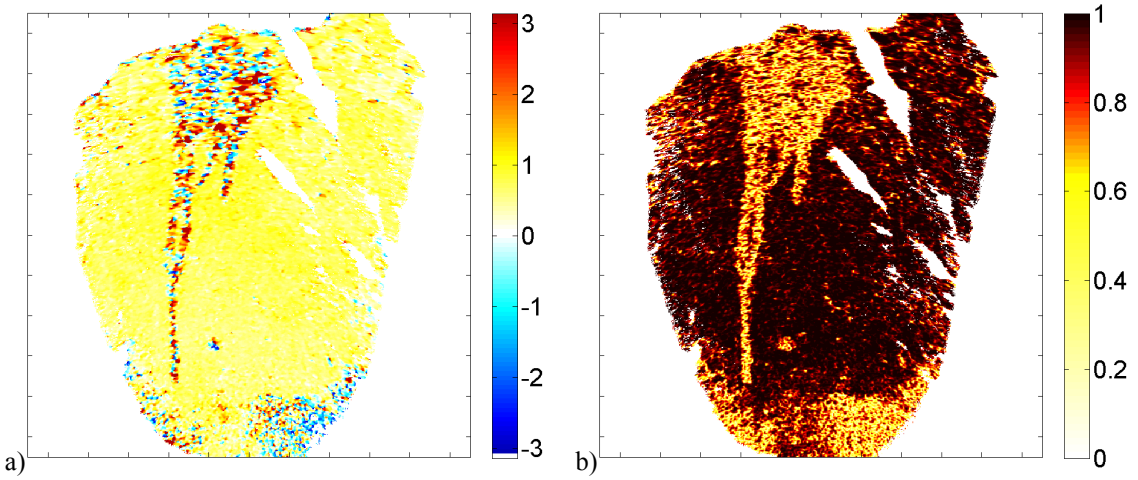

Fig. 7.1. Avalanche signature at C-band in a) interferometric phase (unwrapped) image, ranging from $-\pi$ to $+\pi$ rad; and b) coherence image, ranging from 0 (white pixels) to 1 (dark pixels).

7.2.1. Other sources of decorrelation

Unfortunately, several external causes may lead to coherence decorrelation other than avalanches themselves.

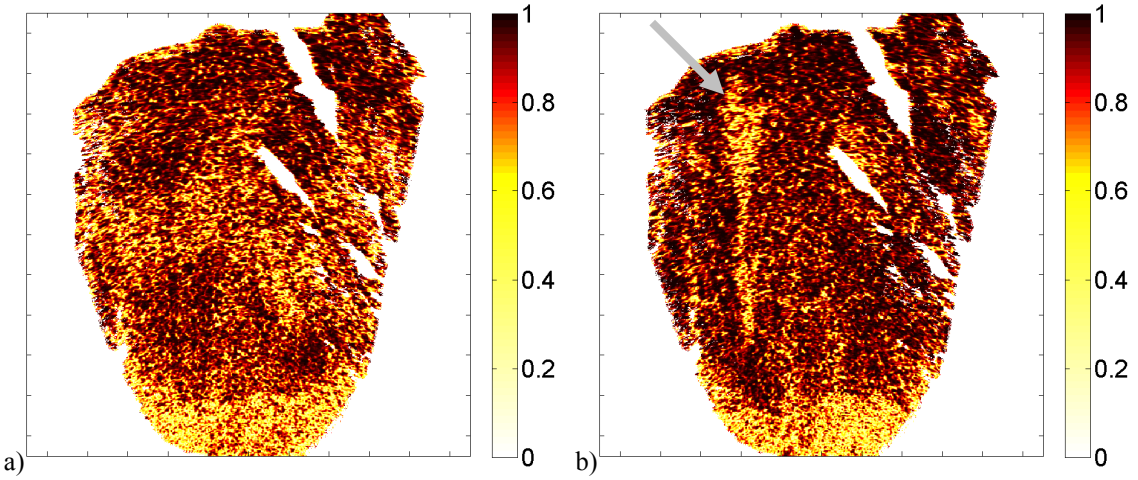

Fig. 7.2. a) Noisy coherence image at C-band because of heavy snow fall; and b) avalanche signalled with a grey arrow in a noisy coherence image.

The main sources for decorrelation appear to be related to weather conditions changing the physical properties of the snow cover itself: heavy snow fall, snow melting, or strong wind causing snow drifts, to cite the most important ones. Figure 7.2 shows a couple of examples corresponding to the Sion Valley on 2005/12/31, when a snow fall

deposited 30 cm of snow during the day. In both examples as well as in Figure 7.1-b the bottom part of the images suffers from low coherence due to the presence of a forested area where even tiny winds cause high decorrelation. This area in fact is masked out when looking for avalanches in the processor. Returning to Figure 7.2-a, a generalized low coherence of the order of 0.5 is discernible in the whole image, while in Figure 7.2-b a snow avalanche is observed starting from the grey arrow, but overlapped to a background clearly more noisy than that observed in Figure 7.1-b.

Perturbations in the atmospheric propagation of the radar signal may also be a source of decorrelation [48]. Regarding atmospheric effects, a compensation method particularly tailored for radar images that lack highly coherent reference points has already been presented in Section 5.3.2. It has also been found in Section 5.4.3 that atmospheric effects have a minimal impact on the images acquired by the LISA instrument in both test sites. The phase stability is guaranteed in the LISA instrument by using commercial VNAs for the radar implementation and by sliding the vector network analyzer together with the RF cables and antennas along the linear rail. This last characteristic of the instrument, already described in Section 3.1.1, makes possible the use of shorter RF cables and avoids the possible bending of cables when synthesizing the linear aperture.

Special attention must be paid to the selection of the radar central frequency, bandwidth and aperture length, since they have a relevant role on the number of artifacts present in the resulting imagery. The parameters used in the Sion test site (Table 4.1) were found more suitable for the application of avalanche identification than those used in the Alagna ski resort (Table 4.3). This fact is pointed out in the analysis performed in Section 7.5.2, although it is worth noting that the sensor parameters play only a second order relevance in the results achieved in each test site. The sensor parameters used in both test sites are, hence, perfectly suited for the application of snow cover monitoring and avalanche identification.

7.2.2. Contrast enhancement

Figure 7.2 shows a clear example of how a human interpreter can be able to discriminate between an avalanche signature and an otherwise decorrelated image. This indicates that the coherence alone may not be sufficient for an automatic process to properly distinguish avalanches. For this reason the differential coherence dco_n was used in the proposed processor:

$$dco_n = m \cdot \left| \langle coh_{n-1} \rangle - \langle coh_n \rangle \right|. \tag{7.2}$$

The factor m is introduced as a function of the coherence values normally observed in the test site in order to maximize the dynamic range of dco_n. Since in practice the coherence images coh_n ranged from 0.5 to 1.0 in both test sites, $m = 2 \times 255$ was used to code the dco_n images into greyscale images of 256 levels. Representing each pixel by an unsigned integer of 1 byte, higher values of dco_n are truncated to 255.

Figure 7.3 shows the propagation of an avalanche signature happening between the instants of time t_{n+2} and t_{n+3}. Note that $\Delta t = t_{n+3} - t_{n+2}$ approximates to 12 minutes according to Tables 4.1 and 4.3. Since avalanches are relatively fast events with a sudden decrease in the coherence, after t_{n+3} the snow cover will reach a stable situation and the coherence

images from coh_{n+4} onwards will no longer show the avalanche signature. Bad weather conditions are, instead, typically slow events that cause a progressive reduction of the coherence. The differential coherence, thus, will tend to cancel out the decorrelation because of bad weather conditions present in successive coherence images.

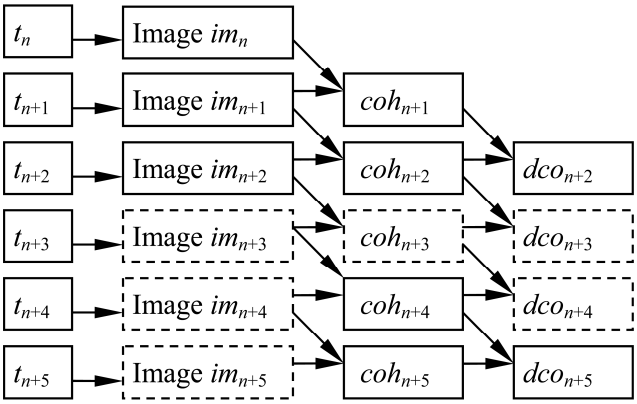

Fig. 7.3. Avalanche signature propagation. Dashed boxes contain the signature of an avalanche happening between the instants of time t_{n+2} and t_{n+3}.

This is possible thanks to the spatial averaging $\langle . \rangle$ introduced in (7.2). Since decorrelation affects coh_n at pixel scale, the direct subtraction of coherence images would lead to an equally noisy image. Spatial averaging, instead, reduces the randomness of the decorrelation and provides a cleaner differential coherence image. This operation has been implemented with a constant square window of 10×10 pixels.

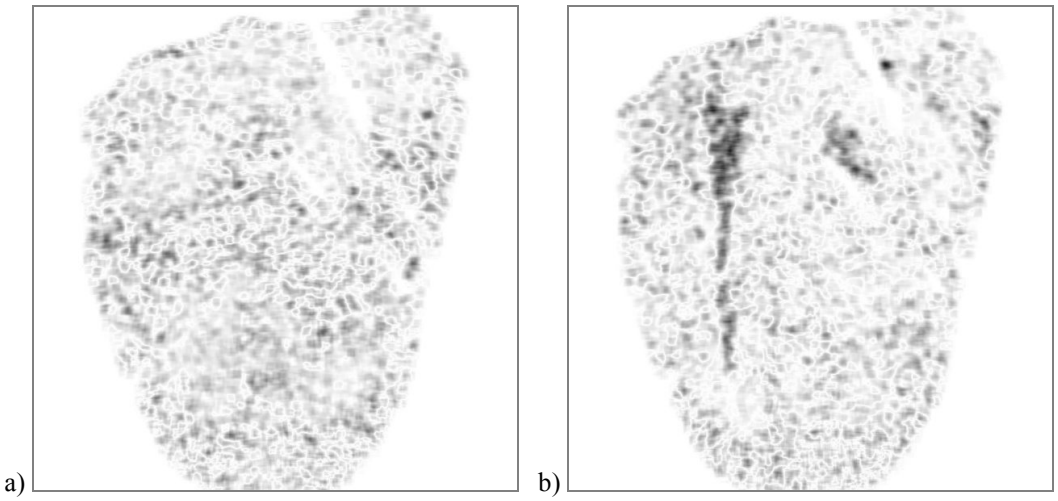

Fig. 7.4. Differential coherence images corresponding to the scenes in Figure 7.2.

The contrast enhancement result for the scenes in Figure 7.2 can be observed in Figure 7.4. Although a noisy background is still present in the images, the avalanche can be better appreciated in Figure 7.4-b than in Figure 7.2-b.

7.2.3. Avalanche identification processor

Figure 7.5 shows a block diagram of the processor, where subscripts *n* denote instant of time. Starting from the raw data acquired by the sensor in the frequency domain, this data is focused to form a complex image im_n with any of the algorithms presented in Section 2.3. Next, the coherence images are computed and filtered out by a mask, taking into consideration only those pixels within a 50 dB dynamic range of the backscattered signal and with coherence values over 0.75 under good weather conditions. Note that the mask is computed only once for a given test site, and then reused for all successive acquisitions.

The differential coherence is then computed according to (7.2) and coded into a greyscale image of 256 levels represented by integer values. Lower values of dco_n correspond to the background (white pixels in Figure 7.4), while spots are represented by higher values and correspond to possible avalanche events to detect and classify (black pixels in Figure 7.4).

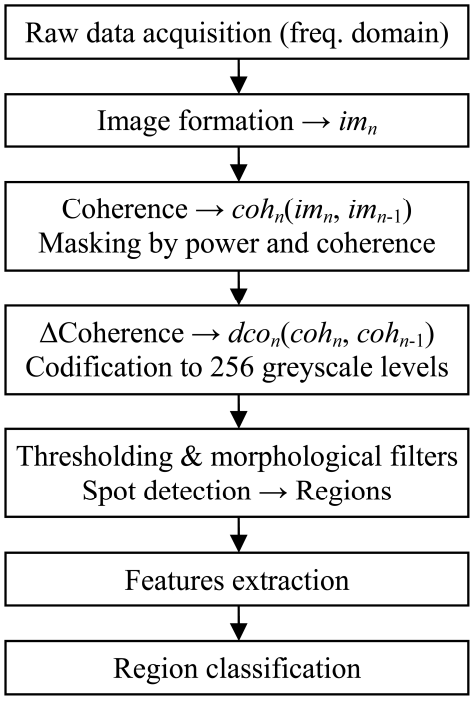

Fig. 7.5. Block diagram of the GB-SAR processor for snow avalanche detection and classification.

The rest of blocks in the processor are explained in more detail in the two sections following.

7.3. Segmentation block

Several algorithms for the detection of dark spots have been proposed for the problem of oil slick detection [67]. Wavelet decomposition, edge detection, mathematical morphology filters and adaptive thresholding appear to be the most successful. Nevertheless, since a ground-based sensor typically acquires data from a fixed position and

avalanches follow a downwards direction, SAR images for avalanche identification benefit from a predictable geometry of the scene and of the backscattered signal not available in satellite images for oil slick detection. These reasons have led us to select a simple solution based on the combination of thresholding plus morphological filtering with dilation and erosion for the segmentation block of the algorithm.

7.3.1. Thresholding

A median filter of the dco_n images followed by a single-scale adaptive threshold based on Otsu's method [71] was initially implemented. Results reported in Section 7.5 (Table 7.4) show poor performance using this solution, so a threshold based on the typical values of differential coherence observed for each test site was used instead.

Unfortunately, very extreme bad weather conditions pose a problem to the fixed threshold solution because under these circumstances the whole image is usually selected as a single region for avalanche classification. A manual observation of these scenes reveals that even a well trained operator cannot distinguish any avalanche, so these images become useless from an operational point of view and, thus, it was decided to automate the option not to process them.

This option is implemented through a parameter called in this PhD thesis differential ratio ($DcRt_n$) and is defined as the mean value of dco_n divided by the Otsu's threshold associated to that differential coherence image. Images with a differential ratio higher than a given threshold –they present a dark background that results in a high mean value– are discarded. Since real avalanches may occupy a substantial portion of the image, their signature contributes also to increase the mean value of the image. In order to avoid missing such avalanche events the mean value is weighted by a function that presents also high values when a dark spot is clearly defined in the image. This weighting function can be any one based on a histogram dichotomization of background and foreground pixels, as for example Otsu's thresholding method [71].

7.3.2. Morphological filtering

Figure 7.6-a shows the binary image corresponding to Figure 7.4-b after the thresholding process (a threshold of 100/255 has been applied). Morphological filters are then applied in order to discard small spots and connect sparse ones that may appertain to the same avalanche signature. An initial erosion filter followed by a dilation one with the same window size of 6×6 pixels cancels small spots while keeping the original size of the remaining spots ([72], pp.158-205) as can be seen in Figure 7.6-b.

Finally, taking advantage of the vertical shape of avalanche signatures in GB-SAR imagery, a dilation filter with a narrow vertical-oriented rectangular window (2×40 pixels in both test sites) is applied in order to interconnect sparse spots belonging to the same vertical region. The result can be observed in Figure 7.7, which is the input for the features extraction and classification blocks of the processor.

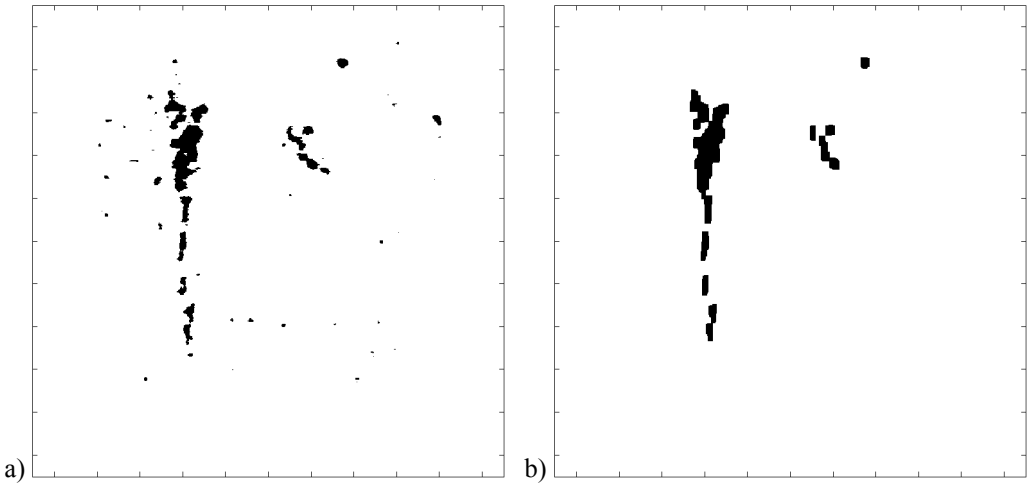

Fig. 7.6. Result of a) thresholding process of 100/255; and b) morphological filtering to discard small spots.

The vertically-oriented rectangular window size is chosen such its length is approximately one third of the maximum axis length allowed for regions to be classified as avalanches (parameter *AxLen* in Table 7.1). According to Table 4.1 the vertical resolution in the Sion site is of 2200/601 m/pixel, so one third of 500 m corresponds approximately to 45 pixels. According to Table 4.3 the vertical resolution in the Alagna site is of 800/641 m/pixel, so one third of 150 m corresponds approximately to 40 pixels. A window of 2×40 pixels (horizontal × vertical) has been chosen as a good compromise for both test sites, which seems a reasonable choice when the zero-cross-range image orientation is close to that of the steepest descent direction of the slope.

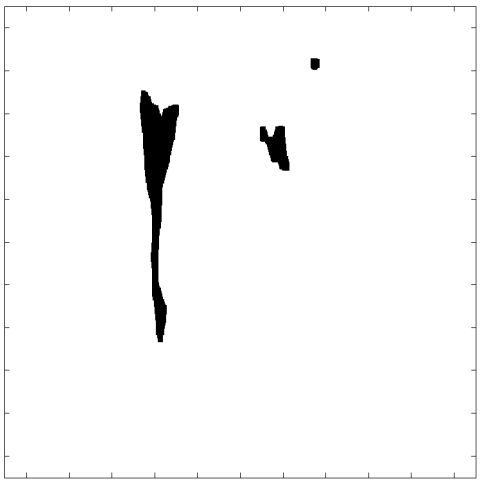

Fig. 7.7. Result of the vertical-oriented dilation filter to combine common spots associated with a possible avalanche.

7.4. Classification block

After the segmentation block, a set of features is computed for each region of interest in the resulting image in order to classify or not the regions as avalanches. Table

7.1 shows the features used for avalanche identification and the values employed at each test site.

Table 7.1. Segmentation and classification parameters

Parameter	Symbol	Sion	Alagna
Threshold	*Thresh*	100/255	60/255
Differential ratio	*DcRt*	0.9	0.9
Axis length (m)	*AxLen*	500	150
Orientation (deg)	*Orient*	45	45
Axis ratio	*AxRatio*	1.6	1.5
Minimum area (m^2)	*MinArea*	5000	2500
Maximum area (m^2)	*MaxArea*	800000	90000

Note that the parameters in Table 7.1 are first selected based on the geometry of the site monitored and the expected avalanche dimensions. A refinement with radar images containing avalanches is later on necessary to fine tune the accuracy of the processor.

7.4.1. Features extraction

No contrast features at region level have been used. Considering the whole image, instead, the threshold (*Thresh*) and differential ratio (*DcRt*) already presented in Section 7.3.1 have been used and are reported in Table 7.1.

Regarding morphological features, avalanche signatures in GB-SAR imagery present a rather constant elongated shape that can be easily modelled by an ellipse. The shape features used, thus, define that hypothetical ellipse that has the same first- and second-order moments as the region:

a) *Axis length* (m): length of the major axis of the equivalent ellipse.

b) *Orientation* (deg): angle between the vertical and the major axis of the equivalent ellipse.

c) *Axes ratio*: quotient between the major and the minor axes of the equivalent ellipse.

d) *Area* (m^2): number of pixels in the region multiplied by the pixel resolution factor.

The features a) and c) represent the minimum values allowed for a region to be classified as avalanche, while the feature b) is the maximum angle in absolute value allowed. For d) a range (minimum and maximum values) has been defined. Figure 7.8-a shows the result of applying the shape features classification to the scene in Figure 7.7. Note that Figure 7.8 incorporates a background mask of the test site in grey colour only for reference. It can be seen how, from the three regions in Figure 7.7, the smallest one has been discarded in Figure 7.8-a because of the high mismatch with the *Area* range defined.

7.4.2. Post-event filtering

An additional important feature is employed prior to the final classification of regions. Intrinsic to the definition of the differential coherence images, as pointed out in Section 7.2.2 avalanche signatures propagate to the differential coherence image related to the avalanche event itself (dco_{n+3} in Figure 7.3, elongated black region on Figure 7.8-a) but also to the successive differential coherence image (dco_{n+4} in Figure 7.3, black region on Figure 7.8-b).

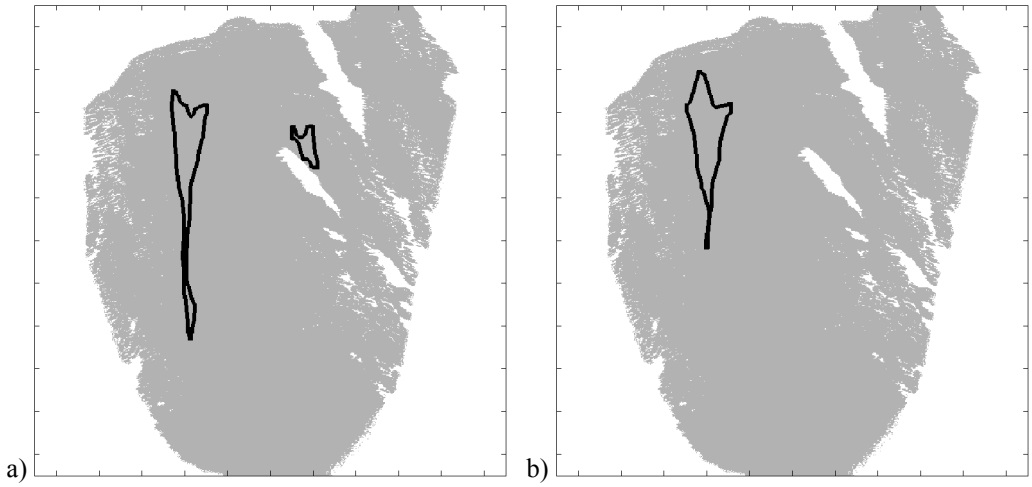

Fig. 7.8. Regions (in black) after shape classification, over a site mask (in grey) at a) t_{n+3}: 11.31h; and b) t_{n+4}: 11.43h of 2005/12/31 in the Sion Valley.

This feature, called *post-event* filtering hereinafter, is easily implemented in the processor, since it is based on the same contrast and shape features already defined, but applied to the successive differential coherence image. The only requirements for the region in the successive image are that: 1) its centre of mass falls inside the smallest rectangle containing the region in the preceding image; and 2) its *Area* and *Orientation* are, within a margin of 50%, equal to those of the region in the preceding image. Under these circumstances, the region identified at t_{n+3} is classified as a snow avalanche.

It is worth noting that the *post-event* filtering introduces a delay of $\Delta t = t_{n+4} - t_{n+3}$ in the detection scheme, since image n+4 needs to be completely acquired in order to classify any region on image n+3. This implies that the total time for avalanche warning approximates to $2\Delta t$ in the worst case (avalanche happening at the very beginning of an image acquisition) and to Δt in the best case (avalanche happening at the end of an image acquisition).

7.4.3. Avalanche classification

Regions passing all the above mentioned filters are classified as avalanches by the processor. As an example, from the three regions of Figure 7.7, only two remain after applying the shape features constraints, as can be seen in Figure 7.8-a. From these two regions, since the smallest one is not present in the successive image (Figure 7.8-b), it is also discarded. Finally, the only region remaining is classified as an avalanche and its features added to a database for later manual verification.

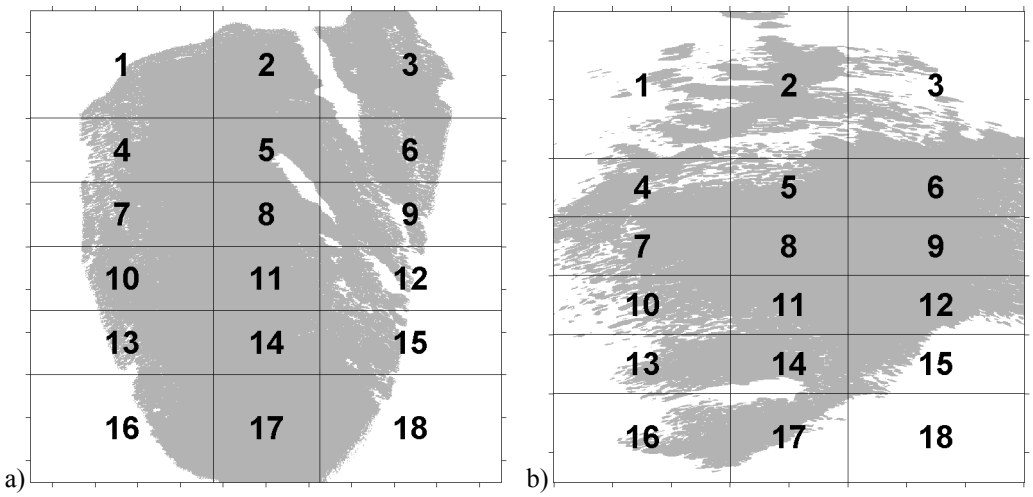

Fig. 7.9. Power and coherence masks over a grid for avalanche start position identification. a) Sion Valley test site; and b) Alagna Valsesia test site.

The features recorded for each region classified are:

a) *Date and time* corresponding to the first differential coherence image containing the avalanche signature (may be delayed up to a maximum of Δt with respect to the actual instant the avalanche took place).

b) *Position* of the avalanche starting point, coded with a number between 1 and 18. For this purpose a grid has been defined in each test site as can be seen in Figure 7.9.

c) *Axes* (horizontal×vertical) in meters of the equivalent ellipse modelling the region classified.

d) *Area* in square meters of the region classified.

e) *Differential ratio* of the differential coherence image containing the avalanche signature.

7.5. Results

The processor presented in this chapter was tested on more than 70000 images acquired with two GB-SAR LISA sensors during a total of 6 winter campaigns in two different test sites as reported in Chapters 3 and 4.

With the massive amount of images generated by a GB-SAR it is virtually impossible to have real ground-truth data to assess all of them. Classical methods of snow avalanche monitoring based on force measurements [13], optical imagery, Doppler radar [13] or geophones [21] either lack the SAR capacity of operating without good visibility conditions, or the capacity to monitor a relatively large area of up to 2 km×2 km. In light of this, it was decided to split up the assessment of the processor into two phases: a first proof-of-concept based on the comprehensive analysis of a reduced set of images performed by a snow avalanche expert together with a radar operator and, in a second place, the assessment of the results of processing the full archive of radar images against

the manual classification of each scene performed by the radar operator (see Annex G for the complete list of avalanches manually classified). This later approach, followed also in [67] and [73] for the oil slick detection problem, entails no guarantee that the manual classification is correct. In order to minimize this issue, the radar operator only marked as avalanches those scenes with a clear signature, discarding all doubtful ones.

7.5.1. Proof-of-concept test

The first test set studied consisted of 55 scenes containing a representative number of avalanches and otherwise decorrelated images. These scenes belong to the test site of the Sion Valley, acquired during the period 2005/01/01 to 2005/04/30 and contain all the natural avalanches identified by traditional means in that period.

Urs Grubber, snow expert from the Swiss Federal Institute for Snow and Avalanche Research (SLF Davos) marked a total of 32 avalanches and 23 otherwise decorrelated images. 17 out of the 32 avalanches were positively identified with the help of the geophones data and the visual imagery available in the test site for that period. The rest, 15, were marked by the SLF snow expert as highly possible considering the weather conditions reported by the meteorological station, the avalanche position and path reported in our radar images and previous personal experience of avalanches observed in the test site.

Table 7.2 summarizes the processor accuracy for this reduced test set. Results show 100% accuracy for otherwise decorrelated images (0% false positive rate, no false alarms) and 81.3% accuracy for avalanches (18.7% false negative rate, 6 avalanches missed by the algorithm out of a total of 32). These figures are in line with those reported in Table IV of [67] for the oil spill classification problem.

Table 7.2. Classification accuracies with reduced test set

	Classified as avalanche	**Classified as look-alike**
Marked as avalanche by snow expert	26/32	6/32
Marked as not avalanche by snow expert	0/23	23/23

Regardless of the results obtained by the automatic identification algorithm, this test demonstrated that all natural avalanches detected by traditional means were also visible in the SAR images. In addition, a relevant number of avalanches not caught by the geophones network or not visible in the pictures during night time were marked by the SLF snow expert as highly possible considering the weather conditions and the avalanche position and path on the radar images.

In addition to the reduced test set of natural avalanches analyzed by the snow expert, three exercises of artificial avalanche triggering were carried out on 2004/01/19, 2005/02/17 and 2006/03/06 on the test site of the Sion Valley. These exercises resulted in a total of 9 artificial avalanches, all of them clearly seen in the radar imagery and properly geo-located confirming the position of the avalanche paths.

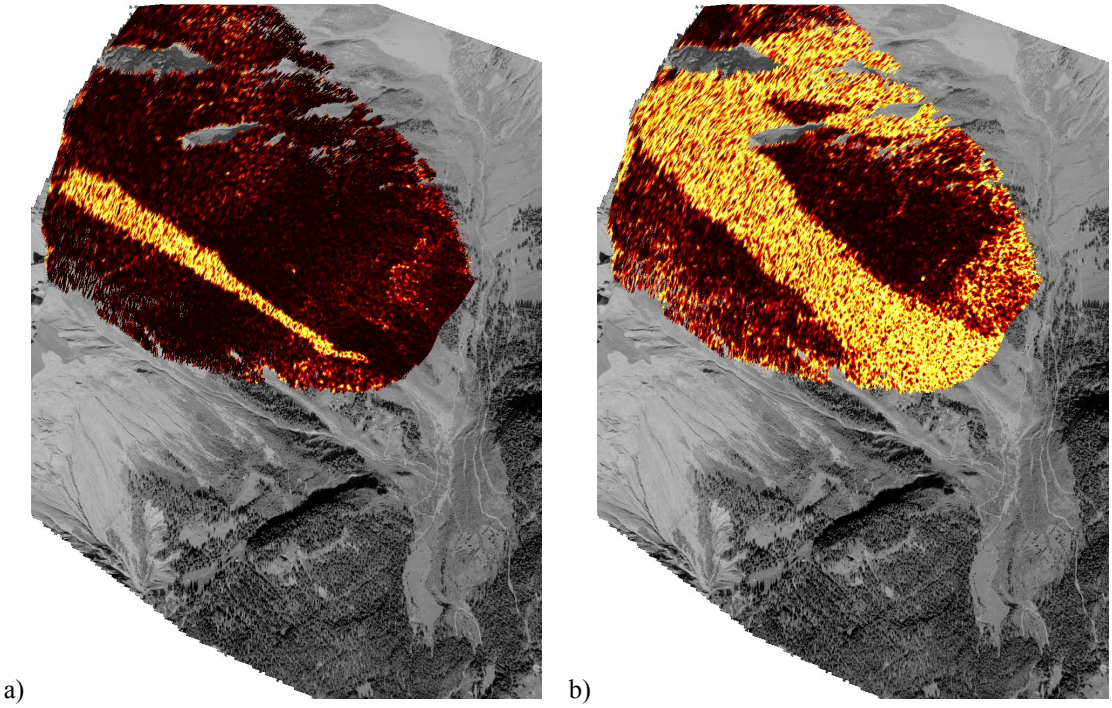

a) b)

Fig. 7.10. Coherence signature of artificial avalanches in the Sion Valley geo-located over DTM and aerial photo. a) 2005/02/17 10.09h; and b) 2006/03/06 10.44h.

Figure 7.10 shows the coherence signature of two of these avalanches while Figure 7.11 shows the photography of the big artificial avalanche on 2006/03/06. Note that the avalanche on 2006/03/06 at 10.44h was exceptionally big, with a channel path 1775 m long and a few hundreds metres wide as it can be appreciated both on the radar image and the visual photography.

Fig. 7.11. Photography of the artificial avalanche in the Sion Valley, 2006/03/06 10.44h.

Regarding the test site of Alagna Valsesia, four exercises of artificial avalanche triggering were carried out on 2007/03/08, 2008/01/13, 2008/03/13 and 2008/03/22 resulting in a total of 9 artificial avalanches. Also these avalanches were properly monitored and geo-located by LISA, confirming the ground-truth observations. Figure 7.12 shows three examples of these artificial avalanches, each marked with a black arrow on their starting position.

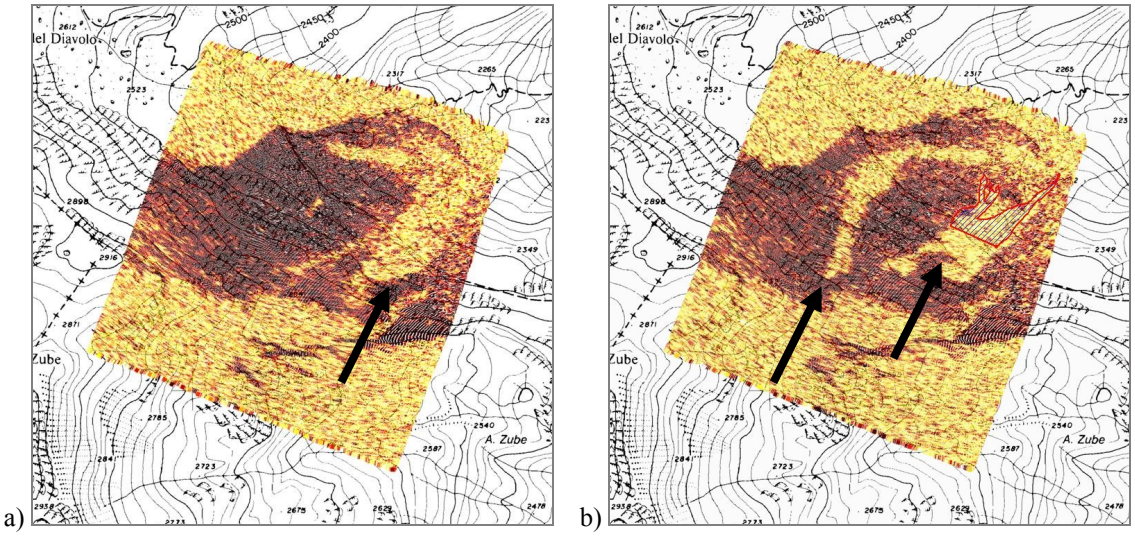

Fig. 7.12. Un-masked coherence signature of artificial avalanches in Alagna Valsesia geo-located over DTM and local map. a) 2007/03/08 08.47h; and b) 2008/03/13 08.30h.

In Figure 7.12-a one of the two avalanches triggered on 2007/03/08 can be seen on the right side of the coherence image. In Figure 7.12-b, instead, the two avalanches triggered on 2008/03/13 are visible on the same radar image.

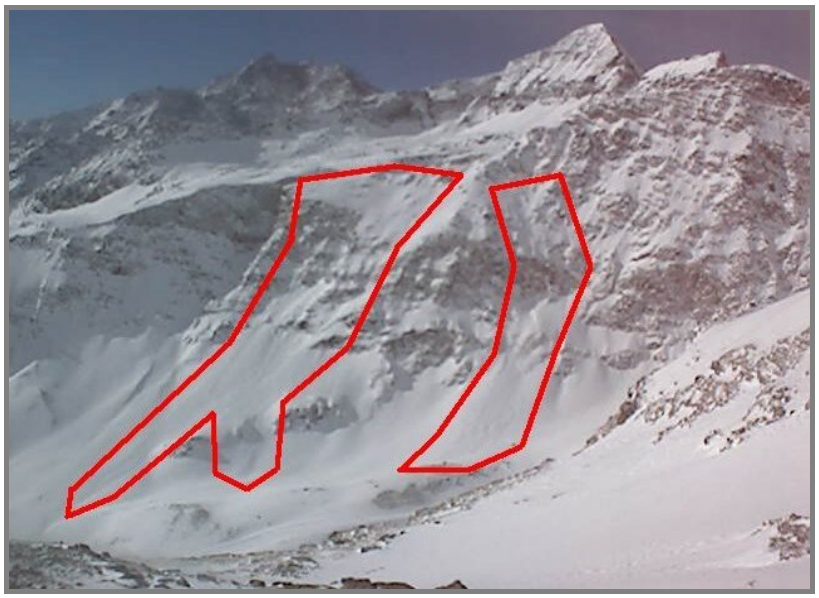

Fig. 7.13. Photography of the artificial avalanches in Alagna Valsesia, 2008/03/13 08.30h.

Note also a partial GPS track on the right most avalanche of Figure 7.12-b confirming the position of the avalanche path in its lower elevation. The upper elevation, where the black arrow is pointing to, is only accessible by helicopter so no GPS track is available. The upper elevation corresponds to the rock formations horizontally crossing both avalanche paths that can be appreciated in Figure 7.13.

Figure 7.13 shows a visual picture of the two artificial avalanches in Alagna Valsesia on 2008/03/13 taken from the radar location. Note that the visual image is rotated approximately by 180 deg with respect to the radar image in Figure 7.12-b because the later image is geo-located over a local map and, thus, North-oriented. The largest avalanche in Figure 7.13 is approximately 300 m long by 100 m wide, considerably smaller than that shown in the Sion Valley in Figure 7.11. This is why it becomes more difficult to identify the avalanche paths over the visual photography and they have been surrounded by a red line in Figure 7.13.

7.5.2. Algorithm benchmarking

Table 7.3 shows the reference frame for benchmarking the results of the processor when analyzing the full archive of GB-SAR images. This table, as explained, has been produced from the manual analysis of all images, marking as avalanches only those scenes showing clear avalanche signatures. The complete list of avalanches manually supervised can be found in Annex G.

Table 7.3. Ground-truth data for benchmarking

	Sion	Alagna	Total
Images analyzed	37519	34964	72483
Regions marked as avalanche	661	374	1035

The following nomenclature and ratios have been used for the benchmark:

a) *Images analyzed*: total number of images processed.

b) *Marked avalanche*: total number of avalanches manually identified by the radar operator.

c) *Processing time*: time in minutes corresponding to the thresholding, features extraction and classification blocks of the processor for all images analyzed.

d) *Images to supervise*: number of images identified by the algorithm as possible avalanches with respect to the total number of images analyzed.

e) *Avalanches confirmed* (or accuracy for avalanches detection): number of avalanches manually confirmed with respect to the total number of possible avalanches identified by the algorithm. The higher it is the better.

f) *Avalanches missed* (or false negative rate): number of avalanches not identified by the algorithm with respect to the total number of manually identified avalanches. The lower it is the better.

Three variants of the snow avalanche identification processor have been analyzed: one referring to the segmentation block and two referring to the classification one.

Regarding the segmentation block, the use of an adaptive (column B) or fixed threshold (column A) is analyzed in Table 7.4. For this benchmark the rest of the processor parameters remains as presented in the preceding sections, that is, with the differential ratio (*DcRt*) and the *post-event* filters active.

Table 7.4. Segmentation benchmarking: A) Fixed thresholding; and B) Adaptive thresholding.

		A		B	
Processing time (min)	**Sion**		338		515
	Alagna		360		575
Images to supervise	**Sion**	2.2%	(832)	4.5%	(1695)
	Alagna	2.2%	(762)	16.4%	(5751)
Avalanches confirmed	**Sion**	73.5%	(612)	32.4%	(550)
	Alagna	44.0%	(335)	4.0%	(228)
Avalanches missed	**Sion**	7.4%	(49)	16.7%	(111)
	Alagna	10.4%	(39)	39.0%	(146)

The processing time row reveals that the adaptive threshold solution is 1.5 times slower than that of the fixed threshold, mainly because of the median filter prior to the computation of the adaptive threshold (results are computed on a 2.8 GHz Windows PC). Nevertheless, considering the time required for analyzing a single differential coherence image (approximately 0.5 s) there is room enough for improving this block with more sophisticated algorithms that will fit into the constraints of a total processing time below approximately 10 minutes.

The three rates computed: images to supervise, avalanches confirmed and avalanches missed confirm that the fixed threshold solution is more suited for this application than the adaptive threshold implemented. The accuracies for avalanche detection are 73.5% for the Sion test site and 44.0% for the Alagna test site, while the false negative rates (avalanches missed) are 7.4% and 10.4% respectively. Both false negative rates and processor accuracy in the Sion site are comparable or even better than those reported for oil slick detection in [67]. The accuracy for avalanche detection in Alagna, instead, shows a poor performance.

The low accuracy for avalanche detection in Alagna is caused by a lower SAR image quality in this site. Two main reasons explain this decrease in image quality:

a) The slope monitored in Alagna is North-oriented, contrary to the South-oriented slope in Sion. This means that the Alagna test site suffers from particularly adverse weather conditions that result in a strong increase of decorrelation and, thus, of false alarms.

b) The sensor parameters used to monitor the site of Alagna are less optimized than those used in Sion. On the one hand, a shorter aperture length results in a decrease of the azimuth resolution up to a 50%. On the other hand, the frequency band in the Alagna site (Ku-Band) is twice that in Sion (C-Band). This makes the imagery in Alagna more sensitive to difficult atmospheric conditions (e.g., heavy snow fall) and to very superficial avalanche events.

While the algorithm accuracy for avalanche detection in the Sion site is approximately twice as good as that in Alagna when using the fixed threshold (73.5% versus 44.0%, column A of Table 7.4), the rate increases up to a factor 8 when using the adaptive threshold (32.4% versus 4.0%, column B of Table 7.4). This leads to two important conclusions: 1) the image quality pays a fundamental role in the algorithm accuracy, and 2) the segmentation block needs to be better adapted to bad weather conditions and the sensor parameters fine-tuned to obtain the better imagery for the avalanche detection application.

Regarding the classification block, the impact of the differential ratio (*DcRt*) and the *post-event* filters is assessed in Table 7.5. In view of the results obtained in Table 7.4 a fixed threshold strategy was used for the segmentation block in this benchmark. Note that column C in Table 7.5 is identical to column A in Table 7.4, since they both correspond to the same benchmark: fixed threshold, *DcRt* active and *post-event* filter also active. The absolute values in Table 7.5 have been skipped in order to fit all the results in a single and clearer table. Processing time has also been skipped because of its minimal impact on this benchmark.

Table 7.5. Classification benchmarking: C) *DcRt* filtering: ON, *Post-event*: ON; D) *DcRt* filtering: ON, *Post-event*: OFF; E) *DcRt* filtering: OFF, *Post-event*: ON; F) *DcRt* filtering: OFF, *Post-event*: OFF.

		C	D	E	F
Images to supervise	**Sion**	2.2%	3.2%	2.5%	4.7%
	Alagna	2.2%	6.3%	5.0%	12.6%
Avalanches confirmed	**Sion**	73.5%	40.7%	64.7%	27.1%
	Alagna	44.0%	11.7%	19.1%	5.9%
Avalanches missed	**Sion**	7.4%	24.2%	6.2%	27.0%
	Alagna	10.4%	30.7%	9.3%	29.6%

Comparing columns C against D and E against F of Table 7.5 the effect of the *post-event* filtering can be observed. It is shown how accuracies are approximately reduced by 50% in the Sion site and by 70% in the case of the Alagna site when not using that filter. A similar trend is observed for the false negative rate, which increases approximately by 300% in both test sites when turning off this filter. These results are consistent in both test sites and show no doubt that the *post-event* filtering is an effective technique for improving the accuracies of the processor.

Comparing columns C against E and D against F of Table 7.5 the effect of the differential ratio (*DcRt*) filter we can be seen. The analysis will be concentrated on columns C and E, since columns D and F correspond to the results when not using the *post-event* filter and it has been demonstrated that the accuracy drastically falls when not using it.

In the columns C and E of Table 7.5 those cells with the better statistics have been highlighted in grey. The results show an expected slight reduction (~18%) of the number of avalanches missed when turning the *DcRt* filter off. In fact, this filter discards noisy images even if they contain an avalanche signature. Although a weighting function is used to minimize the effect of losing scenes with avalanches in them (Section 7.3.1), this benchmark shows that actually some avalanches are filtered out. The price to pay for this false negative improvement is a poorer accuracy of the processor particularly in the Alagna

test site: the number of images to supervise increases in both sites and the number of avalanches confirmed decreases by 12% in Sion and by 56% Alagna.

The *DcRt* filter represents, thus, a trade-off between the false positive and the false negative rates. In the case of Sion this filter could be turned off: false negatives improve by 16% while the accuracy for avalanches detection deteriorates by only 12%. In the case of the Alagna test site, instead, the accuracy for avalanche detection is so much reduced with the filter off that its use becomes absolutely necessary.

Finally, the performance of the processor is compared to the accuracies obtained with the classical method of force sensors in operational scenarios reported by H. Gubler [74]. H. Gubler is the founder of the Swiss company AlpuG (http://www.alpug.ch), specialized in the monitoring and control of alpine natural dangers with more than 10 years experience in the exploitation of operational systems for snow avalanche detection and alarm triggering.

Table 7.6 shows the avalanche detection accuracies comparison between classical force sensors and the GB-SAR technique reported in this chapter. The analysis time base guaranties a consistent comparison of for both sensors results: 5 years divided in several sites in the case of the force sensors, and a total of 6 years divided in 2 test sites in the case of the GB-SAR sensors.

Table 7.6. Avalanche detection accuracies comparison between different systems

	Force sensor H. Gubler		**GB-SAR Sion**		**GB-SAR Alagna**	
Monitoring time (years)		5		3		3
Avalanche alerts		(30)		(832)		(762)
Avalanches ground-truth	42%	(13)	79%	(661)	49%	(374)
Avalanches missed	6%	(1)	7%	(49)	10%	(39)

Regarding the number of avalanche alerts, it can be observed how the GB-SAR sensor provides a substantial higher number of alerts when compared to the force sensors. There are two explanations: first of all, the GB-SAR technique monitors an area of a few square kilometres where avalanches can start or pass by any of the points in the radar FOV to be detected. The force sensor, instead, consists of a single wire that crosses a hypothetical avalanche path by a single line of the path and, hence, only avalanches crossing by this line can be detected. The second explanation for the higher number of avalanche alerts triggered by the GB-SAR technique is related to the size and volume of the avalanches. While force sensors are positioned in order to only detect big avalanches, the GB-SAR technique can be parameterized to detect different sizes of avalanches. Unfortunately, the avalanche volume cannot be retrieved with the proposed GB-SAR technique, so the avalanche dimensions can only be known and filtered for the moment with respect to the area of the avalanche path. This implies that superficial or bigger avalanches are detected with GB-SAR identically and cannot be discriminated.

The most interesting results are instead related to the accuracies of both detection systems. While one could expect that the traditional, robust and relatively simple force sensors should have a very high accuracy and low false alarm, the results reported in [74] (Column H. Gubler in Table 7.6) show 42% accuracy (58% of false alarms) and 6% of avalanches missed by the force sensors. The following two columns in Table 7.6 show the better results achieved with the GB-SAR processor presented in this chapter, that is, those

reported in column A of Table 7.4. The accuracy in avalanche detection is better in both sites studied, and even the poor accuracy obtained in Alagna when compared to the Sion site (49% versus 79%) is better that that obtained with traditional force sensors (42%). Regarding the false alarms, the GB-SAR technique performs slightly worse than the force sensors (7% and 10% versus 6%). Nevertheless, the differences in the Sion test site case are minimal.

As a summary of the algorithm benchmark it can be concluded that the proposed technique represents a realistic operational alternative and/or complement to traditional sensors. Accuracies are in the order of those obtained with force sensors so far, although the GB-SAR technique is relatively young and it can be expected improvements on the accuracies in the near future.

7.6. Operational products

7.6.1. Avalanche alerts

A prototype version of the algorithm presented was experimentally implemented in the test site of Alagna Valsesia from January to March 2008. The personal computer of the LISA instrument processed in real time the radar images after their acquisition, producing the intermediate images and final classification required to send an alert of avalanche. The data acquisition was implemented in LabView, while the processing was partially done in LabView and partially in Matlab.

Figure 7.14 shows an example of the two images initially generated when a radar acquisition is completed and the corresponding SAR image is focused: the coherence (*coh*) and differential coherence (*dco*) of a big avalanche happening on 2008/03/21 at 18.46h.

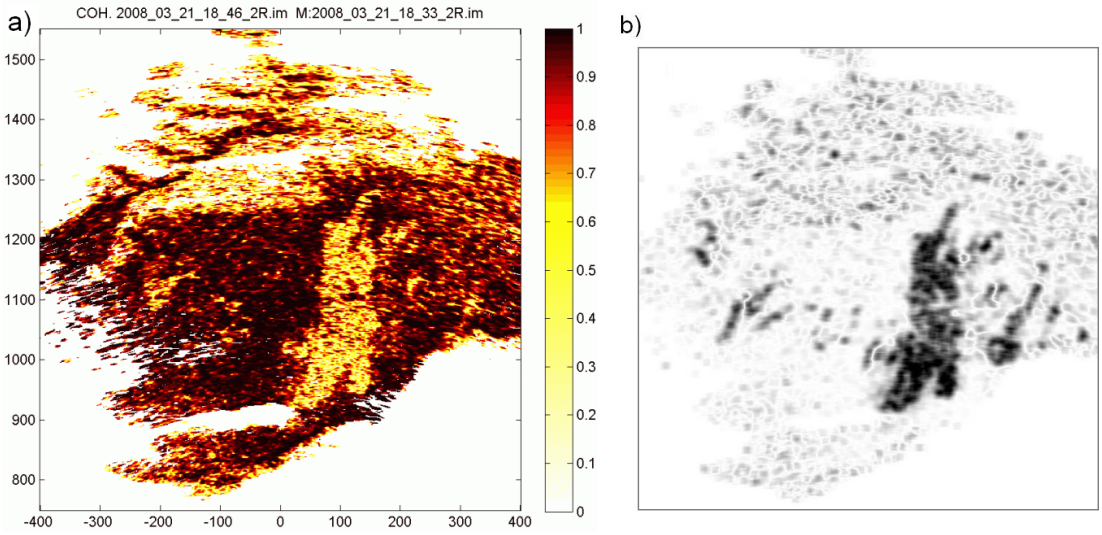

Fig. 7.14. Natural avalanche in the Alagna site on 2008/03/21 at 18.46h. a) Coherence magnitude image (*coh*); and b) differential coherence image (*dco*).

From the differential coherence image the classification block marks the different regions as avalanche candidates or artifacts that can be discarded. Figure 7.15 shows an example of the avalanche classification step corresponding to the differential coherence

image in Figure 7.14-b. A big perimeter in green corresponds to the dark regions clearly identified in Figure 7.14-b, where the number 6 identifies the starting position of the avalanche corresponding to that region according to the grid in Figure 7.9-b. Several smaller regions are signalled in red, and they correspond to regions that fail to pass one or more of the filters defined in Table 7.1. A grey background based on a power mask of the backscattered signal helps to understand the positions of the different regions.

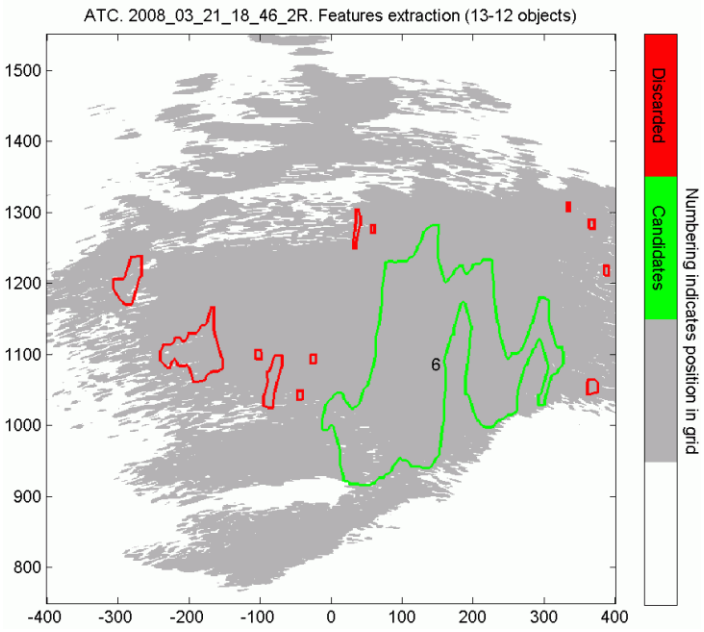

Fig. 7.15. Natural avalanche in the Alagna site on 2008/03/21 at 18.46h automatically classified by the algorithm (in green). Red regions are artifacts discarded.

Once the *post-event* filter is completed and the region is finally classified as avalanche, a text file is created with the region features described in Section 7.4.3. An example of the text file corresponding to Figures 7.14 and 7.15 can be seen below:

```
%================================================
%Date       Time    Pos     Axes        Area    DcRt
%------------------------------------------------
2008/03/21  18.46h    6    250x375     56150    0.57
```

Fig. 7.16. Example of text file containing the information of an avalanche identified by the algorithm.

Finally, the text file together with the corresponding images are sent by e-mail to a pre-defined distribution list and the text file alone is sent by SMS also to a pre-defined distribution list. To this aim, a reliable Internet connection is necessary in the LISA instrument, as was the case for the instrument deployed in Alagna Valsesia.

As stated, the implementation of the whole processing chain including an alert system by e-mail and SMS has proved the operational use of the proposed technique. The total processing time per radar image is approximately 1 minute on an off-the-shelf 2.8 GHz Windows XP computer, including the radar image focusing, the generation of the intermediate images for avalanche detection and classification and the final creation and sending of the text file. In addition, the SMS alert system allowed the visual verification of

a few avalanches happening when Andrea Pierrettori from the University of Turin and Michele Cucchi from the Corpo Guide Alpine d'Alagna where close to the site.

7.6.2. Geo-referenced maps

In order to facilitate the interpretation of the avalanche classification results as a function of the intermediate images, the coherence magnitude and the image containing the perimeter of the region candidate to avalanche have been geo-referenced and sent also by e-mail as part of the alert system mentioned in the preceding section. Figure 7.17 shows an example of both images corresponding to the coherence and classified regions in Figures 7.14-a and 7.15 respectively over a local map of the test site in UTM coordinates.

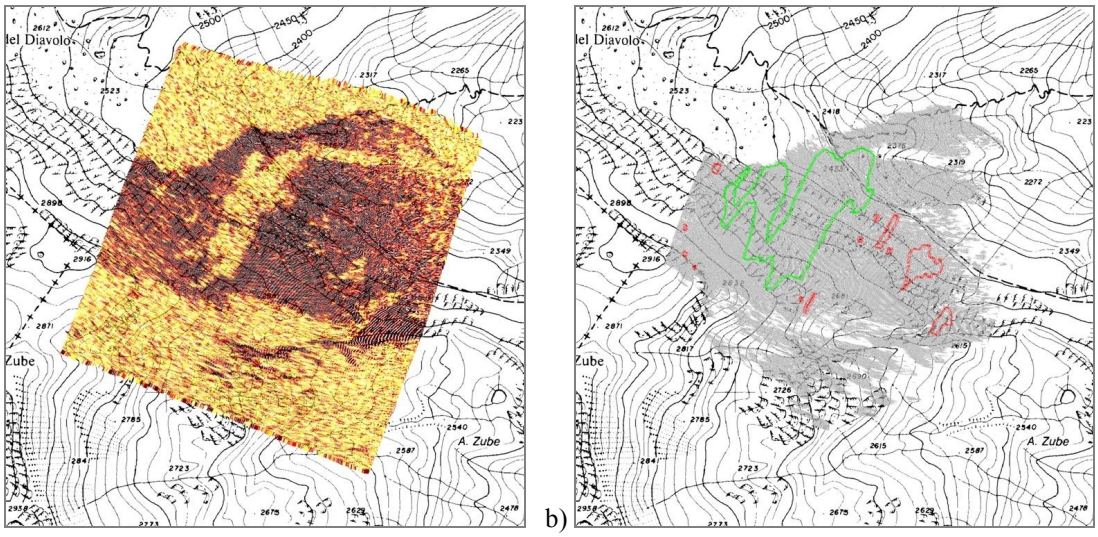

Fig. 7.17. Natural avalanche in the Alagna site on 2008/03/21 at 18.46h. a) Un-masked coherence image geo-referenced; and b) classified regions geo-referenced.

Note that no power mask is applied to the coherence images geo-referenced in Figures 7.12 and 7.17-a for better interpretation of long avalanches that finish in the decorrelated zone corresponding to the bottom part of the radar images. The same images in the sensor local coordinates, instead, are masked out with a backscattered power mask. The coherence image in the sensor local coordinates frame corresponding to Figure 7.17-a can be seen in Figure 7.14-a, where the axes are labelled in metres and range according to the limits reported in Table 4.3 (-400...400 m in azimuth and 750...1550 m in range).

The mathematical details of the geo-referencing step can be found in Annex E. It is worth noting that no high resolution DTM was available for the test site of Alagna, so the procedure presented in Annex E.4 was used to produce the maps in Figure 7.17. In the case of the Sion test site, instead, a high resolution DTM was available from the Swiss Federal Office of Topography, produced from an aeroplane with a state-of-the-art laser scanner [38]. In this later case the procedure described in Annex E.3 was used to create the geo-referenced images corresponding to the Sion test site, as can be appreciated, for example, in Figures 7.10, 7.18 and 7.19.

7.6.3. Hazard maps

The final operational product presented in this chapter was achieved after an extensive monitoring campaign and consists of the spatial accumulation of avalanches paths. The resulting map is a kind of spatial histogram on which the areas with more avalanche activity in a given site are shown in darker colours.

The utility of such maps is double. On one side its examination, once geo-located, serves as a qualitative indicator that the whole processor is providing reasonable results: avalanches should follow the natural channels in the mountain and descend following the line of maximum slope. These essential facts can be statistically checked by observing the spatial histograms corresponding to a whole winter season for example. On the other hand, the histograms can be interpreted as hazard maps where the probability for a point location of being covered by avalanches is colour coded.

Figures 7.18 and 7.19 show two examples of hazard maps corresponding to the test site of the Sion Valley. These maps are geo-referenced over a high resolution DTM. In addition, the DTM is masked by an aerial orthophoto. The hazard map is finally superimposed on the orthophoto.

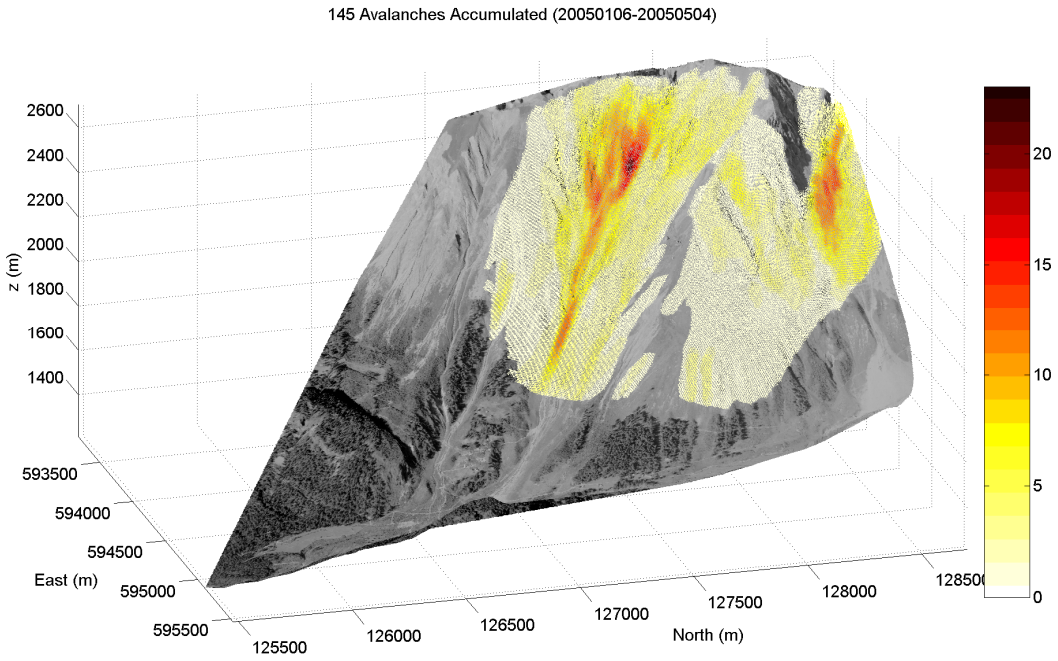

Fig. 7.18. Avalanches accumulated in the Sion Valley test site, winter 2004-2005.

The maps in Figures 7.18 and 7.19 contain all the avalanches monitored by the LISA instrument over a whole winter season: 145 avalanches in the winter 2004-2005 and 439 avalanches in the winter 2005-2006. The colour bar on the right-side of the images indicates the number of avalanches accumulated in each of the pixels in the image.

A closer observation of the images in Figures 7.18 and 7.19 through specific software for 3-D visualization allows checking of the exact location and topography of the avalanches' path. This examination was performed on both test sites, Sion Valley and Alagna Valsesia, qualitatively confirming the validity of the whole processing chain described in this chapter and in Annex E.

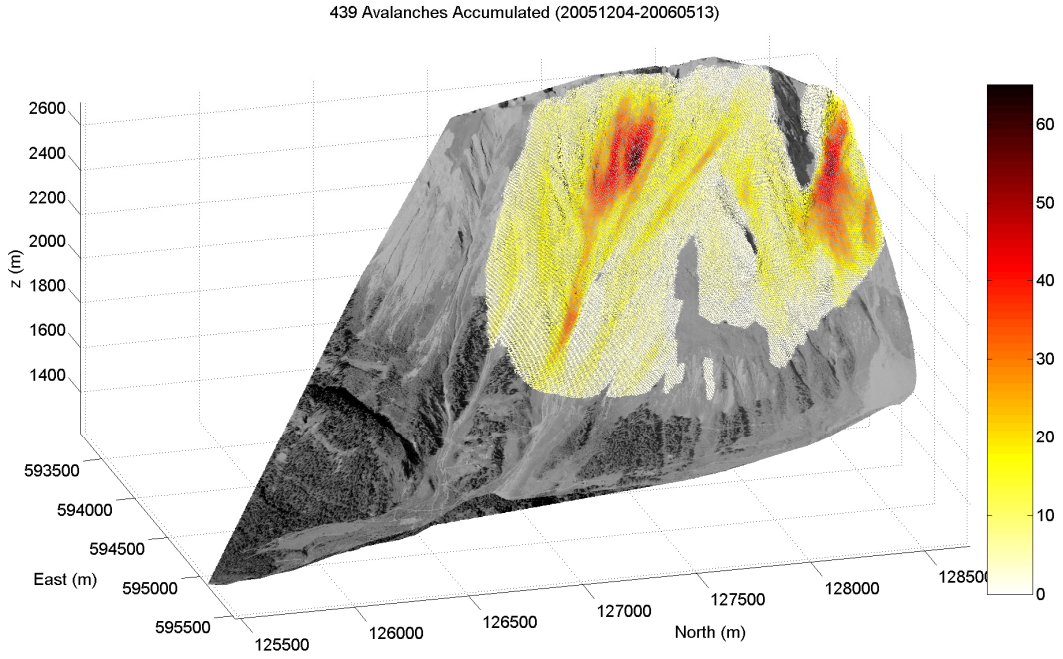

Fig. 7.19. Avalanches accumulated in the Sion Valley test site, winter 2005-2006.

Similarly, Figure 7.20 shows the hazard maps corresponding to two winter seasons in the test site of Alagna Valsesia, this time geo-referenced over a local map.

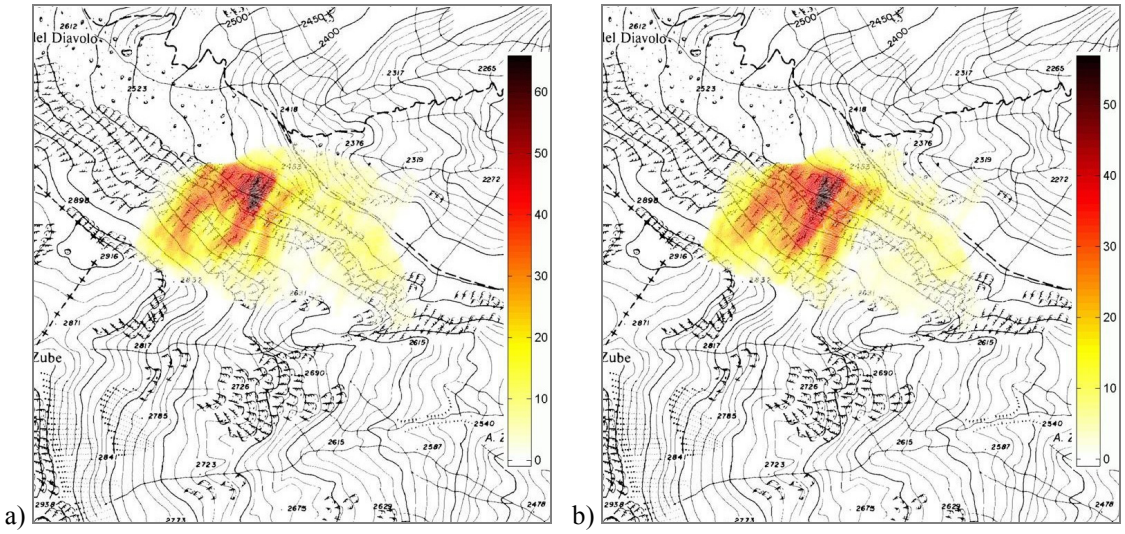

Fig. 7.20. Avalanches accumulated in the Alagna Valsesia test site over local map. a) Winter 2006-2007 (164 avalanches); and b) winter 2007-2008 (121 avalanches).

7.7. Conclusions

A GB-SAR processor for snow avalanche detection and classification has been presented in this chapter. Avalanche signatures can be clearly identified in the coherence

image of two consecutive SAR scenes as a localized decrease of the coherence magnitude with elliptic shape and vertical orientation. This, in addition to the *post-event* filtering intrinsic to the use of differential coherence images, simplifies the classification block of the processor and makes it significantly robust.

The draw-back of this block is the time necessary to launch an alert in case of avalanche detection. If Δt is the time required for a complete SAR acquisition (Δt was 12 minutes in our two field campaigns), the total time required to obtain an output of the algorithm ranges approximately from Δt in the best case to $2\Delta t$ in the worst one.

The most critical block of the processor is, instead, the segmentation one and in particular the thresholding operation. Adverse weather conditions (e.g., heavy snow fall or strong winds) introduce a significant decrease in the coherence magnitude that may confuse the detector. The differential coherence concept has been introduced to deal with this problem and works properly. Nevertheless, results show that there is room for improving the accuracy of the processor by using a more appropriate thresholding technique in the segmentation block. A fixed threshold showed better results than a single-scale adaptive threshold in the benchmark presented in this chapter, but a multi-scale approach for dark spot segmentation or other techniques from the computer vision field such as wavelet decomposition or edge detection should be considered in the future.

It is worth noting that the segmentation and classification parameters both depend on the images' quality and geometry, therefore they are site-specific, as reported in Table 7.1.

Although it has been demonstrated that avalanches not detected by traditional means can be seen with SAR imagery, a weakness of the SAR detection scheme is the lack of information regarding the volume of snow displaced in an avalanche. This means that a loose snow avalanche and a slab avalanche of 1 m high are seen very similarly by the radar as long as the affected area in the slope is the same in both cases. A technical solution could be the use of interferometry, although the sensitivity of the interferometric phase makes it hardly operational for monitoring the snow cover.

Currently, a prototype version of this algorithm is experimentally implemented in the ski resort of Alagna Valsesia. Preliminary results indicate that this technique can effectively complement the manual inspection and the classical techniques used so far.

Although the system presented may be too slow for a critical situation in which an alarm needs to be sent within seconds of the avalanche event, in its current configuration it is an interesting tool for ski resorts management in which a list of avalanche events can be provided each morning in order to better prepare the pistes. The accuracy obtained with the technique presented in this chapter is comparable or even better than that obtained with traditional force sensors. Hence, the operational use of the snow avalanche detection and classification by GB-SAR has a high potential.

8. Conclusions

8.1. Conclusions

The work presented in this PhD thesis is a contribution to assess the potential use of GB-SAR sensors in snow cover monitoring applications. The general problem undertaken in this study, that is, the development of robust monitoring techniques of the snow cover with a GB-SAR sensor, has been addressed through Chapters 3 to 7.

Regarding the specific objectives posed in Section 1.3, they have been addressed as follows:

a) *To upgrade an experimental instrument to allow 24/7 unattended operation during an entire snow season in the Alps.*

   The upgrades made to the experimental instrument LISA have been described in Section 3.2. In its current configuration the instrument is able to operate unattended over a whole winter season (4 months), with capacity to auto-recover from power shut-downs and to store data for a few months of continuous operation. Implementation of remote access allows the periodical control of the instrument status.

b) *To perform continuous measurements with a variety of sensor parameters and environmental conditions in order to obtain a representative data archive.*

   Two field campaigns have been carried out, both of them described in Chapter 4. Two GB-SAR sensors with different parameters have been employed, leading to a data archive of more than 120000 GB-SAR images. The data archive allows for single-pass and repeat-pass interferometry and includes signatures of natural and artificial snow avalanches both at C- and Ku-band.

c) *To develop processing techniques to remotely sense the snow cover and validate them using the GB-SAR data archive.*

   Three novel processing techniques have been developed and are described in Chapters 5, 6 and 7. The techniques are: snow cover depth retrieval by repeat-pass interferometry, snow avalanche volume retrieval by single-pass interferometry (DTM subtraction) and snow avalanche detection and classification by repeat-pass coherence analysis. In addition, a novel processor for the improved DTM generation with GB-SAR imagery in the absence of snow has been presented in Section 6.3.1.

d) *To implement prototype versions of these techniques in a near real-time processing chain of the sensor in order to verify their operational use.*

The most promising technique in terms of operational use is snow avalanche detection and classification (Chapter 7). During the last field campaign carried out in Alagna Valsesia, a near real-time prototype of this technique has been fully implemented, sending alerts by SMS and e-mail to the actors involved in the evaluation and assessment of the results.

Regarding the processing techniques presented in Chapters 5, 6 and 7 to remotely sense the snow cover, specific conclusions have been drawn in each of the chapters but they can be summarized as follows:

A dry snow height retrieval algorithm has been presented and validated in Chapter 5. Accurate snow depth profiles have been successfully created with repeat-pass interferometric data using a single calibration at the beginning of the period under study. The length of the periods analyzed appears to be related to the stability of the snow cover, which can be considered approximately constant over a whole day if the dry snow constraint is guaranteed. Snow height evolution plots have been successfully produced for periods up to four days, although periods longer than a few days may entail significant changes in the snow pack properties and hence in the calibration constants.

A novel processor for the improved generation of DTMs exploiting the high image acquisition rate of GB-SAR sensors has been presented in Chapter 6. Results on snow-free areas show an accuracy improvement of 40% when compared to GB-SAR topographic mapping processors available to date. An attempt has been made to infer the snow volume involved in an avalanche by DTMs subtraction. It has been shown that, with the typical vertical baselines of GB-SAR sensors, the accuracy obtained is of the order of a few metres, while the above mentioned technique requires accuracies of the order of centimetres.

Finally, a GB-SAR processor for snow avalanches detection and classification has been presented in Chapter 7. Avalanche signatures are identified in the coherence image of two consecutive SAR scenes as a localized decrease of the coherence magnitude with elliptic shape and vertical orientation. Morphological and statistical filters have been proposed for the automatic classification of such anomalies in the coherence as avalanche events, with particular emphasis on the discrimination of other sources of decorrelation that may degrade the performance of the processor. Since this technique appears to be the most mature for an operational use, several products regarding avalanche alerts and hazard maps have been presented and an alert system has been proposed to operationally exploit in near real-time the results obtained with the LISA instrument.

8.2. Original contributions

The original contributions of this PhD thesis can be summarized in the following points:

a) A unique data archive has been created with more than 120000 SAR images corresponding to two different snow covered test sites. A variety of signatures

are available that allow future studies that complement or improve those presented in this PhD thesis.

b) A novel technique for remote snow height retrieval has been developed, implemented and assessed. With the availability of an initial ground control point, absolute snow height is inferred for intervals of up to 4 days.

c) A novel processor for the improved generation of DTMs with GB-SAR imagery in the absence of snow has been developed and assessed. The accuracies obtained improve by 40% (from 5 to 3 m) with respect to those reported in the literature.

d) A novel processor for snow avalanches detection and classification with GB-SAR has been developed, implemented and assessed. This processor has operated in near real-time during 3 months at a ski resort, showing to be an interesting support tool for the daily operations of avalanche risk assessment in the ski resort.

8.3. Future research lines

The future research lines opened by this PhD thesis are:

a) Combination of the data acquired by two independent GB-SAR units (each with a single transceiver, 1 Tx and 1 Rx) vertically separated more than 10 m in order to achieve the vertical accuracy necessary for snow avalanche volume retrieval.

b) Combination of the data acquired by a single-pass GB-SAR interferometer (1 Tx and 2 Rx antennas) implementing multiple vertical baselines in order to obtain more accurate DTMs.

c) Inclusion of weather information in the snow avalanche identification algorithm in order to improve its accuracy, particularly under bad weather conditions.

d) Refinement of the snow avalanche identification algorithm by testing different techniques of segmentation and classification: multi-scale adaptive threshold, wavelet decomposition, edge detection, etc.

e) Use of a dual frequency sensor in order to provide an indicator of the snow volume displaced by an avalanche event. This indicator could be integrated into the real-time processing chain of the instrument right after the avalanche identification block.

f) Acquisition of polarimetric data to attempt a polarimetric decomposition of the main scattering mechanisms in snow avalanches. Study the possibility of using this information instead of the coherence magnitude to identify avalanches or even avalanche precursors.

g) Speed up the avalanche identification processor in order to get a classification right after an image acquisition is completed, avoiding the use of the differential coherence and *post-event* filter techniques.

A. List of publications

A.1. Journal articles

1. A. Martinez-Vazquez, J. Fortuny-Guasch and U. Gruber, "Monitoring of the Snow Cover with a Ground-Based Synthetic Aperture Radar." *European Association of Remote Sensing Laboratories, EARSeL eProceedings*, vol.4, n.2, pp.171-178, October 2005.
2. A. Martinez-Vazquez and J. Fortuny-Guasch, "Averaging and Formulation Impact on GB-SAR Topographic Mapping." *IEEE Geoscience and Remote Sensing Letters*, Accepted for publication on June 9th, 2008.
3. A. Martinez-Vazquez and J. Fortuny-Guasch, "A GB-SAR Processor for Snow Avalanche Identification." *IEEE Transactions on Geoscience and Remote Sensing*, Accepted for publication on June 1st, 2008.

A.2. Conference proceedings

4. J.M. Lopez-Sanchez, A.J. Camps, M. Vall-llossera, N. Duffo and A. Martinez, "Polarimetric Emissivity of Vegetation-Covered Soils: Simulation Results." *IEEE Geoscience and Remote Sensing Symposium*, vol.5, pp.2439-2441, July 2001.
5. A. Martinez-Vazquez, A.J. Camps, N. Duffo, M. Vall-llossera and J.M. Lopez-Sanchez, "Full Polarimetric Emissivity of Vegetation-Covered Soils: Vegetation Structure Effects." *IEEE Geoscience and Remote Sensing Symposium*, vol.6, pp.3542-3544, 2002.
6. J. Fortuny-Guasch, A. Martinez-Vazquez, D. Riccio, J.M. Lopez-Sanchez and J.D. Ballester, "Experimental Validation of an Electromagnetic Model for Rice Crops Using a Wide-Band Polarimetric Radar." *IEEE Geoscience and Remote Sensing Symposium*, vol.4, Pages: 2866-2868, July 2003.
7. J. Fortuny, A. Martinez-Vazquez, J.M. Lopez and J.D. Ballester, "Electromagnetic model of Rice Crops for Wide Band POLINSAR". *Proc. SPIE Remote Sensing for Agriculture, Ecosystems, and Hydrology V*, vol.5232, pp.635-643, Barcelona 2003.

8. A. Martinez-Vazquez and J. Fortuny-Guasch, “Monitoring Structural Changes and Stability of the Snow Cover with a Ground-Based Synthetic Aperture Radar.” *URSI 2005 Commission F Symposium*, Barza d'Ispra (Italy), April 2005.

   http://ursi-f-2005.jrc.it/fullpapers/URSI-F-2005-Art_7.3.pdf

9. A. Martinez-Vazquez and J. Fortuny-Guasch, “Avalanche And Snowfall Monitoring With A Ground-Based Synthetic Aperture Radar.” *4th International Workshop on ERS SAR Interferometry FRINGE 2005*, ESA Frascati (Italy), November 2005.

   http://earth.esa.int/workshops/fringe2005/proceedings/papers/23_martinezvazquez.pdf

10. A. Martinez-Vazquez and J. Fortuny-Guasch, “Feasibility of Snow Avalanche Volume Retrieval by GB-SAR Imagery.” *IEEE Geoscience and Remote Sensing Symposium*, Denver 2006.

11. A. Monerris, M. Vall-llossera, A. Camps, R. Sabia, A. Martinez-Vazquez, I. Ledesma and M. Piles, “Field Experiments to Improve the Soil Emission Models at L-band: Contribution of the UPC to the ESA SMOS Mission.” *2nd International Symposium on Recent Advances in Quantitative Remote Sensing: RAQRS'II*. Torrent (Spain), September 2006.

12. A. Martinez-Vazquez and J. Fortuny-Guasch, “Snow Avalanche Detection and Classification Algorithm for GB-SAR Imagery.” *IEEE Geoscience and Remote Sensing Symposium*, Barcelona 2007.

13. A. Martinez-Vazquez and J. Fortuny-Guasch, “UWB MIMO Radar Arrays For Small Area Surveillance Applications.” *European Conference on Antennas and Propagation*, Edinburgh (UK) 2007.

A.3. Other publications

14. A. Martinez-Vazquez and J. Fortuny-Guasch, “Snow Cover Monitoring in the Swiss Alps with a GB-SAR.” *IEEE Geoscience and Remote Sensing Society Newsletter*, pp.11-14. March 2006.

    http://www.grss-ieee.org/files/grsNL0306.pdf

15. A. Martinez-Vazquez and J. Fortuny-Guasch, “3 winters of snow monitoring with the LISA instrument in the Sion Valley (CH): 2003-2006.” *Technical report EUR 22533 EN, ISSN 1018-5593. Office for Official Publications of the European Communities*, Luxembourg, October 2006.

16. G. Antonello, A. Martinez-Vazquez, J. Fortuny-Guasch, M. Freppaz and M. Maggioni, “Il radar “LISA” per le valanghe.” *Magazine Neve e Valanghe of the Associazione Interregionale Neve e Valanghe (AINEVA)*, Italy, November 2007.

17. A. Martinez-Vazquez, J. Fortuny-Guasch and G. Antonello, “Two winters of snow monitoring with the LISA instrument in Alagna Valsesia – Val d’Olen (I): 2005-2007.” *Technical report EUR 22947 EN, ISSN 1018-5593. Office for Official Publications of the European Communities*, Luxembourg, October 2007.

B. Nomenclature

B.1. List of acronyms

1-D	One-Dimensional
24/7	24 hours operation, 7 days a week
2-D	Two-Dimensional
3-D	Three-Dimensional
CH1903	Geodetic datum of the Swiss coordinate system
CTR	Carta Tecnica Regionale
CW	Continuous Wave
DDS	Direct Digital Synthesis
DEM	Digital Elevation Model
DInSAR	Differential Interferometric SAR
DTM	Digital Terrain Model
EC	European Commission
ED50	European Datum, 1950
E-N	Easting-Northing coordinates in an UTM coordinates system
ERS	European Remote-sensing Satellite
FFT	Fast Fourier Transform
FFT2	Two-dimensional Fast Fourier Transform
FM	Frequency Modulated
FOV	Field-of-view
FPFA	Far-field Pseudo-polar Format Algorithm
GB	Giga Byte
GB-SAR	Ground-Based Synthetic Aperture Radar
GPIB	General Purpose Interface Bus

GPS	Global Positioning System
GSM	Global System for Mobile communications
HP-IB	Hewlett Packard Interface Bus
iFFT2	Two-dimensional inverse Fast Fourier Transform
ISAR	Inverse Synthetic Aperture Radar
InSAR	Interferometric SAR
IPSC	Institute for the Proctection and Security of the Citicen
JERS	Japan Earth-Resources Satellite
JRC	Joint Research Centre
LISA	Linear SAR
LOS	Line-of-sight
MB	Mega Byte
PC	Personal Computer
Radar	Radio Detection and Ranging
Roma40	Gauss-Boaga reference datum for Italy, 1940.
SAR	Synthetic Aperture Radar
SIR	Shuttle Imaging Radar
SLAR	Side-Looking Airborne Radar
SMS	Short Message Service
SNR	Signal to Noise Ratio
RAR	Real Aperture Radar
RF	Radio Frequency
Rx	Reception channel or antenna
SERAC	Sensors, Radar Technologies and Cybersecurity
SF	Stepped Frequency
SLF	Schnee- und Lawinenforschung (Snow and Avalanche Research)
SWE	Snow Water Equivalent
TDBA	Time-domain Back-propagation Algorithm
Tx	Transmission channel or antenna
UPS	Uninterrupted Power Supply
USB	Universal Serial Bus
UTM	Universal Transverse Mercator
VNA	Vector Network Analyzer
WGS84	World Geodetic Survey 1984

B.2. List of symbols

B	Baseline
B_{crit}	Critical baseline perpendicular to the line o sight
B_h	Horizontal baseline
B_v	Vertical baseline
BW	Bandwidth
coh	Coherence magnitude
D	Antenna dimension
dco	Differential coherence
$DcRt$	Differential ratio
d_{shift}	Weighted shift displacement for co-registration
f	Central frequency
G	SAR data raw in the frequency domain
g, I	Focused SAR image
L	Aperture length
r	Slant Range
R_U	Unambiguous Range
α	Multiplicative constant for snow height retrieval
β	Additive constant for snow height retrieval
γ	Complex coherence
$\Delta\varphi$	Differential interferometric phase
Δd_s	Differential snow depth
Δr	Interferometric slant-range signal path difference
$\Delta r^{r\text{-}p}$	Signal path difference in a repeat-pass system
$\Delta r^{s\text{-}p}$	Signal path difference in a single-pass system
ΔR	Resolution in range direction
ΔX	Resolution in cross-range direction
Δx_a	Spacing along antenna trajectory
ε	Complex dielectric constant
ε'	Real part of the dielectric constant
ε''	Imaginary part of the dielectric constant
ζ	Averaged topographic slope
θ	Horizontal azimuth angle

θ_h	Look angle with respect to the horizontal plane
θ_i	Incidence angle with respect to the normal of the surface
θ_n	Look angle with respect to the vertical plane
λ, λ_0	Central radar wavelength in free space
λ_s	Central radar wavelength in the snow
ρ_s	Snow density
σ_h	Standard deviation of height
σ_φ	Standard deviation of phase
τ	Angle of the slant-range to the baseline
ω	Angle of the horizontal plane to the baseline

B.3. Radar band designations

HF	3 – 30 MHz	100 m - 10 m
VHF	30 – 300 MHz	10 m - 1 m
UHF	300 – 1000 MHz	100 cm - 30 cm
L	1 – 2 GHz	30 cm - 15 cm
S	2 – 4 GHz	15 cm - 7.5 cm
C	4 – 8 GHz	7.5 cm - 3.75 cm
X	8 – 12 GHz	3.75 cm - 2.50 cm
Ku	12 – 18 GHz	2.50 cm - 1.67 cm
K	18 – 27 GHz	1.67 cm - 1.11 cm
Ka	27 – 40 GHz	1.11 cm - .75 cm
V	40 – 75 GHz	7.5 mm - 4.0 mm
W	75 – 110 GHz	4.0 mm - 2.7 mm
mm	110 – 300 GHz	2.7 mm - 1.0 mm

C. Fingertron actuator

C.1. Control circuit

The electronic circuit for the *Fingertron* control unit was specifically developed for the LISA instrument with the collaboration of Cesar De La Jara Sánchez, electronic engineer from the Jicamarca Radio Observatory (Peru), during a 6 month internship at the Joint Research Centre (Ispra, Italy) in 2006.

As stated in Section 3.2.4, the *Fingertron* is composed of two elements: a solenoid (the electromechanical actuator) that is installed in the device to be switched on and off, and a box containing the power supply and the electronics to control the solenoid. The solenoid used is a tubular push model (Ø20 or Ø25 mm), powered by a 12VDC 1A power supply unit Tracopower model Tom 12112 while the USB interface to the PC was implemented with the FTDI's MM232R development module (http://www.ftdichip.com/Products/EvaluationKits/MM232R.htm).

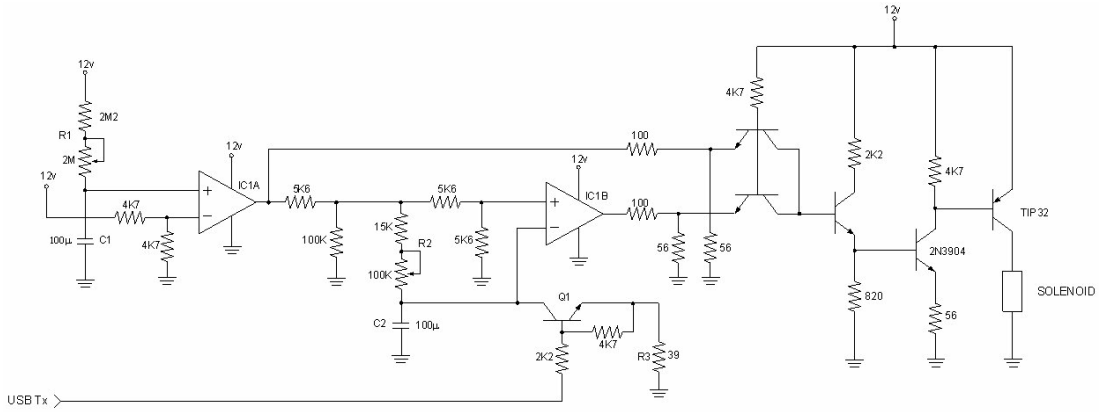

Fig. C.1. Electronic circuit for controlling the *Fingertron*.

Figure C.1 shows a schematic diagram of the electronic circuit controlling the mechanical finger actuator, *Fingertron*. As can be appreciated, it is mostly based on simple and economic discrete components. Note that the USB interface is not included in the electronics schematic: a simple "USB Tx" signal is used coming from the MM232R USB-to-RS232 module. Actually, the above mentioned module outputs the information received by the USB port of the PC in the stream format of the standard RS-232-C physical layer

[75]. Nevertheless, inverse logic is needed in the control circuit for the *Fingertron*, that is, marks are represented by 0V while spaces by a 5V signal level. To this aim a configuration parameter in the MM232R module must be properly set to configure the transmitting pin with inverted logic.

Figure C.2 shows the timing diagram for the control circuit of the *Fingertron* actuator. In the next paragraphs a detailed description of the circuit's operation follows.

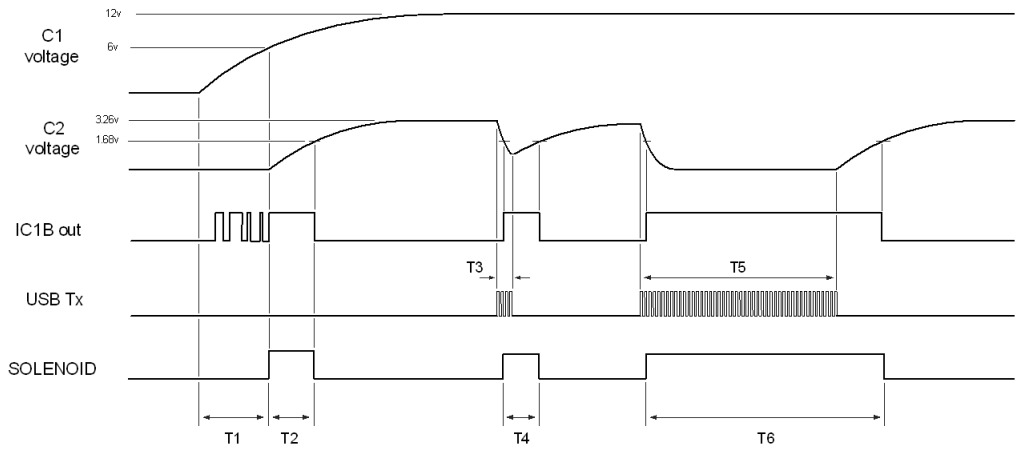

Fig. C.2. Timing diagram of the *Fingertron* control circuit.

T1 is a time delay between the circuit power up and the solenoid activation for implementing the automatic mode of the actuator. This delay, in addition, is used to avoid uncontrolled pulses coming from the USB port and to wait for the stabilization of the 220VAC line. When the circuit is powered, the capacitor C1 starts charging through R1. This voltage is directly applied to the positive input of IC1A and its value is determined by Equation (C.1):

$$V_{\mathrm{C1}}(t) = V_o\left(1 - e^{-t/(\mathrm{R1}\cdot\mathrm{C1})}\right), \tag{C.1}$$

where V_o = 12V, R1 ranges from 2.2 to 4.2 MΩ and C1=100 μF. When V_{C1} is larger than the negative input of IC1A (6V), the output of the operational amplifier goes to high level, sending a pulse to the solenoid. The time interval T1 is given by Equation (C.2):

$$\mathrm{T1} = -\mathrm{C1}\cdot\mathrm{R1}\cdot\ln\left(1 - 6/12\right). \tag{C.2}$$

Considering the range of R1, T1 can be adjusted from 152.49 to 291.1 s (2.54 to 4.85 min).

T2 is the duration of the first pulse sent to the solenoid. When the output of IC1A goes high, the output of IC1B goes also high and a pulse is sent to the solenoid. Then C2 starts charging through R2. If Q1 is cut (no data from the USB interface), the voltage in C2 goes directly to the negative input of IC1B. The output of IC1B will switch low when the voltage in C2 is larger than 1.68V. The time interval T2 is given by Equation (C.3):

$$\mathrm{T2} = -\mathrm{C2}\cdot\mathrm{R2}\cdot\ln\left(1 - 1.68/3.26\right). \tag{C.3}$$

Considering the range of R2 (15 to 115 KΩ), T2 can be adjusted from 1.1 to 8.3 s.

The USB interface of the circuit allows the reception of a signal able to activate the solenoid (manual mode of the *Fingertron* described in Section 3.2.4). An RS-232 typical stream is composed by one start bit, 8 data bits and one stop bit. With the inverted logic set up in the MM232R the start bit will be a high level voltage while the stop bit will be a low level voltage. If transmitting all the data bits to 0 (a 00 hexadecimal word) the inverted logic of the MM232R will output a square 5V signal with 90% of duty cycle at the point "USB Tx" of the circuit.

T4 is the duration of the pulse sent to the solenoid when using the USB interface of the circuit. In the stationary state the solenoid is not powered, the output of IC1A is high, C2 is charged to 3.26V and the output of IC1B is low. A level of 4V or higher at the base of Q1 causes the saturation of the transistor and the discharge of C2 through R3 (the signal from the USB interface is 5V when transmitting 00 words). When the voltage at C2 is below 1.68V, the output of IC1B goes high and sends a pulse to the solenoid.

Considering that the discharging resistor and the time of the low level pulse are much smaller than the charging resistor and the time of the high level pulse, the capacitor will be completely discharged in a few milliseconds. A baud rate of 9600 bps, a data length of 8 bits and one stop bit are recommended for proper operation. Considering the before mentioned parameters, 24 data words with 00 value are enough for completely discharging C2 and thus activating the solenoid for the interval T2.

T3 is the length of a short stream received by the USB interface, that is, a stream that does not fully discharge C2 but causes a voltage drop high enough ($V_{C2} < 1.68$V) to switch low the output of IC1B and send a short pulse to the solenoid. The length of the resultant pulse T4 will be less than T2.

Finally, T5 is the length of a long stream received by the USB interface, that is, a stream that fully discharges C2 and keeps it discharged an additional period. The duration of the resultant pulse will be $T6 = T_{stream} + T_{charge}$, where $T_{charge} = T2$ and T_{stream} is determined by the number of transmitted bytes (theoretically unlimited) over the 24 initially necessary to discharge C2 at 9600 bps.

C.2. Control software

The *Fingertron* allows a manual operation mode through a USB interface by using the MM232R module from FTDI chip. To exploit this functionality a small console application in C++ (FGTRcontrol.exe) has been developed that communicates with the MM232R module to set the necessary parameters and send the data stream defined by the user in a configuration text file (fgtr2send.txt).

```
FINGERTRON 20060909.
Alberto Martinez-Vazquez, Cesar De La Jara, Giuseppe Antonello.

SelfPowered: 0
InvertTXD: 1
BaudRate: 9600
DataFormat: HEX
Data: 00 00 00 00 00 00 00 00 00 00 00 00 00 00 00 00 00 00 00 00 00 00 00 00
```

Fig. C.3. Example of configuration file for *Fingertron*: fgtr2send.txt.

Figure C.3 shows an example of configuration file: there is a header of two lines not parsed by the program and a set of parameters defined by the triplets keyword, colon and value. The accepted keywords and possible values are:

- *SelfPowered*: 0 = bus powered (power the MM232R from the USB hub of the PC); 1 = self powered (power the MM232R from an external power supply).
- *InvertTXD*: 0 = standard RS-232 signal levels. 1 = invert the transmission channel: the serial interface is instructed to work with a logical level high at 0 V and a logical level low at 5V.
- *BaudRate*: velocity of transmission in bps.
- *DataFormat*: format of the data written on the *Data* section. DEC = decimal; HEX = hexadecimal; TXT = plain text.
- *Data*: data stream to transmit in the format specified by *DataFormat*.

The Win32 console application FGTRcontrol.exe simply parses the before mentioned configuration file and sends both the parameters and the data stream to the MM232R module. To this aim, the manufacturer of the module provides the appropriate driver and libraries to use when linking the application. The syntax of the application can be retrieved by executing FGTRcontrol.exe without parameters and is shown in Figure C.4. Note that more than one MM232R module can be simultaneously connected to the PC, so the optional parameter `deviceindex` is used to direct the data stream to the module specified by the user. The option `-listdevices` can be used to retrieve a list of the MM232R modules connected to the PC.

```
FGTRcontrol
Description: Control of the FTDI chip MM232R USB driver
     for the user interface of the FINGERTRON.

Syntax:

  FGTRcontrol -help
  FGTRcontrol -listdevices
  FGTRcontrol -send [deviceindex] [filename]
  FGTRcontrol -send [filename]

The text file [filename] contains the device and transmission parameters
as well as the data to transmit.
```

Fig. C.4. Console application syntax to control the *Fingertron*: FGTRcontrol.exe.

C.3. Scheduled task

As mentioned in the Section 3.2.4, a way of assuring that the device where the *Fingertron* is installed is permanently switched on is by periodically interrogating the device and trying to switch it on in case of no answer.

This solution is applied through a scheduled task that executes a batch script implementing the above mentioned procedure. Figure C.5 shows the batch script used: first of all a network ping command is sent to the IP address of the VNA (it is assumed that both the PC and the VNA are connected to the internal network of the LISA instrument).

In case of no response to the ping it is assumed that the VNA is off, so the program FGTRcontrol.exe is executed to send the appropriate command to the *Fingertron* in order to switch on the instrument.

```
:: FGTRpowerCheck.bat
::
:: Checks that the VNA is up and running, and in case it is not
:: tries to power it on with the Fingertron.
::
:: To be added to the Windows scheduler task manager of the
:: PC, triggered every 15 minutes.
:: Be sure to start the task only if the PC has been idle for at
:: least 15 minutes. Otherwise the action of the Fingertron could
:: switch the instrument off.


:: Sets the IP of the device to control
set FGTRIP=192.168.1.232

:: Logs the date/time of the last call to the batch
echo FGTRpowerCheck: %DATE% %TIME%>>FGTRpowerCheck.log

:: VNA does not respond to ping => VNA off
ping -n 1 %FGTRIP%
IF %ERRORLEVEL%==1 (
   FGTRcontrol -send 0 fgtr2send.txt >> FGTRpowerCheck.log
   echo. >> FGTRpowerCheck.log
)
```

Fig. C.5. Batch script to check the VNA power status and switch it on in case of being off.

D. Data catalogue

D.1. Catalogue organization

This annex lists the days and time intervals where data was acquired by the LISA instrument on both test sites presented in Chapter 4. The catalogue is organized in five columns:

a) ### - This is an incremental number starting with 1 the first day of field campaign in a given test site and increasing by 1 every day of field campaign;

b) Day - Day number in the hydrological year. The hydrological year starts the 1st of October (Day = 1), and finishes the 30th of September. Day = 93, for example, corresponds to the first of January. Note that a line has been intentionally left blank between consecutive hydrological years.

c) Date - Date in the format YYYY/MM/DD of a given day of data acquisition;

d) Time interval - First and last time stamp of the first and last data files acquired that day of measurement;

e) Int - Indicates an interruption on the data acquisition flow where the mark (<-) is present. No mark means uninterrupted measurements between days.

D.2. Sion Valley (Switzerland)

The following is a list with the days and time intervals of the data acquisitions made on the test site of the Sion Valley.

LISA data catalogue in SION VALLEY

###	Day	Date	Time interval	Int
1	78	2003/12/17	16.35h - 23.49h	
2	79	2003/12/18	00.16h - 23.46h	
3	80	2003/12/19	00.13h - 23.44h	
4	81	2003/12/20	00.11h - 23.42h	
5	82	2003/12/21	00.09h - 06.56h	
6	105	2004/01/13	11.10h - 23.34h	<-
7	106	2004/01/14	00.01h - 23.33h	
8	107	2004/01/15	00.01h - 23.32h	
9	108	2004/01/16	00.00h - 23.58h	
10	109	2004/01/17	00.25h - 23.56h	
11	110	2004/01/18	00.23h - 23.39h	
12	111	2004/01/19	00.06h - 23.39h	
13	112	2004/01/20	00.06h - 23.36h	
14	113	2004/01/21	00.03h - 23.33h	
15	114	2004/01/22	00.00h - 23.58h	
16	115	2004/01/23	00.25h - 23.47h	
17	116	2004/01/24	00.11h - 23.44h	
18	117	2004/01/25	00.09h - 23.40h	
19	118	2004/01/26	00.04h - 23.46h	
20	119	2004/01/27	00.12h - 23.19h	
21	140	2004/02/17	13.28h - 23.55h	<-
22	141	2004/02/18	00.21h - 06.09h	
23	150	2004/02/27	12.52h - 13.19h	<-
24	167	2004/03/15	14.39h - 23.40h	<-

```
 25 : 168 : 2004/03/16  00.08h - 23.36h
 26 : 169 : 2004/03/17  00.03h - 23.58h
 27 : 170 : 2004/03/18  00.26h - 23.54h
 28 : 171 : 2004/03/19  00.21h - 23.48h
 29 : 172 : 2004/03/20  00.15h - 23.44h
 30 : 173 : 2004/03/21  00.11h - 23.40h
 31 : 174 : 2004/03/22  00.07h - 23.36h
 32 : 175 : 2004/03/23  00.03h - 23.58h
 33 : 176 : 2004/03/24  00.25h - 23.54h
 34 : 177 : 2004/03/25  00.21h - 23.49h
 35 : 178 : 2004/03/26  00.16h - 23.44h
 36 : 179 : 2004/03/27  00.11h - 23.39h
 37 : 180 : 2004/03/28  00.06h - 23.40h
 38 : 181 : 2004/03/29  00.08h - 23.36h
 39 : 182 : 2004/03/30  00.03h - 23.58h
 40 : 183 : 2004/03/31  00.26h - 23.54h
 41 : 184 : 2004/04/01  00.21h - 23.49h
 42 : 185 : 2004/04/02  00.16h - 23.45h
 43 : 186 : 2004/04/03  00.12h - 23.40h
 44 : 187 : 2004/04/04  00.07h - 23.34h
 45 : 188 : 2004/04/05  00.01h - 23.56h
 46 : 189 : 2004/04/06  00.23h - 23.51h
 47 : 190 : 2004/04/07  00.18h - 23.45h
 48 : 191 : 2004/04/08  00.12h - 23.40h
 49 : 192 : 2004/04/09  00.07h - 23.34h
 50 : 193 : 2004/04/10  00.01h - 23.56h
 51 : 194 : 2004/04/11  00.23h - 23.49h
 52 : 195 : 2004/04/12  00.17h - 23.44h
 53 : 196 : 2004/04/13  00.11h - 23.39h
 54 : 197 : 2004/04/14  00.06h - 23.34h
 55 : 198 : 2004/04/15  00.01h - 23.55h
 56 : 199 : 2004/04/16  00.22h - 23.50h
 57 : 200 : 2004/04/17  00.17h - 23.45h
 58 : 201 : 2004/04/18  00.12h - 23.39h
 59 : 202 : 2004/04/19  00.06h - 23.33h
 60 : 203 : 2004/04/20  00.00h - 23.55h
 61 : 204 : 2004/04/21  00.22h - 23.50h
 62 : 205 : 2004/04/22  00.17h - 23.44h
 63 : 206 : 2004/04/23  00.11h - 23.39h
 64 : 207 : 2004/04/24  00.06h - 23.34h
 65 : 208 : 2004/04/25  00.01h - 23.56h
 66 : 209 : 2004/04/26  00.23h - 23.50h
 67 : 210 : 2004/04/27  00.17h - 23.45h
 68 : 211 : 2004/04/28  00.12h - 23.40h
 69 : 212 : 2004/04/29  00.07h - 23.35h
 70 : 213 : 2004/04/30  00.02h - 23.42h
 71 : 214 : 2004/05/01  00.09h - 23.37h
 72 : 215 : 2004/05/02  00.04h - 23.59h
 73 : 216 : 2004/05/03  00.26h - 23.52h
 74 : 217 : 2004/05/04  00.19h - 23.47h
 75 : 218 : 2004/05/05  00.14h - 23.42h
 76 : 219 : 2004/05/06  00.09h - 23.37h
 77 : 220 : 2004/05/07  00.04h - 23.59h
 78 : 221 : 2004/05/08  00.26h - 14.25h
 79 : 230 : 2004/05/17  15.42h - 23.50h  <-
 80 : 231 : 2004/05/18  00.17h - 23.45h
 81 : 232 : 2004/05/19  00.12h - 23.40h
 82 : 233 : 2004/05/20  00.08h - 23.36h
 83 : 234 : 2004/05/21  00.03h - 23.58h
 84 : 235 : 2004/05/22  00.25h - 23.53h
 85 : 236 : 2004/05/23  00.20h - 23.48h
 86 : 237 : 2004/05/24  00.15h - 23.43h
 87 : 238 : 2004/05/25  00.10h - 23.38h
 88 : 239 : 2004/05/26  00.05h - 23.34h
 89 : 240 : 2004/05/27  00.01h - 23.57h
 90 : 241 : 2004/05/28  00.24h - 23.53h
 91 : 242 : 2004/05/29  00.20h - 23.48h
 92 : 243 : 2004/05/30  00.15h - 23.43h
 93 : 244 : 2004/05/31  00.10h - 23.37h
 94 : 245 : 2004/06/01  00.04h - 23.59h
 95 : 246 : 2004/06/02  00.26h - 23.54h
 96 : 247 : 2004/06/03  00.21h - 23.49h
 97 : 248 : 2004/06/04  00.16h - 23.44h
 98 : 249 : 2004/06/05  00.11h - 23.40h
 99 : 250 : 2004/06/06  00.07h - 23.36h
100 : 251 : 2004/06/07  00.03h - 23.58h
101 : 252 : 2004/06/08  00.25h - 23.54h
102 : 253 : 2004/06/09  00.21h - 23.50h
103 : 254 : 2004/06/10  00.17h - 23.46h
104 : 255 : 2004/06/11  00.13h - 23.42h
105 : 256 : 2004/06/12  00.09h - 23.37h
106 : 257 : 2004/06/13  00.04h - 23.58h
107 : 258 : 2004/06/14  00.25h - 23.53h
108 : 259 : 2004/06/15  00.20h - 23.48h
109 : 260 : 2004/06/16  00.15h - 23.43h
110 : 261 : 2004/06/17  00.10h - 23.38h
111 : 262 : 2004/06/18  00.05h - 23.33h
112 : 263 : 2004/06/19  00.00h - 23.56h
113 : 264 : 2004/06/20  00.23h - 23.50h
114 : 265 : 2004/06/21  00.18h - 23.46h
115 : 266 : 2004/06/22  00.13h - 23.42h
116 : 267 : 2004/06/23  00.10h - 23.38h
117 : 268 : 2004/06/24  00.05h - 23.34h
118 : 269 : 2004/06/25  00.02h - 23.57h
119 : 270 : 2004/06/26  00.24h - 23.52h
120 : 271 : 2004/06/27  00.19h - 23.46h
121 : 272 : 2004/06/28  00.14h - 23.42h
122 : 273 : 2004/06/29  00.09h - 23.37h
123 : 274 : 2004/06/30  00.04h - 23.59h
124 : 275 : 2004/07/01  00.26h - 23.55h
125 : 276 : 2004/07/02  00.22h - 23.50h
126 : 277 : 2004/07/03  00.17h - 23.44h
127 : 278 : 2004/07/04  00.11h - 23.40h
128 : 279 : 2004/07/05  00.08h - 23.36h
129 : 280 : 2004/07/06  00.03h - 23.59h
130 : 281 : 2004/07/07  00.27h - 23.55h
131 : 282 : 2004/07/08  00.23h - 23.51h
132 : 283 : 2004/07/09  00.19h - 23.47h
133 : 284 : 2004/07/10  00.14h - 23.43h
134 : 285 : 2004/07/11  00.10h - 23.39h
135 : 286 : 2004/07/12  00.06h - 23.34h
136 : 287 : 2004/07/13  00.01h - 23.58h
137 : 288 : 2004/07/14  00.25h - 23.54h
138 : 289 : 2004/07/15  00.22h - 23.52h
139 : 290 : 2004/07/16  00.19h - 23.48h
140 : 291 : 2004/07/17  00.15h - 23.45h
141 : 292 : 2004/07/18  00.12h - 23.42h
142 : 293 : 2004/07/19  00.09h - 15.58h

143 :  96 : 2005/01/04  12.47h - 23.50h
144 :  97 : 2005/01/05  00.01h - 23.53h
145 :  98 : 2005/01/06  00.04h - 23.57h
146 :  99 : 2005/01/07  00.08h - 23.51h
147 : 100 : 2005/01/08  00.02h - 23.56h
148 : 101 : 2005/01/09  00.07h - 23.51h
149 : 102 : 2005/01/10  00.02h - 23.57h
150 : 103 : 2005/01/11  00.07h - 23.52h
151 : 104 : 2005/01/12  00.03h - 23.59h
152 : 105 : 2005/01/13  00.10h - 23.56h
153 : 106 : 2005/01/14  00.07h - 23.53h
154 : 107 : 2005/01/15  00.04h - 23.51h
155 : 108 : 2005/01/16  00.01h - 23.59h
156 : 109 : 2005/01/17  00.10h - 23.58h
157 : 110 : 2005/01/18  00.08h - 23.57h
158 : 111 : 2005/01/19  00.07h - 23.57h
159 : 112 : 2005/01/20  00.08h - 23.57h
160 : 113 : 2005/01/21  00.08h - 23.57h
161 : 114 : 2005/01/22  00.08h - 23.58h
162 : 115 : 2005/01/23  00.09h - 23.49h
163 : 116 : 2005/01/24  00.00h - 23.51h
164 : 117 : 2005/01/25  00.01h - 23.53h
165 : 118 : 2005/01/26  00.04h - 23.55h
166 : 119 : 2005/01/27  00.06h - 23.52h
167 : 120 : 2005/01/28  00.06h - 22.43h
168 : 139 : 2005/02/16  13.49h - 23.55h  <-
169 : 140 : 2005/02/17  00.06h - 23.58h
170 : 141 : 2005/02/18  00.08h - 23.56h
171 : 142 : 2005/02/19  00.06h - 23.58h
172 : 143 : 2005/02/20  00.09h - 23.52h
173 : 144 : 2005/02/21  00.03h - 23.58h
```

174 : 145 : 2005/02/22 00.09h - 23.54h
175 : 146 : 2005/02/23 00.05h - 23.50h
176 : 147 : 2005/02/24 00.01h - 23.58h
177 : 148 : 2005/02/25 00.09h - 09.48h
178 : 155 : 2005/03/04 11.11h - 23.55h <-
179 : 156 : 2005/03/05 00.06h - 23.55h
180 : 157 : 2005/03/06 00.07h - 23.56h
181 : 158 : 2005/03/07 00.08h - 23.58h
182 : 159 : 2005/03/08 00.10h - 23.53h
183 : 160 : 2005/03/09 00.04h - 23.55h
184 : 161 : 2005/03/10 00.06h - 23.57h
185 : 162 : 2005/03/11 00.09h - 23.50h
186 : 163 : 2005/03/12 00.02h - 23.54h
187 : 164 : 2005/03/13 00.05h - 23.48h
188 : 165 : 2005/03/14 00.00h - 23.50h
189 : 166 : 2005/03/15 00.02h - 23.50h
190 : 167 : 2005/03/16 00.02h - 23.59h
191 : 168 : 2005/03/17 00.10h - 23.53h
192 : 169 : 2005/03/18 00.04h - 23.56h
193 : 170 : 2005/03/19 00.07h - 23.58h
194 : 171 : 2005/03/20 00.09h - 23.51h
195 : 172 : 2005/03/21 00.02h - 23.55h
196 : 173 : 2005/03/22 00.06h - 23.59h
197 : 174 : 2005/03/23 00.10h - 23.49h
198 : 175 : 2005/03/24 00.00h - 23.49h
199 : 176 : 2005/03/25 00.00h - 23.59h
200 : 177 : 2005/03/26 00.11h - 23.49h
201 : 178 : 2005/03/27 00.00h - 23.54h
202 : 179 : 2005/03/28 00.06h - 23.57h
203 : 180 : 2005/03/29 00.08h - 23.49h
204 : 181 : 2005/03/30 00.00h - 23.53h
205 : 182 : 2005/03/31 00.04h - 23.57h
206 : 183 : 2005/04/01 00.08h - 23.50h
207 : 184 : 2005/04/02 00.01h - 23.56h
208 : 185 : 2005/04/03 00.07h - 23.54h
209 : 186 : 2005/04/04 00.05h - 23.54h
210 : 187 : 2005/04/05 00.05h - 23.55h
211 : 188 : 2005/04/06 00.06h - 23.56h
212 : 189 : 2005/04/07 00.07h - 23.55h
213 : 190 : 2005/04/08 00.06h - 23.51h
214 : 191 : 2005/04/09 00.02h - 23.49h
215 : 192 : 2005/04/10 00.00h - 23.51h
216 : 193 : 2005/04/11 00.03h - 23.49h
217 : 194 : 2005/04/12 00.01h - 23.59h
218 : 195 : 2005/04/13 00.11h - 23.59h
219 : 196 : 2005/04/14 00.10h - 23.49h
220 : 197 : 2005/04/15 00.00h - 23.51h
221 : 198 : 2005/04/16 00.03h - 23.57h
222 : 199 : 2005/04/17 00.08h - 23.55h
223 : 200 : 2005/04/18 00.06h - 23.55h
224 : 201 : 2005/04/19 00.06h - 23.55h
225 : 202 : 2005/04/20 00.06h - 23.56h
226 : 203 : 2005/04/21 00.07h - 23.58h
227 : 204 : 2005/04/22 00.10h - 23.53h
228 : 205 : 2005/04/23 00.04h - 23.53h
229 : 206 : 2005/04/24 00.04h - 23.55h
230 : 207 : 2005/04/25 00.06h - 23.59h
231 : 208 : 2005/04/26 00.10h - 23.55h
232 : 209 : 2005/04/27 00.07h - 23.54h
233 : 210 : 2005/04/28 00.06h - 23.58h
234 : 211 : 2005/04/29 00.09h - 23.49h
235 : 212 : 2005/04/30 00.01h - 23.59h
236 : 213 : 2005/05/01 00.10h - 23.54h
237 : 214 : 2005/05/02 00.05h - 23.59h
238 : 215 : 2005/05/03 00.11h - 23.59h
239 : 216 : 2005/05/04 00.10h - 23.58h
240 : 217 : 2005/05/05 00.09h - 23.56h
241 : 218 : 2005/05/06 00.08h - 23.56h
242 : 219 : 2005/05/07 00.07h - 23.54h
243 : 220 : 2005/05/08 00.05h - 23.53h
244 : 221 : 2005/05/09 00.04h - 23.54h
245 : 222 : 2005/05/10 00.05h - 23.57h
246 : 223 : 2005/05/11 00.09h - 23.56h
247 : 224 : 2005/05/12 00.07h - 23.51h
248 : 225 : 2005/05/13 00.02h - 23.57h
249 : 226 : 2005/05/14 00.07h - 23.59h
250 : 227 : 2005/05/15 00.10h - 23.55h
251 : 228 : 2005/05/16 00.06h - 23.53h
252 : 229 : 2005/05/17 00.04h - 23.52h
253 : 230 : 2005/05/18 00.03h - 23.51h
254 : 231 : 2005/05/19 00.02h - 23.50h
255 : 232 : 2005/05/20 00.01h - 23.49h
256 : 233 : 2005/05/21 00.00h - 23.59h
257 : 234 : 2005/05/22 00.10h - 23.57h
258 : 235 : 2005/05/23 00.08h - 23.55h
259 : 236 : 2005/05/24 00.06h - 23.54h
260 : 237 : 2005/05/25 00.05h - 23.54h
261 : 238 : 2005/05/26 00.05h - 23.57h
262 : 239 : 2005/05/27 00.08h - 23.56h
263 : 240 : 2005/05/28 00.08h - 23.58h
264 : 241 : 2005/05/29 00.09h - 23.51h
265 : 242 : 2005/05/30 00.02h - 23.55h
266 : 243 : 2005/05/31 00.06h - 23.55h
267 : 244 : 2005/06/01 00.06h - 23.52h
268 : 245 : 2005/06/02 00.03h - 23.59h
269 : 246 : 2005/06/03 00.11h - 23.54h
270 : 247 : 2005/06/04 00.05h - 23.59h
271 : 248 : 2005/06/05 00.11h - 23.55h
272 : 249 : 2005/06/06 00.06h - 23.49h
273 : 250 : 2005/06/07 00.00h - 23.51h
274 : 251 : 2005/06/08 00.02h - 23.56h
275 : 252 : 2005/06/09 00.07h - 23.58h
276 : 253 : 2005/06/10 00.10h - 23.57h
277 : 254 : 2005/06/11 00.08h - 23.55h
278 : 255 : 2005/06/12 00.07h - 23.54h
279 : 256 : 2005/06/13 00.05h - 23.52h
280 : 257 : 2005/06/14 00.03h - 23.50h
281 : 258 : 2005/06/15 00.01h - 23.59h
282 : 259 : 2005/06/16 00.10h - 23.57h
283 : 260 : 2005/06/17 00.08h - 23.56h
284 : 261 : 2005/06/18 00.07h - 23.54h
285 : 262 : 2005/06/19 00.05h - 23.54h
286 : 263 : 2005/06/20 00.05h - 23.55h
287 : 264 : 2005/06/21 00.06h - 23.57h
288 : 265 : 2005/06/22 00.08h - 23.59h
289 : 266 : 2005/06/23 00.10h - 23.51h
290 : 267 : 2005/06/24 00.02h - 23.54h
291 : 268 : 2005/06/25 00.05h - 23.51h
292 : 269 : 2005/06/26 00.02h - 23.51h
293 : 270 : 2005/06/27 00.02h - 23.55h
294 : 271 : 2005/06/28 00.06h - 23.49h
295 : 272 : 2005/06/29 00.00h - 23.54h
296 : 273 : 2005/06/30 00.05h - 23.49h
297 : 274 : 2005/07/01 00.00h - 23.57h
298 : 275 : 2005/07/02 00.08h - 23.57h
299 : 276 : 2005/07/03 00.08h - 23.51h
300 : 277 : 2005/07/04 00.02h - 23.57h
301 : 278 : 2005/07/05 00.09h - 23.53h
302 : 279 : 2005/07/06 00.04h - 23.49h
303 : 280 : 2005/07/07 00.00h - 23.49h
304 : 281 : 2005/07/08 00.00h - 23.54h
305 : 282 : 2005/07/09 00.05h - 23.50h
306 : 283 : 2005/07/10 00.01h - 23.58h
307 : 284 : 2005/07/11 00.09h - 23.55h
308 : 285 : 2005/07/12 00.06h - 23.55h
309 : 286 : 2005/07/13 00.07h - 23.49h
310 : 287 : 2005/07/14 00.00h - 23.50h
311 : 288 : 2005/07/15 00.02h - 23.58h
312 : 289 : 2005/07/16 00.10h - 23.55h
313 : 290 : 2005/07/17 00.07h - 23.53h
314 : 291 : 2005/07/18 00.05h - 23.48h
315 : 292 : 2005/07/19 00.00h - 23.49h
316 : 293 : 2005/07/20 00.01h - 23.50h
317 : 294 : 2005/07/21 00.01h - 23.55h
318 : 295 : 2005/07/22 00.07h - 23.59h
319 : 296 : 2005/07/23 00.11h - 23.51h
320 : 297 : 2005/07/24 00.02h - 23.52h
321 : 298 : 2005/07/25 00.04h - 23.52h
322 : 299 : 2005/07/26 00.04h - 23.53h
323 : 300 : 2005/07/27 00.04h - 23.59h

```
324 : 301 : 2005/07/28  00.10h - 23.59h
325 : 302 : 2005/07/29  00.11h - 23.59h
326 : 303 : 2005/07/30  00.11h - 23.49h
327 : 304 : 2005/07/31  00.00h - 23.50h
328 : 305 : 2005/08/01  00.02h - 23.53h
329 : 306 : 2005/08/02  00.05h - 23.55h
330 : 307 : 2005/08/03  00.07h - 23.57h
331 : 308 : 2005/08/04  00.09h - 23.58h
332 : 309 : 2005/08/05  00.09h - 23.49h
333 : 310 : 2005/08/06  00.00h - 23.54h
334 : 311 : 2005/08/07  00.05h - 23.58h
335 : 312 : 2005/08/08  00.10h - 23.51h
336 : 313 : 2005/08/09  00.03h - 23.57h
337 : 314 : 2005/08/10  00.08h - 23.50h
338 : 315 : 2005/08/11  00.02h - 23.53h
339 : 316 : 2005/08/12  00.04h - 23.56h
340 : 317 : 2005/08/13  00.08h - 23.49h
341 : 318 : 2005/08/14  00.01h - 23.52h
342 : 319 : 2005/08/15  00.04h - 23.54h
343 : 320 : 2005/08/16  00.06h - 23.56h
344 : 321 : 2005/08/17  00.08h - 23.59h
345 : 322 : 2005/08/18  00.11h - 23.49h
346 : 323 : 2005/08/19  00.01h - 23.50h
347 : 324 : 2005/08/20  00.02h - 23.52h
348 : 325 : 2005/08/21  00.04h - 23.53h
349 : 326 : 2005/08/22  00.05h - 23.54h
350 : 327 : 2005/08/23  00.05h - 23.55h

351 :  62 : 2005/12/01  16.28h - 23.56h
352 :  63 : 2005/12/02  00.07h - 23.55h
353 :  64 : 2005/12/03  00.07h - 23.55h
354 :  65 : 2005/12/04  00.07h - 22.54h
355 :  66 : 2005/12/05  00.03h - 22.43h  <-
356 :  67 : 2005/12/06  00.33h - 22.50h  <-
357 :  68 : 2005/12/07  00.53h - 22.53h  <-
358 :  69 : 2005/12/08  01.32h - 06.45h  <-
359 :  73 : 2005/12/12  13.33h - 23.51h  <-
360 :  74 : 2005/12/13  00.03h - 23.59h
361 :  75 : 2005/12/14  00.12h - 23.54h
362 :  76 : 2005/12/15  00.06h - 23.56h
363 :  77 : 2005/12/16  00.08h - 23.55h
364 :  78 : 2005/12/17  00.07h - 23.51h
365 :  79 : 2005/12/18  00.03h - 23.28h
366 :  80 : 2005/12/19  00.44h - 23.10h
367 :  81 : 2005/12/20  00.55h - 23.48h
368 :  82 : 2005/12/21  00.00h - 23.50h
369 :  83 : 2005/12/22  00.02h - 23.53h
370 :  84 : 2005/12/23  00.05h - 23.50h
371 :  85 : 2005/12/24  00.02h - 23.54h
372 :  86 : 2005/12/25  00.06h - 23.57h
373 :  87 : 2005/12/26  00.10h - 23.31h
374 :  88 : 2005/12/27  00.49h - 23.50h
375 :  89 : 2005/12/28  00.01h - 23.48h
376 :  90 : 2005/12/29  00.00h - 23.50h
377 :  91 : 2005/12/30  00.04h - 23.56h
378 :  92 : 2005/12/31  00.08h - 23.54h
379 :  93 : 2006/01/01  00.06h - 23.51h
380 :  94 : 2006/01/02  00.04h - 23.54h
381 :  95 : 2006/01/03  00.06h - 23.52h
382 :  96 : 2006/01/04  00.04h - 23.55h
383 :  97 : 2006/01/05  00.10h - 23.53h
384 :  98 : 2006/01/06  00.05h - 23.52h
385 :  99 : 2006/01/07  00.04h - 23.50h
386 : 100 : 2006/01/08  00.02h - 23.48h
387 : 101 : 2006/01/09  00.00h - 23.50h
388 : 102 : 2006/01/10  00.02h - 23.50h
389 : 103 : 2006/01/11  00.02h - 23.56h
390 : 104 : 2006/01/12  00.08h - 23.50h
391 : 105 : 2006/01/13  00.02h - 23.57h
392 : 106 : 2006/01/14  00.09h - 23.51h
393 : 107 : 2006/01/15  00.04h - 23.56h
394 : 108 : 2006/01/16  00.08h - 23.58h
395 : 109 : 2006/01/17  00.10h - 23.57h
396 : 110 : 2006/01/18  00.09h - 23.48h
397 : 111 : 2006/01/19  00.00h - 23.59h
398 : 112 : 2006/01/20  00.10h - 23.51h
399 : 113 : 2006/01/21  00.02h - 23.59h
400 : 114 : 2006/01/22  00.11h - 09.37h
401 : 126 : 2006/02/03  13.22h - 23.56h  <-
402 : 127 : 2006/02/04  00.07h - 23.53h
403 : 128 : 2006/02/05  00.04h - 23.50h
404 : 129 : 2006/02/06  00.01h - 23.59h
405 : 130 : 2006/02/07  00.10h - 23.56h
406 : 131 : 2006/02/08  00.07h - 23.54h
407 : 132 : 2006/02/09  00.05h - 23.52h
408 : 133 : 2006/02/10  00.03h - 23.50h
409 : 134 : 2006/02/11  00.01h - 23.59h
410 : 135 : 2006/02/12  00.10h - 23.57h
411 : 136 : 2006/02/13  00.08h - 23.55h
412 : 137 : 2006/02/14  00.06h - 23.53h
413 : 138 : 2006/02/15  00.04h - 23.51h
414 : 139 : 2006/02/16  00.03h - 23.58h
415 : 140 : 2006/02/17  00.09h - 23.56h
416 : 141 : 2006/02/18  00.07h - 23.53h
417 : 142 : 2006/02/19  00.04h - 23.50h
418 : 143 : 2006/02/20  00.01h - 23.58h
419 : 144 : 2006/02/21  00.09h - 23.55h
420 : 145 : 2006/02/22  00.06h - 23.51h
421 : 146 : 2006/02/23  00.02h - 23.59h
422 : 147 : 2006/02/24  00.10h - 23.54h
423 : 148 : 2006/02/25  00.05h - 23.48h
424 : 149 : 2006/02/26  00.00h - 23.54h
425 : 150 : 2006/02/27  00.05h - 23.48h
426 : 151 : 2006/02/28  00.00h - 23.55h
427 : 152 : 2006/03/01  00.06h - 23.51h
428 : 153 : 2006/03/02  00.02h - 23.58h
429 : 154 : 2006/03/03  00.09h - 23.54h
430 : 155 : 2006/03/04  00.05h - 23.50h
431 : 156 : 2006/03/05  00.01h - 23.55h
432 : 157 : 2006/03/06  00.06h - 23.49h
433 : 158 : 2006/03/07  00.02h - 23.49h
434 : 159 : 2006/03/08  00.01h - 23.54h
435 : 160 : 2006/03/09  00.06h - 23.58h
436 : 161 : 2006/03/10  00.09h - 23.49h
437 : 162 : 2006/03/11  00.01h - 23.53h
438 : 163 : 2006/03/12  00.05h - 23.57h
439 : 164 : 2006/03/13  00.09h - 23.49h
440 : 165 : 2006/03/14  00.01h - 23.53h
441 : 166 : 2006/03/15  00.04h - 23.56h
442 : 167 : 2006/03/16  00.08h - 23.59h
443 : 168 : 2006/03/17  00.11h - 23.51h
444 : 169 : 2006/03/18  00.03h - 23.55h
445 : 170 : 2006/03/19  00.07h - 23.58h
446 : 171 : 2006/03/20  00.10h - 23.49h
447 : 172 : 2006/03/21  00.01h - 23.52h
448 : 173 : 2006/03/22  00.04h - 23.56h
449 : 174 : 2006/03/23  00.07h - 23.59h
450 : 175 : 2006/03/24  00.11h - 23.50h
451 : 176 : 2006/03/25  00.02h - 23.54h
452 : 177 : 2006/03/26  00.06h - 23.52h
453 : 178 : 2006/03/27  00.04h - 23.56h
454 : 179 : 2006/03/28  00.08h - 23.59h
455 : 180 : 2006/03/29  00.11h - 23.50h
456 : 181 : 2006/03/30  00.02h - 23.53h
457 : 182 : 2006/03/31  00.05h - 23.56h
458 : 183 : 2006/04/01  00.08h - 23.48h
459 : 184 : 2006/04/02  00.00h - 23.51h
460 : 185 : 2006/04/03  00.03h - 23.55h
461 : 186 : 2006/04/04  00.07h - 23.59h
462 : 187 : 2006/04/05  00.11h - 23.50h
463 : 188 : 2006/04/06  00.02h - 23.54h
464 : 189 : 2006/04/07  00.06h - 23.57h
465 : 190 : 2006/04/08  00.09h - 23.49h
466 : 191 : 2006/04/09  00.01h - 23.54h
467 : 192 : 2006/04/10  00.06h - 23.57h
468 : 193 : 2006/04/11  00.09h - 23.49h
469 : 194 : 2006/04/12  00.01h - 23.54h
470 : 195 : 2006/04/13  00.05h - 23.58h
471 : 196 : 2006/04/14  00.10h - 23.52h
472 : 197 : 2006/04/15  00.04h - 23.57h
```

```
473 : 198 : 2006/04/16  00.08h - 23.49h
474 : 199 : 2006/04/17  00.01h - 23.55h
475 : 200 : 2006/04/18  00.07h - 23.49h
476 : 201 : 2006/04/19  00.00h - 23.55h
477 : 202 : 2006/04/20  00.07h - 23.49h
478 : 203 : 2006/04/21  00.01h - 23.56h
479 : 204 : 2006/04/22  00.08h - 23.51h
480 : 205 : 2006/04/23  00.03h - 23.59h
481 : 206 : 2006/04/24  00.11h - 23.54h
482 : 207 : 2006/04/25  00.06h - 23.59h
483 : 208 : 2006/04/26  00.11h - 23.52h
484 : 209 : 2006/04/27  00.04h - 23.58h
485 : 210 : 2006/04/28  00.10h - 23.52h
486 : 211 : 2006/04/29  00.03h - 23.58h
487 : 212 : 2006/04/30  00.10h - 23.54h
488 : 213 : 2006/05/01  00.06h - 23.49h
489 : 214 : 2006/05/02  00.01h - 23.56h
490 : 215 : 2006/05/03  00.08h - 23.52h
491 : 216 : 2006/05/04  00.03h - 23.48h
492 : 217 : 2006/05/05  00.00h - 23.53h
493 : 218 : 2006/05/06  00.05h - 23.59h
494 : 219 : 2006/05/07  00.11h - 23.53h
495 : 220 : 2006/05/08  00.05h - 23.59h
496 : 221 : 2006/05/09  00.11h - 23.52h
497 : 222 : 2006/05/10  00.04h - 23.48h
498 : 223 : 2006/05/11  00.00h - 23.53h
499 : 224 : 2006/05/12  00.05h - 23.48h
500 : 225 : 2006/05/13  00.00h - 23.55h
501 : 226 : 2006/05/14  00.07h - 07.42h
```

D.3. Alagna Valsesia (Italy)

Similarly, the following list presents the data catalogue for the test site in Alagna Valsesia (location of the instrument in Cimalegna).

```
LISA data catalogue in ALAGNA VALSESIA
==========================================
###   Day   Date        Time interval   Int
------------------------------------------
  1 : 177 : 2006/03/26  00.07h - 23.59h
  2 : 178 : 2006/03/27  00.08h - 23.56h
  3 : 179 : 2006/03/28  00.05h - 23.56h
  4 : 180 : 2006/03/29  00.06h - 23.59h
  5 : 181 : 2006/03/30  00.09h - 23.56h
  6 : 182 : 2006/03/31  00.05h - 23.54h
  7 : 183 : 2006/04/01  00.03h - 23.58h
  8 : 184 : 2006/04/02  00.08h - 23.54h
  9 : 185 : 2006/04/03  00.03h - 23.57h
 10 : 186 : 2006/04/04  00.07h - 23.56h
 11 : 187 : 2006/04/05  00.05h - 23.54h
 12 : 188 : 2006/04/06  00.04h - 23.53h
 13 : 189 : 2006/04/07  00.02h - 23.51h
 14 : 190 : 2006/04/08  00.00h - 23.58h
 15 : 191 : 2006/04/09  00.08h - 23.56h
 16 : 192 : 2006/04/10  00.06h - 23.54h
 17 : 193 : 2006/04/11  00.03h - 23.52h
 18 : 194 : 2006/04/12  00.01h - 23.50h
 19 : 195 : 2006/04/13  00.00h - 23.57h
 20 : 196 : 2006/04/14  00.06h - 23.55h
 21 : 197 : 2006/04/15  00.04h - 23.51h
 22 : 198 : 2006/04/16  00.01h - 23.58h
 23 : 199 : 2006/04/17  00.08h - 23.55h
 24 : 200 : 2006/04/18  00.04h - 23.58h
 25 : 201 : 2006/04/19  00.07h - 23.57h
 26 : 202 : 2006/04/20  00.06h - 23.56h
 27 : 203 : 2006/04/21  00.05h - 23.54h
 28 : 204 : 2006/04/22  00.03h - 23.52h
 29 : 205 : 2006/04/23  00.01h - 23.51h
 30 : 206 : 2006/04/24  00.00h - 23.58h
 31 : 207 : 2006/04/25  00.07h - 23.56h
 32 : 208 : 2006/04/26  00.05h - 23.54h
 33 : 209 : 2006/04/27  00.04h - 23.53h
 34 : 210 : 2006/04/28  00.02h - 23.50h
 35 : 211 : 2006/04/29  00.00h - 23.57h
 36 : 212 : 2006/04/30  00.07h - 23.56h
 37 : 213 : 2006/05/01  00.05h - 23.51h
 38 : 214 : 2006/05/02  00.00h - 23.56h
 39 : 215 : 2006/05/03  00.05h - 23.51h
 40 : 216 : 2006/05/04  00.00h - 23.55h
 41 : 217 : 2006/05/05  00.04h - 23.50h
 42 : 218 : 2006/05/06  00.00h - 23.58h
 43 : 219 : 2006/05/07  00.07h - 23.56h
 44 : 220 : 2006/05/08  00.05h - 23.54h
 45 : 221 : 2006/05/09  00.03h - 23.51h
 46 : 222 : 2006/05/10  00.00h - 23.58h
 47 : 223 : 2006/05/11  00.08h - 23.56h
 48 : 224 : 2006/05/12  00.05h - 23.53h
 49 : 225 : 2006/05/13  00.03h - 23.53h
 50 : 226 : 2006/05/14  00.02h - 23.51h
 51 : 227 : 2006/05/15  00.00h - 23.53h
 52 : 228 : 2006/05/16  00.03h - 23.53h
 53 : 229 : 2006/05/17  00.02h - 18.40h
 54 : 230 : 2006/05/18  13.26h - 23.55h  <-
 55 : 231 : 2006/05/19  00.07h - 23.54h
 56 : 232 : 2006/05/20  00.06h - 23.52h
 57 : 233 : 2006/05/21  00.05h - 23.51h
 58 : 234 : 2006/05/22  00.03h - 23.59h
 59 : 235 : 2006/05/23  00.12h - 23.58h
 60 : 236 : 2006/05/24  00.10h - 23.56h
 61 : 237 : 2006/05/25  00.09h - 23.55h
 62 : 238 : 2006/05/26  00.08h - 23.54h
 63 : 239 : 2006/05/27  00.06h - 23.52h
 64 : 240 : 2006/05/28  00.04h - 23.50h
 65 : 241 : 2006/05/29  00.02h - 23.59h
 66 : 242 : 2006/05/30  00.12h - 23.54h
 67 : 243 : 2006/05/31  00.06h - 23.49h
 68 : 244 : 2006/06/01  00.01h - 23.52h
 69 : 245 : 2006/06/02  00.04h - 23.55h
 70 : 246 : 2006/06/03  00.07h - 23.58h
 71 : 247 : 2006/06/04  00.11h - 23.49h
 72 : 248 : 2006/06/05  00.01h - 23.52h
 73 : 249 : 2006/06/06  00.05h - 09.12h

 74 :  52 : 2006/11/21  12.59h - 23.55h
 75 :  53 : 2006/11/22  00.01h - 23.54h
 76 :  54 : 2006/11/23  00.01h - 23.53h
 77 :  55 : 2006/11/24  00.00h - 23.56h
 78 :  56 : 2006/11/25  00.03h - 23.54h
 79 :  57 : 2006/11/26  00.01h - 23.53h
 80 :  58 : 2006/11/27  00.00h - 13.54h
 81 :  59 : 2006/11/28  15.31h - 23.54h  <-
 82 :  60 : 2006/11/29  00.00h - 23.59h
 83 :  61 : 2006/11/30  00.06h - 23.59h
 84 :  62 : 2006/12/01  00.06h - 13.58h
 85 :  65 : 2006/12/04  17.31h - 23.59h  <-
 86 :  66 : 2006/12/05  00.05h - 23.55h
 87 :  67 : 2006/12/06  00.02h - 23.59h
 88 :  68 : 2006/12/07  00.05h - 23.56h
 89 :  69 : 2006/12/08  00.03h - 23.56h
 90 :  70 : 2006/12/09  00.03h - 23.54h
 91 :  71 : 2006/12/10  00.00h - 23.55h
```

92	72	2006/12/11	00.02h - 23.54h	
93	73	2006/12/12	00.01h - 23.54h	
94	74	2006/12/13	00.00h - 14.11h	
95	75	2006/12/14	10.37h - 13.34h	<-
96	76	2006/12/15	09.27h - 14.12h	<-
97	77	2006/12/16	09.51h - 23.54h	<-
98	78	2006/12/17	00.01h - 23.56h	
99	79	2006/12/18	00.02h - 23.57h	
100	80	2006/12/19	00.03h - 23.57h	
101	81	2006/12/20	00.04h - 23.53h	
102	82	2006/12/21	00.00h - 23.55h	
103	83	2006/12/22	00.01h - 23.58h	
104	84	2006/12/23	00.05h - 23.56h	
105	85	2006/12/24	00.03h - 14.56h	
106	89	2006/12/28	10.43h - 23.57h	<-
107	90	2006/12/29	00.03h - 15.05h	
108	91	2006/12/30	14.00h - 23.57h	<-
109	92	2006/12/31	00.03h - 23.58h	
110	93	2007/01/01	00.05h - 23.54h	
111	94	2007/01/02	00.01h - 23.56h	
112	95	2007/01/03	00.03h - 23.55h	
113	96	2007/01/04	00.02h - 15.43h	
114	102	2007/01/10	00.09h - 23.53h	<-
115	103	2007/01/11	00.03h - 23.53h	
116	104	2007/01/12	00.03h - 09.09h	
117	108	2007/01/16	00.08h - 23.58h	<-
118	109	2007/01/17	00.11h - 23.57h	
119	110	2007/01/18	00.10h - 23.59h	
120	111	2007/01/19	00.11h - 23.59h	
121	112	2007/01/20	00.12h - 23.47h	
122	113	2007/01/21	00.00h - 23.47h	
123	114	2007/01/22	00.00h - 23.59h	
124	115	2007/01/23	00.12h - 23.47h	
125	116	2007/01/24	00.00h - 23.47h	
126	117	2007/01/25	00.00h - 23.48h	
127	118	2007/01/26	00.00h - 23.59h	
128	119	2007/01/27	00.12h - 23.59h	
129	120	2007/01/28	00.11h - 23.59h	
130	121	2007/01/29	00.12h - 23.48h	
131	122	2007/01/30	00.00h - 23.49h	
132	123	2007/01/31	00.02h - 23.50h	
133	124	2007/02/01	00.03h - 23.51h	
134	125	2007/02/02	00.03h - 23.51h	
135	126	2007/02/03	00.04h - 23.51h	
136	127	2007/02/04	00.04h - 23.52h	
137	128	2007/02/05	00.05h - 23.58h	
138	129	2007/02/06	00.11h - 23.48h	
139	130	2007/02/07	00.00h - 23.48h	
140	131	2007/02/08	00.01h - 23.49h	
141	132	2007/02/09	00.02h - 23.59h	
142	133	2007/02/10	00.12h - 23.48h	
143	134	2007/02/11	00.00h - 23.49h	
144	135	2007/02/12	00.02h - 23.51h	
145	136	2007/02/13	00.04h - 23.53h	
146	137	2007/02/14	00.05h - 23.56h	
147	138	2007/02/15	00.09h - 23.59h	
148	139	2007/02/16	00.12h - 23.49h	
149	140	2007/02/17	00.02h - 23.52h	
150	141	2007/02/18	00.05h - 23.55h	
151	142	2007/02/19	00.08h - 23.59h	
152	143	2007/02/20	00.12h - 23.50h	
153	144	2007/02/21	00.03h - 23.53h	
154	145	2007/02/22	00.06h - 23.57h	
155	146	2007/02/23	00.10h - 23.49h	
156	147	2007/02/24	00.02h - 23.53h	
157	148	2007/02/25	00.06h - 23.57h	
158	149	2007/02/26	00.09h - 23.48h	
159	150	2007/02/27	00.01h - 23.52h	
160	151	2007/02/28	00.05h - 23.55h	
161	152	2007/03/01	00.08h - 23.58h	
162	153	2007/03/02	00.10h - 23.49h	
163	154	2007/03/03	00.02h - 23.47h	
164	155	2007/03/04	00.00h - 23.47h	
165	156	2007/03/05	00.01h - 23.57h	
166	157	2007/03/06	00.09h - 23.48h	
167	158	2007/03/07	00.01h - 23.51h	
168	159	2007/03/08	00.04h - 23.54h	
169	160	2007/03/09	00.06h - 23.55h	
170	161	2007/03/10	00.08h - 23.57h	
171	162	2007/03/11	00.10h - 23.59h	
172	163	2007/03/12	00.12h - 23.49h	
173	164	2007/03/13	00.02h - 23.52h	
174	165	2007/03/14	00.05h - 23.55h	
175	166	2007/03/15	00.07h - 23.58h	
176	167	2007/03/16	00.11h - 23.49h	
177	168	2007/03/17	00.01h - 23.51h	
178	169	2007/03/18	00.04h - 23.55h	
179	170	2007/03/19	00.07h - 23.47h	
180	171	2007/03/20	00.00h - 23.50h	
181	172	2007/03/21	00.03h - 23.53h	
182	173	2007/03/22	00.05h - 23.56h	
183	174	2007/03/23	00.09h - 23.59h	
184	175	2007/03/24	00.12h - 23.50h	
185	176	2007/03/25	00.03h - 23.50h	
186	177	2007/03/26	00.03h - 23.53h	
187	178	2007/03/27	00.06h - 23.56h	
188	179	2007/03/28	00.09h - 23.59h	
189	180	2007/03/29	00.11h - 23.47h	
190	181	2007/03/30	00.00h - 23.50h	
191	182	2007/03/31	00.03h - 23.52h	
192	183	2007/04/01	00.05h - 23.55h	
193	184	2007/04/02	00.08h - 23.58h	
194	185	2007/04/03	00.10h - 23.47h	
195	186	2007/04/04	00.00h - 07.53h	
196	76	2007/12/15	14.15h - 23.48h	
197	77	2007/12/16	00.00h - 23.51h	
198	78	2007/12/17	00.04h - 23.54h	
199	79	2007/12/18	00.07h - 23.55h	
200	80	2007/12/19	00.08h - 23.57h	
201	81	2007/12/20	00.10h - 23.59h	
202	82	2007/12/21	00.12h - 23.48h	
203	83	2007/12/22	00.01h - 23.49h	
204	84	2007/12/23	00.01h - 23.50h	
205	85	2007/12/24	00.02h - 23.50h	
206	86	2007/12/25	00.03h - 23.52h	
207	87	2007/12/26	00.04h - 23.52h	
208	88	2007/12/27	00.04h - 23.52h	
209	89	2007/12/28	00.05h - 23.53h	
210	90	2007/12/29	00.06h - 23.54h	
211	91	2007/12/30	00.06h - 23.54h	
212	92	2007/12/31	00.07h - 23.55h	
213	93	2008/01/01	00.08h - 23.55h	
214	94	2008/01/02	00.08h - 23.55h	
215	95	2008/01/03	00.08h - 23.55h	
216	96	2008/01/04	00.07h - 23.54h	
217	97	2008/01/05	00.07h - 23.55h	
218	98	2008/01/06	00.08h - 23.53h	
219	99	2008/01/07	00.06h - 23.54h	
220	100	2008/01/08	00.06h - 23.53h	
221	101	2008/01/09	00.06h - 23.55h	
222	102	2008/01/10	00.08h - 23.57h	
223	103	2008/01/11	00.09h - 23.59h	
224	104	2008/01/12	00.11h - 23.47h	
225	105	2008/01/13	00.00h - 23.50h	
226	106	2008/01/14	00.02h - 23.54h	
227	107	2008/01/15	00.07h - 23.59h	
228	108	2008/01/16	00.12h - 23.54h	
229	109	2008/01/17	00.07h - 23.47h	
230	110	2008/01/18	00.00h - 23.53h	
231	111	2008/01/19	00.06h - 23.57h	
232	112	2008/01/20	00.10h - 23.51h	
233	113	2008/01/21	00.04h - 23.56h	
234	114	2008/01/22	00.08h - 23.59h	
235	115	2008/01/23	00.12h - 23.53h	
236	116	2008/01/24	00.06h - 23.59h	
237	117	2008/01/25	00.12h - 23.52h	
238	118	2008/01/26	00.05h - 23.57h	
239	119	2008/01/27	00.10h - 23.48h	
240	120	2008/01/28	00.01h - 23.54h	

241 : 121 : 2008/01/29 00.07h - 23.48h
242 : 122 : 2008/01/30 00.00h - 23.50h
243 : 123 : 2008/01/31 00.03h - 23.56h
244 : 124 : 2008/02/01 00.09h - 23.47h
245 : 125 : 2008/02/02 00.00h - 23.53h
246 : 126 : 2008/02/03 00.05h - 23.59h
247 : 127 : 2008/02/04 00.12h - 23.52h
248 : 128 : 2008/02/05 00.05h - 23.58h
249 : 129 : 2008/02/06 00.11h - 10.54h
250 : 130 : 2008/02/07 12.37h - 23.53h <-
251 : 131 : 2008/02/08 00.05h - 23.55h
252 : 132 : 2008/02/09 00.07h - 23.56h
253 : 133 : 2008/02/10 00.09h - 23.59h
254 : 134 : 2008/02/11 00.12h - 23.50h
255 : 135 : 2008/02/12 00.03h - 23.53h
256 : 136 : 2008/02/13 00.05h - 23.56h
257 : 137 : 2008/02/14 00.08h - 23.48h
258 : 138 : 2008/02/15 00.00h - 23.50h
259 : 139 : 2008/02/16 00.03h - 23.53h
260 : 140 : 2008/02/17 00.06h - 23.56h
261 : 141 : 2008/02/18 00.09h - 23.47h
262 : 142 : 2008/02/19 00.00h - 23.51h
263 : 143 : 2008/02/20 00.03h - 23.53h
264 : 144 : 2008/02/21 00.06h - 23.53h
265 : 145 : 2008/02/22 00.05h - 23.57h
266 : 146 : 2008/02/23 00.09h - 23.48h
267 : 147 : 2008/02/24 00.01h - 23.53h
268 : 148 : 2008/02/25 00.05h - 23.57h
269 : 149 : 2008/02/26 00.10h - 23.49h
270 : 150 : 2008/02/27 00.02h - 23.53h
271 : 151 : 2008/02/28 00.06h - 23.49h
272 : 152 : 2008/02/29 00.02h - 23.54h

273 : 153 : 2008/03/01 00.06h - 23.55h
274 : 154 : 2008/03/02 00.07h - 23.58h
275 : 155 : 2008/03/03 00.10h - 23.48h
276 : 156 : 2008/03/04 00.00h - 23.51h
277 : 157 : 2008/03/05 00.03h - 23.54h
278 : 158 : 2008/03/06 00.07h - 23.53h
279 : 159 : 2008/03/07 00.06h - 23.55h
280 : 160 : 2008/03/08 00.08h - 23.58h
281 : 161 : 2008/03/09 00.11h - 23.48h
282 : 162 : 2008/03/10 00.01h - 23.50h
283 : 163 : 2008/03/11 00.03h - 23.54h
284 : 164 : 2008/03/12 00.07h - 23.58h
285 : 165 : 2008/03/13 00.11h - 23.55h
286 : 166 : 2008/03/14 00.08h - 23.59h
287 : 167 : 2008/03/15 00.12h - 23.52h
288 : 168 : 2008/03/16 00.05h - 23.57h
289 : 169 : 2008/03/17 00.10h - 23.49h
290 : 170 : 2008/03/18 00.01h - 23.54h
291 : 171 : 2008/03/19 00.07h - 23.57h
292 : 172 : 2008/03/20 00.10h - 23.58h
293 : 173 : 2008/03/21 00.11h - 23.50h
294 : 174 : 2008/03/22 00.02h - 23.53h
295 : 175 : 2008/03/23 00.06h - 23.58h
296 : 176 : 2008/03/24 00.11h - 23.52h
297 : 177 : 2008/03/25 00.04h - 23.57h
298 : 178 : 2008/03/26 00.10h - 23.50h
299 : 179 : 2008/03/27 00.03h - 23.58h
300 : 180 : 2008/03/28 00.11h - 23.50h
301 : 181 : 2008/03/29 00.03h - 23.55h
302 : 182 : 2008/03/30 00.08h - 23.52h
303 : 183 : 2008/03/31 00.05h - 23.47h

E. Radar images geo-referencing

E.1. Introduction

This annex shows the process of geo-referencing the radar images to a UTM-based coordinate system, for better interpretation of the results derived with the LISA instrument.

As stated in Section 4.2.2, the images obtained with the LISA instrument, as happens with any SAR sensor, are referenced to a local coordinate system with origin in the centre of the synthetic aperture. In that coordinate system, the x axis corresponds to the synthetic aperture itself, the y axis is perpendicular to the synthetic aperture, pointing to the radar FOV (zero-cross-range) and finally the z axis is the vertical elevation, always taking as a reference the central point of the synthetic aperture.

The map used in the Swiss test site is based on the CH1903 datum (Figure 4.4). On the other hand, the map used in the Italian test site is based on the ED50 datum, although it was converted to the worldwide UTM WGS84 datum (Figure 4.9) for easier localization of the *ground-truth* GPS points and tracks. Since the preceding maps are all based on an Easting-Northing coordinates frame, hereinafter we will refer generically to the geo-referencing of the radar images to a UTM-based coordinate system.

A UTM-based coordinate system is defined by the coordinates E (Easting), N (Northing) and z (vertical elevation), where the point of origin is the intersection of the equator and the zone's central meridian. In order to avoid dealing with negative numbers, the central meridian of each zone is given a "false easting" value of 500000 meters. The vertical elevation, instead, is referenced to sea level.

The geo-referencing process can be divided into three steps. These steps are outlined below and further developed in the following sections:

a) A coordinates rotation from x-y to E-N.

b) A projection of the rotated radar images to a DTM (3-D) of the area.

c) A projection of the 3-D radar points to a 2-D map.

E.2. Coordinates rotation

The coordinates rotation step simply consists of a 2-D rotation of the LISA coordinates system (x-y) to the UTM-based coordinates system (E-N) based on a common

point well defined in both systems. Figure E.1 shows the geometry for that step, where *REF* denotes the common point, θ is the angle subtended by the radar zero-cross-range direction and the common point, $\alpha_{x\text{-}y} = \pi/2 - \theta$, $\alpha_{E\text{-}N}$ is the angle subtended by the Easting coordinate and the common point and $\beta_{E\text{-}N}$ is the angle that actually defines the coordinates rotation.

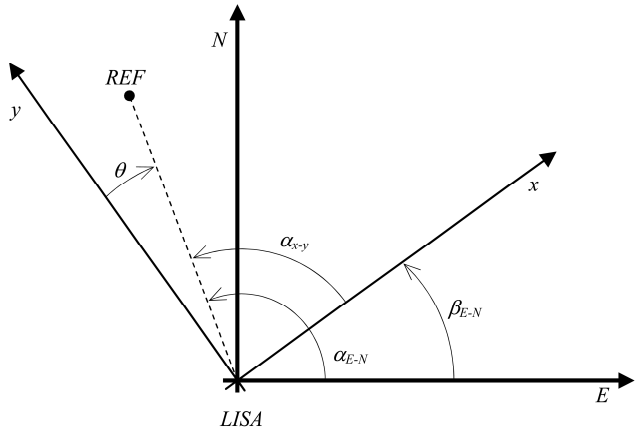

Fig. E.1. Geometry for the coordinates rotation step.

The common point, *REF*, is chosen such that it can be easily identifiable both in the radar images and in the local map or orthophoto of the area. Rock formations with high and constant reflectivity and the borders of shadowed areas with no reflectivity at all are the preferred reference points. Using the zoom and pan capabilities of software for the 3-D visualization of the results it is possible to assess the accuracy of the geo-referencing. Similarly, with the same software it is possible to iterate in the correct definition of the common point up until the best match is achieved.

The reference point will be denoted by its Easting and Northing coordinates as: (REF_E, REF_N) in the UTM-based coordinates system. The same point in the radar coordinates system *x*-*y* will be denoted by: (REF_x, REF_y). The LISA position in UTM coordinates will be denoted as ($LISA_E$, $LISA_N$, $LISA_z$), while the position of the instrument in the local reference system of the radar is (0, 0, 0) by definition of that system.

According to the before mentioned definitions, the azimuth angles of the reference point with respect to the *E* and *x* axis are respectively:

$$\alpha_{E-N} = \operatorname{atan}\left(\frac{REF_N - LISA_N}{REF_E - LISA_E}\right), \tag{E.1}$$

$$\alpha_{x-y} = \operatorname{atan}\left(\frac{REF_y}{REF_x}\right). \tag{E.2}$$

The orientation of the *x* axis in the UTM-based system, and thus of the LISA rail, can be expressed with the parameter $\beta_{E\text{-}N}$. This parameter is characteristic of every field campaign and can been kept constant for the whole field campaign provided the instrument position and orientation are not changed:

$$\beta_{E-N} = \alpha_{E-N} - \alpha_{x-y}. \tag{E.3}$$

E.3. Projection to a 3-D DTM

Radar images are focused natively in a cylindrical coordinates system where only the distance to the target, r or slant-range, and the azimuth angle with respect to the zero-cross-range direction, θ, are known for every pixel where the image is formed. An artificial Cartesian grid x-y can be established such that:

$$\begin{aligned} x &= r \cdot \sin(\theta), \\ y &= r \cdot \cos(\theta). \end{aligned} \tag{E.4}$$

but in that case the coordinates x-y are not equally spaced since they are modulated by the terrain topography. The consequence of this modulation is the impossibility of directly passing from the radar coordinates (r, θ) or (x, y) to the UTM-based coordinates of a commercial map or othophoto (E, N). Additional information on the topography of the terrain is, thus, necessary for the proper geo-referencing of the radar images. The second step of the geo-referencing process is, then, the projection of the rotated radar images to a 3-D Digital Terrain Model (DTM) of the area.

There are two possibilities at this point. Either a high-resolution DTM of the area is available in UTM coordinates, or no *ground-truth* DTM is available and one needs to be created with the topographic mode of the LISA instrument. In the later case the DTM will be referenced in the local radar coordinates system x-y. Actually, a high-resolution DTM was available for the Sion Valley test site but not for the Alagna Valsesia one. The first case is analyzed in the following paragraphs while the second one is addressed in the next section of this annex.

Let us start by assuming a *ground-truth* DTM is available for the area monitored by the radar. Let *pix* be a two dimensional point in the local coordinates system that is to be expressed in the 3-D UTM-based coordinates system (pix_E, pix_N, pix_z), and let *DTM* be a 2-D matrix with the elevations of the area ordered such that the rows of that matrix correspond to the Northing coordinates' array (dtm_N) and the columns to the Easting one (dtm_E). The pixel *pix* can be expressed in the artificial Cartesian grid x-y as (pix_x, pix_y) according to (E.4) or in the original cylindrical grid r-θ as (pix_r, pix_θ) according to:

$$\begin{aligned} r &= \sqrt{x^2 + y^2}, \\ \theta &= \operatorname{atan}\left(x/y\right). \end{aligned} \tag{E.5}$$

The projection of the pixel *pix* to the DTM consists in finding the point in the DTM that corresponds to the given pixel. To this aim, the coordinates of the DTM (DTM_E, DTM_N) are expressed in cylindrical format (DTM_r, DTM_θ) with respect to the radar position and orientation according to (E.6). In this way the DTM coordinates can be directly compared with the native coordinates of the pixel in the radar coordinates system: pix_r, pix_θ.

$$\begin{aligned} DTM_r &= \sqrt{(DTM_E - LISA_E)^2 + (DTM_N - LISA_N)^2 + DTM^2}, \\ DTM_\theta &= \operatorname{atan}\left(\frac{DTM_E - LISA_E}{DTM_N - LISA_N}\right) + \beta_{E-N}. \end{aligned} \tag{E.6}$$

At that point, the indexes (ind_E, ind_N) of the matrix *DTM* that simultaneously minimize the differences of range and azimuth between the pixel and the points of the DTM can be found according to (Matlab pseudo-code):

$$(ind_E, ind_N) = \text{find\_index}\left(\min\left(\left|DTM_r - pix_r\right| \,\&\, \left|DTM_\theta - pix_\theta\right|\right)\right). \tag{E.7}$$

Finally, the pixel is expressed in the 3-D UTM-based coordinates system as:

$$\begin{cases} pix_E = dtm_E(ind_E), \\ pix_N = dtm_N(ind_N), \\ pix_z = DTM(ind_E, ind_N). \end{cases} \tag{E.8}$$

E.4. Projection to a 2-D map

When the coordinates of every pixel of the radar image are available in the UTM-based coordinates system as described in (E.8), the projection of the radar images to a 2-D map in UTM coordinates is simply done by using the coordinates (pix_E, pix_N). In addition, provided the location and orientation of the LISA instrument are not changed during the measurements, a look-up table can be created on a single occasion with the coordinates transformation and reused for every radar image generated afterwards.

On the other hand, when no *ground-truth* DTM is available for the area monitored by the radar, a mid-resolution DTM can be obtained with the topographic mode of the LISA instrument as described in Chapter 6. In this case, let *DTM* be a 2-D matrix with the elevations of the area ordered such that the rows of that matrix correspond to the local *y* coordinate (dtm_y) and the columns to the *x* (dtm_x) one. Again, *pix* is a two dimensional point in the local coordinates system (pix_x, pix_y or equivalently pix_r, pix_θ) that is to be expressed into the UTM-based coordinates system (pix_E, pix_N).

When the DTM is created in the same reference system as the radar images, every pixel of the radar image has a correspondent pixel in the *DTM* matrix so no coordinates transformation is required ($pix_x \leftrightarrow dtm_x$, $pix_y \leftrightarrow dtm_y$). In this case, instead, the projection of the radar images to a 2-D map of the area is of high interest for the interpretation of the results.

The projection of the pixel *pix* to the local map consists in finding the point in the map (pix_E, pix_N) that corresponds to the given pixel. To this aim, the coordinates of the map in array format (map_E, map_N) are expressed as two 2-D matrices (MAP_E, MAP_N) where each element in the matrices corresponds to the Easting and Northing coordinates, respectively, of the corresponding point in the map. The coordinates are then expressed in cylindrical format (MAP_r, MAP_θ) with respect to the radar position and orientation

according to (E.9). This way the map coordinates can be directly compared with the native coordinates of the pixel in the radar coordinates system. Since in this case the projection is to a 2-D map, the ground-range (MAP_{gr}) coordinates are used instead of the slant-range (MAP_r) ones:

$$\begin{aligned} MAP_{gr} &= \sqrt{(MAP_E - LISA_E)^2 + (MAP_N - LISA_N)^2}, \\ MAP_\theta &= \text{atan}\left(\frac{MAP_E - LISA_E}{MAP_N - LISA_N}\right) + \beta_{E-N}. \end{aligned} \tag{E.9}$$

Similarly, the ground-range coordinate of the pixel (pix_{gr}) is used instead of its slant-range coordinate (pix_r):

$$\begin{aligned} pix_r &= \sqrt{pix_x^2 + pix_y^2}, \\ pix_{gr} &= \sqrt{pix_r^2 + (LISA_z - DTM)^2}. \end{aligned} \tag{E.10}$$

At that point, the indexes (ind_E, ind_N) of the map that simultaneously minimize the differences of ground-range and azimuth between the pixel and the points of the map can be found according to (Matlab pseudo-code):

$$(ind_E, ind_N) = \text{find\_index}\left(\min\left(\left|MAP_{gr} - pix_{gr}\right| \,\&\, \left|MAP_\theta - pix_\theta\right|\right)\right). \tag{E.11}$$

Finally, the pixel *pix* of the radar image can be depicted over the map with the coordinates (pix_E, pix_N):

$$\begin{cases} pix_E = map_E(ind_E), \\ pix_N = map_N(ind_N). \end{cases} \tag{E.12}$$

F. Snow height tables

F.1. Tables organization

This annex lists the days for which the snow depth retrieval technique presented in Chapter 5 has been tested. Two different lists are presented, one for each of the two test points where the technique was applied. Every single list is divided into the three winter campaigns for which data was available: winter 2003-2004, 2004-2005 and 2005-2006. At the end of every winter campaign a summary of the results indicates the number of days in which the technique has been successfully applied for the corresponding test point and in both test points simultaneously. Lists are organized in five columns:

a) ### - This is an incremental number starting with 1 the first day of the given winter campaign, and increasing by 1 every day in which the snow height retrieval technique was applied;

b) Date - Date in the format YYYYMMDD of a given day of data acquisition;

c) Calibration - calibration parameters α and β as defined in Section 5.2.2. Note that α is reported in [cm/rad] and β is reported in [cm] in the tables below;

d) Differenc. - Mean and standard deviation in [cm] of the differences between the ground-truth snow height and that retrieved with the DInSAR technique.

e) M - Indicates, where the mark (*) is present, a matching between the ground-truth snow height and that retrieved with the DInSAR technique.

F.2. Test point 1

The following is a list with the days, calibration parameters and differences between the ground-truth snow height and that retrieved with the DInSAR technique for the test point 1. Note that this test point has been also defined in Section 5.4.1.

```
Snow height retrieval: Test point 1
UTM CH1903 [594600.00, 127750.00, 1942.38]

=========================================
    :          : Calibration: Differenc.:
### : Date     : Alpha/Beta : Mean/StDev: M
-----------------------------------------
  1 : 20031217 :  1.3/110.0 :  0.5/ 0.5 : *
  2 : 20031218 :  0.1/108.0 :  1.9/ 1.5 :
  3 : 20031219 :  0.1/105.6 :  1.6/ 1.0 :
  4 : 20031220 :  1.1/102.1 :  1.2/ 0.8 : *
  5 : 20031221 :  0.1/108.8 :  2.5/ 1.9 :
  6 : 20040113 :  0.1/245.9 : 17.0/ 8.4 :
  7 : 20040114 :  0.1/273.0 :  3.0/ 2.2 :
  8 : 20040115 :  3.3/283.0 :  2.4/ 1.7 : *
  9 : 20040116 :  1.5/304.1 :  3.7/ 3.1 : *
```

###	Date	Calibration: Alpha/Beta	Differenc.: Mean/StDev	M
10	20040117	1.3/310.7	1.8/ 2.0	*
11	20040118	2.4/322.0	5.0/ 3.6	*
12	20040119	1.9/303.2	1.7/ 1.9	*
13	20040120	1.6/295.8	1.3/ 1.2	*
14	20040121	1.7/323.8	1.7/ 1.7	*
15	20040122	0.1/310.8	3.0/ 2.9	
16	20040123	0.1/310.1	3.2/ 2.1	
17	20040124	0.8/304.5	1.8/ 2.1	*
18	20040125	0.4/308.6	1.9/ 1.7	*
19	20040126	2.5/305.0	4.1/ 3.4	*
20	20040127	0.7/332.7	1.5/ 1.0	*
21	20040217	0.1/292.0	0.7/ 0.5	
22	20040218	0.1/292.0	0.1/ 0.0	
23	20040227	0.1/283.5	0.4/ 0.6	
24	20040315	0.1/286.2	1.3/ 0.4	
25	20040316	0.5/286.3	0.9/ 0.7	*
26	20040317	0.4/283.0	1.4/ 1.1	*
27	20040318	0.4/280.0	0.8/ 0.7	*
28	20040319	0.1/278.0	1.2/ 1.2	
29	20040320	0.8/276.7	0.6/ 0.7	*
30	20040321	0.1/278.2	0.5/ 0.4	
31	20040322	2.0/280.9	5.3/ 3.7	*
32	20040323	2.9/285.0	2.8/ 2.4	*
33	20040324	8.1/296.9	1.9/ 1.4	*
34	20040325	0.1/307.8	3.3/ 1.8	
35	20040326	0.1/301.8	2.4/ 1.4	
36	20040327	0.9/299.0	1.4/ 1.1	*
37	20040328	0.2/293.0	1.4/ 1.5	*
38	20040329	0.5/291.0	0.8/ 0.6	*
39	20040330	0.1/289.0	0.8/ 0.5	
40	20040331	1.8/287.9	1.1/ 1.3	*

Total matching point 1: 24/40
Total matching points 1&2: 21/40

###	Date	Calibration: Alpha/Beta	Differenc.: Mean/StDev	M
1	20050104	0.1/ 91.9	1.0/ 0.5	
2	20050105	0.9/ 93.0	1.4/ 1.4	*
3	20050106	0.6/ 91.2	1.7/ 0.8	*
4	20050107	0.3/ 89.0	0.7/ 0.7	*
5	20050108	0.1/ 87.1	1.0/ 0.8	
6	20050109	0.1/ 86.2	1.8/ 1.1	
7	20050110	0.3/ 84.1	0.8/ 1.0	*
8	20050111	0.5/ 83.4	1.1/ 1.3	*
9	20050112	0.2/ 83.3	1.1/ 1.1	*
10	20050113	0.1/ 84.0	1.1/ 1.0	
11	20050114	1.4/ 84.2	1.3/ 1.7	*
12	20050115	0.6/ 82.8	1.1/ 1.1	*
13	20050116	0.1/ 82.1	1.3/ 1.3	
14	20050117	0.1/ 81.0	1.2/ 1.0	
15	20050118	1.2/ 82.3	1.9/ 1.8	*
16	20050119	0.8/104.0	1.1/ 1.1	*
17	20050120	0.6/105.4	1.3/ 0.8	*
18	20050121	0.1/114.2	10.6/ 6.7	
19	20050122	2.1/138.0	2.2/ 2.7	*
20	20050123	2.1/161.0	2.3/ 2.1	*
21	20050124	1.5/188.0	4.1/ 3.6	*
22	20050125	0.1/168.0	2.4/ 2.1	
23	20050126	1.2/168.6	1.2/ 1.2	*
24	20050127	1.0/163.0	1.5/ 0.9	*
25	20050128	0.7/156.0	0.7/ 0.7	*
26	20050216	1.0/231.7	0.7/ 0.5	*
27	20050217	3.4/228.0	3.0/ 1.9	*
28	20050218	6.0/221.5	1.7/ 1.0	*
29	20050219	1.0/219.0	1.1/ 1.2	*
30	20050220	1.5/215.8	0.9/ 0.8	*
31	20050221	0.1/213.0	1.6/ 1.3	
32	20050222	1.4/209.5	1.8/ 1.3	*
33	20050223	0.1/207.0	1.5/ 1.9	
34	20050224	0.3/206.0	0.5/ 0.4	*
35	20050225	1.5/205.0	0.3/ 0.3	*
36	20050304	0.1/194.4	0.7/ 0.3	
37	20050305	2.5/195.0	1.5/ 1.5	*
38	20050306	0.1/201.2	1.7/ 1.0	
39	20050307	0.8/199.2	0.8/ 0.7	*
40	20050308	1.0/196.5	0.6/ 0.5	*
41	20050309	0.1/197.0	0.8/ 0.7	
42	20050310	0.1/195.6	1.3/ 1.2	
43	20050311	0.1/194.0	0.9/ 0.8	
44	20050312	0.1/192.1	1.2/ 1.3	
45	20050313	0.1/199.1	1.4/ 1.4	
46	20050314	0.1/199.0	1.8/ 1.6	
47	20050315	0.3/202.1	1.5/ 1.0	*
48	20050316	0.5/198.8	1.9/ 1.9	*
49	20050317	0.3/194.7	1.2/ 0.9	*
50	20050318	0.4/193.0	1.4/ 1.6	*
51	20050319	0.3/188.9	1.2/ 1.1	*
52	20050320	0.2/184.2	1.5/ 1.5	*
53	20050321	0.2/181.9	1.6/ 1.2	*
54	20050322	0.1/181.0	1.2/ 1.4	
55	20050323	0.3/181.0	1.3/ 1.6	*
56	20050324	0.1/178.0	2.0/ 1.8	
57	20050325	1.0/184.0	2.3/ 1.6	*
58	20050326	0.1/177.4	0.8/ 0.9	
59	20050327	0.1/177.0	1.0/ 0.9	
60	20050328	0.6/179.0	1.2/ 1.2	*
61	20050329	0.3/177.5	1.1/ 0.9	*
62	20050330	0.6/177.0	1.2/ 1.0	*
63	20050331	0.1/178.4	0.8/ 0.6	

Total matching point 1: 40/63
Total matching points 1&2: 27/63

###	Date	Calibration: Alpha/Beta	Differenc.: Mean/StDev	M
1	20051201	0.1/ 30.0	0.7/ 0.5	
2	20051202	0.1/ 30.6	0.8/ 0.6	
3	20051203	2.7/ 35.7	2.5/ 1.7	*
4	20051204	4.4/ 42.6	3.3/ 2.9	*
5	20051205	0.8/ 80.9	1.0/ 0.9	*
6	20051206	0.1/ 82.9	5.1/ 3.0	
7	20051207	2.3/ 77.7	1.5/ 1.2	*
8	20051208	0.1/ 77.0	0.0/ 0.1	
9	20051212	0.1/ 67.0	0.6/ 0.5	
10	20051213	0.1/ 67.0	2.3/ 1.5	
11	20051214	0.1/ 63.1	0.7/ 0.8	
12	20051215	0.3/ 62.0	0.4/ 0.5	*
13	20051216	0.7/ 61.0	1.4/ 1.1	*
14	20051217	0.1/ 74.6	8.6/ 5.9	
15	20051218	0.5/ 77.1	4.8/ 3.3	*
16	20051219	0.1/ 75.1	3.0/ 2.0	
17	20051220	1.8/ 73.4	3.2/ 3.2	*
18	20051221	0.1/ 69.0	2.4/ 1.5	
19	20051222	1.5/ 65.9	0.9/ 0.7	*
20	20051223	0.1/ 63.3	1.3/ 0.9	
21	20051224	0.1/ 61.9	1.4/ 1.0	
22	20051225	0.1/ 59.7	1.1/ 1.1	
23	20051226	0.1/ 60.0	0.5/ 0.7	
24	20051227	8.7/ 60.7	25.8/58.2	
25	20051228	0.1/ 59.0	1.4/ 0.7	
26	20051229	0.1/ 61.0	1.4/ 1.7	
27	20051230	1.5/ 59.6	2.5/ 2.2	*
28	20051231	1.8/ 77.2	3.6/ 3.7	*
29	20060101	3.1/112.3	5.5/ 3.5	*
30	20060102	0.1/119.4	5.6/ 2.7	
31	20060103	0.1/126.0	4.3/ 1.9	
32	20060104	2.4/119.8	1.7/ 1.1	*
33	20060105	1.9/114.6	1.9/ 1.5	*
34	20060106	2.3/112.0	2.1/ 2.0	*
35	20060107	0.1/108.9	2.2/ 1.6	
36	20060108	0.1/106.1	1.7/ 1.3	

```
 37 : 20060109 :  0.1/104.0 :  1.6/ 1.3 :
 38 : 20060110 :  0.9/102.1 :  1.5/ 1.6 : *
 39 : 20060111 :  0.9/101.9 :  1.3/ 1.3 : *
 40 : 20060112 :  0.1/101.0 :  0.7/ 0.8 :
 41 : 20060113 :  2.8/ 99.9 :  0.9/ 0.7 : *
 42 : 20060114 :  0.1/ 99.0 :  1.6/ 1.2 :
 43 : 20060115 :  0.1/ 97.0 :  1.2/ 1.2 :
 44 : 20060116 :  1.3/ 98.3 :  2.9/ 2.0 : *
 45 : 20060117 :  3.4/112.7 :  3.7/ 4.3 : *
 46 : 20060118 :  1.4/129.9 :  1.7/ 1.2 : *
 47 : 20060119 :  2.1/145.0 :  3.5/ 2.9 : *
 48 : 20060120 :  0.1/138.3 :  3.2/ 1.8 :
 49 : 20060121 :  0.1/133.1 :  2.1/ 1.4 :
 50 : 20060122 :  0.4/131.0 :  0.7/ 0.7 : *
 51 : 20060203 :  0.1/108.9 :  2.1/ 1.2 :
 52 : 20060204 :  0.1/111.5 :  1.1/ 1.2 :
 53 : 20060205 :  0.3/112.0 :  1.0/ 1.1 : *
 54 : 20060206 :  0.1/111.0 :  0.6/ 0.8 :
 55 : 20060207 :  0.1/111.0 :  1.4/ 1.2 :
 56 : 20060208 :  0.1/109.6 :  1.4/ 1.5 :
 57 : 20060209 :  0.5/112.6 :  1.6/ 1.2 : *
 58 : 20060210 :  0.1/116.2 :  1.4/ 1.2 :
 59 : 20060211 :  0.1/117.0 :  2.9/ 1.7 :
 60 : 20060212 :  0.3/114.9 :  1.2/ 1.3 : *
 61 : 20060213 :  0.1/114.0 :  1.0/ 1.3 :
 62 : 20060214 :  0.9/114.0 :  1.0/ 1.4 : *
 63 : 20060215 :  1.3/111.9 :  0.9/ 0.8 : *
 64 : 20060216 :  1.7/131.9 :  2.4/ 1.8 : *
 65 : 20060217 :  5.8/184.1 : 12.4/ 9.8 :
 66 : 20060218 :  2.6/215.5 :  3.2/ 2.1 : *
 67 : 20060219 :  1.1/247.8 :  0.8/ 0.6 : *
 68 : 20060220 :  3.2/234.9 :  2.8/ 2.6 : *
 69 : 20060221 :  2.3/224.9 :  1.4/ 1.7 : *
 70 : 20060222 :  0.1/216.6 :  4.7/ 2.1 :
 71 : 20060223 :  0.7/209.0 :  1.5/ 1.8 : *
 72 : 20060224 :  0.1/205.0 :  1.2/ 0.8 :
 73 : 20060225 :  2.7/204.0 :  2.0/ 2.3 : *
 74 : 20060226 :  0.1/199.0 :  3.0/ 1.9 :
 75 : 20060227 :  0.1/193.9 :  2.5/ 1.7 :
 76 : 20060228 :  7.4/192.0 :  4.1/ 3.8 : *
 77 : 20060301 :  7.7/221.8 :  3.5/ 2.2 : *
 78 : 20060302 :  3.4/226.1 :  4.1/ 3.9 : *
 79 : 20060303 :  2.2/238.9 :  4.6/ 4.2 : *
 80 : 20060304 :  0.1/282.9 : 19.6/ 9.4 :
 81 : 20060305 :  0.1/306.0 :  3.2/ 1.9 :
 82 : 20060306 :  0.1/300.0 :  7.7/ 3.8 :
 83 : 20060307 :  3.0/289.9 :  4.2/ 2.4 : *
 84 : 20060308 :  0.7/290.1 :  2.1/ 1.5 : *
 85 : 20060309 :  0.8/313.9 :  1.3/ 1.8 : *
 86 : 20060310 :  1.8/319.4 :  1.6/ 1.4 : *
 87 : 20060311 :  0.2/337.1 :  1.9/ 1.4 : *
 88 : 20060312 :  3.9/343.8 :  2.1/ 1.5 : *
 89 : 20060313 :  1.4/328.1 :  0.9/ 0.7 : *
 90 : 20060314 :  2.1/319.1 :  2.0/ 2.1 : *
 91 : 20060315 :  0.1/312.2 :  3.2/ 1.8 :
 92 : 20060316 :  1.6/307.0 :  2.2/ 2.5 : *
 93 : 20060317 :  1.1/303.3 :  2.8/ 2.9 : *
 94 : 20060318 :  0.5/299.0 :  2.1/ 2.3 : *
 95 : 20060319 :  0.9/296.0 :  2.0/ 2.0 : *
 96 : 20060320 :  0.1/290.6 :  1.6/ 0.9 :
 97 : 20060321 :  0.4/289.0 :  0.9/ 0.9 : *
 98 : 20060322 :  1.1/290.0 :  2.0/ 2.1 : *
 99 : 20060323 :  0.3/290.1 :  1.5/ 1.0 : *
100 : 20060324 :  2.1/288.0 :  1.3/ 0.9 : *
101 : 20060325 :  0.1/306.0 :  3.0/ 1.8 :
102 : 20060326 :  1.1/312.3 :  1.5/ 1.0 : *
103 : 20060327 :  0.9/295.8 :  1.2/ 0.9 : *
104 : 20060328 :  1.7/287.0 :  2.5/ 2.7 : *
105 : 20060329 :  2.8/308.6 :  2.3/ 1.5 : *
106 : 20060330 :  0.6/315.2 :  2.1/ 2.7 : *
107 : 20060331 :  0.1/325.2 : 15.9/ 7.0 :

Total matching point 1:    60/107
Total matching points 1&2: 54/107
```

F.3. Test point 2

Similarly, the following list presents the same information for the test point 2. Note also that this test point has been defined in Section 5.4.1.

```
Snow height retrieval: Test point 2
UTM CH1903 [593564.62, 128286.61, 2621.15]

============================================
    :          : Calibration: Differenc.:
### : Date     : Alpha/Beta : Mean/StDev: M
--------------------------------------------
  1 : 20031217 :  1.4/110.0 :  0.6/ 0.6 : *
  2 : 20031218 :  1.7/108.0 :  1.8/ 1.8 : *
  3 : 20031219 :  0.1/105.6 :  1.6/ 1.1 :
  4 : 20031220 :  0.1/102.1 :  1.3/ 1.2 :
  5 : 20031221 :  2.3/108.8 :  0.5/ 0.4 : *
  6 : 20040113 :  4.1/245.9 :  3.1/ 2.3 : *
  7 : 20040114 :  0.3/273.0 :  2.6/ 1.6 : *
  8 : 20040115 :  1.9/283.0 :  1.5/ 1.3 : *
  9 : 20040116 :  0.5/304.1 :  4.4/ 3.5 : *
 10 : 20040117 :  1.6/310.7 :  1.5/ 1.1 : *
 11 : 20040118 :  3.1/322.0 :  7.9/ 6.0 : *
 12 : 20040119 :  0.9/303.2 :  1.3/ 1.4 : *
 13 : 20040120 :  1.8/295.8 :  1.5/ 1.4 : *
 14 : 20040121 :  1.5/323.8 :  1.9/ 1.7 : *
 15 : 20040122 :  1.0/310.8 :  2.5/ 2.9 : *
 16 : 20040123 :  0.1/310.1 :  3.5/ 2.2 :
 17 : 20040124 :  0.1/304.5 :  2.1/ 1.1 :
 18 : 20040125 :  0.3/308.6 :  2.0/ 1.6 : *
 19 : 20040126 :  2.6/305.0 :  4.4/ 2.6 : *
 20 : 20040127 :  0.3/332.7 :  1.6/ 1.1 : *
 21 : 20040217 :  0.1/292.0 :  0.5/ 0.5 :
 22 : 20040218 :  0.1/292.0 :  0.1/ 0.1 :
 23 : 20040227 :  0.1/283.5 :  0.4/ 0.6 :
 24 : 20040315 :  0.1/286.2 :  1.4/ 0.5 :
 25 : 20040316 :  0.2/286.3 :  0.6/ 0.5 : *
 26 : 20040317 :  0.3/283.0 :  1.0/ 0.7 : *
 27 : 20040318 :  0.3/280.0 :  0.6/ 0.6 : *
 28 : 20040319 :  0.2/278.0 :  1.0/ 1.3 : *
 29 : 20040320 :  0.5/276.7 :  1.1/ 0.9 : *
 30 : 20040321 :  0.1/278.2 :  0.5/ 0.4 :
 31 : 20040322 :  0.1/280.9 :  6.6/ 2.7 :
 32 : 20040323 :  2.3/285.0 :  2.5/ 1.9 : *
 33 : 20040324 :  3.9/296.9 :  1.4/ 1.3 : *
 34 : 20040325 :  0.1/307.8 :  3.4/ 1.8 :
 35 : 20040326 :  0.1/301.8 :  2.4/ 1.5 :
 36 : 20040327 :  1.4/299.0 :  0.9/ 0.6 : *
 37 : 20040328 :  0.2/293.0 :  1.3/ 1.5 : *
 38 : 20040329 :  0.2/291.0 :  0.6/ 0.5 : *
 39 : 20040330 :  0.1/289.0 :  0.8/ 0.6 :
 40 : 20040331 :  1.0/288.0 :  1.3/ 1.5 : *

Total matching point 2:    27/40
Total matching points 2&1: 21/40
```

###	Date	Calibration: Alpha/Beta	Differenc.: Mean/StDev	M
1	20050104	0.1/ 91.9	1.2/ 0.6	
2	20050105	0.1/ 93.0	1.7/ 1.3	
3	20050106	0.3/ 91.2	1.3/ 0.7	*
4	20050107	0.1/ 89.0	1.2/ 1.0	
5	20050108	0.1/ 87.1	1.1/ 0.8	
6	20050109	0.1/ 86.2	2.0/ 1.1	
7	20050110	0.1/ 84.1	0.9/ 1.1	
8	20050111	0.1/ 83.4	0.9/ 1.2	
9	20050112	0.1/ 83.3	1.2/ 1.2	
10	20050113	0.1/ 84.0	1.1/ 0.9	
11	20050114	0.4/ 84.2	1.6/ 1.7	*
12	20050115	0.1/ 82.8	1.2/ 1.2	
13	20050116	0.1/ 82.1	1.3/ 1.4	
14	20050117	0.1/ 81.0	1.2/ 1.1	
15	20050118	1.3/ 82.3	1.9/ 2.3	*
16	20050119	0.2/104.0	1.5/ 1.3	*
17	20050120	0.5/105.4	1.3/ 0.7	*
18	20050121	1.0/114.2	0.8/ 0.5	*
19	20050122	3.0/138.0	3.1/ 3.1	*
20	20050123	1.8/161.0	5.0/ 4.8	*
21	20050124	0.1/188.0	11.3/ 7.6	
22	20050125	0.1/168.0	2.2/ 1.9	
23	20050126	2.0/168.6	1.6/ 1.2	*
24	20050127	0.9/163.0	2.0/ 1.1	*
25	20050128	0.8/156.0	1.0/ 0.8	*
26	20050216	0.5/231.7	0.8/ 0.6	*
27	20050217	1.5/228.0	2.1/ 1.8	*
28	20050218	0.3/221.5	2.5/ 1.8	*
29	20050219	0.1/219.0	1.7/ 1.9	
30	20050220	0.1/215.8	1.0/ 1.1	
31	20050221	0.1/213.0	1.7/ 1.3	
32	20050222	1.7/209.5	1.8/ 1.5	*
33	20050223	0.1/207.0	1.5/ 1.9	
34	20050224	0.7/206.0	0.5/ 0.4	*
35	20050225	1.8/205.0	0.3/ 0.3	*
36	20050304	0.1/194.4	0.7/ 0.3	
37	20050305	2.7/195.0	1.7/ 1.5	*
38	20050306	0.1/201.2	1.7/ 1.0	
39	20050307	0.8/199.2	1.0/ 0.8	*
40	20050308	0.7/196.5	0.6/ 0.4	*
41	20050309	0.5/197.0	0.7/ 0.7	*
42	20050310	0.1/195.6	1.1/ 1.0	
43	20050311	0.1/194.0	0.9/ 0.8	
44	20050312	0.1/192.1	1.2/ 1.1	
45	20050313	0.1/199.1	1.5/ 1.4	
46	20050314	0.1/199.0	1.9/ 1.5	
47	20050315	0.3/202.1	1.3/ 0.8	*
48	20050316	0.4/198.8	1.1/ 1.0	*
49	20050317	0.1/194.7	1.3/ 0.8	
50	20050318	0.4/193.0	1.1/ 1.0	*
51	20050319	0.4/188.9	1.4/ 1.3	*
52	20050320	0.1/184.2	1.7/ 1.3	
53	20050321	0.3/181.9	1.5/ 1.2	*
54	20050322	0.1/181.0	1.4/ 1.4	
55	20050323	0.5/181.0	1.2/ 1.6	*
56	20050324	0.1/178.0	2.1/ 1.8	
57	20050325	1.3/184.0	2.9/ 2.0	*
58	20050326	0.1/177.4	0.8/ 0.8	
59	20050327	0.1/177.0	0.9/ 0.9	
60	20050328	0.1/179.0	1.7/ 1.1	
61	20050329	0.5/177.5	1.1/ 1.0	*
62	20050330	0.1/177.0	1.5/ 1.2	
63	20050331	0.1/178.4	0.8/ 0.5	

Total matching point 2: 29/63
Total matching points 2&1: 27/63

###	Date	Calibration: Alpha/Beta	Differenc.: Mean/StDev	M
1	20051201	0.1/ 30.0	0.7/ 0.5	
2	20051202	0.1/ 30.6	0.9/ 0.6	
3	20051203	2.2/ 35.7	2.0/ 1.3	*
4	20051204	4.4/ 42.6	4.8/ 4.3	*
5	20051205	1.3/ 80.9	1.2/ 1.0	*
6	20051206	2.1/ 82.9	2.7/ 2.3	*
7	20051207	2.5/ 77.7	1.4/ 1.4	*
8	20051208	0.1/ 77.0	0.3/ 0.3	
9	20051212	0.1/ 67.0	0.6/ 0.5	
10	20051213	0.1/ 67.0	2.4/ 1.4	
11	20051214	0.1/ 63.1	0.7/ 0.6	
12	20051215	0.2/ 62.0	0.4/ 0.4	*
13	20051216	0.7/ 61.0	2.0/ 1.7	*
14	20051217	0.1/ 74.6	8.6/ 5.9	
15	20051218	0.1/ 77.1	4.8/ 3.3	
16	20051219	0.1/ 75.1	3.2/ 2.2	
17	20051220	0.7/ 73.4	1.2/ 1.8	*
18	20051221	0.1/ 69.0	2.4/ 1.5	
19	20051222	1.0/ 65.9	0.7/ 0.6	*
20	20051223	0.4/ 63.3	1.1/ 0.9	*
21	20051224	0.2/ 61.9	1.2/ 1.1	*
22	20051225	0.1/ 59.7	1.2/ 1.0	
23	20051226	0.1/ 60.0	0.5/ 0.6	
24	20051227	0.2/ 60.7	26.1/59.7	
25	20051228	0.1/ 59.0	1.5/ 0.7	
26	20051229	0.1/ 61.0	1.4/ 1.7	
27	20051230	0.3/ 59.6	4.2/ 4.7	*
28	20051231	2.4/ 77.2	6.4/ 7.8	*
29	20060101	0.1/112.3	5.8/ 2.5	
30	20060102	3.3/119.4	4.9/ 2.6	*
31	20060103	0.1/126.0	4.4/ 1.9	
32	20060104	1.7/119.8	0.6/ 0.6	*
33	20060105	2.0/114.6	1.3/ 1.3	*
34	20060106	0.9/112.0	1.3/ 1.6	*
35	20060107	6.0/108.9	2.0/ 1.7	*
36	20060108	0.1/106.1	1.7/ 1.3	
37	20060109	0.6/104.0	1.3/ 1.3	*
38	20060110	0.5/102.1	1.4/ 1.7	*
39	20060111	1.2/101.9	1.4/ 1.5	*
40	20060112	0.1/101.0	0.6/ 0.7	
41	20060113	0.6/ 99.9	1.0/ 0.8	*
42	20060114	0.1/ 99.0	1.6/ 1.3	
43	20060115	0.1/ 97.0	1.2/ 1.2	
44	20060116	0.6/ 98.3	3.0/ 2.0	*
45	20060117	2.9/112.7	1.7/ 1.2	*
46	20060118	2.2/129.9	2.5/ 2.1	*
47	20060119	0.6/145.0	1.2/ 1.1	*
48	20060120	1.1/138.3	2.2/ 2.1	*
49	20060121	0.5/133.1	1.8/ 1.6	*
50	20060122	0.3/131.0	0.5/ 0.6	*
51	20060203	0.1/108.9	2.1/ 1.2	
52	20060204	0.3/111.5	1.0/ 1.1	*
53	20060205	0.2/112.0	1.0/ 1.1	*
54	20060206	0.1/111.0	0.5/ 0.7	
55	20060207	0.1/111.0	1.4/ 1.3	
56	20060208	0.3/109.6	1.1/ 1.0	*
57	20060209	0.2/112.6	1.7/ 1.2	*
58	20060210	0.1/116.2	1.5/ 1.2	
59	20060211	1.2/117.0	2.1/ 2.4	*
60	20060212	0.3/114.9	1.1/ 1.2	*
61	20060213	0.1/114.0	1.0/ 1.4	
62	20060214	0.4/114.0	1.5/ 1.8	*
63	20060215	1.4/111.9	1.5/ 1.1	*
64	20060216	2.4/131.9	2.3/ 2.6	*
65	20060217	3.3/184.1	3.6/ 3.0	*
66	20060218	4.2/215.5	5.4/ 4.6	*
67	20060219	1.8/247.8	3.0/ 3.2	*
68	20060220	2.7/234.9	3.5/ 2.5	*
69	20060221	2.5/224.9	1.9/ 1.8	*
70	20060222	0.1/216.6	4.8/ 2.2	
71	20060223	0.4/209.0	1.7/ 2.0	*
72	20060224	0.1/205.0	1.2/ 0.8	

```
 73 : 20060225 :  2.1/204.0 :  2.8/ 3.5 : *
 74 : 20060226 :  1.7/199.0 :  2.0/ 2.7 : *
 75 : 20060227 :  0.1/193.9 :  2.5/ 1.8 :
 76 : 20060228 :  0.6/192.0 :  5.8/ 7.8 : *
 77 : 20060301 :  1.9/221.8 :  4.9/ 2.7 : *
 78 : 20060302 :  2.1/226.1 :  3.8/ 3.5 : *
 79 : 20060303 :  2.0/238.9 :  3.0/ 2.0 : *
 80 : 20060304 :  1.3/282.9 :  2.8/ 1.7 : *
 81 : 20060305 :  0.1/306.0 :  3.2/ 1.8 :
 82 : 20060306 :  0.1/300.0 :  7.7/ 3.8 :
 83 : 20060307 :  0.1/289.9 :  4.4/ 2.9 :
 84 : 20060308 :  0.6/290.1 :  3.0/ 1.7 : *
 85 : 20060309 :  1.2/313.9 :  2.6/ 2.6 : *
 86 : 20060310 :  1.6/319.4 :  2.8/ 1.8 : *
 87 : 20060311 :  0.1/337.1 :  2.0/ 1.3 :
 88 : 20060312 :  0.1/343.8 :  6.7/ 5.5 :
 89 : 20060313 :  1.6/328.1 :  1.4/ 1.1 : *
 90 : 20060314 :  0.6/319.1 :  1.6/ 1.7 : *
 91 : 20060315 :  1.1/312.2 :  2.3/ 1.8 : *
 92 : 20060316 :  0.9/307.0 :  2.2/ 2.7 : *
 93 : 20060317 :  0.6/303.3 :  2.3/ 2.3 : *
 94 : 20060318 :  0.3/299.0 :  1.5/ 1.6 : *
 95 : 20060319 :  0.1/296.0 :  2.9/ 1.4 :
 96 : 20060320 :  0.1/290.6 :  1.6/ 0.9 :
 97 : 20060321 :  0.2/289.0 :  1.0/ 1.0 : *
 98 : 20060322 :  1.6/290.0 :  2.2/ 2.0 : *
 99 : 20060323 :  0.3/290.1 :  1.4/ 1.1 : *
100 : 20060324 :  2.3/288.0 :  2.1/ 1.8 : *
101 : 20060325 :  0.5/306.0 :  2.8/ 1.5 : *
102 : 20060326 :  0.8/312.3 :  1.0/ 0.8 : *
103 : 20060327 :  1.1/295.8 :  2.1/ 1.7 : *
104 : 20060328 :  2.6/287.0 :  2.7/ 2.4 : *
105 : 20060329 :  2.7/308.6 :  6.4/ 5.5 : *
106 : 20060330 :  0.3/315.2 :  1.5/ 1.8 : *
107 : 20060331 :  0.1/325.2 : 16.0/ 6.8 :

Total matching point 2:    70/107
Total matching points 2&1: 54/107
```

G. Snow avalanches monitored

G.1. Tables organization

This annex lists all the avalanches monitored by the LISA instrument, either automatically identified by the algorithm presented in Chapter 7 or manually inserted by an operator. Two different lists are presented, one for each of the two test sites. Every single list is divided into the three winter periods for which data was available for each of the sites. At the end of every period a summary of the results indicates the parameters used for the avalanche identification algorithm and the results achieved in terms of number of avalanches to supervise, avalanches confirmed and avalanches missed by the automatic algorithm. Lists are organized in seven columns:

a) Date - Date of the avalanche event in the format YYYY/MM/DD;

b) Time - Time of the avalanche event in the format hour.minutes;

c) Pos - Position of the starting point of the avalanche, numbered from 1 to 18 according to the grids in Figure 7.9;

d) Axes - Horizontal × vertical axes in meters of the avalanche path;

e) Area - Area in square meters of the avalanche path;

f) DcRt - Differential ratio of the differential coherence image associated with the avalanche event;

g) Mn - Indicates, where the mark (*) is present, that the avalanche was manually added by the operator and not automatically identified by the processor in the configuration reported in the column A of Table 7.4.

G.2. Sion Valley (Switzerland)

The following is the list of avalanches monitored in the Sion Valley of Switzerland.

%Avalanches auto-classified supervised
% Period analyzed: 2003/12/17 - 2004/05/31

%Date	Time	Pos	Axes	Area	DcRt	Mn
2004/01/14	20.51h	1	250x450	94550	0.62	
2004/01/15	05.54h	1	50x575	30000	0.86	
2004/01/15	06.48h	5	50x125	6700	0.78	
2004/01/15	07.42h	2	75x425	30550	0.80	
2004/01/15	08.09h	3	575x825	232950	0.64	
2004/01/15	09.04h	2	75x350	22500	0.78	
2004/01/15	09.04h	1	50x800	32500	0.78	
2004/01/15	09.31h	1	100x1775	127400	0.68	
2004/01/15	09.31h	3	175x625	69750	0.68	

2004/01/15	09.31h	2	100x375	21400	0.68	
2004/01/15	09.58h	2	50x500	17850	0.59	
2004/01/15	11.47h	2	50x125	5600	0.74	
2004/01/15	14.57h	5	50x150	7850	0.80	
2004/01/16	10.24h	5	75x225	15700	0.68	
2004/01/16	13.34h	1	300x625	137450	0.53	
2004/01/16	14.28h	1	100x450	35000	0.63	
2004/01/16	14.28h	3	50x275	15050	0.63	
2004/01/16	14.56h	1	50x250	12500	0.81	*
2004/01/16	19.27h	1	50x225	11000	0.85	
2004/01/17	09.01h	5	200x775	106000	0.58	
2004/01/18	04.00h	5	50x175	7450	0.71	
2004/01/19	10.31h	1	325x1750	363600	0.56	
2004/01/19	10.58h	2	800x1650	671750	0.80	*
2004/01/20	09.36h	6	50x125	5700	0.56	
2004/01/20	10.30h	1	100x600	54150	0.65	
2004/01/20	21.47h	5	25x325	10250	0.68	
2004/01/21	15.25h	6	50x225	12450	0.60	
2004/01/21	17.41h	8	50x300	17550	0.83	
2004/01/23	13.36h	4	25x225	7600	0.70	
2004/01/25	04.12h	3	50x525	28800	0.73	
2004/01/26	11.52h	5	75x375	20300	0.75	
2004/01/26	12.41h	1	100x450	26750	0.82	
2004/01/26	12.41h	1	100x450	26750	0.82	
2004/01/26	12.41h	6	50x300	12250	0.82	
2004/01/26	12.41h	5	25x175	5600	0.82	
2004/01/26	16.46h	6	50x350	14650	0.70	
2004/01/26	17.35h	9	50x150	7500	0.74	
2004/01/26	20.28h	5	50x375	15700	0.82	
2004/01/27	02.40h	1	50x325	14950	0.58	
2004/01/27	17.09h	4	25x225	8150	0.68	
2004/03/16	13.13h	1	50x825	40500	0.90	
2004/03/16	13.13h	6	25x225	6450	0.90	
2004/03/16	19.59h	7	100x1175	39350	0.30	
2004/03/17	13.36h	7	50x600	30000	0.93	*
2004/03/17	19.28h	8	50x350	19300	0.55	
2004/03/18	04.56h	9	125x475	46350	0.12	
2004/03/18	13.58h	2	100x1400	140000	0.66	*
2004/03/19	14.21h	4	50x625	26350	0.79	
2004/03/19	17.29h	1	100x1175	85350	0.32	
2004/04/03	16.27h	8	50x100	5500	0.76	
2004/04/07	00.18h	1	50x300	12600	0.75	
2004/04/07	00.45h	2	25x300	7500	0.70	*
2004/04/07	02.06h	3	400x875	158350	0.82	
2004/04/07	02.06h	2	325x975	153400	0.82	
2004/04/07	02.06h	10	75x200	12650	0.82	
2004/04/07	02.06h	4	100x250	17250	0.82	
2004/04/07	03.54h	2	125x375	25100	0.63	
2004/04/07	07.04h	6	50x125	5750	0.68	
2004/04/17	13.22h	13	50x250	11100	0.83	
2004/04/22	13.49h	3	225x400	68750	0.74	
2004/04/22	19.41h	3	50x300	17300	0.61	
2004/04/23	01.06h	10	75x300	13550	0.56	
2004/04/23	12.22h	4	50x675	28600	0.76	
2004/04/23	12.22h	4	50x675	28600	0.76	
2004/04/23	13.44h	6	50x350	18750	0.90	
2004/04/23	23.12h	4	25x225	8500	0.71	
2004/05/02	00.31h	1	25x350	13200	0.44	
2004/05/03	16.39h	4	50x625	26650	0.37	
2004/05/03	23.52h	8	50x225	12000	0.29	
2004/05/06	08.16h	1	125x600	64300	0.44	
2004/05/06	11.53h	1	75x625	38200	0.81	
2004/05/06	13.14h	1	75x400	21850	0.88	
2004/05/06	14.08h	3	50x325	13550	0.78	
2004/05/06	14.35h	2	300x750	120900	0.82	
2004/05/06	15.02h	4	200x625	53400	0.77	
2004/05/06	15.02h	7	50x325	11950	0.77	
2004/05/21	01.52h	4	50x150	6150	0.20	

%Elapsed time: 00:35:34
%Intensity threshold...: 100/255
%Parameters to select/accept/discard regions:
% AxLen...(m)..: 500.00
% Orient..(deg): 45.00
% AxRatio......: 1.60
% MinArea.(m^2): 5000.00
% MaxArea.(m^2): 800000.00
% BrRatio......: 0.90
%Number of avalanches candidates: 117/4643
%Avalanches after supervision: 72+5

%Avalanches auto-classified supervised
% Period analyzed: 2005/01/04 - 2005/05/31

%Date	Time	Pos	Axes	Area	DcRt	Mn
2005/01/06	19.42h	6	100x300	22650	0.43	
2005/01/06	19.42h	7	50x125	5600	0.43	
2005/01/18	16.50h	5	50x100	5050	0.79	
2005/01/18	17.22h	4	50x125	5950	0.35	
2005/01/18	19.20h	1	50x300	12000	0.75	
2005/01/18	19.30h	10	25x400	12200	0.77	*
2005/01/18	20.34h	1	125x950	72650	0.31	
2005/01/18	21.38h	3	75x500	27450	0.61	
2005/01/18	23.35h	1	100x450	23700	0.48	
2005/01/19	07.46h	1	25x225	7150	0.43	
2005/01/20	21.17h	1	50x175	6850	0.38	
2005/01/21	06.32h	6	25x225	7950	0.78	
2005/01/21	07.36h	4	25x300	10600	0.37	
2005/01/21	11.30h	3	125x750	77100	0.65	
2005/01/21	23.36h	1	75x425	22650	0.24	
2005/01/22	00.08h	2	675x1400	728100	0.64	
2005/01/22	00.08h	4	50x200	9950	0.64	
2005/01/22	01.12h	3	175x600	76900	0.21	
2005/01/22	02.37h	3	75x200	13650	0.18	
2005/01/22	02.48h	1	550x1625	676500	0.75	*
2005/01/22	02.48h	3	200x675	54900	0.75	*
2005/01/22	03.09h	2	75x175	10250	0.70	
2005/01/22	03.20h	1	100x525	45350	0.19	
2005/01/22	03.31h	3	225x1025	161400	0.32	
2005/01/22	04.13h	3	275x925	200200	0.32	
2005/01/22	04.13h	2	100x275	22550	0.32	
2005/01/22	04.35h	2	325x1575	296100	0.41	
2005/01/22	04.35h	6	75x250	15700	0.41	
2005/01/22	04.45h	1	25x225	7850	0.42	
2005/01/22	19.31h	1	75x375	22600	0.71	
2005/01/23	04.36h	1	50x400	17200	0.09	
2005/01/23	04.46h	5	50x125	5550	0.08	
2005/01/23	05.50h	1	300x525	83400	0.14	
2005/01/23	06.01h	3	75x575	38200	0.14	
2005/01/23	06.12h	3	225x600	73650	0.29	
2005/01/23	06.22h	2	150x300	45000	0.33	*
2005/01/23	06.33h	1	75x275	18700	0.20	*
2005/01/23	06.44h	6	100x275	21600	0.16	*
2005/01/23	07.05h	5	200x525	61000	0.12	
2005/01/23	07.16h	3	175x650	52550	0.16	
2005/01/23	08.52h	8	75x300	16400	0.05	
2005/01/23	10.07h	4	150x550	65000	0.14	
2005/01/23	10.28h	3	50x275	10550	0.17	
2005/01/23	10.39h	1	200x825	123450	0.23	
2005/01/23	10.39h	5	50x175	9850	0.23	
2005/01/23	10.39h	3	50x125	6150	0.23	
2005/01/23	11.00h	1	50x250	11600	0.16	
2005/01/23	12.15h	2	325x875	206700	0.26	
2005/01/23	12.15h	3	100x625	33000	0.26	
2005/01/23	12.36h	5	100x225	19300	0.17	
2005/01/23	13.08h	6	25x175	7200	0.09	
2005/01/23	15.59h	3	25x625	18150	0.12	
2005/01/24	02.50h	1	50x350	14800	0.55	
2005/01/24	04.59h	6	125x325	33200	0.13	
2005/01/24	11.55h	5	50x625	29150	0.88	
2005/01/24	12.06h	1	75x700	38000	0.93	*
2005/01/24	17.48h	2	275x1900	326750	0.49	
2005/01/25	04.29h	1	275x1000	136400	0.50	
2005/01/25	13.23h	7	75x275	16600	0.90	
2005/01/25	14.05h	3	75x475	24200	0.77	
2005/01/26	02.55h	14	75x300	20400	0.75	

2005/02/17	10.09h	1	150x1650	179850	0.22	
2005/02/17	10.30h	1	75x750	46750	0.11	
2005/02/17	10.51h	2	275x1925	363500	0.40	
2005/03/08	09.34h	5	50x1000	50000	0.20	*
2005/03/10	12.29h	4	50x125	6550	0.81	
2005/03/10	14.12h	3	100x650	52850	0.23	
2005/03/10	14.47h	4	50x225	9850	0.71	
2005/03/12	13.14h	14	75x225	14000	0.68	
2005/03/13	01.50h	1	100x175	14700	0.15	
2005/03/13	04.55h	1	100x300	30000	0.29	*
2005/03/14	14.48h	14	50x225	10950	0.67	
2005/03/15	10.58h	10	50x150	6800	0.77	
2005/03/15	11.09h	3	75x750	45950	0.74	
2005/03/15	12.07h	1	75x1200	54400	0.55	
2005/03/15	12.18h	3	100x500	32150	0.57	
2005/03/15	12.41h	3	175x575	71950	0.42	
2005/03/15	12.41h	11	50x600	24350	0.42	
2005/03/15	12.53h	4	75x250	12950	0.44	*
2005/03/15	13.04h	1	200x750	67650	0.36	
2005/03/15	13.39h	9	125x375	38800	0.27	
2005/03/15	14.02h	15	50x225	10700	0.81	
2005/03/15	14.25h	1	75x1250	69700	0.93	*
2005/03/15	14.37h	4	50x400	20000	0.55	*
2005/03/15	15.34h	1	50x375	15350	0.39	
2005/03/16	11.57h	12	50x125	6800	0.71	
2005/03/16	12.20h	4	75x225	14550	0.63	
2005/03/16	14.50h	15	50x275	11400	0.30	
2005/03/17	13.26h	8	50x225	11300	0.21	
2005/03/17	14.33h	13	50x375	18850	0.19	
2005/03/18	12.56h	7	50x275	13650	0.33	
2005/03/18	14.48h	7	50x300	15000	0.44	*
2005/03/18	14.59h	10	25x275	9000	0.44	
2005/03/18	15.33h	14	25x250	9600	0.41	
2005/03/19	18.00h	11	150x650	72600	0.14	
2005/03/20	16.23h	15	25x200	8150	0.21	
2005/03/22	11.52h	6	50x275	13350	0.14	
2005/03/23	04.50h	9	50x325	13850	0.07	
2005/03/23	06.19h	9	25x250	8800	0.06	
2005/03/24	20.39h	7	50x625	25600	0.15	
2005/03/24	23.38h	7	100x950	54550	0.13	
2005/03/25	12.05h	9	50x225	10850	0.67	
2005/03/28	18.44h	7	75x825	36100	0.11	*
2005/03/31	16.06h	9	75x275	17800	0.14	
2005/04/08	08.08h	5	75x275	16500	0.42	
2005/04/08	08.19h	3	75x425	29600	0.29	
2005/04/08	10.12h	4	50x275	14300	0.40	
2005/04/08	10.34h	1	50x250	9550	0.45	
2005/04/08	15.15h	5	125x1100	95700	0.21	
2005/04/08	15.48h	3	75x375	16800	0.37	
2005/04/08	16.56h	10	25x225	7450	0.35	
2005/04/09	12.46h	1	100x400	27700	0.20	
2005/04/09	14.27h	2	100x325	15900	0.34	
2005/04/09	14.27h	1	50x250	9800	0.34	
2005/04/17	06.36h	5	50x175	7100	0.16	
2005/04/17	06.59h	2	50x150	7100	0.22	
2005/04/17	06.59h	1	50x325	13200	0.22	
2005/04/17	06.59h	2	50x150	7100	0.22	
2005/04/17	07.22h	5	75x175	13000	0.28	
2005/04/17	07.33h	1	100x225	18400	0.28	
2005/04/17	08.19h	3	275x800	118100	0.23	
2005/04/17	08.31h	4	50x225	12250	0.23	
2005/04/17	09.05h	3	100x725	38600	0.19	
2005/04/17	09.16h	2	25x200	7650	0.28	*
2005/04/17	09.28h	3	50x325	10650	0.26	
2005/04/17	10.02h	6	50x150	6650	0.26	
2005/04/17	10.59h	1	25x150	5800	0.34	
2005/04/17	13.50h	1	50x650	30350	0.22	
2005/04/17	14.13h	10	50x250	9000	0.45	
2005/04/17	14.36h	4	50x675	28950	0.40	
2005/04/17	15.33h	10	25x200	5700	0.73	
2005/04/18	09.26h	1	125x350	29600	0.57	
2005/04/19	05.26h	2	50x300	15000	0.14	*
2005/04/19	08.06h	2	100x550	25250	0.31	
2005/04/19	14.00h	6	50x175	8800	0.57	
2005/04/21	14.03h	3	50x125	5700	0.78	
2005/04/26	10.47h	3	25x350	12850	0.88	
2005/04/28	12.19h	3	125x475	42550	0.71	
2005/04/28	12.54h	3	50x475	22100	0.70	
2005/04/28	15.37h	1	100x300	30000	0.73	*
2005/04/29	12.11h	2	50x175	6850	0.59	
2005/04/29	13.44h	4	50x800	40000	0.58	*
2005/04/29	23.49h	6	25x225	7750	0.11	
2005/04/30	03.18h	6	75x375	20750	0.10	
2005/05/04	18.59h	3	75x375	23600	0.11	

%Elapsed time: 01:54:51
%Intensity threshold...: 100/255
%Parameters to select/accept/discard regions:
% AxLen...(m)..: 500.00
% Orient..(deg): 45.00
% AxRatio......: 1.60
% MinArea.(m^2): 5000.00
% MaxArea.(m^2): 800000.00
% BrRatio......: 0.90
%Number of avalanches candidates: 186/15715
%Avalanches after supervision: 127+18

%Avalanches auto-classified supervised
% Period analyzed: 2005/12/01 - 2006/05/14

%Date	Time	Pos	Axes	Area	DcRt	Mn
2005/12/04	05.23h	1	25x275	8300	0.23	
2005/12/16	10.08h	1	50x125	5800	0.25	
2005/12/16	10.32h	1	50x375	14100	0.26	
2005/12/16	12.31h	1	25x175	5600	0.37	
2005/12/16	15.29h	3	100x625	36550	0.26	
2005/12/16	15.41h	3	150x625	68750	0.38	
2005/12/16	17.29h	1	50x425	20600	0.36	
2005/12/17	04.53h	6	75x375	25700	0.72	
2005/12/17	11.05h	4	25x275	9800	0.38	
2005/12/17	12.17h	1	25x400	10000	0.31	*
2005/12/17	12.29h	1	125x600	62100	0.24	
2005/12/17	12.29h	5	25x125	5600	0.24	
2005/12/17	17.20h	3	75x175	11400	0.28	
2005/12/17	19.10h	1	125x400	38000	0.89	
2005/12/17	19.22h	3	125x500	46900	0.79	
2005/12/17	22.13h	6	125x325	31350	0.53	
2005/12/17	22.50h	5	50x225	9400	0.77	
2005/12/17	23.39h	2	25x475	15350	0.90	*
2005/12/23	02.30h	3	50x475	20000	0.18	
2005/12/24	10.26h	1	125x350	36000	0.32	
2005/12/24	10.38h	4	50x225	10600	0.39	
2005/12/24	13.02h	1	50x425	20900	0.50	
2005/12/30	20.00h	1	125x650	57650	0.30	
2005/12/30	20.00h	3	50x125	6450	0.30	
2005/12/30	20.11h	7	75x325	22100	0.38	
2005/12/30	20.11h	2	100x450	25200	0.38	
2005/12/30	20.23h	1	375x725	169950	0.48	
2005/12/30	21.10h	4	250x775	130450	0.39	
2005/12/30	21.10h	10	100x375	34250	0.39	
2005/12/30	21.34h	1	125x750	79900	0.55	
2005/12/30	21.34h	1	125x750	79900	0.55	
2005/12/30	21.46h	1	225x650	77400	0.57	
2005/12/30	21.58h	10	50x525	25350	0.60	
2005/12/30	22.45h	5	50x200	9450	0.33	
2005/12/30	22.57h	2	500x1500	365100	0.47	
2005/12/31	00.08h	6	100x200	14100	0.74	*
2005/12/31	00.43h	8	500x700	259800	0.36	
2005/12/31	02.28h	4	300x1150	257550	0.35	
2005/12/31	02.52h	1	25x250	7900	0.47	
2005/12/31	04.14h	3	175x725	89750	0.25	
2005/12/31	05.24h	1	125x250	21650	0.29	
2005/12/31	05.48h	3	150x525	57200	0.24	*
2005/12/31	05.59h	2	1175x1550	690200	0.61	
2005/12/31	09.56h	3	75x400	22050	0.78	
2005/12/31	11.31h	1	125x1250	85000	0.77	

2006/01/02	08.02h	4	50x125	5350	0.65	
2006/01/02	10.23h	2	150x550	67000	0.43	
2006/01/02	10.23h	1	175x325	38350	0.43	
2006/01/02	10.23h	1	175x325	38350	0.43	
2006/01/02	10.23h	2	150x550	67000	0.43	
2006/01/02	11.21h	1	125x425	43500	0.55	
2006/01/02	14.51h	1	50x250	13050	0.68	
2006/01/02	20.56h	1	125x1250	88100	0.66	
2006/01/02	21.08h	2	50x250	13900	0.68	
2006/01/03	02.14h	2	75x200	15750	0.35	
2006/01/09	18.07h	8	375x825	167450	0.55	
2006/01/09	18.07h	10	75x375	18900	0.55	
2006/01/17	19.44h	3	100x800	53550	0.40	*
2006/01/17	19.56h	3	250x575	88950	0.40	
2006/01/17	20.08h	3	525x700	185250	0.47	
2006/01/17	20.08h	1	100x400	40000	0.47	*
2006/01/17	20.20h	2	25x200	7700	0.39	
2006/01/17	20.32h	3	400x800	230500	0.46	
2006/01/17	20.44h	2	125x525	41350	0.41	
2006/01/17	21.20h	7	50x725	35650	0.32	
2006/01/17	21.20h	1	75x450	29450	0.32	
2006/01/17	21.32h	1	100x375	27650	0.36	*
2006/01/18	04.30h	6	50x225	11600	0.16	
2006/01/18	05.06h	2	1050x1350	643750	0.67	
2006/01/18	06.43h	1	300x1300	231750	0.32	
2006/01/18	06.43h	3	125x775	52500	0.32	*
2006/01/18	07.07h	1	75x675	41600	0.26	
2006/01/18	07.55h	3	75x250	15700	0.33	
2006/01/18	08.07h	1	100x850	60650	0.25	
2006/01/18	08.43h	1	75x225	13850	0.28	
2006/01/18	08.55h	4	250x1225	197350	0.26	
2006/01/18	09.07h	1	100x525	46150	0.31	
2006/01/18	10.55h	4	75x250	17050	0.95	*
2006/01/18	13.44h	1	125x375	32250	0.18	
2006/01/18	19.46h	14	25x150	5500	0.28	
2006/01/19	06.33h	3	75x450	20350	0.17	
2006/01/19	12.11h	3	75x700	38800	0.89	
2006/01/19	17.59h	11	250x550	88800	0.76	
2006/01/20	10.52h	6	50x425	19500	0.63	
2006/01/20	12.13h	4	50x200	12000	0.78	
2006/01/20	12.36h	4	25x450	15300	0.83	
2006/02/05	05.38h	11	125x625	55750	0.10	
2006/02/09	13.17h	3	25x175	6200	0.19	
2006/02/12	15.58h	2	50x125	5950	0.07	
2006/02/15	17.55h	5	50x200	9050	0.23	
2006/02/15	18.06h	1	25x200	7650	0.24	
2006/02/15	18.28h	1	25x300	7500	0.28	*
2006/02/15	18.50h	1	25x425	14900	0.35	
2006/02/15	20.20h	1	100x425	37500	0.21	
2006/02/15	20.20h	3	50x225	12750	0.21	
2006/02/15	20.42h	1	50x250	14550	0.23	
2006/02/16	00.47h	3	125x725	61500	0.10	
2006/02/16	02.05h	7	50x400	14850	0.36	
2006/02/16	02.05h	4	50x125	5950	0.36	
2006/02/16	02.16h	6	50x300	12500	0.47	
2006/02/16	02.50h	3	200x850	114150	0.28	
2006/02/16	03.45h	2	275x825	154750	0.40	
2006/02/16	04.07h	3	100x800	80000	0.73	*
2006/02/16	04.19h	3	225x975	138200	0.71	
2006/02/16	04.30h	3	350x900	251450	0.53	
2006/02/16	04.41h	2	150x400	47350	0.43	
2006/02/16	05.25h	3	75x575	30550	0.54	
2006/02/16	09.08h	5	400x875	245950	0.38	
2006/02/16	10.14h	1	50x500	21100	0.61	
2006/02/16	10.25h	1	75x375	22500	0.52	
2006/02/16	10.48h	2	1200x1475	791250	0.78	
2006/02/16	12.39h	1	50x800	40000	0.53	*
2006/02/16	12.50h	1	50x200	8950	0.84	
2006/02/16	22.18h	3	50x400	17550	0.71	
2006/02/17	10.11h	3	75x150	10800	0.21	
2006/02/17	10.33h	1	125x400	25500	0.44	
2006/02/17	10.44h	1	175x375	48550	0.57	
2006/02/17	10.55h	1	175x500	49950	0.46	
2006/02/17	16.07h	3	50x375	14300	0.67	
2006/02/18	01.59h	5	50x175	8000	0.07	
2006/02/18	02.54h	4	50x300	12600	0.30	
2006/02/18	02.54h	3	50x150	6350	0.30	
2006/02/18	03.05h	6	200x675	91250	0.35	
2006/02/18	03.05h	1	50x475	17350	0.35	
2006/02/18	03.17h	1	125x525	50650	0.34	
2006/02/18	03.28h	4	25x225	5350	0.31	
2006/02/18	05.53h	1	100x1400	140000	0.38	*
2006/02/18	06.26h	4	125x800	52500	0.32	
2006/02/18	06.37h	1	25x400	10000	0.26	*
2006/02/18	06.48h	1	50x400	15250	0.26	
2006/02/18	07.22h	3	100x650	53900	0.32	
2006/02/18	07.33h	9	25x175	6400	0.18	
2006/02/18	09.13h	3	200x1075	164300	0.27	
2006/02/18	09.24h	5	25x250	9800	0.26	
2006/02/18	10.09h	2	150x1600	240000	0.27	*
2006/02/18	10.20h	4	425x1200	215650	0.25	
2006/02/18	10.20h	1	150x1600	240000	0.25	*
2006/02/18	11.27h	2	50x575	27750	0.25	
2006/02/19	13.26h	7	50x600	23100	0.89	
2006/02/20	12.05h	4	25x200	7100	0.35	
2006/02/23	10.59h	3	50x125	5150	0.32	
2006/02/23	11.44h	3	125x425	32650	0.29	
2006/02/27	14.43h	4	50x225	10950	0.15	
2006/02/28	17.48h	2	50x125	6550	0.29	
2006/02/28	18.32h	1	75x375	27200	0.25	
2006/02/28	18.54h	1	50x300	10200	0.28	
2006/02/28	19.05h	2	125x350	38350	0.23	
2006/02/28	19.17h	3	50x100	5050	0.22	
2006/02/28	19.50h	3	50x150	6400	0.11	
2006/02/28	21.08h	1	25x450	13850	0.26	
2006/03/01	00.06h	6	75x250	14500	0.14	
2006/03/01	01.02h	6	75x375	23550	0.27	
2006/03/01	01.13h	3	50x475	22950	0.32	
2006/03/01	01.24h	3	50x400	16950	0.53	
2006/03/01	01.24h	3	50x400	16950	0.53	
2006/03/01	01.35h	2	25x275	7500	0.42	
2006/03/01	02.31h	3	125x375	38000	0.21	
2006/03/01	02.53h	4	50x350	15200	0.55	
2006/03/01	03.15h	8	50x225	9300	0.32	
2006/03/01	03.26h	3	125x500	43600	0.26	
2006/03/01	03.37h	1	100x625	31900	0.24	
2006/03/01	04.00h	1	575x1100	304000	0.60	
2006/03/01	04.11h	6	150x300	24700	0.53	
2006/03/01	04.44h	3	225x475	55650	0.35	
2006/03/01	04.55h	9	50x200	11450	0.37	
2006/03/01	06.47h	10	25x200	5350	0.37	
2006/03/01	07.54h	3	225x550	90900	0.28	
2006/03/01	12.21h	1	50x275	11350	0.64	
2006/03/01	13.27h	6	100x350	30050	0.12	
2006/03/01	17.43h	2	325x925	131650	0.30	
2006/03/01	17.43h	2	325x925	131650	0.30	
2006/03/02	17.06h	1	25x275	5750	0.15	
2006/03/02	17.40h	3	50x100	5300	0.18	
2006/03/03	01.27h	3	250x950	144200	0.30	
2006/03/03	01.27h	1	175x450	47350	0.30	
2006/03/03	01.49h	3	50x225	9050	0.34	
2006/03/03	02.23h	3	125x750	70850	0.12	
2006/03/03	02.56h	3	75x625	25050	0.19	
2006/03/03	03.07h	1	150x750	82400	0.35	
2006/03/03	03.19h	2	275x775	157350	0.41	
2006/03/03	03.19h	6	75x350	22400	0.41	
2006/03/03	03.52h	3	250x825	147000	0.23	
2006/03/03	04.59h	1	100x250	13900	0.43	
2006/03/03	05.54h	7	100x800	80000	0.22	*
2006/03/03	06.06h	1	375x925	219850	0.52	
2006/03/03	06.17h	1	225x1625	206500	0.45	
2006/03/03	06.17h	3	75x425	32750	0.45	
2006/03/03	06.17h	2	100x450	25450	0.45	
2006/03/03	06.28h	3	100x700	52950	0.50	
2006/03/03	06.39h	1	50x325	15050	0.21	
2006/03/03	07.01h	3	50x625	27200	0.33	
2006/03/03	07.12h	1	275x1425	225000	0.41	
2006/03/03	07.12h	3	150x1100	64800	0.41	
2006/03/03	07.23h	3	150x1275	82750	0.43	
2006/03/03	07.23h	9	100x500	38250	0.43	

2006/03/03	07.35h	3	225x1300	86050	0.37	
2006/03/03	07.35h	9	100x600	53300	0.37	
2006/03/03	07.46h	3	250x675	90300	0.28	
2006/03/03	08.08h	3	25x425	13050	0.21	
2006/03/03	08.08h	5	50x200	8450	0.21	
2006/03/03	08.19h	6	250x550	97700	0.31	
2006/03/03	08.19h	2	50x300	12750	0.31	
2006/03/03	09.04h	1	50x275	13200	0.53	
2006/03/03	09.26h	3	50x375	17450	0.12	
2006/03/03	10.21h	3	100x650	33950	0.19	
2006/03/03	10.55h	1	125x325	26500	0.32	
2006/03/03	11.39h	1	350x1375	371000	0.41	
2006/03/03	11.39h	1	350x1375	371000	0.41	
2006/03/03	12.02h	3	25x175	7150	0.79	
2006/03/03	12.24h	2	275x700	123250	0.60	
2006/03/03	12.24h	3	50x200	8600	0.60	
2006/03/03	12.46h	1	125x550	53500	0.75	
2006/03/03	13.42h	5	325x1350	185450	0.66	
2006/03/03	14.37h	1	50x150	7750	0.84	
2006/03/03	19.04h	1	50x200	10000	0.75	
2006/03/03	20.00h	1	100x375	34700	0.68	
2006/03/03	22.14h	9	50x150	8050	0.73	
2006/03/03	23.54h	3	100x675	56950	0.50	
2006/03/04	00.27h	1	625x1050	363050	1.02	*
2006/03/04	02.07h	1	100x500	43600	0.72	
2006/03/04	06.12h	1	75x350	21650	0.89	
2006/03/04	08.37h	3	325x1050	272400	0.62	
2006/03/04	21.03h	3	125x975	89000	0.49	
2006/03/05	04.39h	1	50x325	16200	0.43	
2006/03/05	05.12h	5	50x150	8950	0.74	
2006/03/05	11.30h	1	75x175	11350	0.34	
2006/03/06	09.54h	1	475x1425	532300	0.58	
2006/03/06	10.44h	2	1300x1775	1054400	0.93	*
2006/03/06	11.18h	1	150x1800	270000	0.20	*
2006/03/06	13.00h	1	350x925	184150	0.84	
2006/03/07	03.23h	3	75x425	26950	0.10	
2006/03/08	10.55h	3	50x250	10400	0.56	
2006/03/08	11.42h	1	50x400	18500	0.52	
2006/03/08	12.40h	3	225x625	74100	0.42	
2006/03/08	13.16h	1	325x900	188400	0.31	
2006/03/08	13.16h	10	125x275	26450	0.31	
2006/03/08	13.27h	1	450x1175	354850	0.49	
2006/03/08	13.27h	5	50x225	10450	0.49	
2006/03/08	13.39h	3	400x1000	204950	0.48	
2006/03/08	13.39h	11	75x300	20750	0.48	
2006/03/08	14.15h	3	150x825	89450	0.18	
2006/03/08	15.13h	3	225x500	74100	0.22	
2006/03/08	16.01h	3	250x700	117600	0.21	
2006/03/08	16.24h	2	400x1100	237950	0.44	
2006/03/08	16.24h	1	275x775	148700	0.44	
2006/03/08	17.59h	3	50x375	16450	0.28	
2006/03/08	19.33h	3	325x800	97600	0.37	
2006/03/08	22.43h	2	525x1225	283300	0.53	
2006/03/08	23.54h	4	225x1125	171350	0.54	
2006/03/08	23.54h	3	150x525	64500	0.54	
2006/03/09	03.46h	3	50x450	19900	0.57	
2006/03/09	06.53h	3	50x225	9900	0.50	
2006/03/10	03.50h	1	75x425	24200	0.46	
2006/03/10	03.50h	1	75x425	24200	0.46	
2006/03/10	15.56h	5	50x150	8450	0.37	
2006/03/10	16.32h	1	150x1125	130650	0.34	
2006/03/10	16.43h	5	50x200	10800	0.37	
2006/03/10	16.55h	6	75x300	21400	0.51	
2006/03/10	16.55h	5	50x225	10500	0.51	
2006/03/10	17.07h	1	75x1125	55000	0.48	
2006/03/10	17.07h	6	50x225	9350	0.48	
2006/03/10	17.19h	3	150x375	29550	0.57	
2006/03/10	17.54h	6	50x275	9950	0.35	
2006/03/10	17.54h	3	50x175	7650	0.35	
2006/03/11	00.24h	9	50x200	9000	0.08	
2006/03/11	06.49h	3	100x200	16650	0.13	
2006/03/11	06.49h	6	75x250	17850	0.13	
2006/03/11	11.06h	3	50x175	8800	0.13	
2006/03/11	21.43h	1	50x325	15900	0.17	
2006/03/11	21.43h	1	50x325	15900	0.17	
2006/03/11	22.30h	4	25x225	6950	0.35	
2006/03/11	23.29h	1	75x725	37150	0.26	
2006/03/11	23.41h	2	25x225	7650	0.32	
2006/03/11	23.41h	5	50x125	7800	0.32	
2006/03/11	23.53h	3	50x325	18900	0.41	
2006/03/12	00.05h	2	100x1275	59650	0.43	
2006/03/12	00.17h	13	50x225	11050	0.45	
2006/03/12	00.40h	3	175x825	81600	0.44	
2006/03/12	01.03h	1	25x175	6450	0.32	
2006/03/12	01.26h	1	125x1250	103750	0.43	
2006/03/12	01.38h	1	200x1225	157800	0.60	
2006/03/12	02.13h	2	75x1050	60100	0.77	
2006/03/12	02.47h	1	75x675	40500	0.75	
2006/03/12	19.12h	1	50x350	19050	0.43	
2006/03/16	17.17h	14	50x150	8550	0.12	
2006/03/17	12.50h	5	50x225	9800	0.79	
2006/03/17	16.10h	14	50x250	14150	0.12	
2006/03/19	10.36h	10	75x500	28450	0.81	
2006/03/21	15.01h	13	50x175	8300	0.26	
2006/03/21	20.43h	8	75x425	23500	0.11	
2006/03/22	06.28h	14	25x200	7750	0.08	
2006/03/22	16.38h	10	50x250	10100	0.63	
2006/03/22	16.50h	14	50x300	15800	0.16	
2006/03/23	09.50h	2	50x100	5600	0.58	
2006/03/23	15.07h	14	50x200	9600	0.84	
2006/03/23	15.42h	14	50x150	6500	0.75	
2006/03/24	22.27h	1	75x400	24850	0.15	
2006/03/25	02.33h	3	75x375	22300	0.57	
2006/03/25	09.21h	5	50x525	23300	0.47	
2006/03/25	09.21h	6	25x250	8950	0.47	
2006/03/25	09.56h	1	100x600	49450	0.87	
2006/03/25	11.07h	1	200x1000	200000	0.90	*
2006/03/25	21.43h	11	50x225	7900	0.56	
2006/03/25	23.06h	14	25x175	6300	0.50	
2006/03/26	01.27h	13	25x125	5050	0.41	
2006/03/26	11.04h	2	75x425	23000	0.88	
2006/03/26	12.04h	2	150x1700	118700	0.76	
2006/03/26	13.39h	14	50x275	10800	0.90	*
2006/03/26	14.26h	1	100x1525	120200	0.27	
2006/03/26	15.13h	14	50x400	14600	0.50	
2006/03/26	16.00h	8	75x350	22850	0.35	
2006/03/26	19.20h	4	25x250	9400	0.50	
2006/03/27	09.23h	14	50x425	20450	0.58	
2006/03/27	12.43h	4	100x925	53750	0.64	
2006/03/27	14.17h	7	125x850	67100	0.41	
2006/03/27	14.17h	6	75x475	27000	0.41	
2006/03/27	15.39h	5	25x250	6900	0.79	
2006/03/28	20.25h	1	125x350	33400	0.76	
2006/03/28	23.59h	3	75x700	30300	0.64	
2006/03/29	07.57h	5	50x150	7100	0.35	
2006/03/29	08.32h	3	50x125	6100	0.29	
2006/03/29	08.43h	4	125x375	26550	0.30	
2006/03/29	08.55h	3	100x600	41450	0.28	
2006/03/29	09.07h	1	150x625	70950	0.31	
2006/03/29	09.42h	6	75x225	18250	0.42	
2006/03/29	09.42h	1	50x250	9950	0.42	
2006/03/29	10.05h	3	50x425	22150	0.34	
2006/03/29	13.36h	2	175x450	61900	0.27	
2006/03/30	11.07h	9	50x250	13050	0.31	
2006/03/30	14.50h	3	50x325	14500	0.63	
2006/03/30	15.02h	6	50x150	6250	0.65	
2006/03/30	15.49h	5	50x125	7250	0.62	
2006/03/30	16.24h	5	100x275	20000	0.52	
2006/03/30	16.48h	1	200x450	54850	0.54	
2006/03/30	17.11h	5	25x125	5400	0.60	
2006/03/30	17.35h	3	50x175	9750	0.67	
2006/03/30	21.31h	1	75x475	34400	0.58	
2006/03/31	02.24h	3	175x800	74700	0.45	
2006/03/31	03.11h	3	50x325	15150	0.62	
2006/03/31	06.17h	1	125x400	41450	0.56	
2006/03/31	06.41h	2	150x400	60000	0.45	*
2006/03/31	06.52h	3	75x575	39750	0.57	
2006/03/31	08.02h	1	75x1025	48300	0.53	
2006/03/31	14.53h	1	100x1150	74900	0.55	
2006/03/31	14.53h	2	100x975	72300	0.55	

2006/04/01	09.28h	8	50x250	11650	0.59
2006/04/01	18.05h	12	50x150	7000	0.59
2006/04/02	03.29h	15	25x200	6850	0.58
2006/04/05	09.30h	3	25x300	8950	0.50
2006/04/05	10.52h	5	100x225	19200	0.41
2006/04/05	11.51h	3	75x650	42300	0.31
2006/04/05	13.25h	6	50x325	12350	0.36
2006/04/05	14.00h	1	225x1550	159450	0.28
2006/04/05	14.35h	3	75x250	15200	0.42
2006/04/06	10.20h	7	50x150	6300	0.43
2006/04/06	10.32h	4	75x175	12950	0.49
2006/04/06	10.55h	9	75x325	20550	0.58
2006/04/06	11.30h	5	50x150	6600	0.61
2006/04/09	20.44h	14	25x225	7700	0.42
2006/04/10	04.45h	1	25x325	7400	0.40
2006/04/10	22.58h	4	50x125	5450	0.45
2006/04/11	01.07h	3	75x300	13000	0.60
2006/04/11	01.30h	3	50x250	11900	0.67
2006/04/11	01.42h	3	50x425	20100	0.24
2006/04/11	02.05h	2	25x225	7850	0.32
2006/04/11	02.17h	1	50x450	20550	0.22
2006/04/11	02.28h	3	50x375	15750	0.24
2006/04/11	04.13h	2	150x350	40800	0.28
2006/04/11	04.36h	3	150x750	66850	0.54
2006/04/11	04.48h	1	200x425	56050	0.42
2006/04/11	04.48h	2	50x175	8000	0.42
2006/04/11	05.11h	1	100x675	54250	0.30
2006/04/11	05.11h	3	75x525	28650	0.30
2006/04/11	05.58h	2	150x400	45550	0.51
2006/04/11	12.48h	3	50x225	13600	0.24
2006/04/12	23.42h	3	25x200	6300	0.71
2006/04/13	16.05h	2	25x450	14250	0.29
2006/04/13	17.51h	4	75x725	40300	0.16
2006/04/14	07.45h	4	75x150	10800	0.50
2006/04/14	14.24h	2	125x725	44800	0.87
2006/04/15	14.18h	14	25x250	5650	0.79
2006/04/15	23.09h	14	25x200	7400	0.35
2006/04/16	15.44h	7	125x800	53100	0.37
2006/04/17	14.16h	9	125x275	26700	0.59
2006/04/17	14.51h	2	150x925	112050	0.33
2006/04/19	12.41h	4	50x150	7550	0.65
2006/04/19	16.25h	5	25x300	9550	0.58
2006/04/19	17.12h	5	75x575	30250	0.46
2006/04/20	15.09h	9	25x200	7150	0.44
2006/04/21	13.06h	6	50x375	19050	0.50
2006/04/21	13.17h	14	50x200	8750	0.36
2006/04/21	13.29h	3	75x900	54600	0.26
2006/04/21	14.04h	6	25x125	5100	0.50
2006/04/21	14.52h	9	25x275	9950	0.50
2006/04/22	10.40h	4	75x500	27350	0.68
2006/04/22	11.27h	6	50x375	16550	0.67
2006/04/22	11.50h	2	25x250	6500	0.50
2006/04/22	12.14h	6	25x175	6750	0.61
2006/04/22	12.37h	1	75x675	49450	0.38
2006/04/22	12.37h	6	50x250	12450	0.38
2006/04/22	13.36h	4	75x975	55150	0.29
2006/04/22	21.40h	1	75x700	44900	0.31
2006/04/23	11.21h	7	100x1050	66400	0.43
2006/04/23	11.21h	1	100x500	50000	0.43 *
2006/04/23	11.45h	6	50x300	16200	0.61
2006/04/23	12.08h	7	50x400	22250	0.53
2006/04/23	12.56h	4	75x1075	64600	0.70
2006/04/23	13.07h	4	150x575	70600	0.58
2006/04/23	13.19h	1	200x600	60450	0.68
2006/04/23	13.43h	1	75x575	35450	0.60
2006/04/23	14.30h	2	50x250	9750	0.65
2006/04/23	15.17h	6	50x175	6800	0.57
2006/04/23	15.29h	7	50x325	14100	0.47
2006/04/24	11.41h	13	25x125	5350	0.74
2006/04/24	14.13h	5	75x650	39800	0.43 *
2006/04/25	01.27h	6	50x200	7950	0.75
2006/04/25	23.11h	3	100x700	51200	0.16
2006/04/26	12.51h	5	75x750	40150	0.58
2006/04/26	13.26h	2	25x150	5600	1.00 *
2006/04/26	16.34h	5	100x250	18850	0.52
2006/04/26	17.09h	9	50x350	15150	0.43
2006/04/27	10.11h	2	75x350	21950	0.59
2006/04/27	13.08h	1	75x575	38000	0.73
2006/05/03	14.47h	1	25x575	18150	0.68
2006/05/03	16.45h	2	175x1000	146000	0.32
2006/05/03	16.45h	2	175x1000	146000	0.32
2006/05/04	00.03h	3	50x425	20750	0.46
2006/05/04	18.03h	6	25x200	6600	0.41
2006/05/05	22.54h	11	75x375	18300	0.41
2006/05/06	15.18h	3	200x475	54300	0.46
2006/05/06	16.29h	9	75x325	17650	0.63
2006/05/07	13.02h	2	50x200	8100	0.55
2006/05/07	13.14h	3	100x600	35200	0.40
2006/05/07	15.23h	1	75x600	38400	0.19
2006/05/09	11.05h	4	25x225	6050	0.65
2006/05/09	13.02h	4	75x250	15650	0.69
2006/05/09	13.26h	1	50x525	21000	0.71
2006/05/13	02.31h	4	50x450	20300	0.28
2006/05/13	19.58h	4	50x275	12150	0.58

%Elapsed time: 02:08:43
%Intensity threshold...: 100/255
%Parameters to select/accept/discard regions:
% AxLen...(m)..: 500.00
% Orient..(deg): 45.00
% AxRatio......: 1.60
% MinArea.(m^2): 5000.00
% MaxArea.(m^2): 800000.00
% BrRatio......: 0.90
%Number of avalanches candidates: 529/17161
%Avalanches after supervision: 413+26

G.3. Alagna Valsesia (Italy)

The following is the list of avalanches monitored in Alagna Valsesia, Italy.

%Avalanches auto-classified supervised
% Period analyzed: 2006/03/26 - 2006/05/15

%Date	Time	Pos	Axes	Area	DcRt Mn
2006/03/26	09.44h	7	25x150	4050	0.52
2006/03/26	10.20h	8	100x300	13500	0.47
2006/03/26	10.38h	5	25x250	7700	0.56
2006/03/26	10.47h	2	50x475	10850	0.55
2006/04/01	15.26h	8	25x175	3050	0.48
2006/04/05	02.27h	6	50x250	12500	0.45 *
2006/04/05	06.11h	3	50x275	9900	0.72
2006/04/05	06.20h	2	250x275	34750	0.70
2006/04/05	06.29h	6	25x175	3450	0.70
2006/04/05	06.56h	2	125x375	37200	0.72
2006/04/05	06.56h	3	75x375	9600	0.72
2006/04/05	06.56h	3	50x200	8100	0.72
2006/04/05	07.14h	5	50x325	10200	0.47
2006/04/05	07.41h	3	50x225	9050	0.59
2006/04/05	07.50h	8	50x125	6000	0.56
2006/04/05	07.59h	9	25x175	5300	0.45

2006/04/05	08.35h	3	175x375	42850	0.56	
2006/04/05	09.02h	5	25x225	5850	0.45	
2006/04/05	09.57h	11	25x100	2750	0.22	
2006/04/05	10.15h	6	25x100	2750	0.24	
2006/04/05	12.04h	11	25x100	3450	0.46	
2006/04/05	14.39h	9	25x125	3500	0.26	
2006/04/05	14.58h	3	25x150	4300	0.25	
2006/04/05	15.16h	5	25x200	5100	0.34	
2006/04/05	15.34h	9	25x150	4150	0.31	
2006/04/05	16.02h	3	25x150	4350	0.29	
2006/04/09	12.43h	5	25x200	4400	0.48	
2006/04/09	13.01h	5	25x250	5700	0.25	
2006/04/09	13.01h	5	25x75	2500	0.25	
2006/04/10	11.37h	6	25x100	2700	0.30	
2006/04/10	12.22h	5	100x250	15500	0.49	
2006/04/10	14.03h	6	75x400	20000	0.44	
2006/04/10	14.12h	3	50x275	11100	0.55	
2006/04/10	14.12h	3	75x200	9900	0.55	
2006/04/10	14.21h	3	100x300	17550	0.54	
2006/04/10	15.07h	11	50x100	3800	0.33	
2006/04/10	15.52h	8	50x150	7850	0.53	
2006/04/11	00.03h	3	75x225	16200	0.79	
2006/04/11	05.34h	2	200x375	45300	0.89	
2006/04/16	08.22h	7	25x200	4600	0.59	
2006/04/16	09.34h	7	25x100	2700	0.71	
2006/04/16	10.19h	11	50x75	4000	0.62	
2006/04/16	10.19h	6	25x150	2850	0.62	
2006/04/18	00.30h	3	75x250	12800	0.47	
2006/04/18	00.39h	5	75x225	9950	0.61	
2006/04/18	12.44h	11	25x125	3100	0.25	
2006/04/18	13.20h	11	25x100	3500	0.42	
2006/04/21	12.30h	8	25x100	3150	0.50	
2006/04/22	17.13h	6	25x250	5800	0.63	
2006/04/24	13.20h	3	25x200	4650	0.52	
2006/04/24	13.29h	3	50x125	5350	0.59	
2006/04/24	17.09h	5	25x100	2500	0.58	
2006/04/24	19.19h	4	25x75	2650	0.32	
2006/04/25	16.03h	5	75x375	13450	0.81	
2006/04/25	16.31h	5	25x325	7950	0.68	
2006/04/25	16.40h	4	25x225	5800	0.57	
2006/04/26	14.30h	5	25x100	3500	0.43	
2006/04/26	15.43h	8	25x125	2700	0.56	
2006/04/27	13.51h	9	25x125	2500	0.59	
2006/04/27	14.46h	5	25x125	3100	0.45	
2006/05/03	14.51h	8	25x225	4450	0.32	
2006/05/05	12.44h	8	25x225	4950	0.84	
2006/05/06	11.40h	8	50x175	5900	0.65	
2006/05/06	18.32h	8	50x275	10450	0.31	
2006/05/07	09.31h	5	25x75	3150	0.76	
2006/05/07	10.07h	6	25x125	2600	0.67	
2006/05/07	11.38h	6	50x250	12500	0.44 *	
2006/05/07	11.47h	8	25x175	3500	0.43	
2006/05/07	12.42h	8	25x250	6350	0.29	
2006/05/07	13.09h	5	25x225	5100	0.45	
2006/05/07	13.27h	5	50x250	12500	0.44 *	
2006/05/07	14.04h	4	50x150	7500	0.24 *	
2006/05/07	14.59h	4	50x150	7500	0.21 *	
2006/05/07	15.08h	8	25x100	2700	0.29	
2006/05/07	15.17h	11	50x125	3350	0.28	
2006/05/09	00.56h	3	200x450	61150	0.95 *	
2006/05/09	01.14h	5	50x250	7500	0.93 *	
2006/05/10	21.57h	3	200x475	62500	0.78	
2006/05/10	22.25h	8	100x200	12550	0.77	
2006/05/11	07.25h	7	75x125	4900	0.62	
2006/05/11	07.34h	6	100x325	16200	0.70	
2006/05/11	07.52h	5	175x250	25850	0.88	
2006/05/11	10.53h	3	75x375	25200	0.74	
2006/05/11	11.11h	6	50x150	5750	0.83	
2006/05/12	10.24h	3	50x225	9100	0.66	
2006/05/12	10.51h	3	150x250	19550	0.66	
2006/05/12	14.48h	4	25x100	3750	0.69	
2006/05/13	10.04h	5	50x125	4950	0.46	
2006/05/15	23.06h	4	150x150	12400	0.85	

```
%Elapsed time: 01:21:08
%Intensity threshold...: 60/255
%Parameters to select/accept/discard regions:
%   AxLen...(m)..: 150.00
%   Orient..(deg): 45.00
%   AxRatio......: 1.50
%   MinArea.(m^2): 2500.00
%   MaxArea.(m^2): 90000.00
%   BrRatio......: 0.90
%Number of avalanches candidates: 191/8057
%Avalanches after supervision: 82+7



%Avalanches auto-classified supervised
%   Period analyzed: 2006/12/01 - 2007/04/04
```

%Date	Time	Pos	Axes	Area	DcRt	Mn
2006/12/07	00.05h	6	50x225	10450	0.39	
2006/12/07	00.05h	6	50x225	7600	0.39	
2006/12/07	00.11h	6	50x250	10500	0.46	
2006/12/07	11.22h	9	25x100	3400	0.46	
2006/12/08	15.46h	6	75x250	18750	0.41	*
2006/12/08	15.53h	3	250x450	74300	0.73	
2006/12/08	15.59h	6	150x300	45000	0.80	*
2006/12/08	16.12h	11	25x100	3650	0.48	
2006/12/08	16.25h	4	125x350	34900	0.67	
2006/12/08	16.25h	6	75x250	12600	0.67	
2006/12/08	18.14h	3	175x350	37500	0.56	
2006/12/08	18.33h	6	50x200	10000	0.58	*
2006/12/08	18.46h	2	50x350	17500	0.88	*
2006/12/08	19.00h	6	50x125	6500	0.60	
2006/12/08	19.00h	6	25x225	4850	0.60	
2006/12/08	19.52h	3	100x400	29350	0.43	
2006/12/08	20.05h	9	25x200	4700	0.38	
2006/12/08	20.38h	6	100x300	25450	0.55	
2006/12/08	20.38h	7	50x75	4400	0.55	
2006/12/08	20.51h	6	100x250	15400	0.48	
2006/12/08	20.57h	6	50x275	11200	0.46	
2006/12/08	21.17h	7	125x225	18600	0.87	
2006/12/08	21.24h	3	150x400	32600	0.78	
2006/12/08	22.10h	6	50x275	12400	0.50	
2006/12/08	22.17h	6	100x275	15950	0.55	
2006/12/08	22.17h	7	100x200	13800	0.55	
2006/12/08	22.23h	6	100x300	19900	0.60	
2006/12/08	22.23h	9	25x150	4100	0.60	
2006/12/08	22.36h	5	50x250	12500	1.00	*
2006/12/08	23.03h	3	25x250	5750	0.81	
2006/12/08	23.10h	3	25x250	5800	1.00	*
2006/12/08	23.43h	6	125x325	27350	0.86	
2006/12/09	00.03h	4	75x175	12550	0.35	
2006/12/09	01.14h	9	25x175	3100	0.80	
2006/12/09	01.20h	5	50x250	7650	0.75	
2006/12/09	02.19h	6	25x175	5550	0.56	
2006/12/09	06.01h	8	25x100	2650	0.33	
2006/12/09	06.19h	6	125x200	17600	0.37	
2007/01/02	19.01h	9	50x100	2800	0.32	
2007/01/23	08.35h	6	25x225	7700	0.47	
2007/01/23	08.35h	11	25x125	2550	0.47	
2007/01/23	08.47h	11	50x100	4750	0.49	
2007/01/23	09.13h	6	125x275	14850	0.58	
2007/01/23	09.25h	6	50x350	13800	0.65	
2007/01/23	09.38h	9	100x175	13050	0.59	
2007/01/23	13.25h	6	50x225	9550	0.59	
2007/01/23	13.25h	6	25x250	6100	0.59	
2007/01/23	13.25h	5	25x200	4250	0.59	
2007/01/23	13.38h	9	75x175	6650	0.71	
2007/01/23	14.16h	3	150x250	21150	0.85	
2007/01/23	14.16h	9	75x175	6550	0.85	
2007/01/23	15.31h	3	275x450	85100	0.80	
2007/01/23	15.57h	8	50x100	5000	1.00	*
2007/01/24	01.02h	3	75x300	10600	0.68	

2007/01/24	01.15h	5	175x250	22500	0.63	
2007/01/24	01.27h	3	250x350	58100	0.87	
2007/01/24	01.40h	6	100x200	20000	0.86	*
2007/01/24	01.52h	5	50x100	5000	0.97	*
2007/01/24	03.33h	5	50x150	7500	0.84	*
2007/01/24	05.38h	6	200x325	34050	0.54	
2007/01/24	05.51h	6	150x300	29850	0.68	
2007/01/24	05.51h	3	50x100	4700	0.68	
2007/01/24	16.35h	3	25x400	10000	1.17	*
2007/02/12	12.30h	9	25x225	3200	0.58	
2007/03/01	21.00h	9	25x225	6050	0.47	
2007/03/02	01.00h	6	50x325	8400	0.73	
2007/03/02	01.13h	3	25x325	5300	0.71	
2007/03/02	03.42h	3	175x400	35300	0.75	
2007/03/02	07.39h	3	150x400	42350	0.53	
2007/03/02	07.52h	3	150x400	44600	0.57	
2007/03/03	06.15h	9	25x175	4200	0.71	
2007/03/03	06.53h	6	75x225	8700	0.54	
2007/03/03	07.18h	11	25x75	2750	0.71	
2007/03/05	15.32h	11	50x125	5300	0.45	
2007/03/07	02.43h	3	125x375	21900	0.52	
2007/03/07	03.08h	6	200x300	60000	0.89	*
2007/03/07	03.32h	3	125x350	31800	0.65	
2007/03/07	04.22h	5	50x350	10400	0.27	
2007/03/07	06.14h	9	50x175	8200	0.49	
2007/03/07	06.52h	6	175x325	30900	0.45	
2007/03/07	07.04h	6	75x225	15550	0.59	
2007/03/07	07.17h	5	50x150	7500	0.61	*
2007/03/07	07.29h	3	75x325	13000	0.52	
2007/03/07	08.07h	4	75x175	8450	0.53	
2007/03/07	08.19h	3	150x400	42050	0.63	
2007/03/07	08.57h	6	150x275	22750	0.52	
2007/03/07	08.57h	2	75x375	18800	0.52	
2007/03/07	12.55h	8	75x200	13350	0.44	
2007/03/07	16.03h	6	50x200	8900	0.46	
2007/03/07	16.16h	6	75x300	13850	0.56	
2007/03/07	16.29h	6	50x325	8150	0.61	
2007/03/07	16.41h	6	75x250	12200	0.62	
2007/03/07	16.41h	6	50x175	9000	0.62	
2007/03/07	16.54h	6	125x300	27650	0.57	
2007/03/07	16.54h	5	25x125	2600	0.57	
2007/03/07	20.28h	9	75x150	5400	0.57	
2007/03/08	08.34h	5	200x325	40500	0.41	
2007/03/08	08.47h	4	150x275	26250	0.38	
2007/03/11	13.54h	11	50x125	5500	0.50	
2007/03/12	12.28h	11	25x75	2500	0.52	
2007/03/25	03.57h	6	25x225	5400	0.52	
2007/03/25	03.57h	9	25x100	4200	0.52	
2007/03/25	04.10h	6	75x200	9450	0.53	
2007/03/25	07.04h	3	100x225	14200	0.85	
2007/03/25	07.04h	6	75x200	13200	0.85	
2007/03/25	08.44h	5	50x250	12500	0.83	*
2007/03/25	11.02h	9	25x100	3150	0.73	
2007/03/25	11.40h	3	125x400	18600	0.81	
2007/03/25	11.52h	8	150x175	14450	0.80	
2007/03/25	11.52h	5	100x200	7500	0.80	
2007/03/25	12.30h	6	100x300	14400	0.72	
2007/03/25	12.42h	6	150x325	28600	0.65	
2007/03/25	12.42h	3	125x275	14150	0.65	
2007/03/25	13.07h	6	50x200	6600	0.83	
2007/03/25	13.32h	3	100x425	22400	0.67	
2007/03/25	13.32h	4	50x150	8350	0.67	
2007/03/25	13.45h	5	50x250	12500	0.60	*
2007/03/25	14.48h	4	25x50	2350	0.96	*
2007/03/25	15.00h	6	50x200	10000	1.08	*
2007/03/26	11.42h	9	150x250	24600	0.47	
2007/03/26	12.20h	11	75x125	7850	0.22	
2007/03/26	13.22h	6	150x200	17950	0.41	
2007/03/26	14.00h	3	250x325	59750	0.62	
2007/03/26	14.38h	9	50x150	6300	0.33	
2007/03/26	16.06h	3	25x125	2650	0.47	
2007/03/27	03.37h	9	25x225	4650	0.52	
2007/03/27	04.02h	8	50x250	4150	0.58	
2007/03/27	04.39h	3	125x200	20100	0.83	
2007/03/27	05.29h	6	175x400	46700	0.62	
2007/03/27	05.29h	5	25x225	5250	0.62	
2007/03/27	05.42h	5	75x250	10150	0.66	
2007/03/27	06.07h	3	300x525	70400	0.68	
2007/03/27	06.07h	6	25x300	6650	0.68	
2007/03/27	07.09h	4	125x225	17200	0.63	
2007/03/27	07.21h	3	275x375	56650	0.63	
2007/03/27	07.21h	4	125x175	11650	0.63	
2007/03/27	09.02h	6	50x250	9000	0.42	
2007/03/27	10.04h	3	100x375	21600	0.38	
2007/03/27	10.17h	3	150x375	25900	0.43	
2007/03/27	12.10h	6	50x275	7450	0.57	
2007/03/27	12.10h	9	25x100	2850	0.57	
2007/03/27	12.22h	7	50x75	3250	0.59	
2007/03/27	12.35h	11	50x125	6600	0.42	
2007/03/27	13.38h	5	25x200	5350	0.40	
2007/03/27	15.18h	4	25x100	2550	0.47	
2007/03/27	15.56h	5	75x250	18750	0.67	*
2007/03/27	16.09h	5	75x300	22500	0.66	*
2007/03/30	14.48h	6	50x275	11750	0.54	
2007/03/30	16.28h	6	50x275	11800	0.54	
2007/03/31	21.33h	6	200x400	43600	0.52	
2007/03/31	21.46h	9	50x150	7500	0.55	*
2007/03/31	21.58h	9	75x175	7100	0.60	
2007/04/01	12.59h	11	25x100	2500	0.97	*
2007/04/01	13.24h	3	175x400	39600	0.62	
2007/04/01	13.49h	9	100x175	13400	0.53	
2007/04/01	14.02h	6	125x250	21750	0.60	
2007/04/01	14.02h	8	25x175	2650	0.60	
2007/04/01	14.14h	6	125x300	20600	0.76	
2007/04/01	14.27h	6	75x300	19350	0.73	
2007/04/01	22.52h	6	25x250	4000	0.75	
2007/04/02	00.58h	6	25x150	3850	0.46	
2007/04/02	12.50h	5	25x175	4600	0.83	
2007/04/04	04.33h	9	25x100	4000	0.72	
2007/04/04	04.58h	5	25x200	5000	0.57	*

```
%Elapsed time: 02:15:49
%Intensity threshold...: 60/255
%Parameters to select/accept/discard regions:
%   AxLen...(m)..: 150.00
%   Orient..(deg): 45.00
%   AxRatio......: 1.50
%   MinArea.(m^2): 2500.00
%   MaxArea.(m^2): 90000.00
%   BrRatio......: 0.90
%Number of avalanches candidates: 300/14742
%Avalanches after supervision: 142+22




%Avalanches auto-classified supervised
%   Period analyzed: 2007/12/15 - 2008/03/31
%================================================
%Date       Time   Pos    Axes       Area   DcRt Mn
%------------------------------------------------
2007/12/17  11.17h   6    25x200     6000   0.44
2008/01/06  00.45h   3   150x275    27100   0.60
2008/01/06  00.45h   5   150x250    25450   0.60
2008/01/06  00.57h   6   175x300    36950   0.58
2008/01/06  01.10h   3   150x350    33900   0.46
2008/01/06  02.00h  11    50x100     5250   0.23
2008/01/06  02.12h   7    25x75      2900   0.23
2008/01/06  02.24h   3   150x350    37100   0.44
2008/01/06  03.51h   3   175x375    52450   0.57
2008/01/06  03.51h   7    25x75      2650   0.57
2008/01/12  06.36h   3    50x375    20500   0.95 *
2008/01/12  06.49h   6   225x400    45000   0.70 *
2008/01/12  07.01h   3   275x475    70000   0.84
2008/01/12  08.29h   3   250x350    65250   0.67
2008/01/12  08.41h  11    25x125     3800   0.80
2008/01/12  09.19h   8   125x250    19050   0.79
```

2008/01/12	10.34h	3	125x400	31850	0.74	
2008/01/12	11.25h	3	150x400	32050	0.62	
2008/01/12	12.15h	6	50x200	10250	0.61	
2008/01/12	13.43h	3	250x450	78500	0.85	
2008/01/12	14.08h	6	150x375	44100	0.61	
2008/01/12	14.33h	6	75x300	12750	0.61	
2008/01/12	16.26h	3	275x350	52650	0.65	
2008/01/12	17.29h	3	25x325	6000	0.69	
2008/01/12	17.29h	6	25x275	4900	0.69	
2008/01/12	19.35h	5	100x400	25200	0.44	
2008/01/13	03.19h	3	100x375	25250	0.53	
2008/01/13	15.00h	3	250x375	62800	0.70	
2008/01/13	15.00h	5	75x400	19900	0.70	
2008/01/14	23.54h	6	50x250	50000	0.46	*
2008/01/15	01.47h	6	50x300	12200	0.53	
2008/01/15	01.47h	6	25x225	6850	0.53	
2008/01/15	02.24h	2	25x325	8550	0.37	
2008/01/15	03.01h	3	175x350	33450	0.49	
2008/01/15	03.26h	5	75x250	12850	0.34	
2008/01/15	03.51h	9	25x175	4200	0.53	
2008/01/15	07.48h	6	50x300	6650	0.57	
2008/01/15	11.47h	5	25x250	3950	0.59	
2008/01/15	12.37h	3	50x375	12000	0.53	
2008/01/16	12.53h	6	225x250	42650	0.54	
2008/01/16	12.53h	7	25x100	3000	0.54	
2008/01/16	13.31h	3	175x375	43700	0.53	
2008/01/16	13.31h	11	50x100	5150	0.53	
2008/02/04	16.01h	6	50x275	14300	0.79	
2008/02/04	16.14h	3	150x325	32150	0.76	
2008/02/04	16.14h	8	75x175	8100	0.76	
2008/02/04	16.26h	8	50x175	5800	0.63	
2008/02/04	16.26h	10	25x75	3000	0.63	
2008/02/04	16.39h	6	25x200	5000	0.58	
2008/02/04	16.52h	2	300x350	72800	0.76	
2008/02/04	17.17h	6	225x325	55550	0.69	
2008/02/04	17.43h	3	100x350	26650	0.48	
2008/02/04	18.08h	6	25x275	6300	0.45	
2008/02/04	18.08h	6	25x250	6050	0.45	
2008/02/04	18.08h	5	25x275	3750	0.45	
2008/02/04	18.21h	3	50x300	8750	0.40	
2008/02/04	19.12h	6	50x200	7650	0.47	
2008/03/10	18.47h	6	25x200	4950	0.64	
2008/03/10	19.00h	11	25x125	2950	0.50	
2008/03/10	19.00h	12	25x75	2800	0.50	
2008/03/10	19.00h	9	25x75	2650	0.50	
2008/03/10	19.25h	6	250x425	70850	0.72	
2008/03/10	19.25h	4	25x125	2800	0.72	
2008/03/10	19.50h	7	75x150	6100	0.66	
2008/03/10	20.03h	5	25x100	3050	0.56	
2008/03/10	20.03h	8	25x75	2700	0.56	
2008/03/10	20.15h	5	50x175	6600	0.53	
2008/03/10	20.28h	3	25x150	3650	0.56	
2008/03/10	20.41h	6	150x300	27600	0.66	
2008/03/10	22.47h	9	25x125	2700	0.50	
2008/03/11	18.25h	5	25x150	2950	0.52	
2008/03/11	20.06h	3	75x250	17700	0.67	
2008/03/11	20.06h	4	50x175	8100	0.67	
2008/03/11	20.44h	6	25x200	6350	0.68	
2008/03/12	00.56h	6	25x325	8000	0.57	
2008/03/12	00.56h	8	25x175	3350	0.57	
2008/03/12	14.30h	9	50x150	7500	0.95	*
2008/03/13	08.30h	5	100x325	23500	0.47	
2008/03/13	08.30h	7	175x275	19100	0.47	
2008/03/21	11.51h	9	50x100	4100	0.58	
2008/03/21	12.16h	6	50x350	12450	0.42	
2008/03/21	12.29h	9	75x225	9550	0.51	
2008/03/21	12.41h	6	75x300	17700	0.57	
2008/03/21	12.54h	3	150x350	37650	0.52	
2008/03/21	13.19h	6	125x300	24450	0.52	
2008/03/21	14.34h	6	175x250	25500	0.62	
2008/03/21	15.24h	3	225x375	45350	0.69	
2008/03/21	17.05h	11	50x150	5950	0.44	
2008/03/21	17.18h	9	25x175	3900	0.50	
2008/03/21	17.43h	6	125x250	13200	0.85	
2008/03/21	17.56h	6	125x300	23950	0.66	
2008/03/21	17.56h	9	100x175	8000	0.66	
2008/03/21	18.08h	6	100x225	14750	0.72	
2008/03/21	18.08h	6	50x275	11400	0.72	
2008/03/21	18.21h	6	75x250	13200	0.65	
2008/03/21	18.46h	6	250x375	56150	0.57	
2008/03/21	20.40h	3	125x375	39450	0.47	
2008/03/22	08.21h	5	100x250	25000	0.76	*
2008/03/22	08.21h	6	100x250	25000	0.76	*
2008/03/22	08.34h	5	50x250	12500	0.86	*
2008/03/27	17.25h	9	100x175	14100	0.63	
2008/03/27	17.50h	6	100x225	20250	0.72	
2008/03/27	17.50h	7	75x100	6150	0.72	
2008/03/27	18.03h	6	50x250	8600	0.62	
2008/03/27	18.16h	3	125x350	18050	0.66	
2008/03/27	18.28h	5	25x150	3600	0.58	
2008/03/27	19.31h	5	75x250	11700	0.63	
2008/03/27	19.31h	4	100x175	11200	0.63	
2008/03/27	19.44h	6	200x300	27750	0.60	
2008/03/27	20.10h	3	275x400	63200	0.63	
2008/03/27	20.22h	6	100x250	25000	0.75	*
2008/03/27	20.22h	6	50x250	12500	0.75	*
2008/03/27	20.48h	11	25x125	3450	0.74	
2008/03/27	21.13h	8	75x175	9650	0.69	
2008/03/27	21.26h	3	125x325	23550	0.71	
2008/03/27	21.26h	8	25x150	5600	0.71	
2008/03/27	22.04h	3	200x325	46250	0.64	
2008/03/27	22.16h	3	250x450	75000	0.81	
2008/03/27	22.42h	5	150x300	45000	0.91	*
2008/03/27	23.07h	2	75x350	20050	0.52	
2008/03/31	17.39h	9	25x200	5450	0.44	

```
%Elapsed time: 01:55:26
%Intensity threshold...: 60/255
%Parameters to select/accept/discard objects:
%   AxLen...(m)..: 150.00
%   Orient..(deg): 45.00
%   AxRatio......: 1.50
%   MinArea.(m^2): 2500.00
%   MaxArea.(m^2): 90000.00
%   BrRatio......: 0.90
%Number of avalanches candidates: 271/12165
%Avalanches after supervision: 111+10
```

Bibliography

[1] K. Seidel et al., "Remote sensing of snow cover for operational forecasts," *in Proc. Int. Symp. Operationalization of Remote Sensing*, pp. 134–145, 1993.

[2] C. Mätzler, "Passive microwave signatures of landscapes in winter," *Meteorol. Atmosph. Phys.*, vol. 54, pp. 241–260, 1994.

[3] M. Hallikainen and P. Jolma, "Comparison of algorithms for retrieval of snow water equivalent from Nimbus-7 SSMR data in Finland," *IEEE Trans. Geosci. Remote Sensing*, vol. 30, pp.124-131, Jan. 1992.

[4] J. Koskinen, L. Kurvonen, V. Jääskeläinen and M. Hallikainen, "Capability of radar and microwave radiometer to classify snow types in forested areas," *in Proc. IGARSS'94 Symp.*, Pasadena, CA, pp.1283–1286, 1994.

[5] S. Jiancheng, J. Dozier and H. Rott, "Snow mapping in alpine regions with synthetic aperture radar," *IEEE Trans. Geosci. Remote Sensing*, vol. 32, n.1, pp.152-158, January 1994.

[6] J. Shi, J. Dozier and H. Rott, "Deriving snow liquid water content using C-band polarimetric SAR," *in Proc. IGARSS'93 Symp.*, Tokyo, Japan, pp. 1038–1041, 1993.

[7] J.T. Koskinen, J.T. Pulliainen and M.T. Hallikainen, "The use of ERS-1 SAR data in snow melt monitoring," *IEEE Trans. Geosci. Remote Sensing*, vol. 35, n.3, pp.601-610, May 1997.

[8] Y. Yamaguchi, M. Mitsumoto, M. Sengoku and T. Abe, "Human Body Detection in Wet Snowpack by an FM-CW Radar," *IEEE Trans. Geosci. Remote Sensing*, vol. 30, pp.186-189, Jan. 1992.

[9] P. Kanagaratnam, T. Markus, V. Lytle, B. Heavey, P. Jansen, G. Prescott and S.P. Gogineni, IEEE"Ultrawideband Radar Measurements of Thickness of Snow Over Sea Ice," *IEEE Trans. Geosci. Remote Sensing*, vol.45, no. 9, September 2007.

[10] D. McClung and P. Schaerer, "The Avalanche Handbook," *The Mountaineers*, Seattle, 1993.

[11] J.R. Wang, A. T.C. Chang and A.K.Sharma, "On the Estimation of Snow Depth from Microwave Radiometric Measurements", *IEEE Trans. Geosci. Remote Sensing*, vol. 30, pp.785-792, Jul. 1992.

[12] R. Rice, R. Decker, N. Jensen, R. Patterson, S. Singer, C. Sullivan and L. Wells, "Avalanche hazard reduction for transportation corridors using real-time detection and alarms," *Cold Regions Science and Technology* 34, 2002.

[13] H. Gubler, "Remote Avalanche Warning, Alarm and Control Systems, Fundamentals, Applications and Experience," *Proc. of the International Snow Science Workshop*, Banff, Canada 1996.

[14] H. Rudolf, D. Leva, D. Tarchi and A.J. Sieber, "A mobile and versatile SAR system," Proc. *IEEE Geosc. and Remote Sens. Symposium*, Hamburg 1999.

[15] M. Pieraccini, G. Luzi and C. Atzeni, "Terrain mapping by ground-based interferometric radar," *IEEE Transactions on Geoscience and Remote Sensing*, vol.39, pp.2176-2181, Oct. 2001.

[16] A. Aguasca, A. Broquetas, J. Mallorqui and X. Fàbregas, "A solid state L to X-band flexible ground-based SAR system for continuous monitoring applications," *Proc. IGARSS*, pp.757-760, Anchorage, 2004.

[17] J.C. Bennett, K. Morrison, A.M. Race, G. Cookmartin and S. Quegan, "The UK NERC fully portable polarimetric ground-based synthetic aperture radar (GB-SAR)," *Proc. IGARSS*, Honolulu, 2000.

[18] A. Martinez-Vazquez, J. Fortuny-Guasch and U. Gruber, "Monitoring of the Snow Cover with a Ground-Based Synthetic Aperture Radar." *European Association of Remote Sensing Laboratories, EARSeL eProceedings*, vol.4, n.2, pp.171-178, October 2005.

[19] GALAHAD. "Advanced Remote Monitoring Techniques for Glaciers, Avalanches and Landslides Hazard Mitigation," *Project N. 018409, European Commission - 6th Framework Programme*, 2005-2008. http://www.galahad.it

[20] K. Morrison, H. Rott, T. Nagler, H. Rebhan and P. Wursteisen, "The SARALPS-2007 measurement campaign on X and Ku-Band Backscatter of snow", *Proc. IEEE Geosc. and Remote Sens. Symposium*, July 2007.

[21] R.A. Sommerfeld, "Preliminary observations of acoustic emissions preceding avalanches," *IGS Journal of Glaciology*, 19(81), 399-409, 1977.

[22] R. Buderi, "The invention that changed the world," *Simon & Schuste*, New York, 1996.

[23] W.G. Carrara, R.S. Goodman and R.M. Majewski, "Spotlight Synthetic Aperture Radar, Signal Processing Algorithms," *Artech House*, 1995.

[24] C. Elachi, "Spaceborne radar remote sensing: applications and techniques," *IEEE Press*, 1987.

[25] D. Mensa, "High Resolution Radar Cross Section Imaging, 2nd rev." *Artech House*, 1991.

[26] J. Fortuny-Guasch, "A fast and accurate far-field pseudo-polar format radar imaging algorithm," *IEEE Transactions on Geoscience and Remote Sensing*, submitted for publication in May 2008.

[27] F. K. Li and M. Goldstein, "Studies of Multibaseline Spaceborne Interferometric Synthetic Aperture Radars," *IEEE Transactions on Geoscience and Remote Sensing*, vol.28(1), pp. 88-97, 1990.

[28] J.O. Hagberg, L.M.H. Ulander and J. Askne, "Repeat-pass SAR interferometry over forested terrain," *IEEE Transactions on Geoscience and Remote Sensing*, vol.33(2), pp.331-340, March 1995.

[29] A.K. Gabriel, R.M. Goldstein and H.A. Zebker, "Mapping Small Elevation Changes Over Large Areas: Differential Radar Interferometry," *Journal of Geophysical Research*, vol.94(B7), pp.9183-9191, 1989.

[30] R.F. Hanssen, "Radar Interferometry, Data Interpretation and Error Analysis," *Kluwer Academic Publishers*, The Netherlands, 2001.

[31] F. Gatelli, A.M. Guamieri, F. Parizzi, P. Pasquali, C. Prati and F. Rocca, "The wavenumber shift in SAR interferometry," *IEEE Transactions on Geoscience and Remote Sensing*, vol.32, pp.855-865, July 1994.

[32] G. Nico, D. Leva, J. Fortuny-Guasch, G. Antonello and D. Tarchi, "Generation of Digital Terrain Models With a Ground-Based SAR System." *IEEE Transactions on Geoscience and Remote Sensing*, vol.43, no. 1, January 2005.

[33] D.C. Ghiglia and M.D. Pritt, "Two-Dimensional Phase Unwrapping. Theory, Algorithms and Software," *John Wiley & Sons*, 1998.

[34] A.J. Sieber, "The European Microwave Signature Laboratory," *EARSeL Advanced in Remote Sensing*, vol.2, pp.192-207, January 1993.

[35] G. Nico, D. Leva, G. Antonello and D. Tarchi, "Ground-Based SAR Interferometry for Terrain Mapping: Theory and Sensitivity Analysis," *IEEE Trans. Geosc. Remote Sensing Communications*, Vol. 42, No. 6, June 2004.

[36] T. Strozzi and C. Matzler, "Backscattering Measurements of Alpine Snowcovers at 5.3 and 35 GHz," *IEEE Trans. Geosc. Remote Sensing*, vol.36, pp.838-848, May 1998.

[37] F. Dufour, U. Gruber, B. Sovilla and P. Bartelt, "A new Swiss test-site for avalanche Experiments in the Vallée de la Sionne / Valais," http://www.wsl.ch/slf/schnee-lawinen/Lawinendynamik/VdlS/vdls-haupt-en.html

[38] Digital Height Model DOM. Federal Office of Topography, swisstopo, Switzerland. http://www.swisstopo.admin.ch/internet/swisstopo/en/home/products/height/dom_dtm-av.html

[39] A. Martinez-Vazquez and J. Fortuny-Guasch, "3 winters of snow monitoring with the LISA instrument in the Sion Valley (CH): 2003-2006," Technical report EUR 22533 EN, ISSN 1018-5593. *Office for Official Publications of the European Communities* (Luxembourg). October 2006.

[40] A. Martinez-Vazquez, J. Fortuny-Guasch and G. Antonello, "Two winters of snow monitoring with the LISA instrument in Alagna Valsesia – Val d'Olen (I): 2005-2007," Technical report EUR 22947 EN, ISSN 1018-5593. *Office for Official Publications of the European* Communities (Luxembourg). October 2007.

[41] M. Lehning, "The Swiss snow cover model SNOWPACK." Swiss Institute for Snow and Avalanche Research, SLF. http://www.slf.ch/snowpack/welcome-en.html

[42] T. Guneriussen, K.A. Hogda, H. Johnsen and I. Lauknes, "InSAR for estimation of changes in snow water equivalent of dry snow", *IEEE Transactions on Geoscience and Remote Sensing*, vol.39, pp.2101-2108, Oct. 2001.

[43] S. Oveisgharan and H.A. Zebker, "Estimating Snow Accumulation from InSAR Correlation Observations." *IEEE Transactions on Geoscience and Remote Sensing*, vol.45(1), pp.10-20, January 2007.

[44] T. Nagler and H. Rott, "Retrieval of Wet Snow by Means of Multitemporal SAR Data." *IEEE Transactions on Geoscience and Remote Sensing*, vol.38(2), pp.754-765, March 2000.

[45] J. Shi and J. Dozier, "Estimation of snow water equivalence using SIR-C/X-SAR. II. Inferring snow depth and particle size." *IEEE Transactions on Geoscience and Remote Sensing*, vol.38(6), pp.2475-2488, November 2000.

[46] C. Mätzler, "Microwave permittivity of dry snow." *IEEE Transactions on Geoscience and Remote Sensing*, vol.34(2), pp.573-581, 1995.

[47] C. Mätzler, "Applications of the interaction of microwaves with the natural snow cover." *Remote Sensing Review*, vol.2, pp.259-387, 1987.

[48] G. Luzi, M. Pieraccini, D. Mecatti, L. Noferini, G. Guidi, F. Moia and C. Atzeni, "Ground-based radar interferometry for landslides monitoring: atmospheric and instrumental decorrelation sources on experimental data," *IEEE Transactions on Geoscience and Remote Sensing*, vol.42, pp.2454-2466, November 2004.

[49] L. Noferini, M. Pieraccini, D. Mecatti, G. Macaluso, G. Luzi and C. Atzeni, "DEM by Ground-Based SAR Interferometry." *IEEE Geoscience and Remote Sensing Letters*, vol.4, pp.659-663, October 2007.

[50] L. Noferini, M. Pieraccini, D. Mecatti, G. Luzi, C. Atzeni, A. Tamburini and M. Broccolato, "Permanent Scatterers Analysis for Atmospheric Correction in Ground-Based SAR Interferometry." *IEEE Transactions on Geoscience and Remote Sensing*, vol.43, pp.1459-1471, July 2005.

[51] L. Pipia, X. Fabregas, A. Aguasca and C. López-Martínez, "Atmospheric Artifact Compensation in Ground-Based DInSAR Applications." *IEEE Geoscience and Remote Sensing Letters*, vol.5, pp.88-92 January 2008.

[52] M. Hallikainen, F. Ulaby and M. Abdelrazik, "Dielectric properties of snow in the 3 to 37 GHz range." *IEEE Transactions on Antennas and Propagation*, vol.34, pp.1329- 1340, November 1986.

[53] A. Martinez-Vazquez and J. Fortuny-Guasch, "Averaging and Formulation Impact on GB-SAR Topographic Mapping." *IEEE Geoscience and Remote Sensing Letters*, Accepted for publication on June 9th, 2008.

[54] A. Shaban, G. Faour, M. Khawlie and C. Abdallah, "Remote sensing application to estimate the volume of water in the form of snow on Mount Lebanon." *Journal of Hydrological Sciences*, vol.49(4), pp.643-653, August 2007.

[55] B. Sovilla, "Field experiments and numerical modelling of mass entrainment and deposition processes in snow avalanches," *PhD Thesis No. 15462*, ETH Zurich, Switzerland, 2004.

[56] B. Sovilla, S. Margretha and P. Bartelta, "On snow entrainment in avalanche dynamics calculations," *Cold Regions Science and Technology, International Snow Science Workshop*, vol.47(1-2), pp.69-79, September 2004.

[57] J. Vallet, J. Skaloud, O. Koelbl and B. Merminod, "Development of a Helicopter-Based Integrated System for Avalanche Mapping and Hazard Management," *International Archives of Photogrammetry and Remote Sensing,* vol. XXXIII(B2). Amsterdam 2000.

[58] J. Vallet, U. Gruber and F. Dufour, "Photogrammetric avalanche volume measurements at Vallee de la Sionne, Switzerland," *Annals of Glaciololgy*, no.32, pp.141-146, 2001.

[59] A. Martinez-Vazquez and J. Fortuny-Guasch, "Feasibility of Snow Avalanche Volume Retrieval by GB-SAR Imagery." *IEEE Geoscience and Remote Sensing Symposium*, Denver 2006.

[60] H.A. Zebker, S.N. Madsen, J. Martin et al., "The TOPSAR Interferometric Radar Topographic Mapping Instrument," *IEEE Transactions on Geoscience and Remote Sensing*, vol.30, no.5, September 1992.

[61] M. Bilker and H. Kaartinen, "The Quality of Real-Time Kinematic (RTK) GPS Positioning," *Reports of the Finnish Geodetic Institute*, 2001.

[62] L. Jong-Sen, K.W. Hoppel, S.A. Mango and A.R. Miller, "Intensity and phase statistics of multilook polarimetric and interferometric SAR imagery," *IEEE Transactions on Geoscience and Remote Sensing*, vol.32(5), pp.1017-1028, September 1994.

[63] E. Rodriguez and J. Martin, "Theory and design of interferometric synthetic aperture radars," *Radar and Signal Processing, IEE Proceedings F*, vol. 139(2), pp.147-159, April 1992.

[64] H.A. Zebker and J. Villasenor, "Decorrelation in interferometric radar echoes," *IEEE Transactions on Geoscience and Remote Sensing*, vol.30(5), September 1992.

[65] A. Martinez-Vazquez, J. Fortuny-Guasch, "Snow Cover Monitoring in the Swiss Alps with a GB-SAR," *IEEE Geoscience and Remote Sensing Society Newsletter*, pp.11-1, March 2006.

[66] A. Wiesmann, U. Wegmüller, M. Honikel, T. Strozzi and C.L. Werner, "Potential and methodology of satellite based SAR for hazard mapping," *Proc. IEEE Geoscience and Remote Sensing Symposium*, vol.7, pp.3262-3264, July 2001.

[67] A.H.S. Solberg, C. Brekke and P.P. Husoy, "Oil Spill Detection in Radarsat and Envisat SAR Images," *IEEE Transactions on Geoscience and Remote Sensing*, vol.45, pp.746-755, March 2007.

[68] F. Girard-Ardhuin, G. Mercier, F. Collard and R. Garello, "Operational oil-slick characterization by SAR imagery and synergistic data," *IEEE Journal of Oceanic Engineering*, vol.30, pp.487-495, July 2005.

[69] A. Martinez-Vazquez and J. Fortuny-Guasch, "Snow Avalanche Detection and Classification Algorithm for GB-SAR Imagery," *Proc. IEEE Geoscience and Remote Sensing Symposium*, Barcelona, 2007.

[70] A. Martinez-Vazquez and J. Fortuny-Guasch, "A GB-SAR Processor for Snow Avalanche Identification." *IEEE Transactions on Geoscience and Remote Sensing*, Accepted for publication on June 1st, 2008.

[71] N. Otsu, “A Threshold Selection Method from Gray-Level Histograms,” *IEEE Transactions on Systems, Man and Cybernetics*, vol.9, pp.62-66, Jan. 1979.

[72] R.M. Haralick and L.G. Shapiro, “Computer and Robot Vision, Vol. I,” *Addison-Wesley*, 1992.

[73] A.H.S. Solberg, G. Storvik, R. Solberg and E. Volden, “Automatic detection of oil spills in ERS SAR images,” *IEEE Transactions on Geoscience and Remote Sensing*, vol.37, pp.1916-1924, July 1999.

[74] H. Gubler, “Five years experience with avalanche-, mudflow- and rockfall- alarm systems in Switzerland,” *Proceedings of the International Snow Science Workshop*, Big Sky, Montana, 2000.

[75] Electronics Industries Association, “EIA Standard RS-232-C Interface Between Data Terminal Equipment and Data Communication Equipment Employing Serial Data Interchange”, August 1969, reprinted in *Telebyte Technology Data Communication Library*, Greenlawn NY, 1985.

Printed: 28 September 2008